

Electrodeposition of Crystalline MoS₂-based Heterostructures and Amorphous MoS_x-based Alloys and Matrixes as Catalysts for the Hydrogen Evolution Reaction

A Dissertation Presented to the Faculty of the School of Engineering and Applied Science
University of Virginia

In partial fulfillment of the requirements for the degree of
Doctor of Philosophy in Materials Science and Engineering

Lee Michael Kendall

April 19, 2024

Abstract

With increasing global energy consumption, increased ammonia demands, ever decreasing fuel reserve, and severe climate change, there has been a large drive to explore various clean, renewable, and affordable energy sources. However, several prolific renewable energy sources, such as wind and solar, suffer from intermittent availability. To overcome this, several strategies have been explored to enable the storage of excess energy in chemical bonds to be utilized later during high demand. H_2 has the highest energy density among all chemical fuels and can be combusted to release “clean” energy, with water being the only product. Currently, the primary methods of generating H_2 is through steam reforming, coal/oil coke/biomass gasification, and H_2O splitting. As all but the latter generate enormous amounts of CO_2 , there is a drive to develop H_2O splitting, a pollution-free, low-cost, and efficient H_2 and O_2 production technology.

The hydrogen evolution reaction (HER) is a pivotal process in the field of energy conversion and storage, particularly in the context of sustainable hydrogen production. Current electrocatalysts for HER, while effective, are often reliant on precious metals such as platinum, which are expensive and scarce. This highlights the urgent need for the development of new, cost-effective, and abundant electrocatalysts. In this context, molybdenum disulfide (MoS_2) based materials have emerged as promising candidates for HER. MoS_2 , a transition metal dichalcogenide, offers several advantages including natural abundance, cost-effectiveness, and tunable electronic properties. However, the catalytic performance of bulk MoS_2 is limited due to a low density of active sites, however, recent research has shown that the catalytic activity of MoS_2 can be significantly enhanced by engineering its morphological and structural properties.

This thesis will first explore the challenges and advancements of existing MoS₂-based electrocatalysts. Through the rest of the thesis, we use electrodeposition to form various MoS₂-based heterostructures, such as CoS_x/MoS₂, ZnO/MoS₂, and ZnO/ZnS/MoS₂, as well as the amorphous MoS_x phases and several MoS_x-based alloys, such as MoS_xSe_y, MoS_xO_y, and MoTe_y/MoS_x. We utilize a combination of substrate modifications and post-synthesis treatments to modify the overall morphology, crystallinity, and chemistry of the studied material. Using a variety of characterization techniques, this thesis studies the processing-structure-properties of the various electrocatalysts towards the hydrogen evolution reaction with the goal of enabling viable HER electrocatalysts.

Acknowledgements

The work presented here would not have been possible if not for those around me. When I first toured the Materials Science and Engineering department back in early 2019, the thing that stuck out to me was the companionship that the graduate students had with one another, regardless of their year or research focus. This fellowship, especially within my cohort, is what helped me get through the rough days, no matter if was class work, research, or just general life things.

I would also like to thank my research advisors, Professors Stephen McDonnell and Giovanni Zangari. Throughout my time, they supported me through constant discussions, XPS fitting sessions, presentation critiques, and *trying* to just get me to answer the question instead of going off on tangents. As I have started working prior to finishing this thesis, I can look back and say with confidence that I was equipped to succeed in my transition to the work force. I would also like to thank each of my committee members, Professors Rob Kelly, James Fitz-Gerald, Gary Koenig, and Thomas Beechem for their time and effort through various points of my PhD experience.

I would also like to thank several of the other researchers that have helped along the way. Dr. Zach Piontkowski of Sandia National Laboratory was critical in contributing his Raman expertise to my first paper. Other critical researchers have been the entire NMCF staff, especially Dr. Cathy Dukes, Diane Dickie, and Dr. Joe Thompson for their efforts in training me on the equipment, answering questions, and helping troubleshoot when things don't go to plan.

Finally, I want to thank all of those around me, notably those within the McDonnell and Zangari lab groups. Dr. Meg Sales, Dr. Peter Litwin, Gaby Abad, and Vicker Wallemacq from the McDonnell group were indispensable in supporting me in the lab and just letting me vent about

life. Even before I started, Meg and Peter made me feel so welcome and supported by the group. From the Zangari group I would like to thank Dr. Yunkai Sun, Dr. Qiyuan Lin, Dr. Yin Xu, Dr. Ali Akbari Sehat, and Dr. Amir Chamaani for their many discussions, from everything electrochemistry all the way to life outside the US and their many life stories. I also want to thank Dawn, who forced me to slow down, explain things, and think about things in a different way, both in lab and in life. I swear I will probably work for her one day. I would also like to thank the 3rd-floor and B-floor teams for all of your emotional and scientific support (and for always giving me a good laugh with our office door décor). Thanks to my team over at Coherent, notably Chick, for supporting me and hiring me under the assumption that I would finish this thesis “one day”.

I want to thank my family for all their encouragement and support that got me to this point. Shout out to the goofball that is my dog, Loki, for always bringing a smile to my face and having a play-mate. Lastly, I want to thank my wonderful wife, Katie, that supported me not only when we were close, but also when we lived apart. You always brought comfort and support to me and always pushed me to do my best.

I am so grateful to everyone that I met along this journey, I could not have done this without you.

Table of Contents

1.0 Introduction	9
1.1 Background and Motivation	9
1.2 Alternative MoS₂-based Electrocatalysts	11
1.3 Thesis Objectives	15
2.0 Experimental Methods	17
2.1 Synthesis Methods	17
2.1.1 Electrodeposition	17
2.1.2 Annealing	19
2.2 Characterization Methods	20
2.2.1 X-ray Photoelectron Spectroscopy	20
2.2.2 Raman Spectroscopy	26
2.2.3 UV-Visible Spectroscopy	28
2.2.4 X-ray Reflectivity	31
2.2.5 X-ray Diffraction	31
2.2.6 Scanning Electron Microscopy	32
2.2.6 Electrochemical Measurements	33
3.0 Crystalline MoS₂-based Heterostructures	37
3.1 Study of Electrodeposited Molybdenum Disulfide on Zinc Oxide and Zinc Oxide/Zinc Sulfide Nanowires	37
3.1.1 Background and Motivation	37
3.1.2 Synthesis Methods	40
3.1.3 Results	42
3.1.4 Conclusions	61
3.2 The Electrodeposition of Cobalt Sulfide/Molybdenum Sulfide Heterostructures for HER in Acidic and Alkaline Solutions	63
3.2.1 Background and Motivation	63
3.2.2 Synthesis Methods	65
3.2.3 Results	68
3.2.3 Conclusions	80
4.0 Incorporation of Chalcogens into Amorphous, Polymeric MoS_x	82

4.1 The Influence of Oxygen Incorporation on the HER Catalytic Activity of Electrodeposited MoS_xO_y Electrocatalysts	82
4.1.1 Background and Motivation	82
4.1.2 Synthesis Methods	83
4.1.3 Results of As Deposited, Oxidized, Inert Anneal, and Sulfur Anneals	91
4.1.4 Conclusions.....	103
4.2 Selenium Incorporation into MoS_x via Electrodeposition to form a Ternary Se-MoS_x Alloy for HER.....	105
4.2.1 Background and Motivation.....	105
4.2.2 Synthesis Methods	106
4.2.3 Results of Se-MoS _x	111
4.2.4 Conclusions.....	130
4.3 Te Incorporation into MoS_x via Electrodeposition to Form a Two Phase MoTe_x/MoS_x Matrix.....	131
4.3.1 Background and Motivation.....	131
4.3.2 Synthesis Methods	131
4.3.3 Results.....	135
4.3.4 Conclusions.....	152
5.0 Future Works.....	153
5.1 Designing an Amorphous MoO₃/Se-MoS_x Catalyst for OER.....	153
5.1.1 Background and Motivation.....	153
5.1.2 Research Methodology	154
5.1.3 Preliminary Data	155
5.1.4 Summary	157
5.2 Growth of MoS_{2x}Se_{2(1-x)}.....	157
5.2.1 Background and Motivation.....	157
5.2.2 Research Methodologies.....	158
5.2.3 Preliminary Data	158
5.2.4 Summary	160
6.0 Thesis Conclusions	161
7.0 Appendix	164
7.1 Attempt at Synthesizing Free-standing MoS ₂ nanowires	164
7.2 Attempt at Synthesizing c/CoS _x /MoS ₂ via sulfurization of metal Electrodeposition	165

7.3 Raman Analysis of Amorphous MoS_x	168
8.0 References	170

1.0 Introduction

1.1 Background and Motivation

With the increase in global energy consumption, increased ammonia demands, ever decreasing fuel reserve, and severe climate change, there has been a large drive to explore various clean, renewable, and affordable alternative energy sources.¹ One strategy that has been explored includes converting clean energies to electric power to store them in chemical carriers, such as H₂.² H₂ has the highest energy density among all chemical fuels, as shown in Figure 1.1, (theoretically 142 MJ/kg) and can be combusted to release “clean” energy, with water being the only product.³ As such, there has been a drive to develop pollution-free, low-cost, and efficient H₂ production technologies.

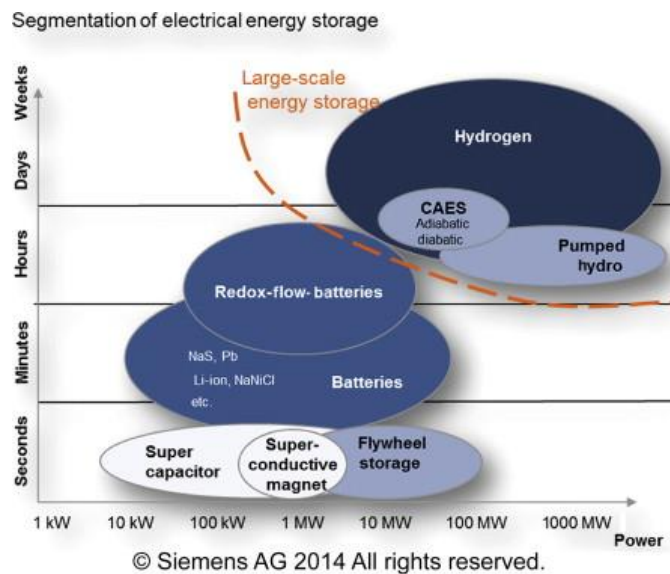


Figure 1.1: Diagram demonstrating the capabilities of energy storage techniques as a function of time and power

Currently, the primary method of generating hydrogen is through steam reforming, coal/oil coke/biomass gasification, and H₂O splitting. These processes, which account for 95% of the

global H₂ production, involve the use of fossil fuels, releasing pollutants and greenhouse gases in the process. As such, these techniques account for nearly 1% of the world's annual CO₂ emissions and require roughly 1% of the world's energy production.⁴ This H₂ is then used in other high demand industrial processes, such as oil refining and fertilizer production.⁵ In comparison, by splitting H₂O into H₂ and O₂ using renewable energies, H₂ can be produced in a clean, green, and sustainable way while also supplying O₂, which has extensive industrial applications.^{5,6}

There are a number of approaches to splitting water, such as electrolysis, photolysis, photoelectrolysis, pyrolysis, and biolysis.^{7,8} Out of these techniques, electrolysis is inarguably the most promising technique due to its simple, clean, safe, and scalable process that manufacture high purity products. However, the main obstacle to the widespread and large-scale production is the large energy consumption needed.⁷ To minimize this, researchers have heavily investigated materials that would lower the electrode polarization, thereby reducing the overpotential of the hydrogen evolution reaction (HER) by lowering the activation energy and accelerating the reaction rate.⁹ While platinum and other noble metal-based electrocatalysts are well known to catalyze the HER efficiently, their widespread use is restricted by high cost and scarce geological reserves.⁵

1.2 Alternative MoS₂-based Electrocatalysts

For this reason, alternative electrocatalysts based on naturally abundant transition metal sulfides, phosphides, nitrides, and carbides^{10–13} are increasingly being pursued. One prominent and the most heavily investigated example is the transition metal dichalcogenide (TMDC), MoS₂, and MoS₂-based catalysts. Crystalline MoS₂ is comprised of sandwiched S – Mo – S layers and can be categorized into three polymorphs, hexagonal (2H), trigonal (1T), and rhombohedral symmetry (3R). Among the three crystalline phases, 2H and 1T are the most widely utilized. In 2005, MoS₂ was first reported as a promising electrocatalyst due to its edge sites being able to effectively drive HER. Calculations showed that the Gibbs adsorption energy for H⁺, $\Delta G_{0,ads}^H$, of the ($\bar{1}010$) edge site is around 0.08 eV, which is very close to that of Pt (~ 0 eV), as shown in Figure 1.2a.^{14–19} However, this low $\Delta G_{0,ads}^H$ is only observed along the edge planes of crystalline MoS₂, thus inherently limiting the number of active catalytic sites as shown in Figure 1.2b.²⁰ Recent efforts have attempted to increase the number of active sites in MoS₂, as well as in transition metal selenides, via several approaches, such as: heterostructure design, increasing edge sites (such as vertically aligned synthesis), purposeful creation of sulfur vacancies, the use of nanoparticles, or nanowires.

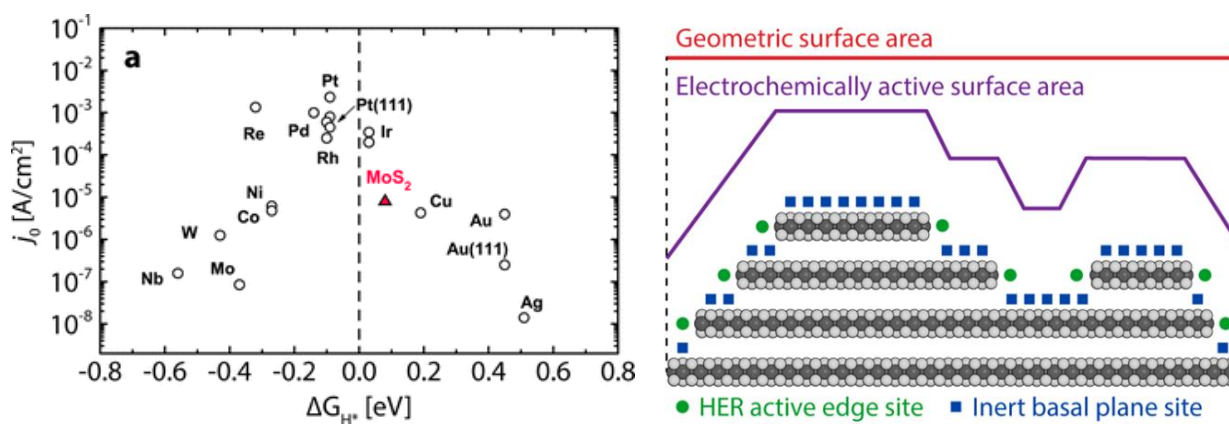


Figure 1.2 a) Volcano plot for the adsorption of H⁺ and b) schematic of MoS₂ and its active and inert sites

A common strategy for enhancing the HER performance is to maximize the specific area of the catalytically active edge sites. This has been accomplished by synthesizing MoS₂ in and on via various morphologies, such as nanoparticles, nanosheets, vertical nanoflakes, and what will be discussed in this thesis, nanowires. This has become even more relevant as it was shown that the HER catalytic activity of the MoS₂ increases linearly with the number of edge sites.²¹ A brief overview of these follows.

MoO₃-MoS₂ core shell nanowires were synthesized via the sulfurization of MoO₃ nanowires in an H₂S atmosphere.²² This nanowire morphology allowed for high surface area of the catalytically active MoS₂ by exposing a larger number of active edge sites per geometric area. Additionally, the authors noted that the MoO₃ core facilitated charge transport along the nanowires and the catalyst performed reasonably well, requiring 250 mV to reach 10 mA/cm². However, TEM revealed a lower density of exposed edge sites than anticipated, with a significant portion of the MoS₂ basal wrapping around the nanowires. Overall, this proved a positive step towards the use of MoS₂ based nanowires, albeit requiring a toxic environment.

MoS₂ nanoparticles have been synthesized in a variety of manners, such as thermal sulfurization, chemical reduction, and chemical exfoliation to name a few.²³⁻²⁵ This again was to maximize the exposed active edge sites of MoS₂ while minimizing the inert basal plane. The most promising approach was the solvothermal synthesis using (NH₄)MoS₄ and hydrazine in dimethylformamide. The resulting MoS₂ was then supported on reduced graphene oxide (r-GO) which saw a substantial improvement over non-supported MoS₂. This led to a reduction in potential required to drive the hydrogen evolution reaction (HER) via improved dispersion and charge transport. More work has followed with other carbon-based materials as the supporting electrode, such as carbon paper and graphene.²⁶⁻²⁸

Another approach has been to use flat substrates, but to vertically align the MoS₂ so that the edge sites are exposed.²⁹ This allows for fast electron transport through the MoS₂ layers while limiting the exposure of the basal plane. This vertical structure was synthesized using electron beam deposited Mo that was annealed in a sulfur environment. Unfortunately, this morphology had limited success due to its large Tafel slope and low turnover frequency.

Another tact that will be explored in this thesis is the formation of heterostructures, as it has been shown that the interface between MoS₂ and other materials can be highly catalytically active, thereby increasing the catalytic activity over the individual species.³⁰⁻³³ They also afford for variations in the morphology, allowing for various geometries to be explored and optimized for HER, like the MoS₂-MoO₃ nanowires discussed earlier. A variety of different materials with MoS₂ have been investigated and have been shown to modulate the HER performance. For example, MoS₂/Mo₂C, 1T-MoS₂/CoS, Ni(OH)₂/MoS₂, MoS₂/NiCo-based layered double hydroxide, Ni₂P/MoS₂/carbon nanotubes, and MoS₂/MoP₂ have all been investigated.³⁴⁻⁴¹ Through these studies, MoS₂ demonstrated fast adsorption of H_{ads} when synthesized as a heterostructure with other materials, such as carbides, phosphides, oxides, etc. by increasing the slow Volmer step in the hydrogen evolution reaction. The wide materials space as well as the modulation of the interface is a likely path forward when designing MoS₂-based heterostructure catalysts for the hydrogen evolution reaction. This thesis will focus on two primary heterostructures, that of MoS₂ with ZnO and ZnS, and that of MoS₂ with Co₉S₈ and CoS₂. Both of these topics will be explored more thoroughly in their respective chapters.

The final approach this thesis will explore is focused on highly disordered and alloyed polymeric MoS_x . Coordinated polymeric MoS_x chains, typically termed amorphous MoS_x or a-MoS_x , exhibit excellent catalytic activity for HER, owing to the combination of structural heterogeneity that increases catalytic site density combined with short-range atomic arrangements that enable adequate electronic conductivity for use in electrochemical processes.^{11,42–46} Amorphous MoS_x is comprised of polymeric aggregations of Mo^{4+} clusters, with a variety of bonded sulfurs such as bridging S_2^{2-} , terminal S_2^{2-} , unsaturated S^{2-} , and apical S^{2-} ligands, as seen in Figure 1.3. This structure is based on the building blocks of $[\text{Mo}_3\text{S}_{13}]^{2-}$ clusters and share similar

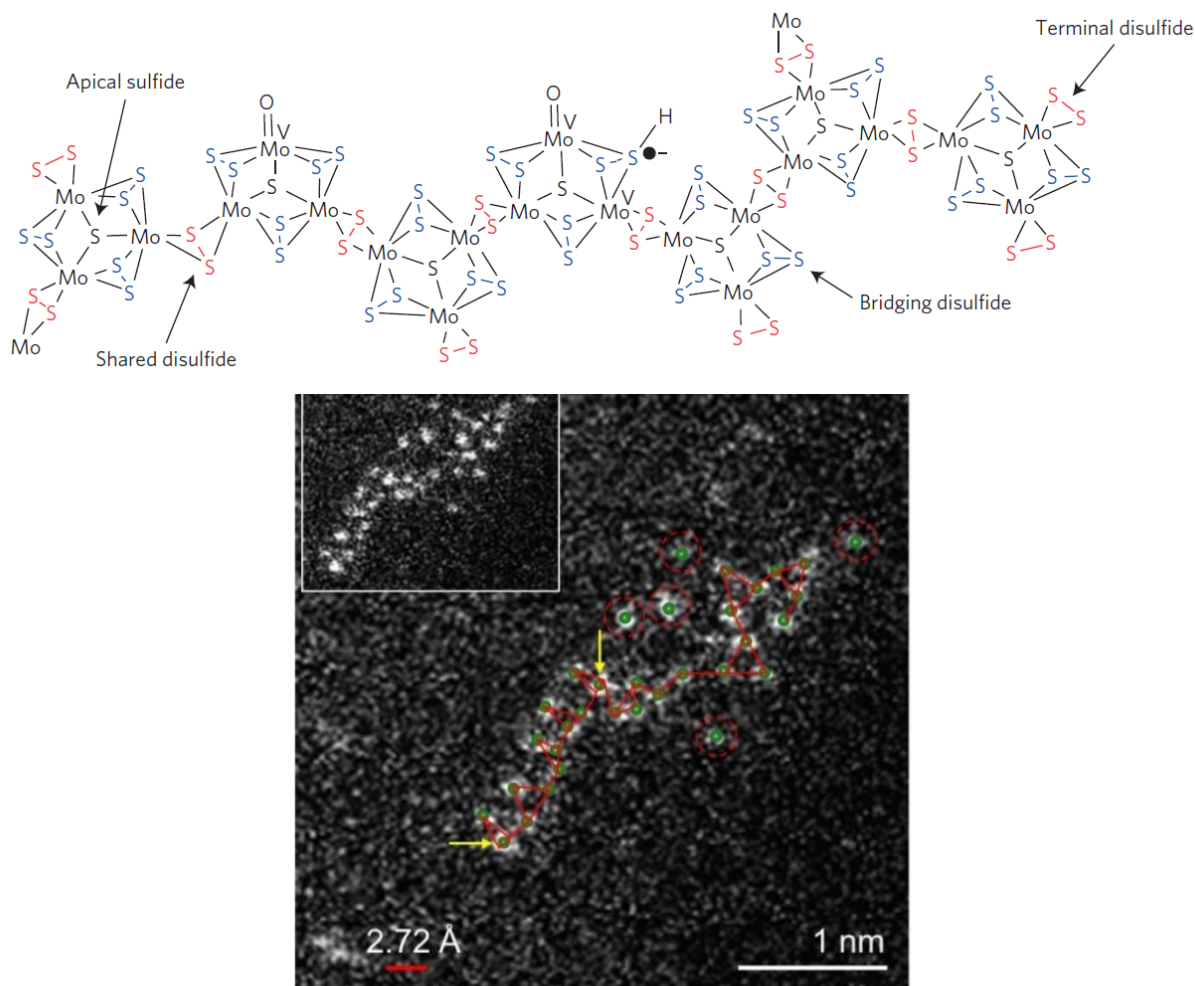


Figure 1.3: Amorphous MoS_x coordination polymer with $[\text{Mo}_3\text{S}_{13}]^{2-}$ building block units to form a chain¹¹ b) HAADF-STEM images of $(\text{Mo}_3\text{S}_{13})^{2-}$ clusters and a-MoS_x chains¹¹

characteristics to each other. Bridging sulfurs connect two adjacent Mo within the cluster or two Mo between clusters and are analogous in configuration to the edge plane in crystalline MoS₂. Apical sulfides lie completely within the cluster and are bonded to 3 Mo atoms and are analogous to the basal plane sulfides in crystalline MoS₂. Finally terminal disulfides are bonded to a single Mo and do not have a strong analogy to the crystalline system.

While a-MoS_x has been known for several decades, their excellent catalytic activity towards HER was discovered only recently.^{10,43,47,48} They have been synthesized in a variety of manners, such as electrodeposition, hydrothermally, via wet chemical reactions, and even through the use of ionic liquids.^{10,43,49} A-MoS_x have proven to be highly active and versatile catalysts for HER in acidic conditions. They are able to be prepared in significantly milder conditions and faster synthesis cycles than their crystalline counterparts. Their short-range atomic arrangements give rise to interesting catalytic properties that can be manipulated to increase catalytic activity.^{42,47,50} Their simple, mild, and low cost preparation make a-MoS_x-based materials very attractive for the development of cost-effective electrochemical hydrogen producing materials.

1.3 Thesis Objectives

While achievements and progress has been made on MoS₂-based electrocatalysis for HER, further improvements must be made to move towards a commercial hydrogen generating material. Each mentioned technique above has its weaknesses that limit the effectiveness of the catalyst. Novel MoS₂ and a-MoS_x materials are still hotly investigated, however many of the strategies for modulating the surface/interface require complicated, toxic, or expensive equipment to achieve. As such, this thesis will focus on the modification of MoS₂-based materials via several low-cost, easily expandable, and simple strategies to enable an increase in the HER catalytic activity. This will be approached via the synthesis of MoS₂ on ZnO and ZnO/ZnS nanowires, c-CoS_x/MoS₂

based heterostructures, and the investigation of MoS_x and its various chalcogen alloys. Namely, there will be five primary chapters:

1 The heterostructure of ZnO/MoS_2 and $\text{ZnO}/\text{ZnS}/\text{MoS}_2$ was investigated to determine the impact the increase in surface area and the different interface band alignments have on the HER catalytic activity in both acidic and alkaline conditions.

2 The heterostructure of $\text{CoS}_x/\text{MoS}_2$ was investigated as a function of $\text{CoS}_x:\text{MoS}_2$ ratios to elucidate the impact that the difference in structure, interfaces, and chemistry has on the HER catalytic activity in both acidic and alkaline conditions.

3 The influence of oxygen on the HER catalytic activity of amorphous MoO_xS_y was investigated and identified via in-depth XPS and Raman analysis.

4 The influence of selenium alloyed with MoS_x deposited via electrodeposition is investigated as a function of selenium fraction to determine the effect that selenium alloying has on the catalytic properties of Se- MoS_x towards HER.

5 The influence of the MoTe_y phase with MoS_x deposited via electrodeposition is investigated as a function of tellurium content to determine the effect that tellurium-based heterostructures have on the catalytic properties of Mo towards HER.

2.0 Experimental Methods

2.1 Synthesis Methods

2.1.1 Electrodeposition

Electrodeposition is a thin film growth technique in which the growth of the film is controlled by the electrochemical reduction of ions from the electrolyte.⁵¹ The electrolyte is a carefully controlled ionic conductor that supports the chemical species of interest, usually in water. This process was first developed in 1799 where a galvanic cell between zinc as the anode, and copper as a cathode, and a copper salt, resulted in the plating of copper at the cathode.⁵² What we would consider modern electrodeposition began in 1840 with John Wright's discovery of the electrodeposition of silver from a metal cyanide electrolyte.⁵² Since this, electrodeposition has been used in a wide range of fields, from metallurgy through microelectronics and nanotechnology.

53

The general process of metal electrodeposition follows the generic formula of



where L is a molecule, ion, or radical tightly bound to the metal ion, M, and thus forms a complexing species which will take in the charge transfer process. x is the number of species involved, n is the net number of electrons that will be transferred in the process per deposited atom while z is the charge of the electroactive species in electron units. Overall, this is an inner-sphere electron, or covalent linkage, process that involves the adsorption of the ion onto the electrode

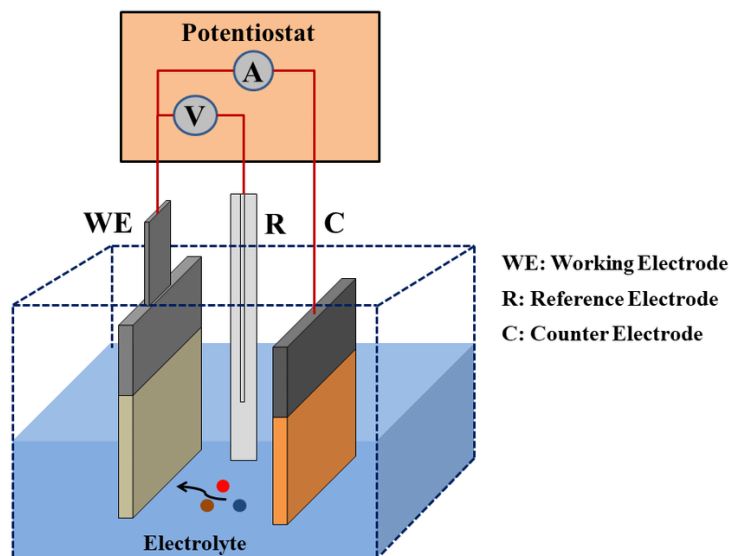


Figure 2.1: Schematic of electrodeposition in a typical three electrode setup⁵⁴

surface, followed by the transfer of electrons to reduce the ion. Therefore, this process is controlled by several factors, such as the diffusion of ions from the electrolyte to the surface, the electrode-electrolyte interface, charge-transfer kinetics, and the specific electrodeposition mechanism. The overall process can be seen in Figure 2.1.⁵⁴

The deposition of thin films is a heavily researched area with many varying techniques, so it begs the question, why electrodeposition, and why for TMDs? Currently, the most utilized techniques for synthesizing TMDs are chemical vapor deposition/transport, molecular beam epitaxy, and mechanical/liquid exfoliation. However, all these techniques suffer from a variety of synthesis constraints or issues, such as the need for ultrahigh vacuum, high temperature, use of dangerous chemical such as H_2S streams, and/or expensive and specialized equipment. By using electrodeposition for TMD synthesis, many of these limitations are removed as it allows for the synthesis at room temperature, atmosphere pressure, and is overall much simpler, quicker, and scalable than other methods. Additionally, electrodeposition has less stringent substrate requirements than other techniques and allows for the deposition on complex, 3D substrates, such

as carbon paper, allowing for an increase in overall total active area per unit area, thereby increasing the overall performance of the catalyst.

Overall, our materials will be deposited from two primary electrolyte baths, (i) those of metal chalcogen complexes, such as $(\text{MoS}_4)^{2-}$, or of elemental species, where the metal and chalcogen are not bonded when deposited. The latter method is used when the sulfur containing precursor, Na_2S , causes complete precipitation of the transition metal, such as cobalt.⁵⁵ The electrolyte preparation will be discussed in more detail within their respective sections.

2.1.2 Annealing

Depending on the deposition and desired film characteristics, a post-deposition annealing process can be employed. Two primary regimens will be explored, annealing below and above the crystallization temperature. In the former, this is done to achieve the modification, such as the removal of oxygen or addition of sulfur, of the amorphous MoS_x film while retaining the amorphous characteristics. The high temperature anneals are primarily done to react the non-reacted metal and chalcogen to form the TMDC and be catalytically active, such as in our crystalline- $\text{CoS}_x/\text{MoS}_2$ work.

Most of the anneals accomplished in this work were achieved in an MTI OTF-1200X tube furnace. Prior to annealing, the tube was purged with the inert gas of choice, such as high purity nitrogen or forming gas (5% H_2 /95% Ar) for 30 minutes. Annealing was accomplished by ramping the temperature by $7.5^\circ\text{C}/\text{minute}$ to the desired set-point. Slower or faster ramp rates could be achieved, but for consistency a constant ramp-rate was maintained. The flow of the inert gas was kept constant through the annealing process at a flowrate of roughly 200 - 250 ccm, depending on the gas. Following the anneal, the furnace was allowed to cool down naturally, again with the constant flow of inert gas.

2.2 Characterization Methods

2.2.1 X-ray Photoelectron Spectroscopy

2.2.1.1 Fundamentals

X-ray photoelectron spectroscopy (XPS) is a characterization technique that utilizes the photoelectric effect to obtain both elemental and chemical information of a material. The photoelectric effect works by irradiating the sample with photons, in this case x-rays, that interact with the electrons. This interaction causes the electrons to be “ejected” from the material, hence the term photoelectron. Following ejection, the photoelectron passes through a hemispherical analyzer which consists of two concentric hemispherical electrodes. These electrodes are held at a particular voltage so that electrons with kinetic energy equal to the pass energy follow a circular trajectory. As the photoelectrons pass through the hemispherical analyzer, the photoelectrons are linearly dispersed depending on their kinetic energy. When acquiring a spectrum in constant analyzer energy mode, the voltages of the two hemispheres are fixed while the voltages of the electrostatic lenses in front of the analyzer are swept. This allows for each detector channel to count the photoelectrons with the selected kinetic energy for a selected amount of time. Due to the conservation of energy, the binding energy of the electron can be determined if the photon energy is known following

$$KE = h\nu - BE - \phi_{sample} \quad (2)$$

where KE is the kinetic energy of the photoelectron measured by the analyzer, $h\nu$ is the energy of the incident X-ray, BE is the binding energy of the photoelectron, and ϕ_{sample} is the sample work function. This phenomenon can be seen visually in Figure 2.2.⁵⁶

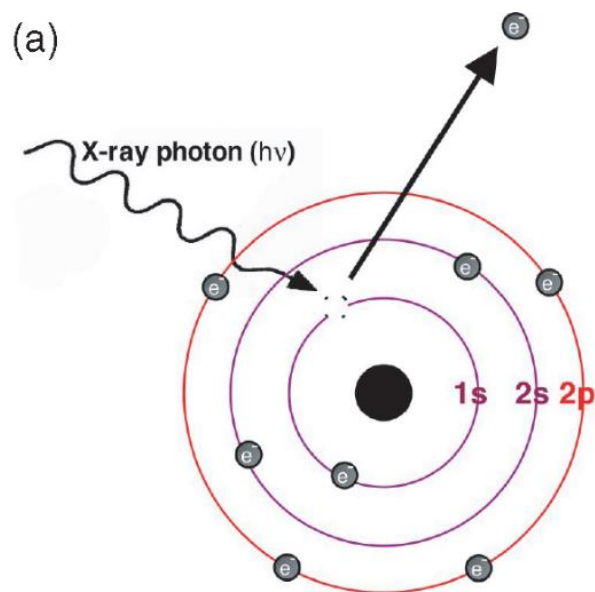


Figure 2.2: Schematic of the photoemission process where a known energy x-ray ejects a core level electron, leaving behind a core-hole.⁵⁶

As each core level electron's binding energy related to the number of protons in the nucleus, the density of electrons around the atom, and electron-electron interactions, each element has a unique set of core-level binding energies.⁵⁶ Therefore, XPS is a highly effective tool in determining composition as well as chemical analysis at the surface. XPS is conventionally plotted with intensity as a function of binding energy, as seen in the survey scan in Figure 2.3a and it can be used as an element identification tool as seen by the Au, Mo, and S, with adventitious carbon and oxygen from atmospheric exposure.

However, when atoms are bonded to differing atoms, a redistribution of charge will occur due to the formation of chemical bonds. This will cause a change in the binding energy of the core level, also known as a chemical shift. Figure 2.3b shows the high-resolution spectra of the Mo 3d core level. As can be seen, there are three distinct chemical states of Mo from the varying bonding

environment, e.g., sulfur vs. two oxygen atoms vs. three oxygen atoms. As such, XPS can be used to identify the shift of chemical environments.

As can be seen in Figure 2.3b, there are two peaks for each associated chemical state. This arises from spin-orbit coupling which occurs because of the interaction between the electron's spin, s , and its orbital angular momentum, l . By summing these two together, the total angular momentum, j , of the electron can be calculated by $j = |l + s|$. As electrons are fermions, they will have a $\pm\frac{1}{2}$ spin associated with them. The orbital angular momentum will be 0, 1, 2, or 3, depending on the core level being observed (e.g., s, p, d, f). In Figure 2.3b, the Mo 3d spectra is shown, so by following the $j = |l + s|$ equation, the total angular momentum can be calculated to be $j = 5/2$ or $3/2$ with the $5/2$ being the peak with the lower binding energy. The ratio between the areas of the two associated peaks are also governed by physical underpinnings, that being relative degeneracy for the energy levels. This can be calculated with the equation $2j + 1$, so 6 for $j=5/2$ and 4 for $j=3/2$, yielding a ratio of roughly 3:2. This ratio will be roughly 2:1 for p orbitals and 4:3 for f orbitals.

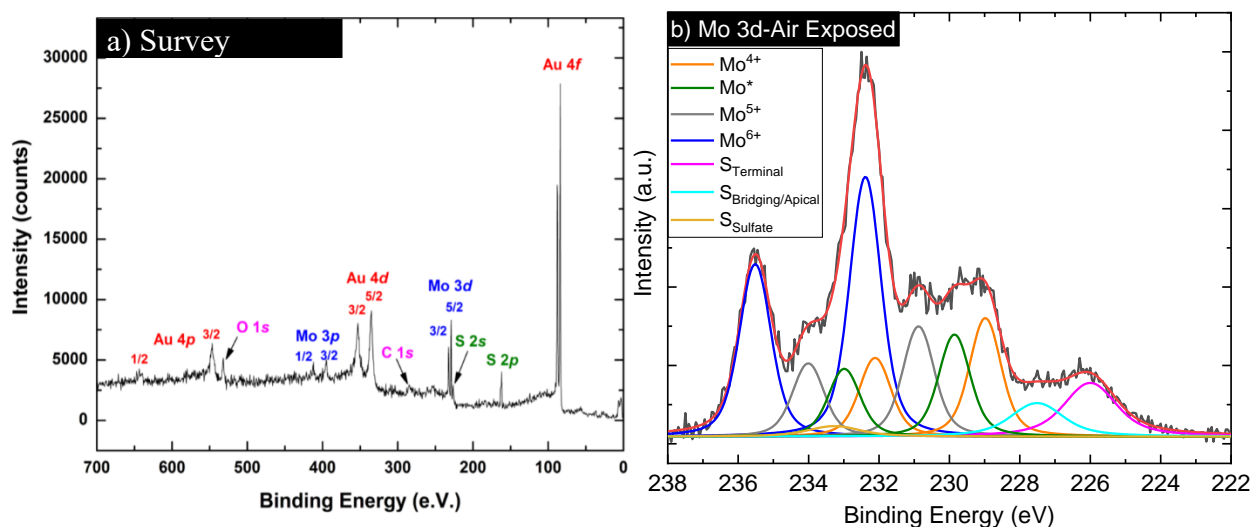


Figure 2.3: a) Survey XPS scan of gold deposited on MoS₂. Figure courtesy of K. Freedy and b) MoS_xO_y sample with surface oxidation demonstrating the ability to distinguish varying chemical states.

2.2.1.2 Quantitative analysis

For quantitative analysis, we can use the peak intensity of the chemical species of interest.

The intensity of the peak is a function of several factors as follows:

$$I = nF\sigma\phi yT\lambda \quad (3)$$

where n is the number of electrons from the photoemission process per unit volume, F is the flux of x-rays, σ is the partial photoionization cross-section, ϕ represents the angular distribution, y represents the fraction of σ retained, T is a transmission function, and λ is the inelastic mean free path. Together, the term $\sigma\phi yT\lambda$ can be referenced as the relative sensitivity factor (RSF) of the particular core level electron. Each core level has its own unique RSF value which is dependent on the system being used. Given a constant X-ray flux, we can normalize the intensity of each peak with their specific RSF value, resulting in a RSF normalized intensity. This can then be used to compare atomic concentrations and get chemical compositions of our samples.

2.2.1.3 Chemical Shifts

In addition to analyzing elemental and chemical composition, we can also use XPS to identify any electronic changes in our material. For the majority of this work, we will be focusing on electronic changes that manifest themselves due to a change in chemistry, and therefore will be called chemical shifts. In the simplest cases, if our material originally has two elements and a third is added, a few things can happen. If the new atom has a lower electronegativity than the atom it is replacing, then we would expect a peak shift of the other atoms bonded to it to shift towards a lower binding energy. Conversely, if it is bonded to a new atom with a higher electronegativity, we would expect a shift towards higher binding energy.

2.2.1.4 Valence Band

The valence band (VB) spectra is the region that lies close to 0 eV as can be seen in Figure 2.4a. The valence band maximum (VBM) can be determined via the intersection between the extrapolated lines from the linear region of the drop-off spectra and the noise level, as shown in. Where they intersect is what will be referred to as the VBM as can be seen in Figure 2.4b.⁵⁷

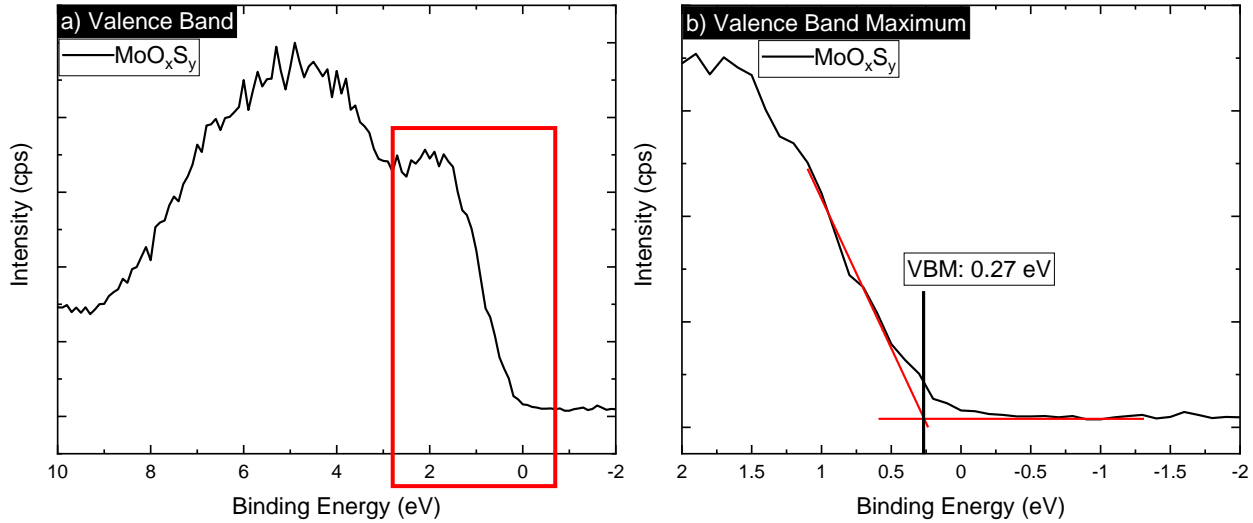


Figure 2.4: a) Valence Band Spectra of MoO_xS_y with the red box representing the zoomed in section represented in b) Valence band spectra with linear fits to calculate the VBM.

2.2.1.5 Overlayer Thickness Calculations

We can use XPS to estimate the thickness of an overlayer by using the intensities from the substrate without the overlayer, the bulk overlayer without any substrate signal, and comparing it to the intensities of the sample that has the substrate with the overlayer present. The basic premise of this technique is that since any photoelectrons that are generated will have to pass through the overlayer, attenuating them. As such, the intensity of the overlayer ($I_{\text{overlayer}}$) and substrate ($I_{\text{substrate}}$) with an overlayer thickness d , can be calculated with the following equations:

$$I_{overlayer} = I_{overlayer}^{\infty} [1 - \exp\left(\frac{-d}{\ell_{overlayer\ CL} \cos\theta}\right)] \quad (4)$$

$$I_{substrate} = I_{substrate}^{\infty} [\exp\left(\frac{-d}{\ell_{substrate\ CL} \cos\theta}\right)] \quad (5)$$

The $I_{overlayer}^{\infty}$ and $I_{substrate}^{\infty}$ represent the intensities of bulk samples of the overlayer and substrate, respectively. The $\ell_{overlayer\ CL}$ and $\ell_{substrate\ CL}$ are the effective attenuation lengths (EAL) of the core levels that come from the overlayer and substrate and pass through the overlayer. θ is the take-off angle with respect to the surface normal. The National Institute of Standards and Technology (NIST) EAL databases are used to find and calculate the appropriate EALs for the different overlayer/substrate chemistries.^{58,59} We use EAL instead of the inelastic mean free path in these calculations as it accounts for elastic scattering effects as well as accounting for instrument specific geometry.⁶⁰

2.2.1.6 Analysis Systems

All XPS conducted within this study was carried out on either the McDonnell instrument or the NMCF Phi Versaprobe III. The McDonnell instrument is equipped with a monochromated Al K α source with an energy of 1486.7 eV and are generated with a XM1200 monochromated X-ray source with a 500 mm Rowland circle diameter and a spot size of \sim 1mm. The photoelectrons are collected by a R3000 ScientaOmicron analyzer that is 135 mm in diameter and is equipped with three curved and three straight slits for balancing intensity with resolution. Our resolution at 2 eV pass energy and 20 eV kinetic energy is <3 meV. kolXPD was used for spectral deconvolution of the core-level spectra, with Voight line shapes for spectral features and a Shirley background. With metallic features, Doniach-Sunjic line chapes are used to fit the profile of metallic materials more accurately.⁶¹

2.2.2 Raman Spectroscopy

2.2.2.1 Fundamentals

Raman spectroscopy is a non-destructive spectroscopic technique used to determine the vibrational modes of materials. The technique relies on the inelastic scattering of photons, also known as Raman scattering. The photon source in the form of monochromatic light, usually from a laser, is used. This photon interacts with the phonon or other excitations of the system which results in the energy of the photons being shifted up or down, as can be seen in Figure 2.5. There are two types of scattering that can occur, elastic and inelastic. Elastic, also known as Rayleigh scattering, is by far the most common and corresponds to when the molecule gets excited by a photon, inducing a rise in energy to a virtual state that is proportional to the incident photon's energy, and then immediately relaxes back to the ground state it was in previously. This releases a photon of the same energy as the incident photon and carries no molecular information. The other type of scattering, inelastic, also known as Raman scattering, occurs when the scattered photons have a different energy than the incident photons. Stokes Raman scattering occurs when the molecule returns to a higher vibrational ground state energy level than it was in before, leading to releasing a photon with a longer wavelength than the incident photon. This transition occurs only

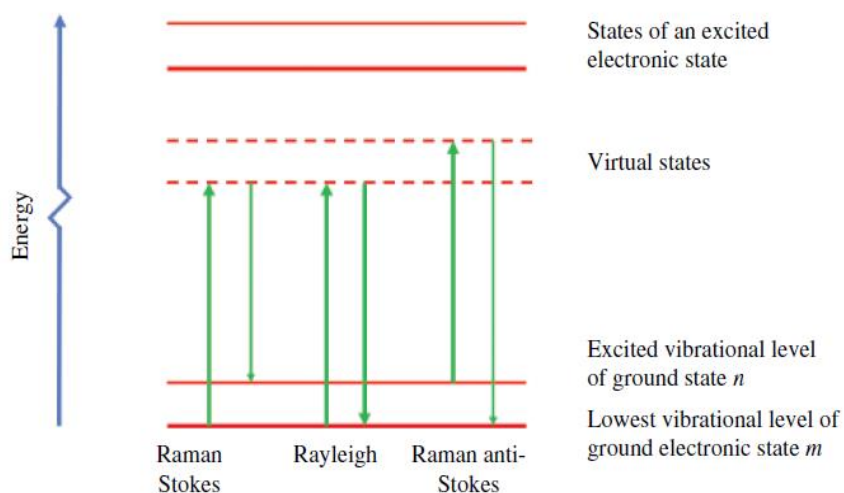


Figure 2.5: Jablonski diagram of the different scattering phenomenon

approximately 1 in every 10 million excitations.⁶² Anti-Stokes Raman scattering occurs when the excited molecule returns to a lower vibrational ground state energy releases a photon with a shorter wavelength than the incident photon. Anti-Stokes Raman scattering occurs even less frequently than Stokes Raman scattering.

This shift in wavelength of interest is then measured as the Raman shift, as given by

$$\Delta\tilde{\nu} = \left(\frac{1}{\lambda_0} - \frac{1}{\lambda_1}\right) \quad (6)$$

where $\Delta\tilde{\nu}$ is the Raman shift expressed in wavenumber, λ_0 is the excitation wavelength, and λ_1 is the Raman spectrum wavelength.

These shifts are vital to understanding the investigated material, as each molecule has a unique Raman spectrum due to their unique vibrational, rotational, and electronic modes, also known as rovibronic states, that can be excited to these virtual states. However, these vibrational and rotational modes are only Raman active if they result in a change of polarizability in the molecule. As shown in the simplified Equation (7)

$$\mu_{induced} = \alpha * E_{field} \quad (7)$$

where α is the polarizability, E_{field} is the constant electric field produced by the excitation light source, and $\mu_{induced}$ is the induced dipole moment. The polarizability correlates with the magnitude of the Raman effect as it measures the ease with which the electron cloud around a molecule can be distorted and undergo rotational and vibrational modes. As such, in order for a vibrational mode to be Raman active, the polarizability must change during the vibration, and for a rotation to be

Raman active, the polarizability much change as the molecule rotates in an electric field. The intensity of Raman scattering is given by

$$I = Kl\alpha^2\omega^4 \quad (8)$$

where K consists of constants such as the speed of light, l is the laser power, ω is the frequency of the incident radiation, and α is the polarizability as mentioned before. The data is typically represented as the intensity vs Raman shift (cm^{-1}). These wavenumber shifts are characteristic of specific vibration modes within the material and can be used to determine the chemical and crystal structure of the material.

2.2.2.2 Analysis System

All Raman conducted within this study was conducted with the NMCF Renishaw InVia Confocal Raman microscope. The laser used was a 514 nm laser with both 1800 gr/mm and 3000 gr/mm for gratings. The detector is a CCD detector.

2.2.3 UV-Visible Spectroscopy

2.2.3.1 Fundamentals

UV-visible spectroscopy (UV-Vis) is an adsorption or reflectance spectroscopy technique that is based on the Beer-Lambert Law which is as follows

$$A = \alpha lc = \log_{10} \frac{I_0}{I} \quad (9)$$

where A is the absorbance, α is the absorptivity, l is the optical length path, c is the concentration of the attenuating species, and I_0 and I are the intensity of the incident light and transmitted intensity, respectively. As such, it is a technique that measures the number of discrete wavelengths that are absorbed or transmitted through the sample. Similar to Raman spectroscopy, irradiating

the sample with photons causes the molecules to increase in energy, with the total potential of the molecule being represented by the sum of its discrete levels of electronic, vibrational, and rotational energies. When the incident light has enough energy (i.e. particular wavelength) to cause transitions between electronic energy levels, a narrow absorbance band is measured that is characteristic of that particular transition. However, vibrational and rotational energy levels are superimposed on the electronic energy levels, broadening the measured bands as shown in Figure 2.6⁶³

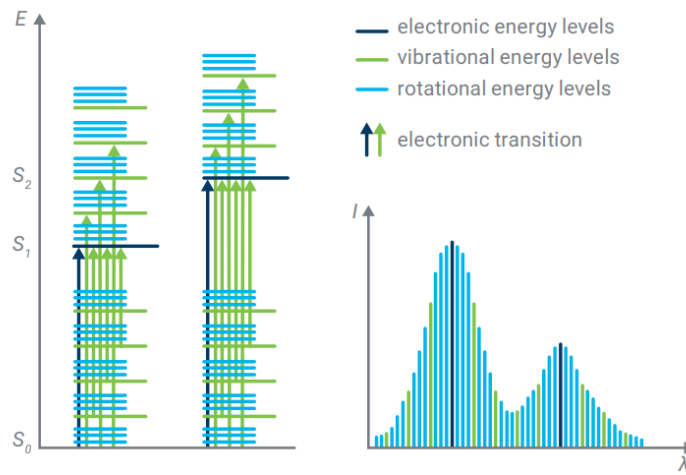


Figure 2.6: Electronic transitions and UV-visible spectra

The near-edge absorbance region can be used to determine the optical bandgap by fitting it with a simple expression in which the intercept gives the band-gap, known as Tauc plots. The Tauc method assumes that the energy-dependent absorption coefficient, α , is expressed by Equation (10).

$$(\alpha * hv)^{\frac{1}{n}} = B(hv - E_g) \quad (10)$$

where h is the Planck constant, ν is the photon frequency, E_g is the band gap, and B is a constant. The γ is a factor that depends on the nature of the transition, direct or indirect, and is equal to $\frac{1}{2}$ or 2, respectively.⁶⁴ α can be calculated using Equation (9) to get

$$\alpha = \frac{2.303 * A}{t} \quad (11)$$

where t is the thickness of the layer of the sample. To obtain the optical band gap, the left-hand side of Equation (10) is plotted as a function of the right-hand side. This will give a sharp, linear region that is characteristic of semiconductor materials. The x-axis intersection of the linear region yields the optical band gap energy, as shown in Figure 2.7.

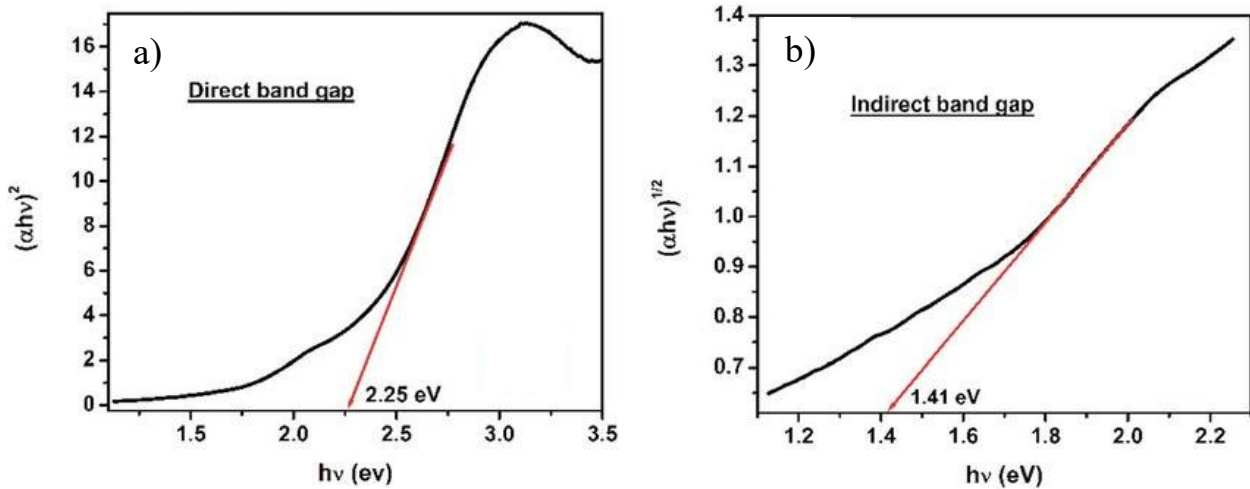


Figure 2.7: Tauc plot for a) direct and b) indirect bandgap

2.2.3.2 Analysis System

The instrument utilized was the Agilent Cary 5000 UV-Vis-NIR Spectrophotometer with a range from 175 to 3300 nm using a PbSmart NIR detector. The visible light source is a tungsten halogen lamp, and the UV source is a deuterium arc source. It is set up in a double beam

arrangement with an out-of-plane double Littrow monochromator to accurately ensure background subtraction. We want to thank Professor Zebarjadi for allowing us to use her instrument.

2.2.4 X-ray Reflectivity

2.2.4.1 Fundamentals

X-ray reflectivity (XRR) was briefly used in this study as a non-destructive technique to measure the thickness of thin film samples. It works by irradiating the film with glancing angle X-rays that interact with the interfaces, producing a reflection from each interface. For example, X-rays will interact with the thin film/air interface and the substrate/thin film interface. The interference between these reflected X-rays will change with the angle of reflection (controlled by the beam side optics) and this periodic oscillation in intensity can be plotted as a function of incident angle. This will form periodic oscillations in the intensity, known as Kiessig fringes.⁶⁵ This Kiessig fringes can be fit to calculate sample characteristics such as thickness, roughness, and density.

2.2.4.2 Analysis System

The NMCF's Malvern-Panalytical Empyrean diffractometer was used throughout this study. It is equipped with a Cu anode that radiated Cu K α radiation with a wavelength of 1.5406 Å.

2.2.5 X-ray Diffraction

2.2.5.1 Fundamentals

While the amorphous MoS_x cannot be detected via XRD, this technique is especially important when analyzing the crystalline MoS₂ and its alloys, as in the cobalt sulfide/molybdenum sulfide as well as in the ZnO/MoS₂ work. XRD's underlying principle follows the Ewald sphere in which constructive interference occurs when the diffraction vector is also a reciprocal lattice vector. It can be more simply described via Bragg's law, which follows as

$$n\lambda = 2d \sin \theta \quad (12)$$

where n is an integer that represents the diffraction order. When Bragg's Law is satisfied, the incident X-rays scatter at the angle θ . The diffracted rays are collected at the detector and are plotted in intensity vs. 2θ . The peak designations are then indexed using knowledge of the sample and expected crystal structure, providing insights into the structure properties relationship.

As the majority of the XRD work in this study was carried out on 3D, complex substrates, Bragg Brentano mode was used to encompass as much of the sample as possible. In this geometry, the divergent and diffracted beams are focused on a fixed radius from the sample position. This geometry has the advantage of high peak intensity with minimal noise as well as excellent resolution due to the focused beam.

2.2.5.1 Analysis System

The NMCF's Malvern-Panalytical Empyrean diffractometer was used throughout this study. It is equipped with a Cu anode that radiated Cu $K\alpha$ radiation with a wavelength of 1.5406 Å.

2.2.6 Scanning Electron Microscopy

2.2.6.1 Fundamentals

In SEM, an image of a sample is produced by scanning the sample surface with a focused beam of high-energy electrons and measuring the resultant signals that emerge due to the energy dissipation of the decelerating electrons. The resultant signals include secondary electrons (SE), backscattered electrons (BSE), diffracted backscattered electrons (EBSD), and photons used for energy-dispersive X-ray spectroscopy. This work will primarily be using SE, BSE, and the EDS capabilities of the instrument. SE are the most valuable for demonstrating morphology and topography while BSE are useful for illustrating contrasts between areas of different chemical

composition. The X-rays generated from the inelastic collisions between the incident electrons with the electrons that are in discrete orbitals around the atom are specific in their energy and therefore are characteristic of a particular element, allowing for the generation of an elemental map overlay on an image. SEM will be useful to image our sample's morphology and elemental distribution which will aid in determining the origin of the various properties of the catalysts.

2.2.6.2 Analysis System

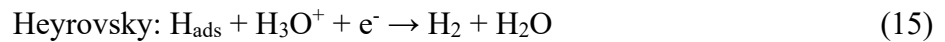
A mixture of NMCF's scanning electron microscopes were used throughout this study. Primarily, the Thermo Scientific Phenom XLG2 SEM and the FEI Quanta 650 SEM. The Phenom uses a CeB₆ source and the Quanta 650 uses a Field Emission Gun for the electron beam.

2.2.6 Electrochemical Measurements

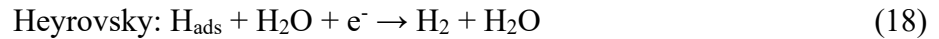
2.2.6.1 Linear Sweep Voltammetry

The primary electrochemical measurement that will be carried out is linear sweep voltammetry (LSV), which generates polarization curves. This is achieved via a potentiostat and a three-electrode setup to deliver potential to the solution and measure the change in current. The three-electrode setup consists of the working, reference, and counter electrodes. A potential, supplied by the potentiostat, is delivered to the working electrode and this is where the oxidation/reduction reaction occurs with the opposite reaction occurring at the counter electrode. As the reduction/oxidation of the species at the working electrode takes place, the products diffuse away from the surface and new species can contact the surface of the working electrode. This reaction is monitored by measuring the current, or flow of electrons, into or out of the working electrode; this is a direct measurement of the electron exchange between the electrode/electrolyte interface.

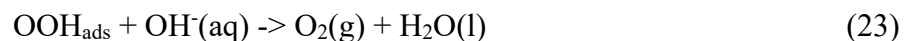
One primary reaction will be studied, the hydrogen evolution reaction (HER), with future work proposed for the oxygen evolution reaction (OER). The HER is measured by sweeping towards a negative potential to cause a reduction. The HER mechanism involves three known elementary reaction steps in acidic media:



and three known elementary reaction steps in alkaline media:



OER is measured by sweeping towards a positive potential to cause oxidation. The OER mechanism is as follows.



The efficacy of the catalyst towards either reaction will be quantified by the overpotential required to reach 10 mA/cm^2 when scanning at 10 mV/sec and by the Tafel slope, where the Tafel slope can

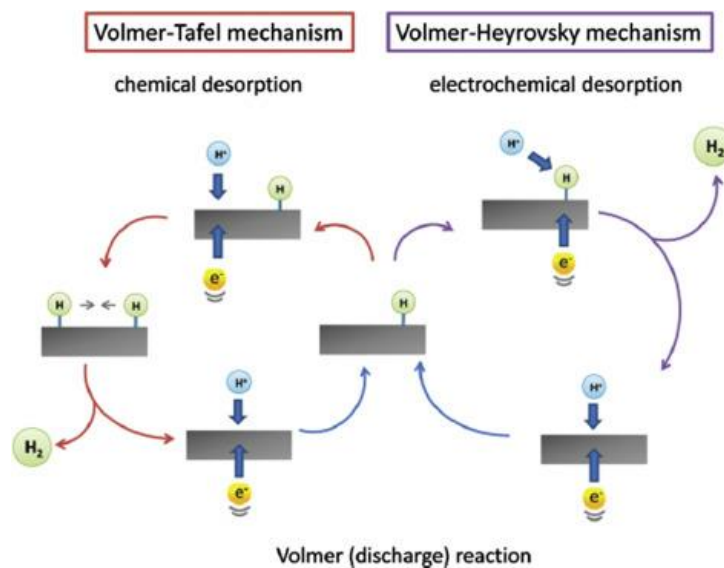


Figure 2.8: The two possible reaction pathways for HER to occur.⁶⁶

help us understand the rate limiting step of the reaction. For HER, the Volmer reaction will be followed by either the Tafel or Heyrovsky reaction; therefore, there are two possible reaction pathways with those being the Volmer-Tafel and Volmer-Heyrovsky pathways. These reactions can be seen in Figure 2.8.⁶⁶ If the Volmer adsorption reaction is the rate limiting step, a Tafel slope of 120 mV/dec would be expected. If the Tafel or Heyrovsky recombination's are rate limiting, the Tafel slopes would fall between $30 - 40 \text{ mV/dec}$. The reactions are strongly dependent on the inherent surface chemistry, crystallinity, and electronic structure of the catalyst and, through these electrochemical measurements, we can determine the processing-structure-property relationships.

3.0 Crystalline MoS₂-based Heterostructures

3.1 Study of Electrodeposited Molybdenum Disulfide on Zinc Oxide and Zinc Oxide/Zinc Sulfide Nanowires

3.1.1 Background and Motivation

In this work, we demonstrate a simple hydrothermal, electrochemical, and annealing method to fabricate and control various phases of ZnO, ZnS, and MoS₂ layered nanowires on carbon paper (CP) for use as an effective HER catalyst.

Recently, hybrid core/sheath nanostructures consisting of a metal oxide semiconductor core (ZnO, TiO₂, MnO, etc.) covered by transition metal dichalcogenides (TMDC) layers and other chalcogenides, such as ZnSe, CdS, and CdSe, have been explored as potential efficient catalysts due to their more efficient charge separation.⁶⁷⁻⁷¹ Among the metal oxides, ZnO is an important group II-IV semiconductor with a band gap of 3.37 eV and a Hall mobility on the order of 200 cm²V⁻¹s⁻¹. Its low cost, non-toxicity, ease of synthesis and crystallization, and natural abundance make it an ideal and promising material for catalytic applications, most notably as a photocatalyst. It is currently regarded as the best alternative to TiO₂ for electrochemical applications due to its faster charge transfer and prolonged electron lifetime when compared to TiO₂. However, ZnO by itself is inactive for HER and suffers from degradation in both acidic and alkaline conditions due to its amphoteric nature. As such, it is often coated with an active species that can be enhanced by the ZnO while also serving to protect it.

The ZnO/MoS₂ and other ZnO/TMDC interfaces have been studied previously and have shown promise given a reduction in band gap, maintained charge mobility, and improved charge separation due to the lattice mismatch. These studies have been accomplished with a variety of

methods, from drop-casting, solvothermal, and metal-organic chemical vapor deposition⁷²⁻⁷⁷ with a variety of morphologies, from films, nanoparticles, nanorods, and nanowires.^{74,77-79} However, these studies have all been conducted on flat, 2D substrates, limiting their overall active surface area. As such, our study will be conducted on a 3D, porous substrate to maximize the overall active surface area.

Taking this a step further, it is possible to elevate the catalytic activity via charge movement engineering by incorporating an additional semiconductor with the appropriate band structure and forming a ternary heterostructure. When done, the electrons can be further spatially confined through the creation of electron and hole sinks, further enhancing charge separation.^{80,81} Furthermore, the ternary heterostructure generates an additional interface with further lattice mismatch, modifying the band structure and leading to increased catalytic activity.⁸²

Finally, the impact of band alignment will be explored. The two primary types of band alignments that will be explored are type-I (straddling) and type-II (staggered) and can be seen in Figure 3.1.1. There is a type-III (broken), but this isn't relevant to the investigated heterostructures. In a type-I, the conduction band minimum of SC-A is higher than that of SC-B where the valence band maximum of SC-A is lower than that of SC-B. Therefore, both electrons and holes from SC-A are transported to the conduction band and valence band of SC-B, not resulting in better charge separation. Type-II differs in that the electrons from SC-A are transferred to SC-B whereas the holes from SC-B are transferred to SC-A, resulting in better charge separation.⁸³

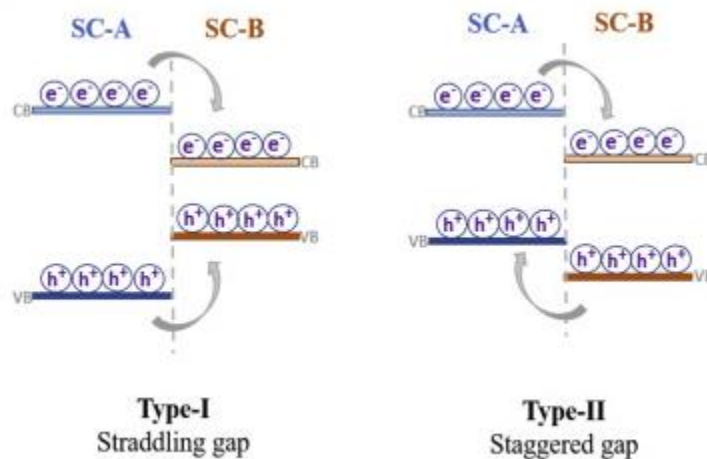


Figure 3.1.1: Different types of band alignment in a heterojunction⁸³

In the ZnO/MoS₂ and the ZnO/ZnS/MoS₂ heterostructure, both type-I and type-II band alignments have been reported. However, as mentioned earlier, there is a non-consensus on the location of the relative band positions depending on synthesis and characterization technique as can be seen in Figure 3.1.2^{72,84–88}. As can be seen, there is a variety of type-I and type-II alignments for the same heterojunction, both between ZnO/ZnS, ZnO/MoS₂, and ZnS/MoS₂. To this end, differences in band structure, even with systems with identical constituent materials synthesized in similar manners, are quite common. This is particularly true for materials with conduction and/or valence bands located at a similar level. Additionally, this is further compounded by the fact that the band structure is extremely sensitive to, among others, the density of defects, presence of doping, and technique used to measure the band alignment (XPS, impedance-based measurements, photoluminescence, etc.). A change in synthesis conditions, synthesis methods, and choice of substrate is likely to impact the band structure and alignment of the materials.

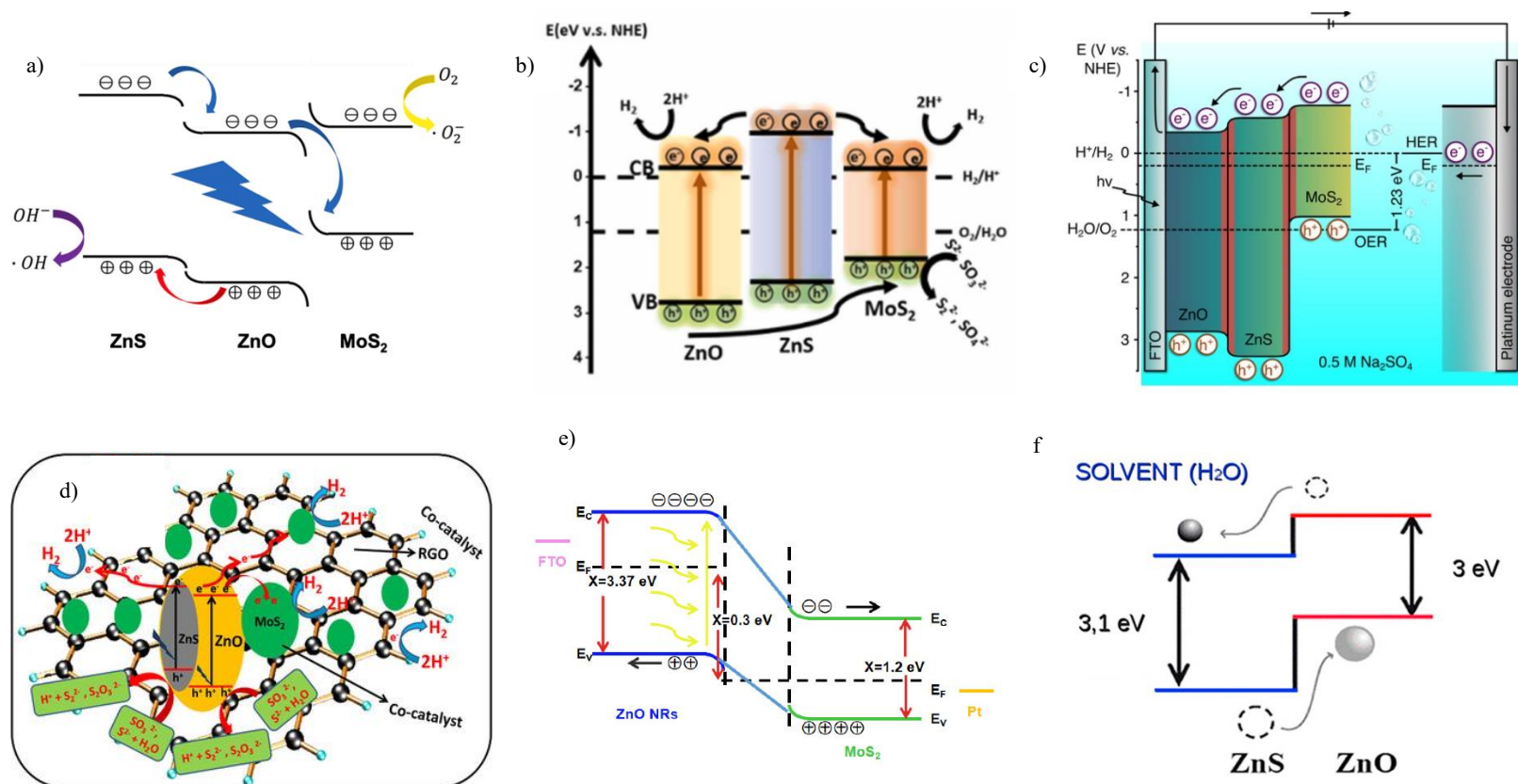


Figure 3.1.2: Energy band diagrams of a) ZnO/ZnS/MoS₂ piezoelectric nanoarrays⁷² b) ZnO/ZnS/MoS₂ heterostructures⁸⁸ c) ZnO/ZnS/MoS₂ nanostructure⁸⁴ d) ZnS-ZnO-MoS₂ heterostructure supported on RGO⁸⁵ e) ZnO@MoS₂ nanocomposite⁸⁷ f) ZnO@ZnS nanostructures⁸⁶

3.1.2 Synthesis Methods

3.1.2.1 Synthesis of ZnO Nanowires

To synthesize ZnO nanowires (NWs), a simple hydrothermal technique was used. Briefly, carbon paper (CP) was first heated to 500°C for 1 hour in air to increase its wettability. Then, the CP was soaked in an aqueous solution containing 0.1M potassium permanganate (KMnO₄) for 1 hour to form a seed layer. Then, this seeded CP was placed into an autoclave with a solution containing 15 mM zinc nitrate hexahydrate (Zn(NO₃)₂)*6H₂O), 15 mM hexamethylenetetramine ((CH₂)₆N₄), and 0.4 parts ammonia (e.g. 100 mL solution with 96 mL H₂O and 4 mL ammonia). The autoclave was then sealed and placed into the MTI Compact Forced Air Oven at 90°C for 24

hours. After cooling to room temperature, the CP/ZnO NWs was water washed and dried at 80°C for 3 hours.⁸⁹

3.1.2.2 Electrodeposition of MoS_x on ZnO NWs

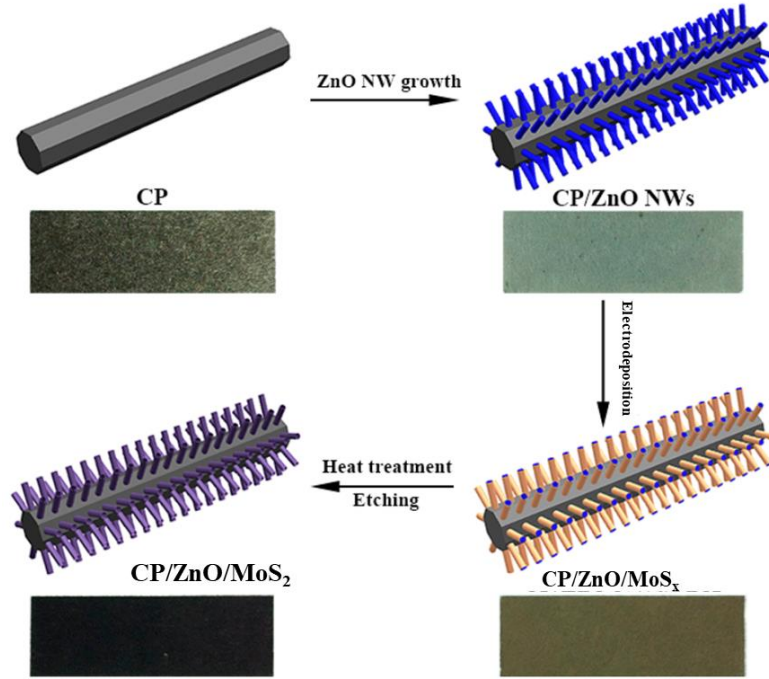
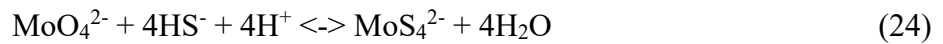


Figure 3.1.3 Synthesis steps for CP-ZnO-MoS₂

The approach is explained in more detail in Chapter 4.1 but will be described here briefly. MoS_x was electrodeposited from a chemical bath containing 50 mM sodium molybdate dihydrate (Na₂MoO₄*2H₂O) and 0.2 M sodium sulfide and was based on Levinas et al.'s work.⁹⁰ The general equation for the sulfidation of MoO₄²⁻ when titrated from a pH of 13 to a pH of 8 follows



The MoS₄²⁻ anion was electrodeposited under potentiostatic conditions at a potential of -1.5 V_{MSE} for 30 minutes with the CP/ZnO as the substrate. It was then removed immediately from the electrolyte and rinsed with DI water.

3.1.2.3 Formation of ZnO/MoS₂ and ZnO/ZnS/MoS₂ nanowires

To crystallize, the MoS_x coated nanowires were annealed in an MTI OTF1200X single zone tube furnace under flowing ultra-pure nitrogen. They were initially annealed at a variety of temperatures with 550°C being used for all further testing which will be covered in this section. To form the ZnO-ZnS-MoS₂ nanowires, elemental sulfur was placed upstream to sulfurize the ZnO and to form a ZnS region between ZnO and MoS₂.

3.1.3 Results

3.1.3.1 Impact of Annealing Temperature

Figure 3.1.4 shows the SEM images of the synthesized CP/CT substrates. As it can be seen in Figure 3.1.4a, the ZnO NWs are densely packed and are uniformly distributed. These NWs possess a high aspect ratio with diameters in the hundreds of nanometers and lengths of several micrometers. Figure 3.1.4b/c demonstrates that following anneals at 450°C and 550°C the nanowires structure is retained. Above these temperatures, the nanowire morphology is lost as seen in Figure 3.1.4d-f. In addition to the loss of morphology, a small mass loss was also measured via differential scanning calorimetry starting around 550°C.

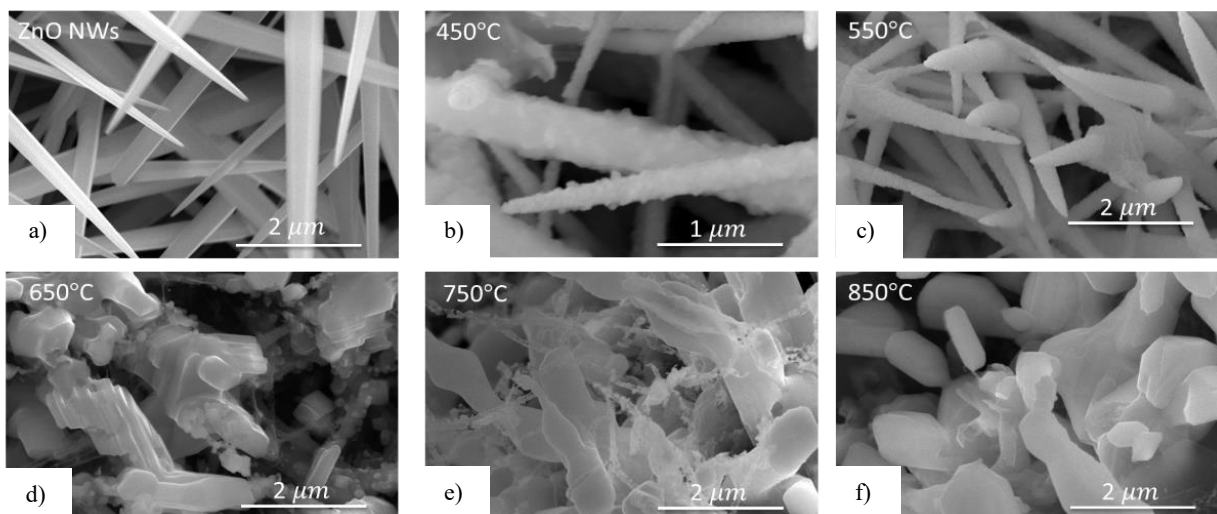


Figure 3.1.4: SEM images of a) ZNO NWs, b) ZnO-MoS₂ annealed at 450°C, c) ZnO-MoS₂ annealed at 550°C, d) ZnO-MoS₂ annealed at 650°C, e) ZnO-MoS₂ annealed at 750°C, f) ZnO-MoS₂ annealed at 850°C

Raman spectroscopy was carried out to understand how the crystal structure evolved as a function of temperature and of sulfur presence while annealing, shown in Figure 3.1.5. A brief analysis of the Raman spectrum is given here with a more detailed analysis later in the chapter. The main MoS₂ peaks are located at 382 cm⁻¹ and 408 cm⁻¹ and generally dominate the spectra. The primary ZnS peak is given at 348 cm⁻¹ and the primary ZnO is given at 438 cm⁻¹ but is generally buried under the broad longitudinal acoustic mode of MoS₂ that is located at 450 cm⁻¹. Additionally, fluorescence can be seen on the right-hand side of the figure which is due to the presence of the ZnS phase. As such, a few takeaways can be derived from this data. One, the presence of sulfur during annealing encourages the formation of a ZnS phase and is most pronounced at 550°C while without the presence of sulfur no ZnS is formed. This is further confirmed by the lack of fluorescence which is caused by the presence of the ZnS phase. Additionally, this demonstrates that the MoS₂ phase is stable at all tested temperatures, even if the

ZnO scaffolding is not. Therefore, all samples from here on will be annealed at 550°C for comparisons.

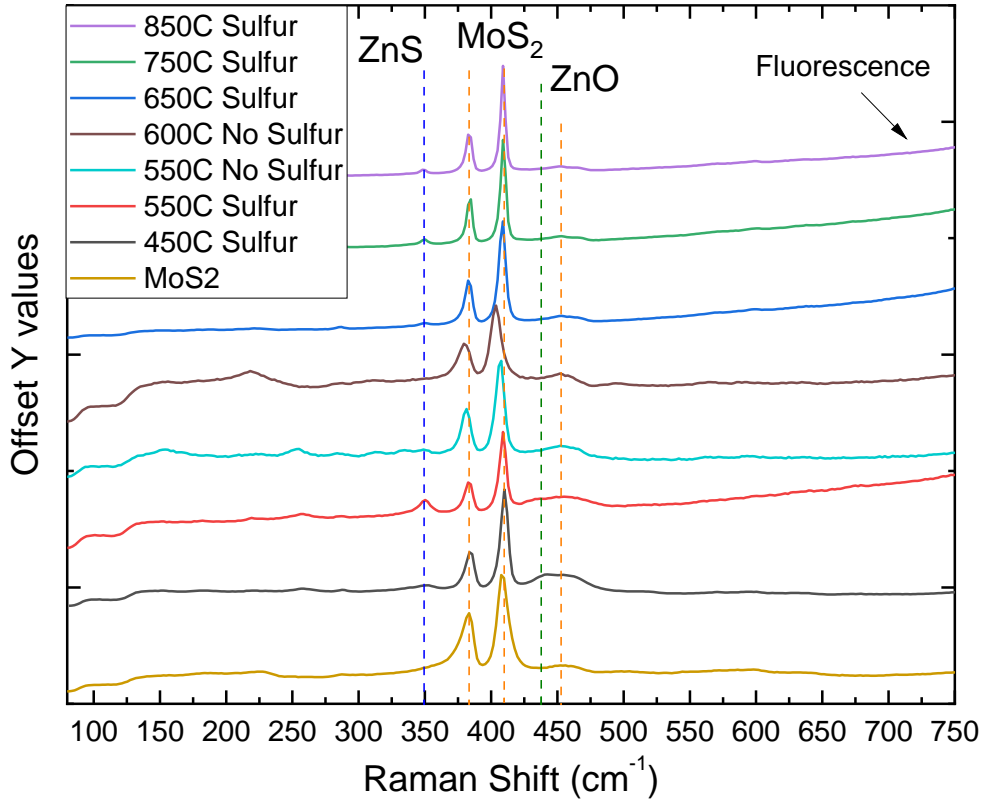


Figure 3.1.5: Raman spectra of the CP-ZnO-MoS₂ as a function of annealing temperature and presence of sulfur while annealing. The blue dashed lines represent the ZnS phase, the orange lines are attributed to the MoS₂ phase, and the green dashed line is attributed to the ZnO phase

3.1.3.2 Structural Properties of ZnO/MoS₂ and ZnO/ZnS/MoS₂

To compare the impact that annealing in the presence of sulfur has on the morphology of the nanowires, sulfur was placed upstream in the furnace. Figure 3.1.6 shows typical SEM images of the various treatments and the well-preserved nanowire structure. The ZnO/ZnS/MoS₂ NWs are distinctly more textured than when no sulfurization takes place. This potentially occurs while both ZnO and ZnS are cubic materials, ZnS has a significantly larger lattice parameter than that of ZnO and of hexagonal MoS₂.

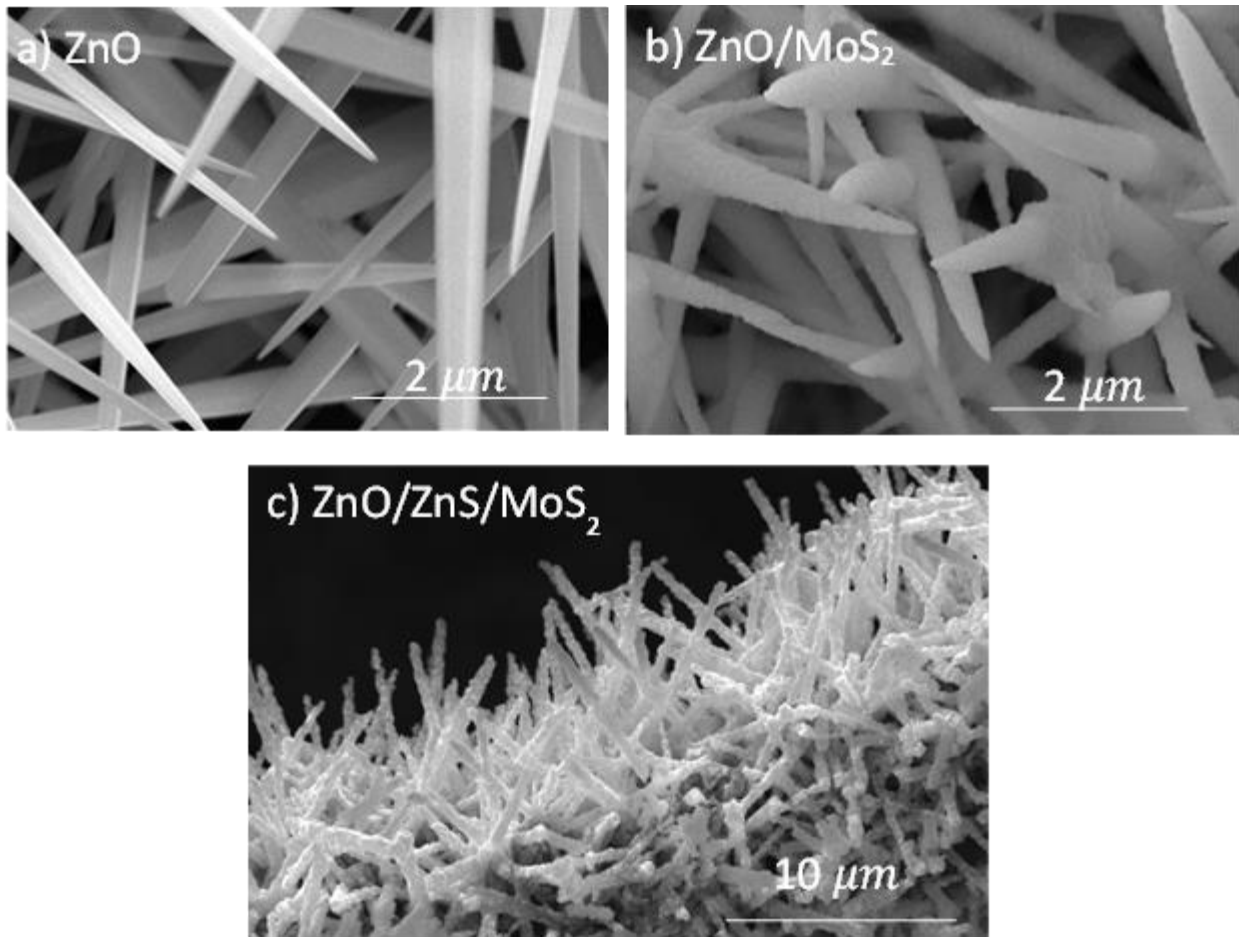


Figure 3.1.6: SEM micrographs of a) ZnO NWs, b) ZnO/MoS₂ NWs, and c) ZnO/ZnS/MoS₂ nanowires

XRD patterns of the various nanowires are shown in Figure 3.1.7. The Bragg diffraction hump at $2\theta \approx 14.17^\circ$ was indexed to the (002) plane of hexagonal MoS₂ (ICDD 01-075-1539).⁹¹ The peaks located at $2\theta \approx 17^\circ, 27.8^\circ, 32.7^\circ, 48.66^\circ, 52.25^\circ,$ and 57.28° are attributed to leftover Na₂MoO₄ precursor (ICDD 98-004-4523). The peaks located at $2\theta \approx 31.9^\circ, 34.5^\circ, 36.4^\circ, 47.6^\circ, 56.7^\circ, 63.0^\circ$ are attributed to the cubic ZnO phase (ICDD 01-086-8923). The peaks at $2\theta \approx 27.8^\circ, 28.6^\circ, 30.6^\circ, 43.3^\circ, 47.6^\circ, 51.8^\circ,$ and 56.5° are attributed to the cubic phase of ZnS (ICDD 04-007-

9852). Finally, the peaks at $2\theta \approx 26.6^\circ$, 29.5° , and 54.75° are attributed to the substrate, graphic carbon (ICDD 01-075-2078). However, there is a peak at $2\theta \approx 12^\circ$ and 14.8° that is unidentified.

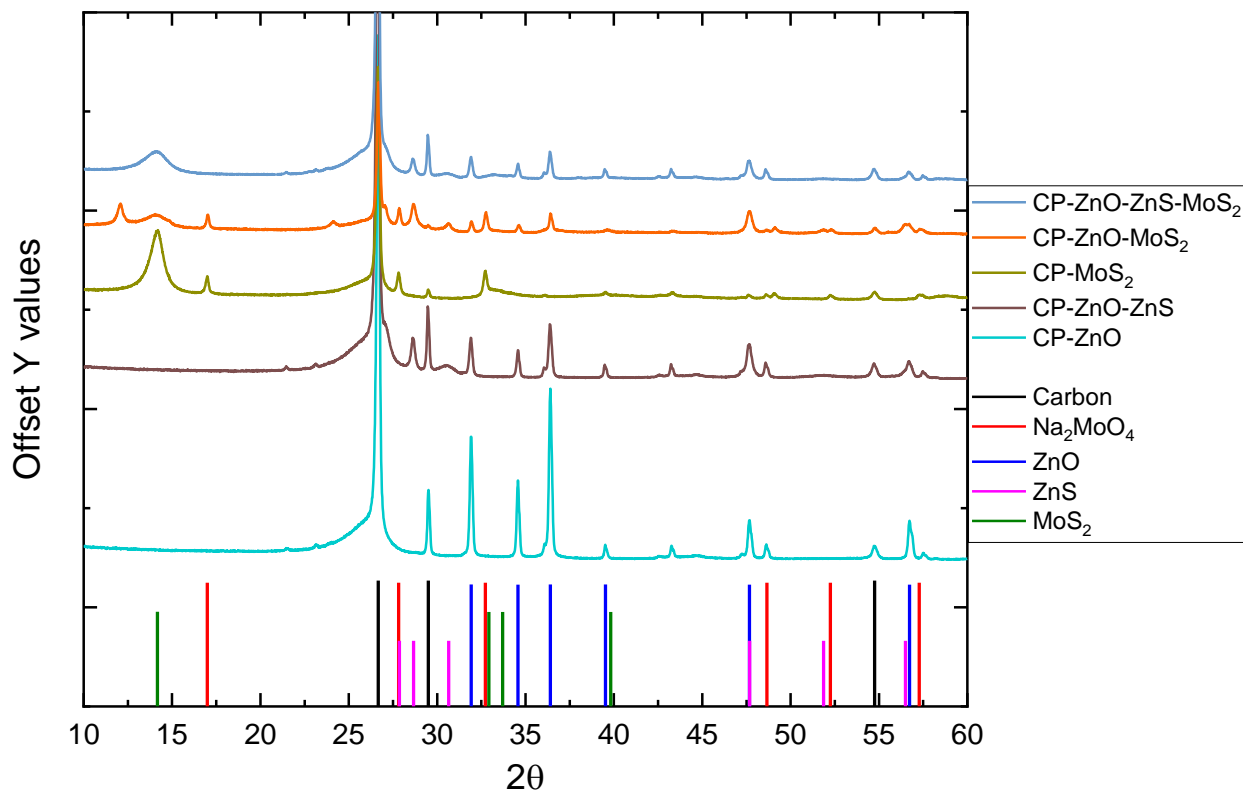


Figure 3.1.7: XRD pattern of the various nanowire electrocatalyst

The zoomed in region between 10° - 20° can be seen in Figure 3.1.8. As can be seen, there is an extra peak at $2\theta = 12.08^\circ$ and a small hump at 14.83° in the ZnO-MoS₂ sample. This has been duplicated and therefore is unlikely an outlier. Regarding the peak at 12.08° , we hypothesize that this is associated to an expanded c-axis MoS₂, a phenomenon that is reported in literature when MoS₂ is intercalated with various ions, or the formation of the 1T phase. However, applying Bragg's Law, the interlayer spacing is expanded by 104 pm from normal MoS₂, suggesting that oxygen is the intercalant given the atomic radius of oxygen which ~ 50 pm. This has been reported in literature and is consistent with our findings.^{92,93} This would also help explain why this peak is not present in the sulfurized sample, as the excess sulfur environment would preferentially bond and prohibit the oxygen from diffusing between the MoS₂ sheets. It is interesting to note the sharpness of the 12.08° peak. The peak at 14.83° would suggest that the interlayer spacing has shrunk by ~ 26.2 pm. This has been attributed to the interface between ZnO and MoS₂ cause by lattice mismatch.^{94,95} Both the ZnO-MoS₂ and ZnO-ZnS-MoS₂ samples have significant

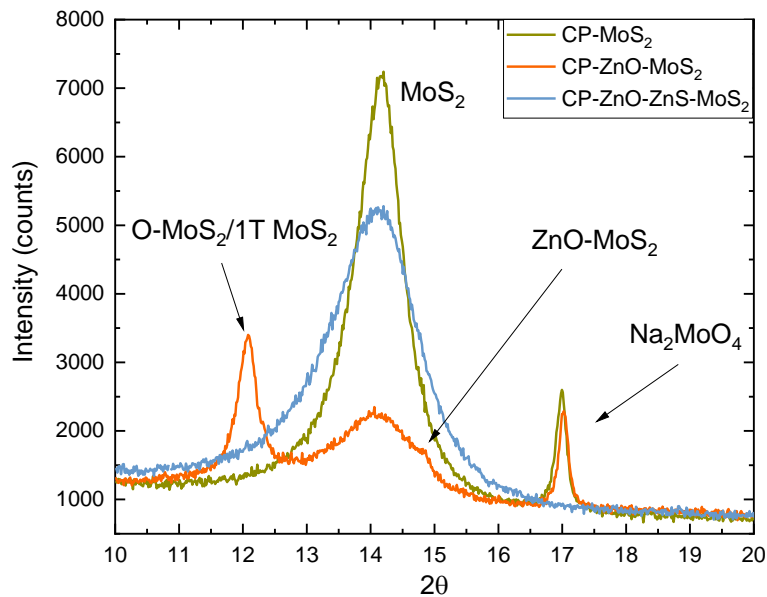


Figure 3.1.8: XRD patterns of the primary MoS₂ region of the MoS₂ containing nanowires

broadening and decreased intensity over the reference MoS₂, suggesting a decrease in crystallite size.

A closer look at the Raman data from Figure 3.1.5 is plotted below in Figure 3.1.9. In the spectrum, the peaks at roughly 384 cm⁻¹ and 407 cm⁻¹ are attributed to the in-plane E_{2g} mode and the out-of-plane A_{1g} mode, respectively.⁹⁶ In addition, the forbidden E_{1g} mode is present in all samples, indicating broken symmetry and is associated with edge species.⁹⁷ In addition to the Raman modes for 2H-MoS₂, distinct phonon modes at 154 (J₁), 219 (J₂), and 327 cm⁻¹ (J₃) are noted. These modes are characteristic of the metallic 1T-MoS₂, a reported side effect of the intercalation of ions.⁹⁸⁻¹⁰⁰ This further supports the XRD results found in Figure 3.1.8. Additionally, the primary modes of A_{1g} and E_{1g} have shifted by ~2.2 cm⁻¹, indicating that the MoS₂ is under tensile stress.^{101,102} Finally, the E₂ mode of ZnO and the E₁ mode can be seen at 439 and 349 cm⁻¹, respectively.

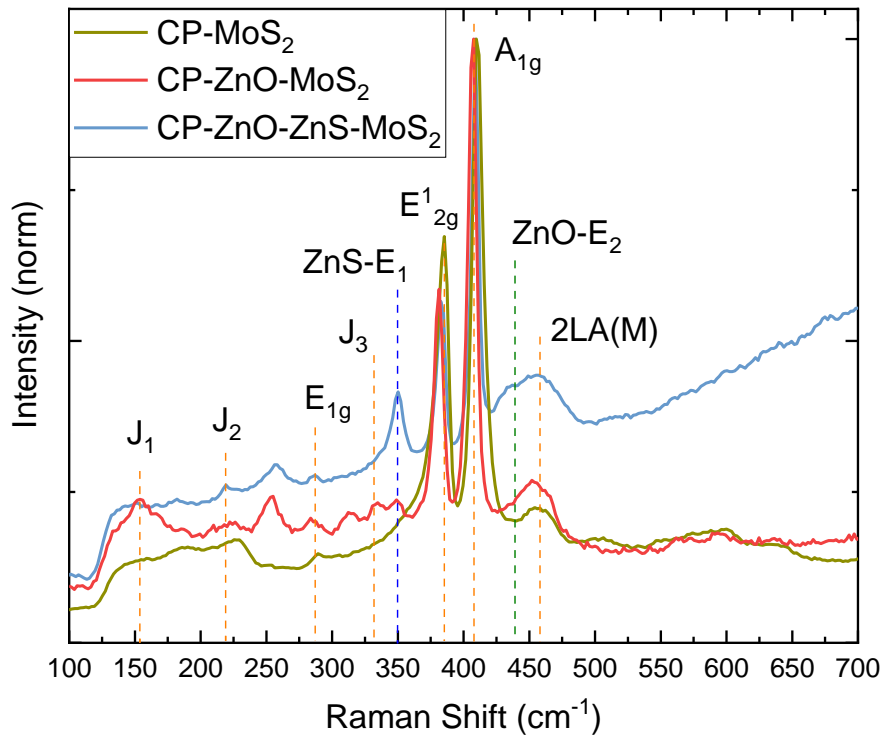
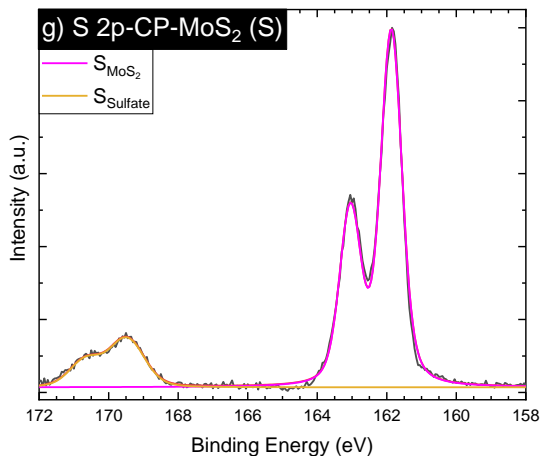
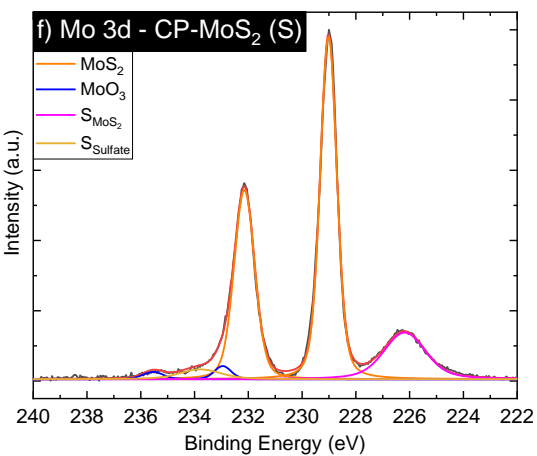
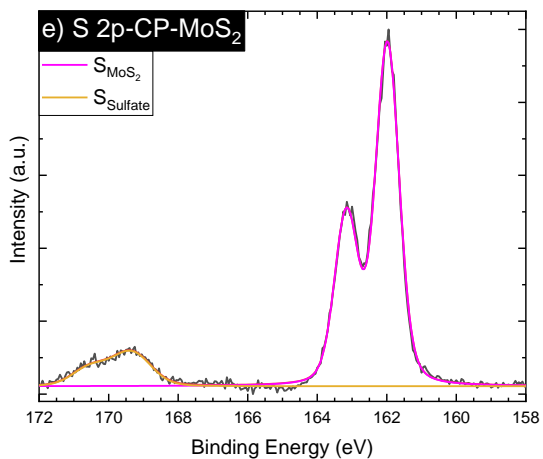
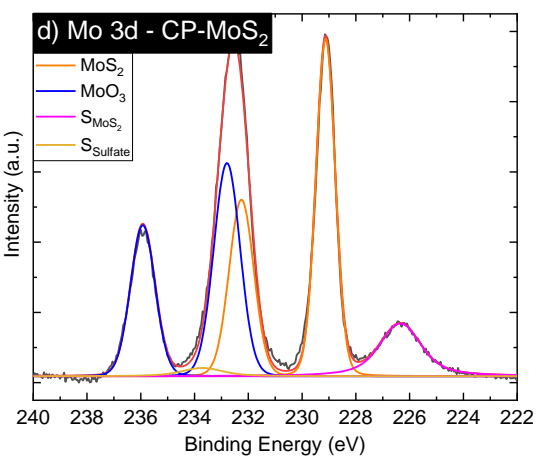
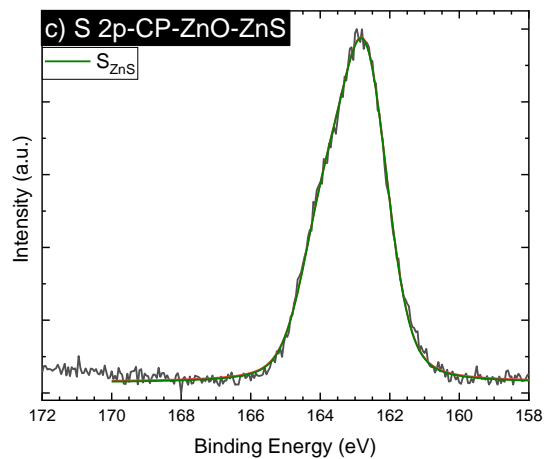
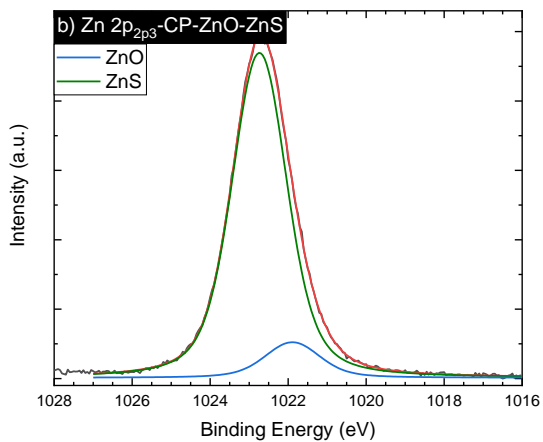
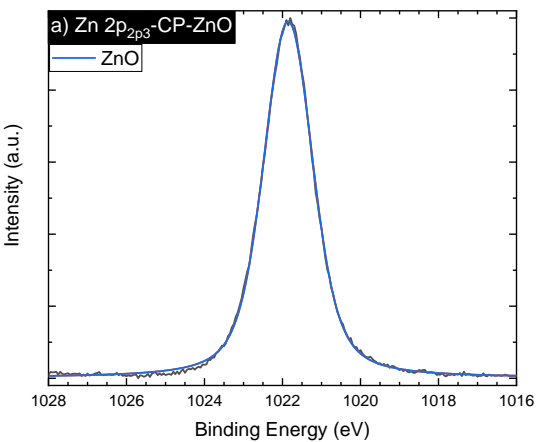


Figure 3.1.9: Raman of CP-MoS₂, CP-ZnO-MoS₂, and CP-ZnO-ZnS-MoS₂

3.1.3.3 Chemical Properties of ZnO/MoS₂ and ZnO/ZnS/MoS₂

To understand the chemical structure of the various nanowires, XPS was conducted to understand the chemical structure of the various nanowire heterostructures and can be seen in Figure 3.1.10. Within the Zn 2p_{3/2} spectra, two species are present, with ZnO being the lower binding energy species at ~1021.9 eV and ZnS present at higher binding energies at 1022.9 eV. Within the S 2p spectra, there are three primary species, those corresponding to MoS₂ at ~161.9 eV, ZnS at ~162.8 eV, and sulfate species at ~169.7 eV. The sulfur spectrum was deconvoluted with two doublets, with the constraints of an energy difference of 1.18 eV between the 2p_{3/2} and 2p_{1/2} and with an intensity ratio of 2:1. The 2p_{3/2} and 2p_{1/2} were summed together for ease of viewing. The Mo 3d spectra can be deconvoluted into distinctive doublet (3d_{5/2} and 3d_{3/2}) peaks. The primary constituents are 1T-MoS₂, 2H-MoS₂, MoO₂, and MoO₃, with the 3d_{5/2} located at 229 eV, 229.3 eV, 230.8 eV, and 232.4 eV respectively. The Mo 3d peaks were deconvoluted with a binding energy difference of 3.13 eV between the 3d_{5/2} and 3d_{3/2} and with a fixed intensity ratio of 3:2. The sulfur 2s is also present within the Mo 3d spectra and is fit using parameters from the S 2p spectra.



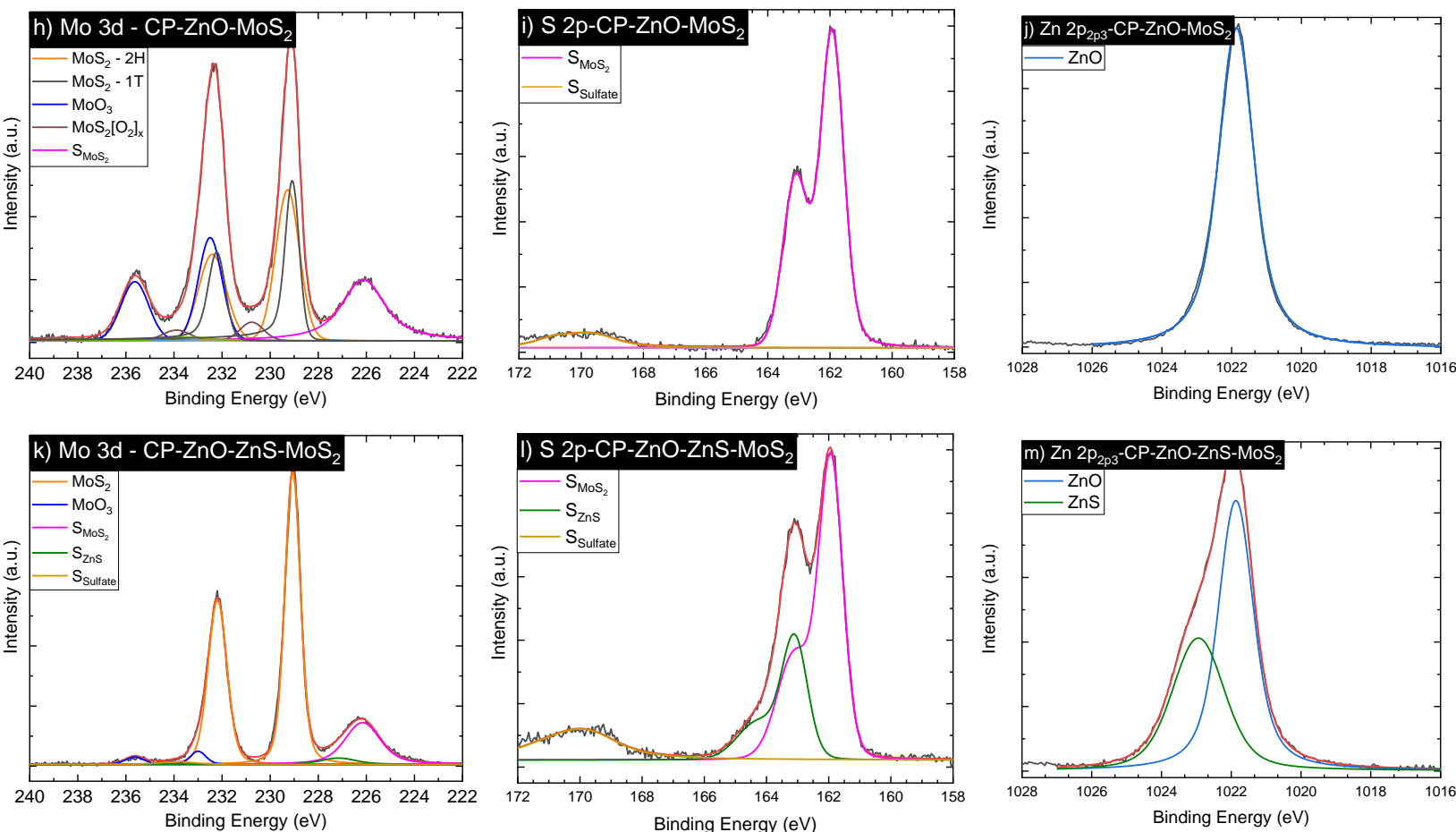


Figure 3.1.10 XPS of a) CP-ZnO nanowires, b,c) CP-ZnO-ZnS nanowires, d,e) CP-MoS₂ annealed with no sulfur, f,g) CP-MoS₂ annealed with sulfur, h,i,j) CP-ZnO-MoS₂ nanowires, and k,l,m) CP-ZnO-ZnS-MoS₂ nanowires

Starting from the top of Figure 3.1.10, the main differences between the CP-ZnO and CP-ZnO-ZnS is that only ZnO is present in the ZnO sample, whereas the spectra is dominated by ZnS in the CP-ZnO-ZnS sample. Moving down to Figure 3.1.10 d-g, which are the CP-MoS₂ samples without and with sulfur annealing, the primary difference is the large presence of the MoO₃ oxide phase in the MoS₂ sample that was annealed without any sulfur. This is expected as the unsaturated bonds would oxidize quickly to form MoO₃. Comparing the CP-ZnO-MoS₂ and CP-ZnO-ZnS-MoS₂ samples, again a major difference is the presence of the MoO₃ oxide phase in the sample that didn't see sulfur annealing, CP-ZnO-MoS₂. In addition, the CP-ZnO-MoS₂ also exhibits the

asymmetric peak characteristic of 1T MoS₂. While the peak positions are close, the spectra could not be fit without the addition of the asymmetric peak, further supporting the XRD and Raman results. Finally, a feature that has been attributed to MoS₂[O₂]_x is present in the CP-ZnO-MoS₂ and not present in any of the other samples. This has been shown to be present in oxygen intercalated MoS₂ by forming a superlattice, again supporting the idea that oxygen is acting as the intercalant.¹⁰³⁻¹⁰⁷ Regarding Zn, only ZnO is present in the CP-ZnO-MoS₂ sample whereas there is a mixture of ZnO and ZnS in the CP-ZnO-ZnS-MoS₂ sample.

To determine the band offsets, the method by Kraut et al. is utilized where the valence band offset can be determined via¹⁰⁸

$$\Delta V = \Delta E_{CL} + (E_{Mo\ 3d}^{MoS_2} - E_{VBM}^{MoS_2}) - (E_{Zn\ 2p}^{ZnO} - E_{VBM}^{ZnO})$$

where $\Delta E_{CL} = E_{Zn\ 2p}^{ZnO/MoS_2} - E_{Mo\ 3d}^{ZnO/MoS_2}$ is the energy difference between Zn 2p and Mo 3d core levels (CL) obtained by measuring the ZnO/MoS₂ heterojunction. $E_{Mo\ 3d}^{MoS_2} - E_{VBM}^{MoS_2}$ and $E_{Zn\ 2p}^{ZnO} - E_{VBM}^{ZnO}$ are the energy differences between the Mo 3d, ZnO 2p CLs and the valence band maximums for the reference MoS₂ and ZnO samples. A method of linearly extrapolating the valence band spectra leading edge to the baseline is used to determine the positions of the valence band maximums in the valence band spectra.^{108,109} The valence band spectra are shown below in Figure 3.1.11 and the values are listed in Table 3.1.1.

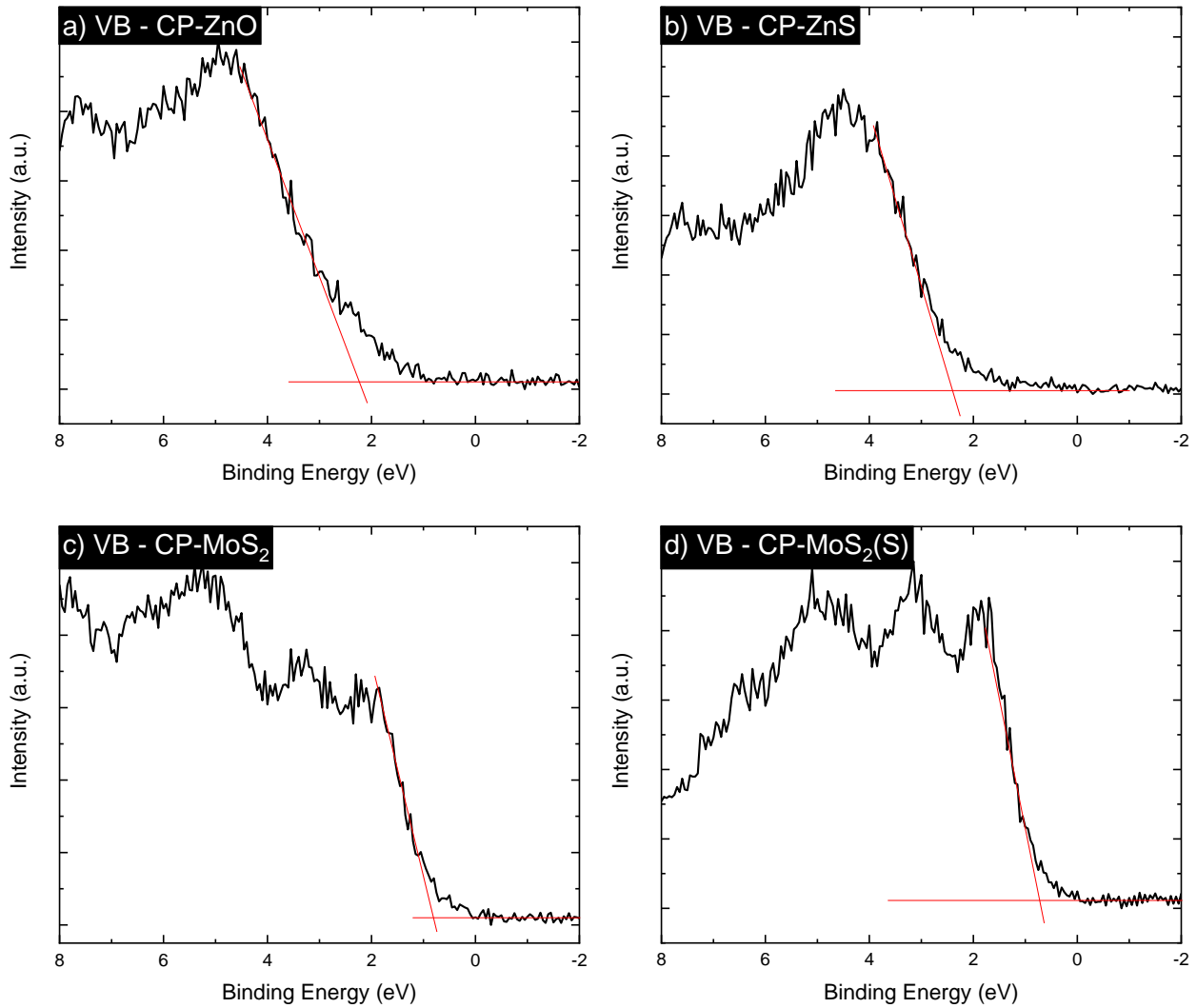


Figure 3.1.11: Valence band measurements of a) CP-ZnO nanowires b) completely sulfurized CP-ZnS nanowires c) CP-MoS₂ and d) CP-MoS₂ annealed in sulfur

Table 3.1.1: Binding Energies for the various chemical states

Sample	State	Binding Energy (eV)
CP-ZnO	Zn 2p	1021.86
	VBM	2.32
CP-ZnS	Zn 2p	1022.74
	VBM	2.4
CP-MoS ₂	Mo 3d	229.126
	VBM	0.8
CP-MoS ₂ (S)	Mo 3d	229.017
	VBM	0.72
CP-ZnO-MoS ₂	Zn 2p	1021.87
	Mo 3d	229.276
CP-ZnO-ZnS-MoS ₂	Zn 2p (ZnO)	1021.83
	Zn 2p (ZnS)	1022.99
	Mo 3d	229.064

By following the above approach, a band diagram of the two studies nanowires can be constructed. However, we do want to caution that like the papers mentioned in the introduction,

there is uncertainty for this approach. The method of linear extrapolation is commonly used in determining the VBM of semiconductors but is somewhat subjective where the linear line is drawn and its relationship with the Urbach tail. Another potential for systematic error is the spatially averaged nature of XPS. This leads to an uncertainty in exactly what is being analyzed, i.e. if there is any underlying, unbonded ZnO, ZnS, or MoS₂ that is not part of the nanowires. However, the complex geometry protruding from the surface, the surface sensitivity of the technique, and the minimal signal of carbon substrate, this impact is likely minimal. Finally, this does not consider any band bending. The band diagrams can be seen in Figure 3.1.12.

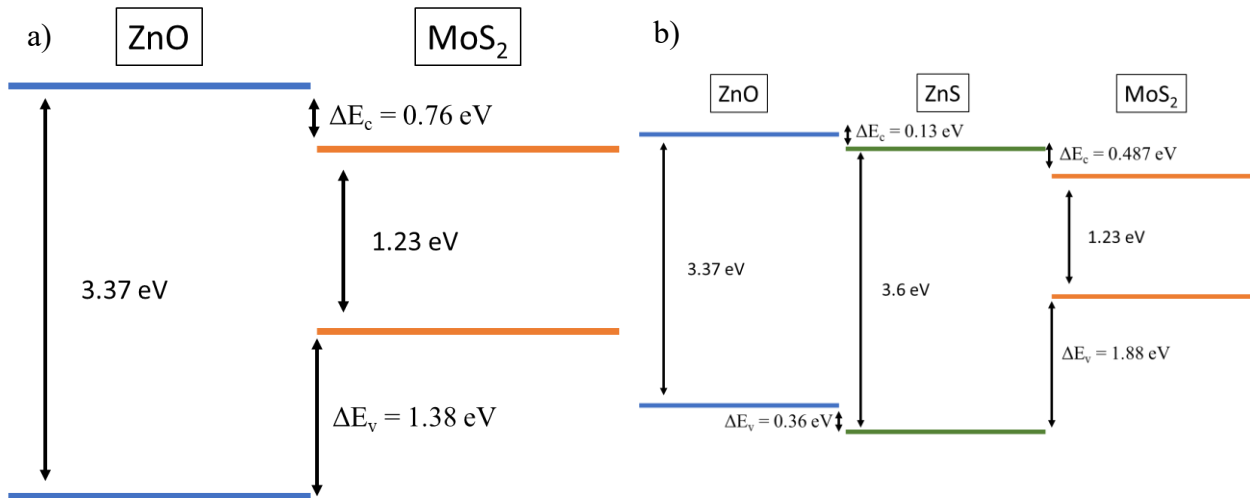


Figure 3.1.12: a) Band alignment diagram of CP-ZnO-MoS₂ nanowires and b) of the CP-ZnO-ZnS-MoS₂ nanowires

In the first of the examined structures, the CP-ZnO-MoS₂ nanowires exhibited a type-I band alignment where the MoS₂ is straddled by the ZnO. This is consistent with some of the findings mentioned earlier.^{85,88} This would facilitate electron transfer from ZnO to MoS₂, but would not provide any benefit from charge separation and the holes would also flow from ZnO to MoS₂. In the CP-ZnO-ZnS-MoS₂ nanowire structure, a mixed type-II/type-I band alignment is noted. The interface between ZnO/ZnS exhibits a type-II band alignment where the electrons

would flow from ZnO to ZnS but the holes would move from the ZnS to ZnO, providing some charge separation. The interface between ZnS and MoS₂ is a type-I band alignment where both the holes and electrons would accumulate in the MoS₂. This mixed band alignment is consistent with one of the mentioned papers.⁸⁸ Overall, having the electrons accumulate in the MoS₂ where they can immediately perform water reduction at the surface would result in a net positive for catalysis.

3.1.3.4 Electrochemical Properties of ZnO/MoS₂ and ZnO/ZnS/MoS₂

To examine the impact the heterostructures have on the HER properties of the catalysts in acidic and alkaline conditions, polarization experiments were performed, shown in Figure 3.1.13. A standard way of comparing catalysts is to determine the overpotential to reach 10 mA/cm². In both acidic and alkaline conditions, ZnO and ZnO-ZnS showed little activity, especially in alkaline conditions. The CP-MoS₂ sample annealed with the presence of sulfur performed notably better than the CP-MoS₂ without sulfur, likely due to the saturated bonds and the lack of the insulating MoO₃ phase. As can be seen, the CP-ZnO-ZnS-MoS₂ exhibited the lowest overpotential in both the acidic and alkaline conditions. CP-ZnO-MoS₂ demonstrated promising results in acidic conditions, performing greater than either ZnO or MoS₂ individually, but did not perform well in alkaline conditions. The performance and Tafel slopes are recorded in Table 3.1.1. The Tafel slope (b), i.e., the slope of the linear, low overpotential regime, is the overpotential required to increase the current density by one order of magnitude. As the Tafel slope is dictated by the reaction mechanism laid out in the experimental section, we can determine that the Volmer-Heyrovsky is the reaction mechanism for the ZnO-ZnS whereas the Volmer-Tafel mechanism is the reaction mechanism for all MoS₂ containing catalysts.¹¹⁰

Additionally, the slowest step for the MoS₂-containing catalysts is the Tafel reaction which involves the transfer of electrons along with the adsorption of the reacting species.

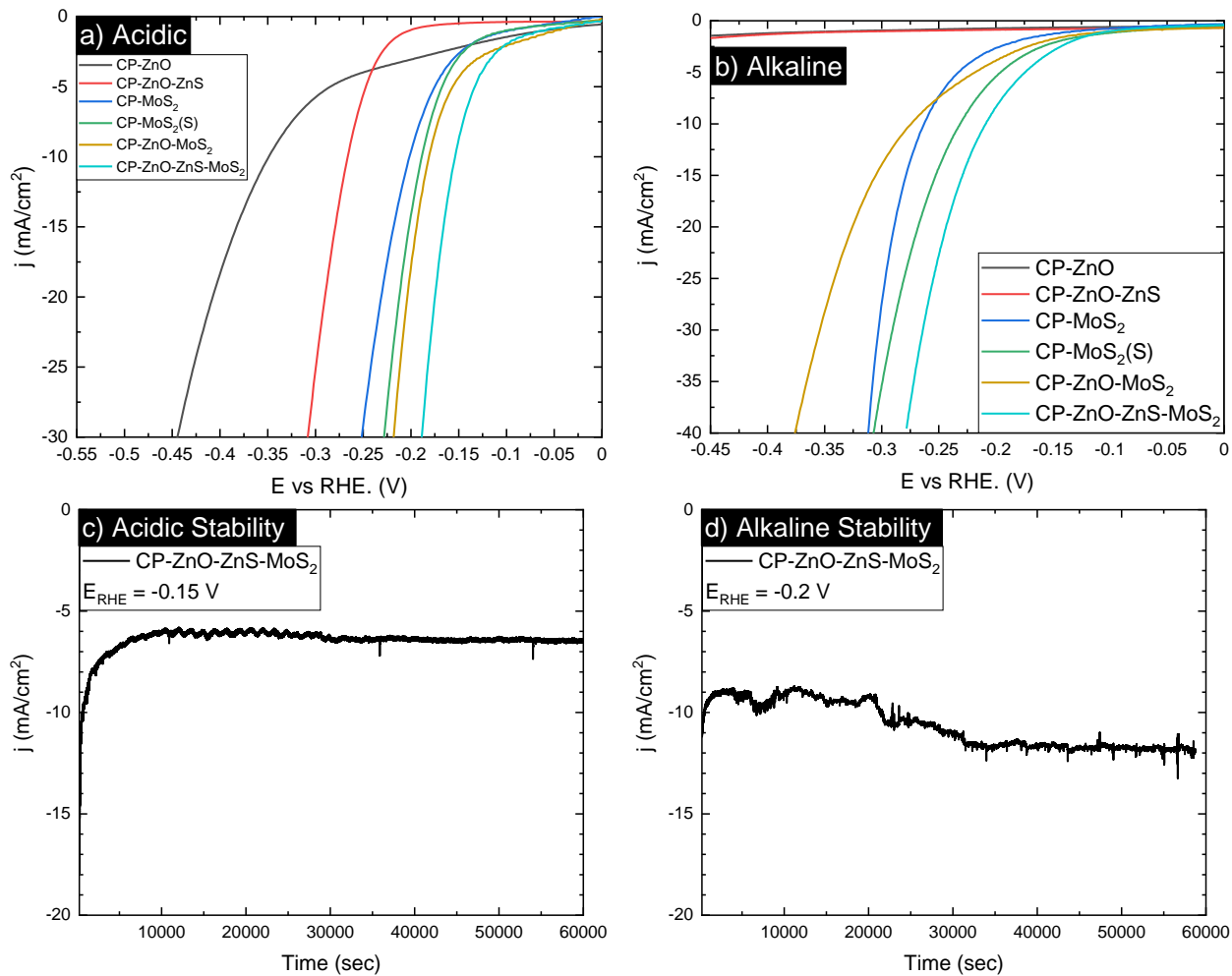


Figure 3.1.13 a) Polarization curves for samples in 0.5 M H₂SO₄ b) Polarization curves for samples in 1 M KOH. Stability measurements in c) acidic and d) alkaline conditions

Table 3.1.1 Performance metrics for the various electrocatalysts

Catalyst	Acidic		Alkaline		C_{dl} (mF/cm ²)	Ref
	η_{10} (mV)	Tafel Slope (mV dec ⁻¹)	η_{10} (mV)	Tafel Slope (mV dec ⁻¹)		
CP-ZnO	349	127	NA	NA	8.45	This work
CP-ZnO-ZnS	266	60	NA	NA	-	This work
CP-MoS ₂	202	113	263	110	16.6	This work
CP-MoS ₂ (S)	188	105	230	135	-	This work
CP-ZnO-MoS ₂	181	104	274	142	23.8	This work
CP-ZnO-ZnS-MoS ₂	154	103	209	128	25.0	This work
ZnO-MoS ₂ nanocomposite	255	56	-	-	3.56	111
Nanosized ZnO coated MoS ₂	-	-	550	192	1.78	112
MoS ₂ /ZnS	271	94.2	-	-	-	113
ZnS-ZnO-MoS ₂ /Ti ₃ C ₂ T _x	327.6	79.5	-	-	7.3	114
Nb ₂ /MoS ₂ -CNF	180	29.5	125	33	-	115
ZnS@MoS ₂	194	73	-	-	2.07	116
ZnS@MoS ₂ Core/shell	106	74	-	-	6.68	117

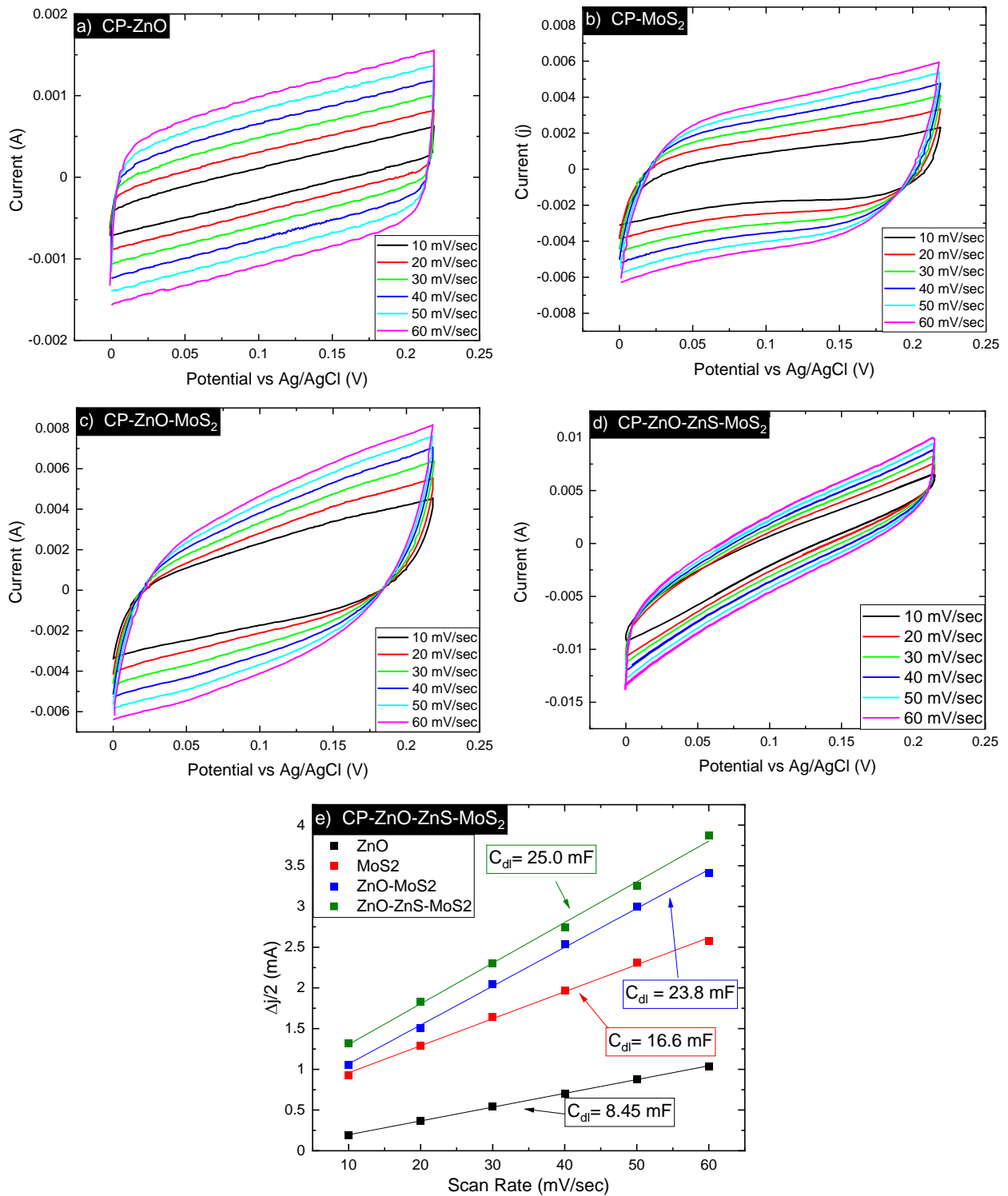


Figure 3.1.14: a) cyclic voltammograms of CP-ZnO b) cyclic voltammograms of CP-MoS₂ c) cyclic voltammograms of CP-ZnO-MoS₂ d) cyclic voltammograms of CP-ZnO-ZnS-MoS₂ and f) plot of $\Delta j/2$ as a function of scan rate

To complement the polarization curves, the double layer capacitance (C_{dl}) of select catalysts was conducted to give insight into the electrochemically active surface area (ECSA). This is useful when working with substrates that have changing complex geometries. ECSA can be determined from the C_{dl} and the specific capacitance (C_s) of any investigated electrode material according to the equation¹¹⁸

$$ECSA = \frac{C_{dl}}{C_s}$$

Determination of C_s has been identified as one of the main challenges with this technique and it has been common practice to use a single C_s value to obtain the ECSA value, regardless of the material's nature. This has led to significant deviations in reported literature.^{118,119} It is still an ongoing discussion within the community for how to accurately determine this value, however the comparison between C_{dl} is still useful for comparisons between the same material and within the same study.¹²⁰

A common method for obtaining the C_{dl} consists of recording cyclic voltammograms at various scan rates within a potential region where no redox reactions take place as shown in Figure 3.1.14a-d. This works on the basis of when an electrode surface is subjected to a voltage ramp, a steady-state capacitive current is observed in a short time (i_c) if the only process is the charging of the double layer, i.e. the movement of ions on either side of the electrode/electrolyte interface. For ideal capacitors, i_c is related to the capacitance (C) and to the scan rate (v) as shown below

$$i_c = v * C$$

Then the i_c for the anodic and cathodic scans are the difference is plotted as a function of scan rates, as shown in Figure 3.1.14e, and then extract C_{dl} by taking the slope of the resulting plot.

C_{dl} can also be obtained from EIS, however the difference between the techniques has been shown to be within 5%.¹²⁰⁻¹²² As can be seen in Figure 3.1.14e, all samples show significantly greater C_{dl} over the bare ZnO-NWs even though the ZnO NWs have a significant surface area advantage over CP-MoS₂. This compliments our results earlier of CP-ZnO having poor catalytic performance. The C_{dl} of CP-MoS₂, CP-ZnO-MoS₂, and CP-ZnO-ZnS-MoS₂, are somewhat similar however the nanowire structures exhibit a slightly higher C_{dl} , suggesting that there is an increase in ECSA attributable to the increased surface area that the ZnO nanowire structure provides. This increase in surface area compliments the formation of the heterojunctions as shown in Figure 3.1.12 where the lower CBM of the MoS₂ relative to ZnO and to ZnO-ZnS. This facilitates the more effective transfer of electrons to the increased surface area of the MoS₂ to enhance the active sites of MoS₂ to undergo the hydrogen evolution reaction. While it is not possible to completely separate the two effects here, given that the surface area between the ZnO-MoS₂ and ZnO-ZnS-MoS₂ structures are quite similar, and that even without the presence of the very active 1T phase, the ZnO-ZnS-MoS₂ is more active, the band alignment appears to be a large contributor to the increased performance.

3.1.4 Conclusions

This study developed a facile and scalable 3-step hydrothermal, electrodeposition, and annealing technique to synthesize a variety of nanowire heterostructures. The heterojunction catalysts of CP-ZnO-MoS₂ and CP-ZnO-ZnS-MoS₂ both saw an increase in catalytic activity in the acidic regime, with overpotentials to reach 10 mA/cm² of 181 mV and 154 mV respectively, over their constituent materials. The CP-ZnO-ZnS-MoS₂ catalysts also saw an increase in catalytic activity in the alkaline conditions, requiring only 209 mV to reach 10 mA/cm². This has been attributed primarily to the synergistic properties of the band alignment structure and the increased surface area afforded by the nanowire structure. The 1T phase was also noted in the CP-ZnO-MoS₂

sample, suggesting that this also played a role in increasing the catalytic activity of the sample. Overall, the synthesized nanowire heterostructures were found to be highly performing and gives insight into how the changing band alignment and morphology can play a significant role in increasing the catalytic performance towards HER.

3.2 The Electrodeposition of Cobalt Sulfide/Molybdenum Sulfide Heterostructures for HER in Acidic and Alkaline Solutions

3.2.1 Background and Motivation

In this work, we demonstrated a simple electrochemical deposition and annealing method to fabricate and control the phase of various CoS_x structures heterostructured with MoS_2 on carbon cloth for use as an HER catalyst.

In recent years, great attention has been given to other transition metal sulfides besides MoS_2 , such as Co, Ni, and Fe. Among the most successful have been those of Co sulfides, such as Co_9S_8 , CoS , Co_3S_4 , and CoS_2 , showing strong electrocatalytic activity towards HER in both acidic and alkaline conditions, while remaining inexpensive and readily available.^{123–126} Within this broad range of phases, various morphologies have also been explored. Some examples are Co_9S_8 and CoS_2 hollow-spheres, cotton-like Co_9S_8 , and CoS_2 nanoarrays, all exhibiting various catalytic properties.^{127–129} However, these solely cobalt sulfide materials still cannot compete with the state-of-the-art catalysts, and therefore various strategies have been employed to increase their activity, such as doping or alloying MoS_2 with cobalt and cobalt sulfide, respectively.

Bonde et al. demonstrated that doping Co-atoms on the edges of MoS_2 greatly enhanced the HER activity, owed to the decrease of adsorption energy of hydrogen.²³ Another example showed the synergistic effect, such as decreasing the overpotential by between Co_9S_8 and MoS_2 towards HER in alkaline environments.¹³⁰ Finally it has been shown that the interface between cobalt sulfides and molybdenum sulfide is critical to the HER performance because the formation

of nano-interfaces facilitates enhanced charge transfer between Co and Mo through S-linkage as shown in Figure 3.2.1.¹³¹

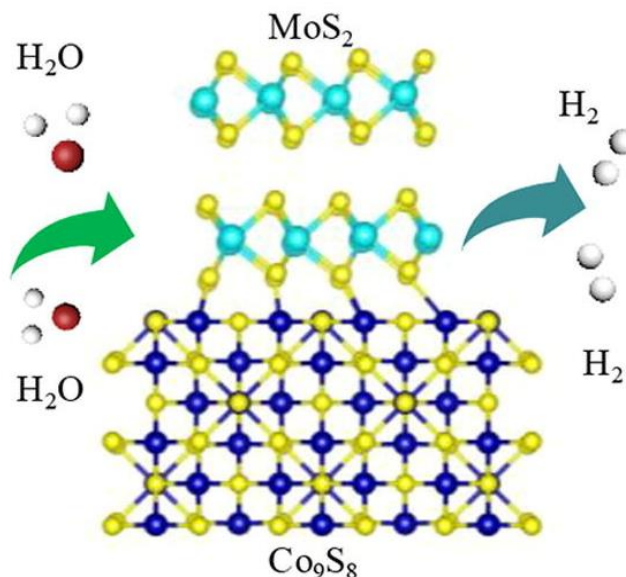


Figure 3.2.1: Diagram illustrating the linking disulfides between Co₉S₈ and MoS₂

In order to increase the catalytic performance of these materials further and to take full advantage of any synergistic impacts, the active area needs to be increased further. As was discussed in the earlier chapter, increasing the total active surface area per unit area is also vital to the overall improvement of catalytic properties. As such, various 3D, porous substrates have been explored to increase the “loading” of the catalyst and expose as much material to the electrolyte as possible. However, many catalysts for HER require a polymer binder to anchor the catalyst to the 3D, porous working electrode, increasing resistance and hindering active sites or causing long-term stability issues.^{132–134} Therefore, direct growth of the catalyst on the current collector can increase the HER performance of the catalyst towards HER. Carbon paper exhibits high conductivity, good mechanical strength, is inexpensive, and is flexible, making it an excellent candidate for the substrate. In addition, carbon paper is a porous material with a three-dimensional

morphology, allowing more active sites per unit area. Additionally, it has been shown that MoS₂ on carbon paper provides higher catalytic activity when compared to a traditional flat substrate.¹³⁵⁻

137

In this work, several compositions were tested to elucidate the optimal conditions, as well as help determine the underlying factors that influence the overall HER properties. By controlling the electrolyte bath parameters, such as the cobalt concentration; various morphologies, such as platelets, clusters, and nanostrips, and crystal structures were measured and exhibited drastically different HER properties. It was observed that while all samples were stable and exhibited promising HER properties in acidic conditions, only the sample from the equimolar electrolyte was stable in an alkaline environment while exhibiting extremely high activity. This performance was explored with a variety of techniques and together, these results highlight the synergistic effects among various cobalt sulfide species and MoS₂ towards HER.

3.2.2 Synthesis Methods

3.2.2.1 Electrolyte Preparation

To determine the optimal conditions for the synthesis of c-CoS_x-MoS₂, two separate approaches were examined. The first approach was to electrodeposit a metallic Co-Mo alloy, which was then followed by a sulfurization step. Since this process was unsuccessful, the details and discussion are included in the appendix. The main electrolyte of interest was the electrodeposition of cobalt sulfide in conjunction with molybdenum oxide which was then followed by a sulfurization step.

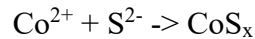
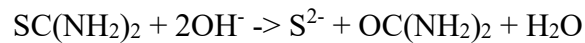
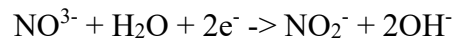
The Co-Mo sulfide catalysts were electrodeposited from an electrolyte containing precursors of Co, Mo, and S. The electrolyte was prepared from cobalt nitrate hexahydrate (Co(NO₃)₂ · 6H₂O), sodium molybdate dihydrate (Na₂MoO₄ · 2H₂O), and thiourea (CH₄N₂S). The

sodium molybdate dihydrate concentration was held at 75 mM and the thiourea concentration was held at 0.2 M while the cobalt nitrate hexahydrate concentration was varied from 5 mM up to 100 mM. Samples will be referred by their Co – Mo precursor concentrations in mM, e.g., 25-75 will be in reference to 25 mM $\text{Co}(\text{NO}_3)_2 \cdot 6 \text{H}_2\text{O}$ – 75 mM $\text{Na}_2\text{MoO}_4 \cdot 2\text{H}_2\text{O}$.

Table 3.2.1: Component concentrations (M) in electrolytes for Co-Mo oxide electrodeposition

Sample ID	$\text{Co}(\text{NO}_3)_2$ (M)	Na_2MoO_4 (M)	$\text{CH}_4\text{N}_2\text{S}$ (M)
5-75	0.005	0.075	0.2
15-75	0.015	0.075	0.2
25-75	0.025	0.075	0.2
50-75	0.050	0.075	0.2
75-75	0.075	0.075	0.2
100-75	0.100	0.075	0.2

The CoS_x component was grown on carbon paper using a facile electrodeposition with the species pertaining to the CoS_x deposition being $\text{Co}(\text{NO}_3)_2$ and $\text{CH}_4\text{N}_2\text{S}$. During the deposition, the OH^- ions generated from reduced NO_3^- ions react with $\text{CH}_4\text{N}_2\text{S}$ to form S^{2-} ions. The following reactions can describe the process



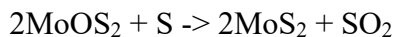
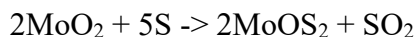
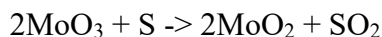
Based on the charges of the Co and S ions, one would expect to form CoS, as found in Liu et al. study.¹³⁸ However, a cyclic voltammetry deposition method was utilized in their study, whereas in this study a potentiostatic deposition method and annealing was utilized, resulting in a

different stoichiometry. In regards to MoS₂, the primary formation occurs during the annealing step, as the MoO₄²⁻ ion has a high energy of formation (-1354 kJ mol) it cannot be easily separated into Mo ions to react with the S ions via electrodeposition as it far exceeds the cathodic potential required for the discharge of hydrogen.¹³⁹ Therefore, the formation of MoS₂ occurs during the annealing step, described later, when the excess sulfur reacts with the deposited molybdenum oxide.

3.2.2.2 Crystallization of c-CoS_x/MoS₂

To crystallize the samples, annealing was carried out in an MTI OTF-1200X tube furnace. Annealing was performed by heating the sample to 450°C at a ramp rate of 14°C/minute where it was held for 60 minutes before being naturally cooled back to ambient temperature. All anneals took place in the presence of flowing forming gas (5% H₂ / 95% Ar) with 3 grams of elemental sulfur upstream of the substrate. Forming gas is critical to removing the oxides to allow for sulfurization.¹⁴⁰ Prior to the anneal, the chamber was purged with excess forming gas for 45 minutes to minimize the presence of any impurities within the furnace. Natural cooling was carried out under the forming gas prior to the samples being removed from the furnace.

The general sulfurization process from molybdenum oxide to molybdenum sulfide follows the following reactions:¹⁴¹



3.2.3 Results

3.2.3.1 Structural Properties of c-CoS₂/MoS₂

To understand the structural and morphological features of the catalysts, SEM images were collected. In Figure 3.2.2, a low magnification image shows uniform coverage of the carbon paper substrate. The high magnification SEM images revealed that the morphology drastically changed depending on the concentration ratio of the Co and Mo precursors as seen in that the MoS₂ (002) diffraction peak increases in intensity as the Co concentration increases. This increase in MoS₂ is being attributed to the co-deposition of Mo with Co, in which the Co induces more Mo to be deposited during the electrodeposition process.²⁴ This is the case as the redox potential of Mo metal is quite negative, preventing Mo from depositing without the co-deposition process.²⁴ Additionally, the diffraction peaks decrease in intensity and sharpness as the Co concentration increases, indicating that the crystallite size is decreasing. Upon applying the Scherrer equation, we calculate that the initial 5-75 has a crystallite size of 26 nm with 100-75 an average crystallite size of 16.7 nm. As the Co precursor concentration increases, the diffraction peaks associated with Co₉S₈

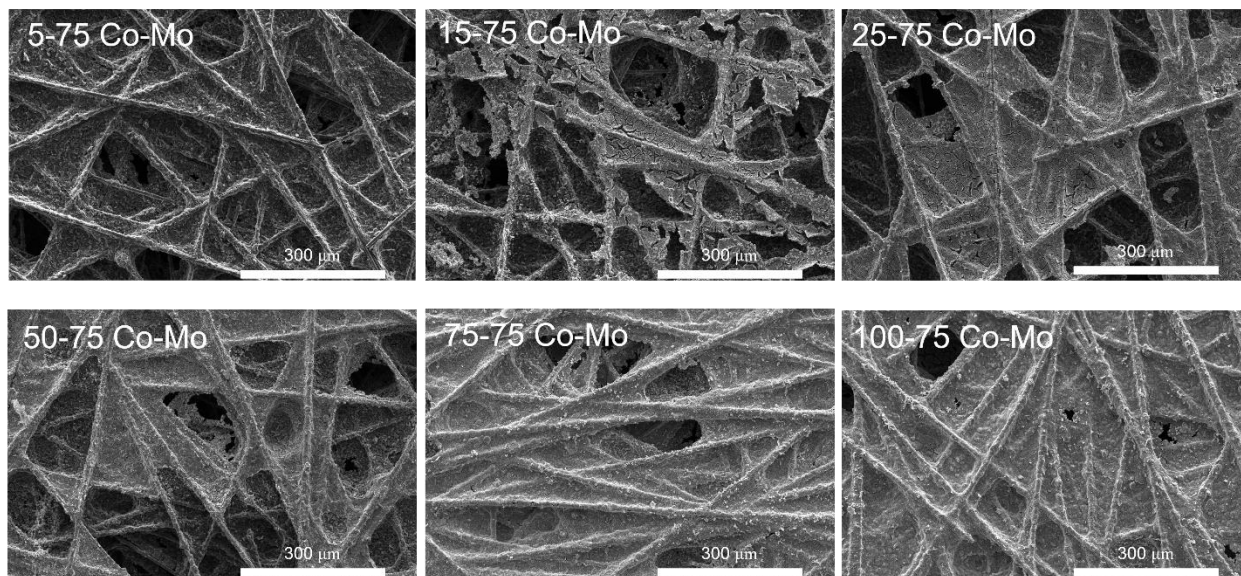


Figure 3.2.2: Low magnification of the Co-Mo Sulfide catalysts

decrease in relative intensity while the diffraction peaks associated with CoS_2 increase in relative intensity.

In the sample with the lowest Co concentration, 5-75, thin sheets with small clusters are observed along the edges. When the Co was increased to 15-75, the sheets are no longer observed, and instead large plate-like structures are formed showing clustering on the surface. In the 25-75 sample, the plates grew, however the surface was largely featureless and little clustering was observed. The morphology continued to change in 50-75 as the large plate-like structures are no longer observed and instead a much rougher, scaled surface is formed with clusters of sheets on the surface. The 75-75 sample lacked the scaled surface and instead exhibited round, textured structures with long, flat, and wide features protruding perpendicular to the surface. Finally, the 100-75 sample is even more textured than 75-75 and lacks the flat sheets protruding from the surface.

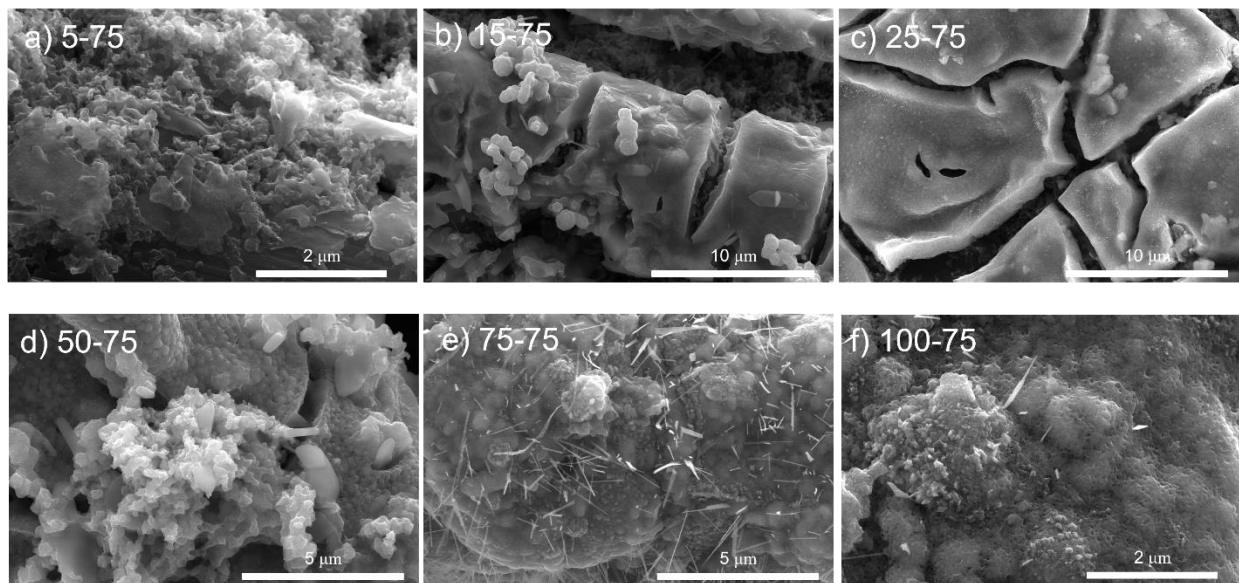


Figure 3.2.3: SEM images of a) 5-75, b) 15-75, c) 25-75, d) 50-75, e) 75-75, and f) 100-75

XRD patterns shown in Figure 3.2.4 provide crystallographic information on the catalysts. The Bragg diffraction hump located at $2\theta \approx 14.5^\circ$ was indexed to the (002) plane of hexagonal

MoS₂.⁹¹ The peaks located at $2\theta \approx 29.5, 39.4,$ and 47.5° are indexed as the (311), (331), and (333) planes of cubic Co₉S₈ respectively.¹⁴² The diffraction peaks associated with the (200) and (210) planes of cubic CoS₂ were observed at $2\theta \approx 32.4,$ and 36.3° respectively.¹⁴³ It is noticed that the

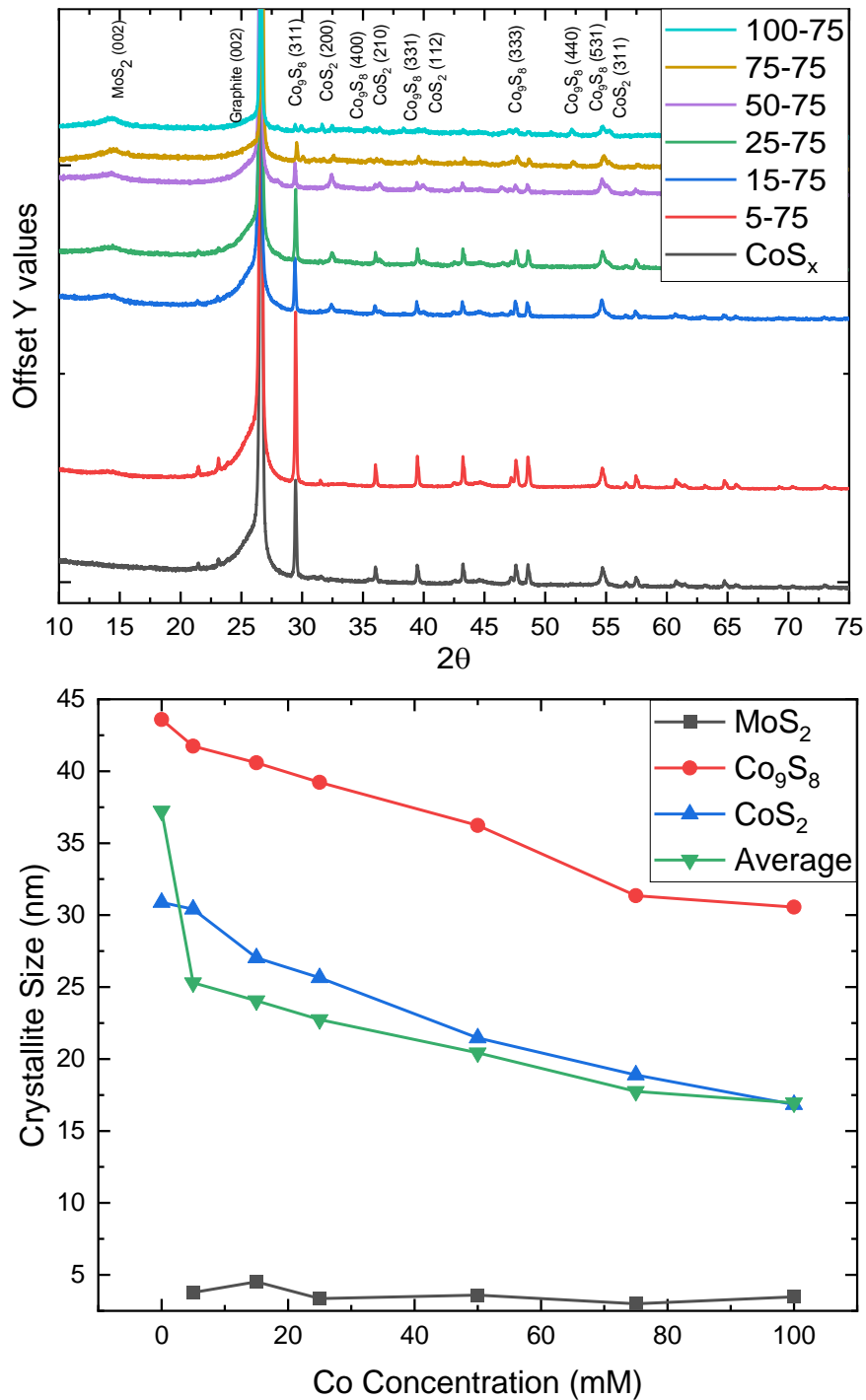


Figure 3.2.4: a) XRD patterns of the various catalysts and b) crystallite size of different species calculated via the Scherrer equation

MoS₂ (002) diffraction peak increases in intensity as the Co concentration increases. This increase in MoS₂ is being attributed to the co-deposition of Mo with Co, in which the Co induces more Mo to be deposited during the electrodeposition process.¹⁴⁴ This is the case as the redox potential of Mo metal is quite negative, preventing Mo from depositing without the co-deposition process.¹⁴⁴ Additionally, the diffraction peaks decrease in intensity and sharpness as the Co concentration increases, indicating that the crystallite size is decreasing. Upon applying the Scherrer equation, we calculate that the initial 5-75 has a crystallite size of 26 nm with 100-75 an average crystallite size of 16.7 nm. As the Co precursor concentration increases, the diffraction peaks associated with Co₉S₈ decrease in relative intensity while the diffraction peaks associated with CoS₂ increase in relative intensity.

To further elucidate the crystalline structure of the grown materials, Raman spectroscopy was performed on all materials as shown in Figure 3.2.5a. The peaks at roughly 384 cm⁻¹ and 407 cm⁻¹ are attributed to the in-plane E_{2g} mode and the out-of-plane A_{1g} mode, respectively.⁹⁶ The peaks at 289 cm⁻¹, 318 cm⁻¹, and 393 cm⁻¹ are ascribed to the E_g, T_g(1), and A_g modes of CoS₂ with the shoulder at roughly 418 cm⁻¹ the T_g(2) mode.¹⁴⁵ The peak found at 680 cm⁻¹ is attributed to

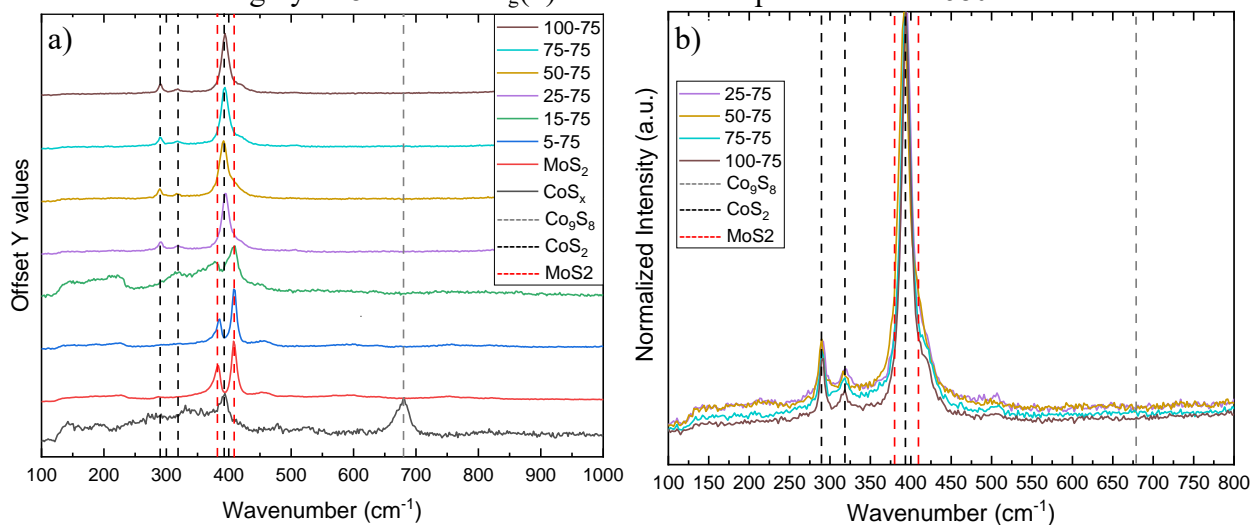


Figure 3.2.5 a) Raman spectra for all the catalysts and b) Raman spectra of 25-65 through 100-75 to demonstrate any subtle changes within the data

the primary vibration mode of Co_9S_8 .¹⁴⁶ The primary peaks for the different species are labelled with a dashed line in Figure 3.2.5. In the CoS_x sample, both peaks associated with CoS_2 and Co_9S_8 are present. However, when in the presence of Mo species, the Co_9S_8 vibration modes are extinguished and are not seen at any Co/Mo ratio. At low Co/Mo ratio, as in 5-75 and 15-75, the MoS_2 features dominate the spectra. As the Co/Mo ratio increases to 25-75 and beyond, the CoS_2 features dominate the spectra as can be seen in more detail in Figure 3.2.5b.

3.2.3.2 Chemical Properties of c-CoS₂/MoS₂

To determine elemental and chemical composition of the 75-75 catalyst, XPS was conducted. However, depending on where the sample was scanned, different spectra would appear as can be seen in Figure 3.2.6. While different chemical composition ratios and chemical shifts are present, the same chemical species were present in all samples. However, it is difficult to give a complete picture of the sample's composition using XPS due to the lateral variability. A representative scan can be seen in Figure 3.2.7. The Mo 3d spectra can be deconvoluted into distinctive peaks of a single double ($3d_{5/2}$ and $3d_{3/2}$) of Mo⁴⁺ and singlets of the various overlapping

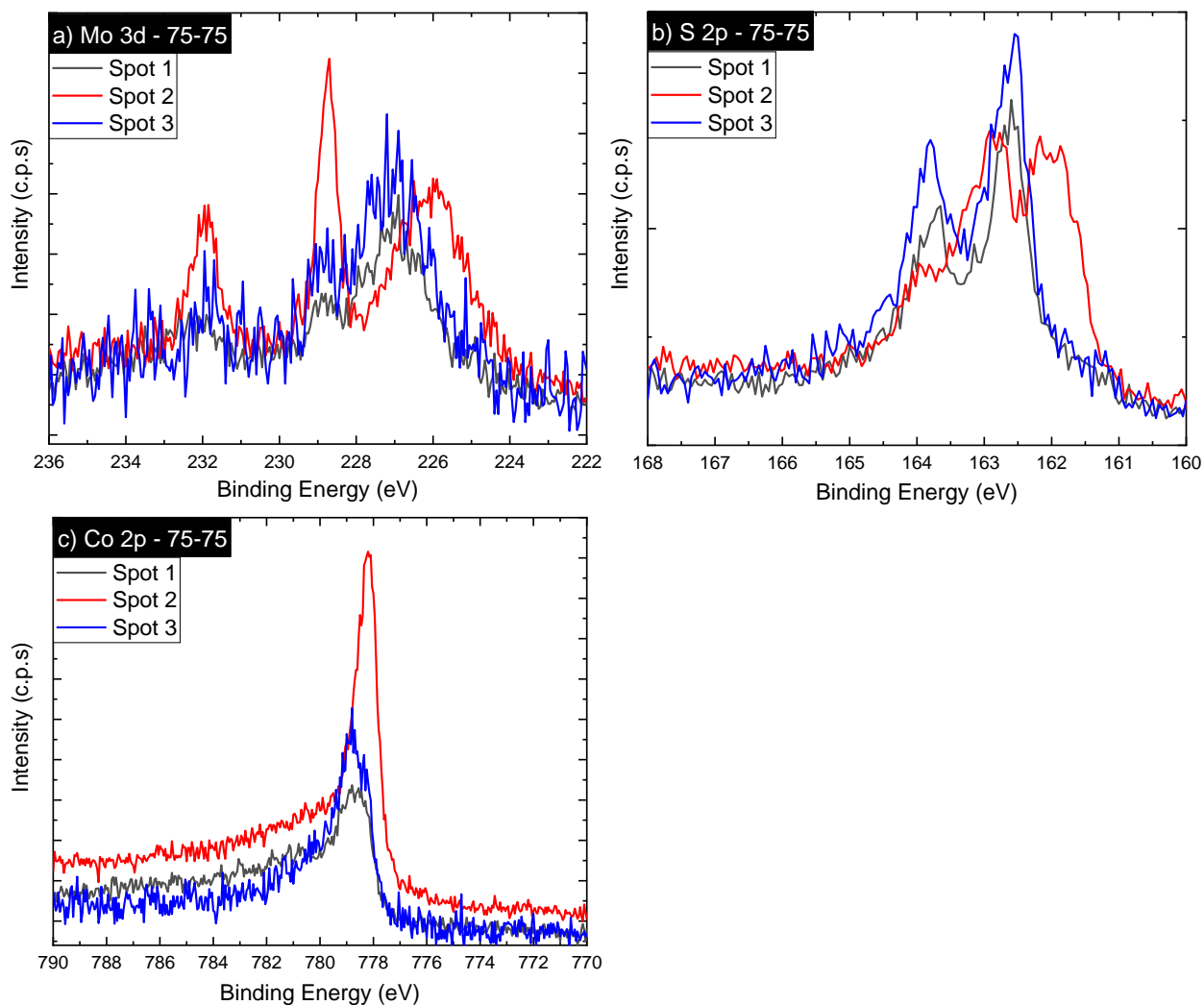


Figure 3.2.6: Raw, unnormalized spectra at varying spots on the 75-75 sample with a) Mo 3d, b) S 2p, and c) Co 2p

S 2s states that occur in the same energy range.^{50,147,148} The Mo 3d peaks were deconvoluted with a binding energy difference of 3.13 eV between the 3d_{5/2} and 3d_{3/2} and with a fixed intensity ratio of 3:2. In the sulfur spectrum, the presence of S²⁻ and S₂²⁻ was detected; this is consistent with previous literature.^{147,149} The sulfur spectrum was deconvoluted with two doublets, with the constraints of an energy difference of 1.18 eV between the 2p_{3/2} and 2p_{1/2} and with an intensity ratio of 2:1. The cobalt 2p_{3/2} spectrum was deconvoluted with two primary features at 777.96 eV, 778.6 eV corresponding to Co³⁺ and Co²⁺ respectively, and with a large satellite peak at higher binding energy.^{126,150–152}

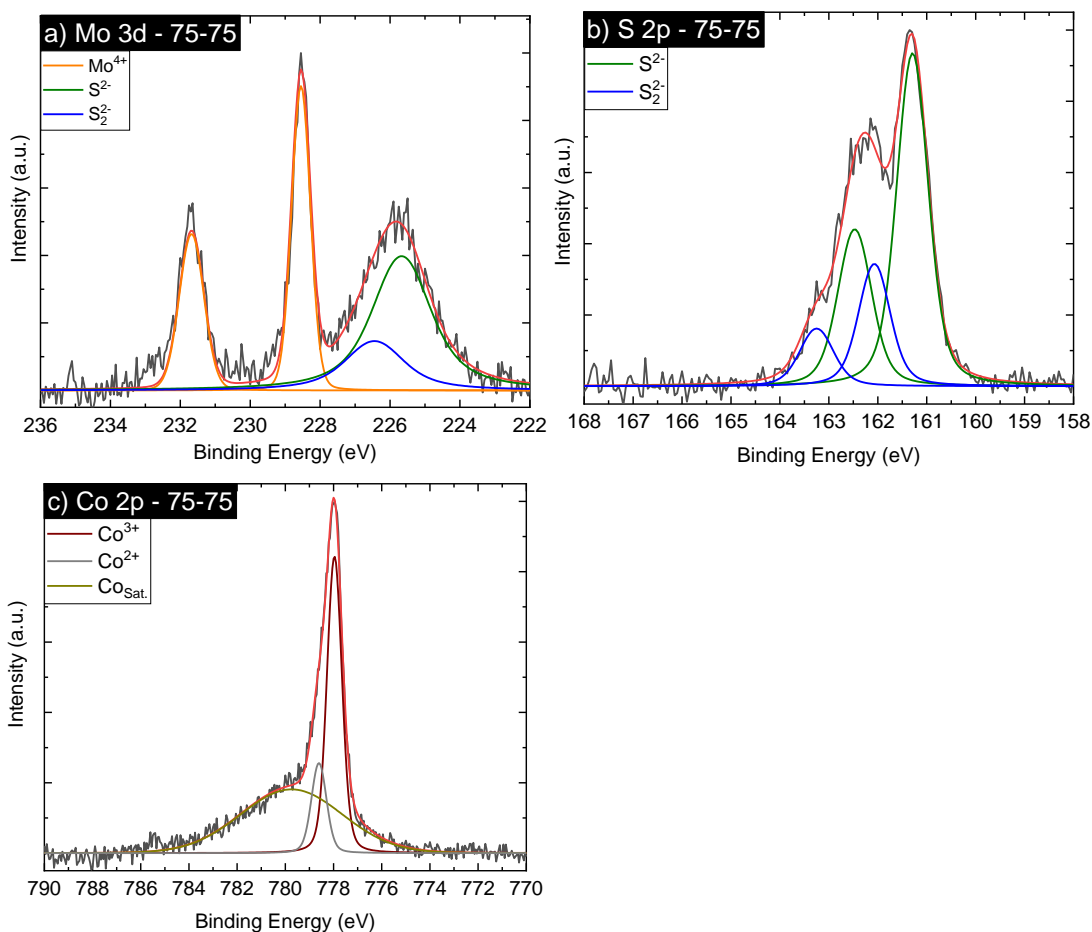


Figure 3.2.7: Deconvoluted XPS Spectra of a) the Mo 3d, b) S 2p, and c) Co 2p_{3/2}

3.2.3.3 Electrochemical Properties of c-CoS₂/MoS₂

The impact of the Co/Mo precursor ratio on the HER properties of the catalysts in acidic conditions, polarization experiments were performed, shown in Figure 3.2.8. The overpotential required to reach the cathodic current density of 10 mA/cm² (η_{10}) was used to compare the catalytic activity of the HER catalysts and these are shown in the subset of Figure 3.2.8. As seen in Figure 3.2.8, the 75-75 sample performed the best by exhibiting the lowest overpotential (112 mV) to reach 10 mA/cm². The other values of the catalysts η_{10} can be seen in the Figure 3.2.8 subset plotted against their Co/(Co+Mo) as well as in Table 3.2.2. This performance of 75-75 was greater than that of either CoS_x or MoS₂ and equal or superior to that of similar cobalt sulfide-based catalysts as seen Table 3.2.3. One sample of note is the Co-Mo-P@C which outperforms the other compared material. This is due to certain phosphide materials being more catalytically active than the sulfide counterparts. However, this could open up future work where our superior material is modified with their phosphide, further improving the performance.

Table 3.2.2: Electrochemical values for the various catalysts, (-) indicates the sample was unstable in indicated conditions, standard deviation of three samples is given in parenthesis with the average reported value the given value ()

Sample	Co/(Co+Mo)	Acidic η_{10} (mV)	Acidic b (mV/dec)	Alkaline η_{10} (mV)	Alkaline b (mV/dec)
5-75	0.282	190 (1.63)	157	-	-
15-75	0.482	159 (3.09)	106	-	-
25-75	0.597	149 (3.85)	84	-	-
50-75	0.626	123 (2.45)	111	-	-
75-75	0.635	112 (2.05)	113	60 (3.86)	81
100-75	0.653	121 (2.09)	114	-	-
MoS ₂	0	232 (0.82)	123	-	-
CoS _x	1	175 (4.02)	87	-	-

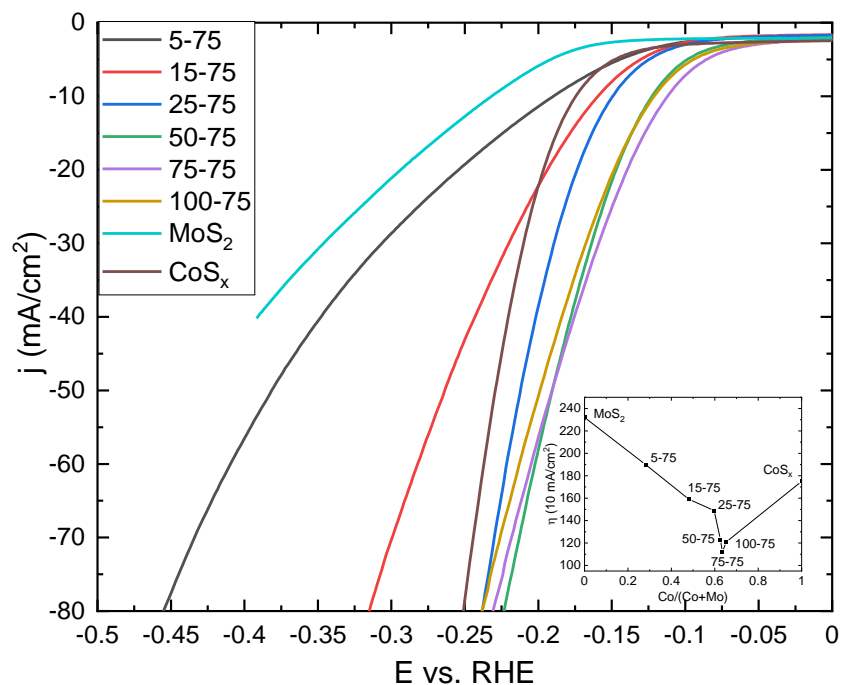


Figure 3.2.8: Polarization curves in 0.5M H₂SO₄ of the various catalysts; subset η_{10} vs Co/(Co+Mo)

HER in alkaline medium is also of high interest due to the widespread usage of alkaline water electrolysis in industry, as well reducing the corrosion of electrolytic cells found in acidic cells. Polarizations in 1 M KOH were carried out to investigate the Co-Mo sulfide catalyst's affinity towards HER in basic condition. The sample 75-75 showed good stability, as can be seen in Figure 3.2.9. Additionally, 75-75 showed an extremely low η_{10} value of 60 mV, one that competes with state-of-the-art catalysts in alkaline medium¹⁵³. This overpotential is among the best reported in current literature as seen in Table 3.2.4. Only the 75-75 sample was stable in alkaline medium, with all others degrading rapidly. The subset of Figure 3.2.9 shows the degradation of the 25-75 sample as an example of the instability found in other samples. The origin of this lack of stability will be discussed in later sections.

Table 3.2.3: HER of other Cobalt-Molybdenum Sulfide catalysts in Acidic Conditions

Catalyst	Electrolyte	$\eta(\text{HER})$ at $j = 10 \text{ mA cm}^{-2}$ (mV)	Tafel slope (mV dec^{-1})	Reference
CP-CoS_x/MoS₂	0.5 M H₂SO₄	112	113	This Work
Co ₉ S ₈ @MoS ₂ /CNFs	0.5 M H ₂ SO ₄	190	110	154
Co-Mo-P@C	0.5 M H ₂ SO ₄	96	53	155
MoS ₂ /CoS ₂ /CC	0.5 M H ₂ SO ₄	118	37	30
Co-MoS _x /CFP	0.5 M H ₂ SO ₄	199	51	31
CoMoS ₂ -C	0.5 M H ₂ SO ₄	135	50	147
CoMoS _x /CC	0.5 M H ₂ SO ₄	100	70	156

The Tafel slope (b), i.e., the slope of the linear, low overpotential regime in the Tafel plot, is the overpotential required to increase the current density by one order of magnitude. As such, it is optimal to have a catalyst with a lower Tafel slope for HER applications. See Experimental chapter for more details. The Tafel slopes for the Co-Mo sulfide catalysts are listed in Table 3.2.2 and suggest a Volmer-Heyrovsky mechanism, or electrochemical desorption with an adsorbed hydrogen reacting with a H⁺ in the electrolyte, consistent with literature^{89,150,157}.

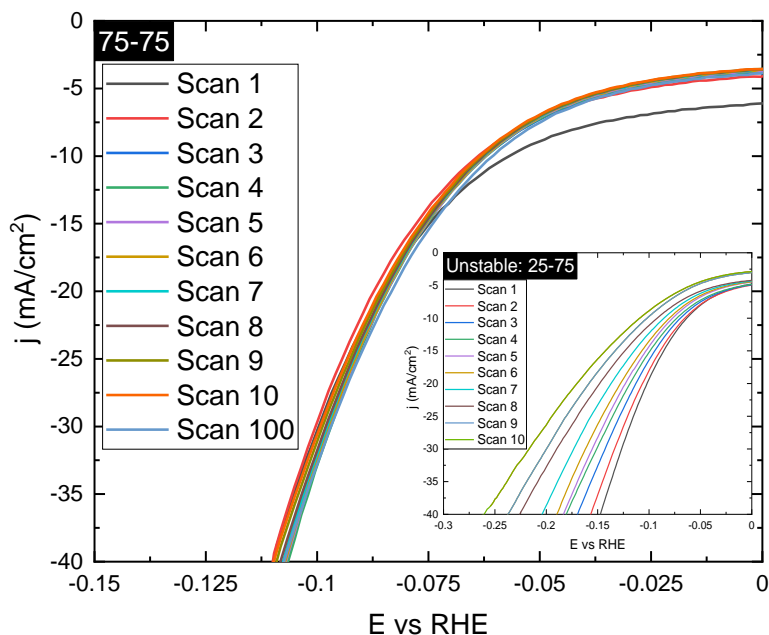


Figure 3.2.9: Polarizations curves in 1 M KOH for the various catalysts; subset) example of unstable

Table 3.2.4: HER of other Cobalt-Molybdenum Sulfide catalysts in Alkaline Conditions

Catalyst	Electrolyte	$\eta(\text{HER})$ at $j = 10 \text{ mA cm}^{-2}$ (mV)	Tafel slope (mV dec^{-1})	Reference
CP-CoS_x/MoS₂	1M KOH	60	81	This Work
CP/CTs/Co-S	1M KOH	190	131	158
MoP	1M KOH	140	48	159
MoC _x	1M KOH	151	59	160
CC/CoP	1M KOH	209	129	161
Ti foil/Ni _{0.33} Co _{0.67} S ₂ NWs	1M KOH	88	151	162
CoS _x @MoS ₂	1M KOH	146	56	150
Co ₃ S ₄ -L	1M KOH	270	124	163
Co-Mo-P@C	1M KOH	162	34	155
Co ₃ S ₄ /MoS ₂ /Ni ₂ P	1M KOH	178	98	164
CoS ₂ HNSs	1M KOH	290	100	165
Ni _x Co _{3-x} O ₄ NWs	1M KOH	370	60	166
Co-MoS ₂ /CC	1M KOH	40	66	167
Co(OH) ₂ /MoS ₂	1M KOH	117	60	168

As the Raman data demonstrates, the samples with more CoS₂ like structures had the highest performance in acidic conditions compared to those with a more MoS₂ like spectra. This is to be expected as previous literature has demonstrated that cobalt sulfide based materials have superior catalytic performance over crystalline MoS₂.^{15,18,31,89,157,169,170} However, while the samples 25-75 through 100-75 have similar Raman spectra, they have very different catalytic activities in acidic conditions and stability in alkaline conditions.

Diffraction patterns of various catalysts obtained via XRD can help elucidate the origin of these performances as the XRD between the samples are quite different. At high cobalt fraction, the crystallite size of the cobalt sulfide phases decreases, allowing an increase in the concentration of linking disulfide anions (Figure 3.2.1), the catalytically active sites, to be exposed to the electrolyte.¹⁷¹ As smaller grains mean more of these nano-interfaces form, a higher density of active sites which led to an improvement of the electrocatalytic activity was observed.^{131,150,154}

Additionally, the increase in the MoS₂ phase with the higher Co/Mo ratios likely contributes to this increase in overall catalytic activity of the catalyst due to their synergistic properties, such as better charge transfer and facilitation of H- containing species adsorption-desorption at the active sites^{30,150,156}.

However, this does not directly explain the difference in stability and overall performance of 75-75 compared to the rest of the synthesized catalysts in alkaline conditions. As the only major difference in the high Co/Mo ratio catalysts is the morphology and crystallite size, we suggest that this stability is related to the morphology and crystallography of the 75-75 catalyst. As seen in Figure 3.2.4, the 75-75 sample is the only catalyst to exhibit the wide, flat, and protruding features. In an effort to determine the composition of the strands, SEM and EDS were carried out as shown in Figure 3.2.10. However, due to the large penetration depth of SEM and the very similar signal between sulfur K α and molybdenum L α (difference of 0.014 eV) the sample looks homogeneously distributed in Co, Mo, and S. Therefore, we are unable to determine the exact components that

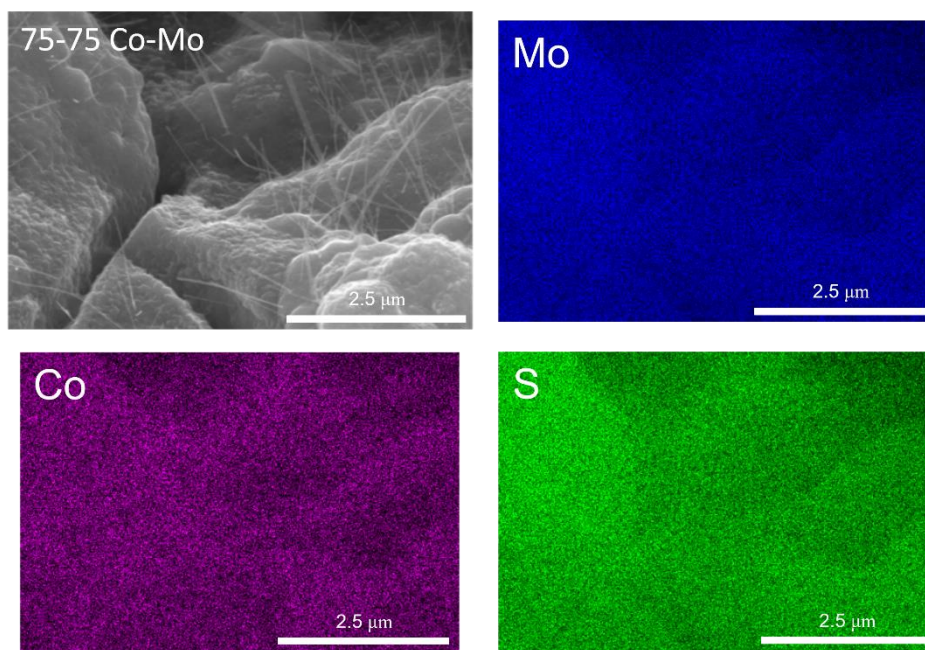


Figure 3.2.10: SEM EDX of the 75-75 catalyst

make up the specific morphological feature of the heterostructure. Overall, we suggest that at low Co concentration, the less alkaline stable Co_9S_8 limits the stability during HER whereas at high Co concentration the continued reduction in crystallite size and increased accessibility to the disulfide anions reduces the stability of 100-75 in alkaline conditions.¹⁷¹

3.2.3 Conclusions

This study developed a facile and scalable electrodeposition technique and annealing methods for catalytically active $\text{CoS}_x/\text{MoS}_2$. These catalysts are extremely active for HER in acidic conditions and one of the best performances in alkaline conditions, with overpotentials to reach 10 mA/cm^2 of 112 mV and 60 mV and with Tafel slopes of 113 mV/dec and 81 mV/dec, respectively. The 75-75 exhibited excellent stability in both acidic and alkaline conditions and performed superior to all other samples. This has been attributed to the synergistic properties evolving through the intimate growth of alloys between Co and Mo sulfides, such as better charge transfer and facilitating the adsorption-desorption of hydrogen at the interface of the electrode/electrolyte, as well as increased nano-interfaces between the CoS_x and MoS_2 features. In addition, an unusual morphology was found in the 75-75 catalysts that has not been reported on before. Overall, these scalable catalysts are some of the highest performing HER catalysts while remaining noble-metal free.

4.0 Incorporation of Chalcogens into Amorphous, Polymeric MoS_x

4.1 The Influence of Oxygen Incorporation on the HER Catalytic Activity of Electrodeposited MoS_xO_y Electrocatalysts

4.1.1 Background and Motivation

The synthesis of a-MoS_x catalysts are traditionally carried out via several techniques, such as electrodeposition, chemically, or hydrothermally, all requiring the usage of an ammonium tetrathiomolybdate ion ((NH₄)₂MoS₄).^{11,42-44,172} However, this ammonium-based salt is relatively expensive, extremely hygroscopic, making it difficult to store for long periods of time, and requires a complicated synthesis procedure involving H₂S gas streams and ammonium.¹⁷³ As such, this chapter will explore the synthesis of a-MoS_x and a-MoS_xO_y based catalysts without the use of purchased ((NH₄)₂MoS₄) and explore the origin of catalytic behavior of the catalysts synthesized via the alternative route. **To accomplish this, a sample set of As Deposited, Air Exposed, Inert Anneal, and a Sulfur Anneal were synthesized and the impact their chemistry and structure has on HER is examined.**

In regards to HER catalysis of a-MoS_xO_y, it was originally argued that the removal of the terminal sulfur ligands and the subsequent formation of M=O species was the primary catalytic site.¹¹ In other work, the incorporation of oxygen was shown to improve the catalytic performance⁴². However, independent work utilized in-operando Raman spectroscopy to identify the breaking of bridging S-S bonds within the MoS_x chains during HER. This implies that the bridging S-S bonds are the primary sites of catalytic activity.^{44,172} Therefore, the incorporation of oxygen increases the overall catalytic activity by either accentuating the catalytic activity of the

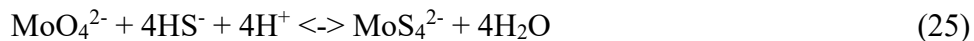
broken bridging S-S bonds or by other means, such as acting as catalytic sites themselves. It has been hypothesized that oxygen could serve as a dopant increasing the electrical conductivity of the a-MoS_x and thus its electrochemical efficiency or as an additional catalytically active site.^{11,42} Overall, it is generally accepted that the presence of oxygen during the deposition of a-MoS_x is a net “win” for catalyzing HER. However, not all oxygen species are beneficial, and as such a detailed study needs to be accomplished on this material to better understand the role oxygen has.

To develop an a-MoS_x catalyst that does not involve purchased (NH₄)₂MoS₄, we expanded upon Levinas et al.’s study, in which the MoS₄²⁻ anion is synthesized in solution. There was a lack of chemical and structural analysis within their work. Through our investigation, this material was found to have an appreciable amount of incorporated oxygen, and we report that this material had greater HER catalytic performance than those synthesized via (NH₄)₂MoS₄.

4.1.2 Synthesis Methods

4.1.2.1 Electrolyte Preparation

The MoS_xO_y films were electrodeposited from a chemical bath containing Mo⁶⁺ and S²⁻ ions. The electrolyte was prepared from sodium molybdate dihydrate (Na₂MoO₄ · 2H₂O) and sodium sulfide hydrate (Na₂S · H₂O) and were mixed in a ratio of Mo/S = ¼, similar to that of the Mo₃S₁₃ monomer that the MoS_x chain is comprised of. The sulfidation of the molybdate ion to tetrathiomolybdate (MoS₄²⁻) is a four-step reaction where each step is a replacement of oxygen atoms by sulfur atoms and can be described by the following equation:



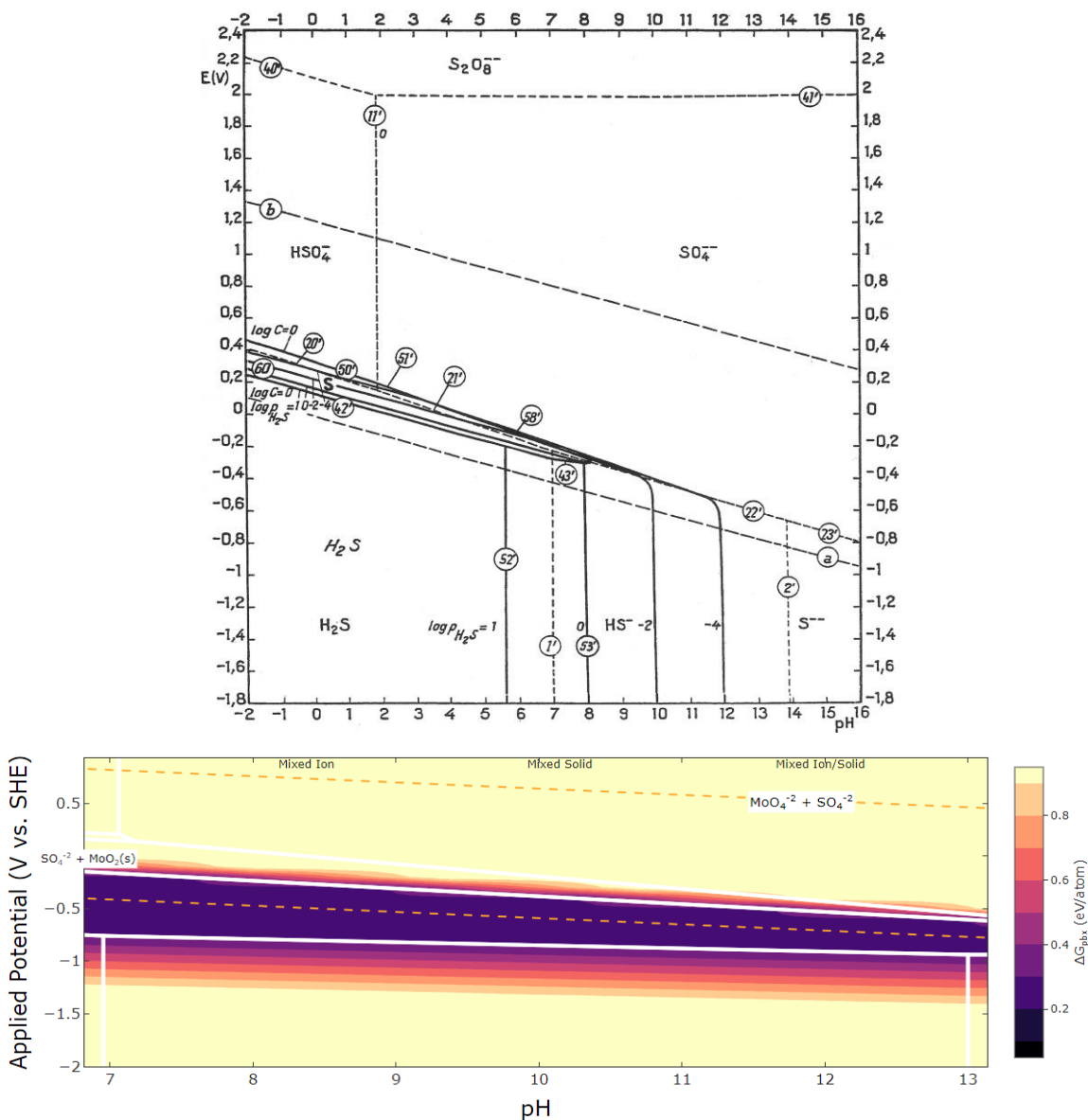


Figure 4.1.1: a) Pourbaix diagram for Sulfur-water¹⁷⁴ and b) heatmap of $(MoS_4)^{2-}$ ions on a calculated Pourbaix diagram from The Materials Project^{174–178}

The overall synthesis of HS^- and the concentration of the $(MoS_4)^{2-}$ ion can be seen in the Pourbaix diagrams in Figure 4.1.1.^{174–178} Using these diagrams, we can check thermodynamically the ideal synthesis conditions for the synthesis of the $(MoS_4)^{2-}$ ion. When making the electrolyte, the initial pH of the electrolyte is approximately 13 and is a clear, colorless electrolyte prior to the reaction taking place. Upon titrating to a pH of 8 with sulfuric acid and pushing the reaction to

the right, the electrolyte transitions to a deep red, demonstrating that the MoS_4^{2-} is being produced.

This reaction can be seen in Figure 4.1.2.

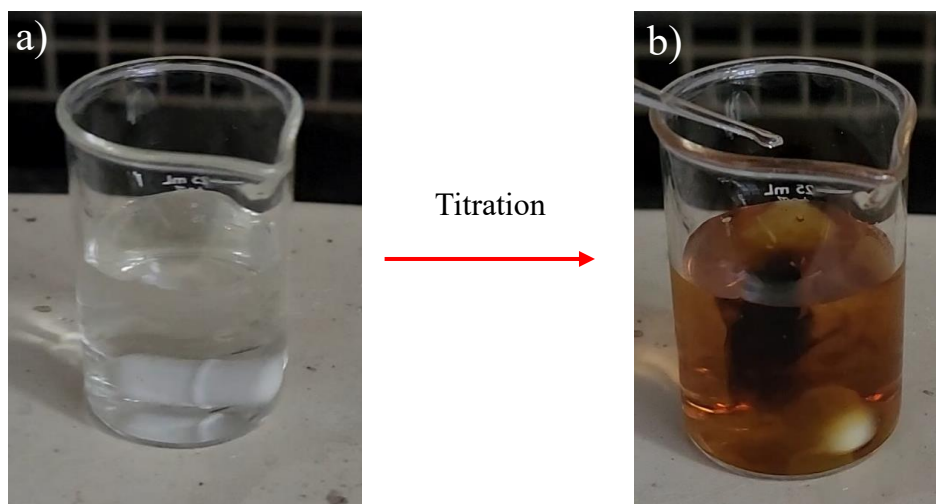


Figure 4.1.2: a) Electrolyte prior to titrating with sulfuric acid and b) electrolyte as titration is occurring.

To further confirm the reaction is taking place, UV-Vis spectroscopy was carried out on the electrolyte before and after titration, as shown in Figure 4.1.3. The peak at 225 nm is attributed to the $(\text{MoO}_4)^{2-}$ anion and matches literature well.¹⁷⁹ The peaks measure at 463 nm, 312 nm, and 207 nm have been attributed to the $(\text{MoS}_4)^{2-}$ ion, the peak at 395 nm to the $(\text{MoS}_3\text{O})^{2-}$, and the peak at 287 nm to the $(\text{MoS}_2\text{O}_2)^{2-}$, matching well with literature.^{179–181} However, note that for all oxysulfide absorption peaks, there is a significant overlap between some and/or all the various chemical states. As such, the peaks have been labelled with the primary absorption species, but it is difficult to say if only one species is present at a time.

The final pH of 8 was identified as ideal based on the Pourbaix diagram and Levinas et al.'s study. This pH increases the concentration of the final reactants, limits intermediates, and

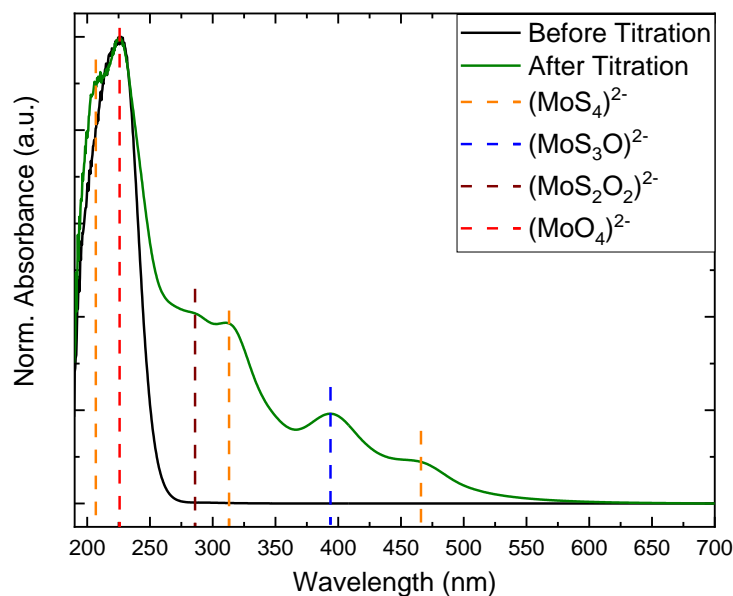


Figure 4.1.3: UV-Vis spectra of the electrolyte before and after titration

prohibits the formation of H₂S gas. Additionally, this was shown in literature to have the best performance regarding sample homogeneity and HER performance.⁹⁰ With the final pH in mind, determining the correct potential to deposit at is critical. Too low of potential, no redox reactions will occur, and nothing will be deposited. Too high of a potential, and the competing HER reaction prohibits the deposition of a uniform film. This was explored extensively in Levinas et al.'s study, but to confirm chemically if there was a significant difference or not, I deposited a film at the lowest potential able to yield a film, -1.5 V_{MSE}, and at a substantially higher overall potential, -1.8 V_{MSE}. What was found was almost no chemical difference within the Mo 3d spectra with some difference within the S 2p spectra, notably an increase in the higher binding energy feature, which is attributed to the S_{Bridging/Apical} bonds.^{182,183} This is likely due to a difference in the degree of

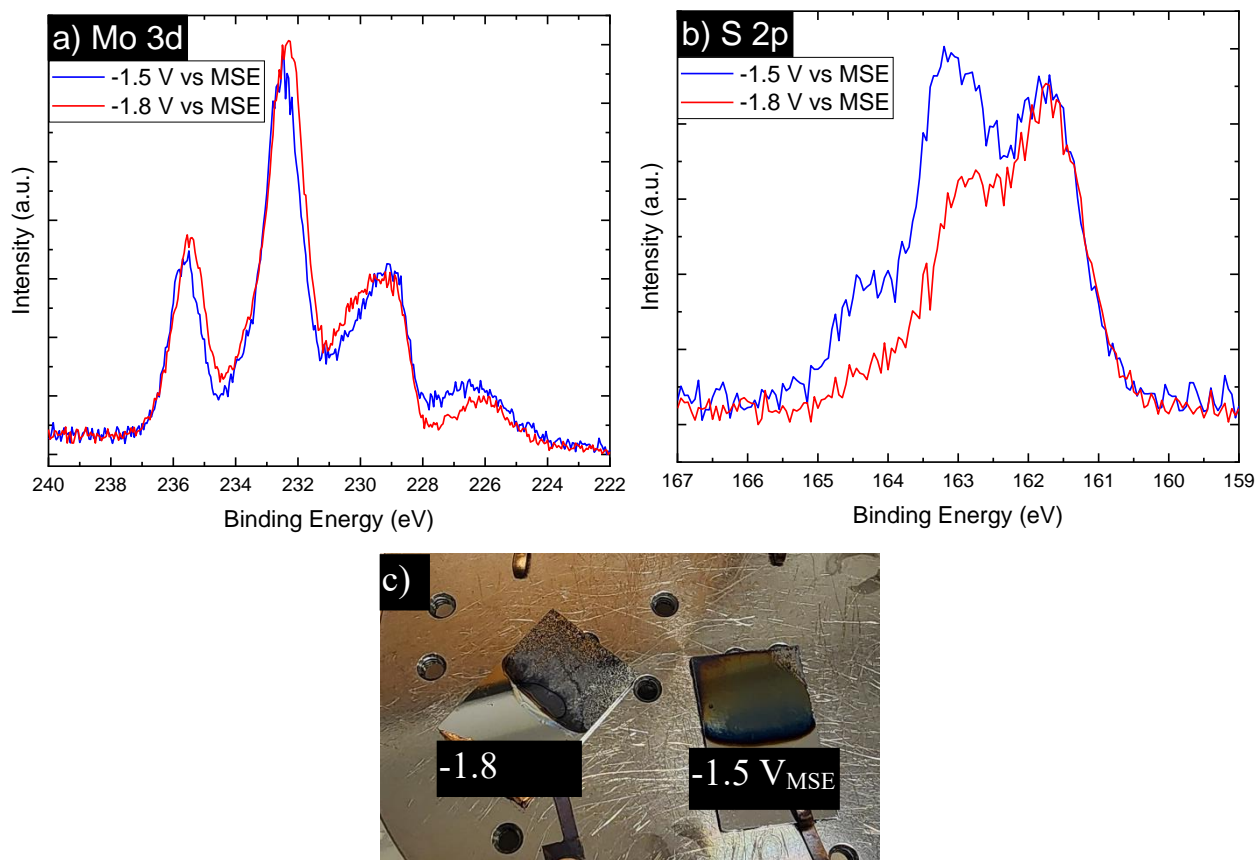


Figure 4.1.4: a) Mo 3d and b) S 2p XPS spectrum of a-MoS_x deposited at -1.5 V_{MSE} and -1.8 V_{MSE}. c) is an image of the films deposited at different potentials

oxidation as S_{terminal} bonds are more easily replaced via oxygen. While there isn't a large chemical difference, there was a significant difference in the overall homogeneity and film quality of the sample, with the -1.5 V_{MSE} exhibiting significantly more uniformity than that of the -1.8 V_{MSE} sample which had significant pitting and delamination from the competing HER reaction at this potential as can be seen in Figure 4.1.4c. Consistent with Levinas et al.'s study, the -1.5 V_{MSE} yielded overall better samples.

4.1.2.2 Oxidation of MoS_xO_y

As the film deposition is carried out in an air exposed electrolyte, it is important to understand the air stability of the deposited films as they will be immediately exposed upon removal from the electrolyte. To accomplish this, the sample was immediately loaded into the

XPS chamber to limit the oxidation as best as possible. Following the XPS scan, the sample was then removed from the chamber and allowed to sit in atmosphere for a given time. It was then reintroduced and scanned again to determine the level of oxidation that has occurred. This was repeated until no further oxidation could be detected. This is represented in Figure 4.1.5a where we can see the growth of the oxide peak at ~ 232.5 eV growing in relative intensity as a function of time. After roughly an hour, there was little difference when left in atmosphere longer. In addition, a series of Raman scans in atmosphere where 5 seconds scans were taken back-to-back over several hour is shown in Figure 4.1.5b-d. What we found mostly matched the XPS data in that we hit an oxide saturation, as represented by the increase in peaks between $800\text{-}1000\text{ cm}^{-1}$. I

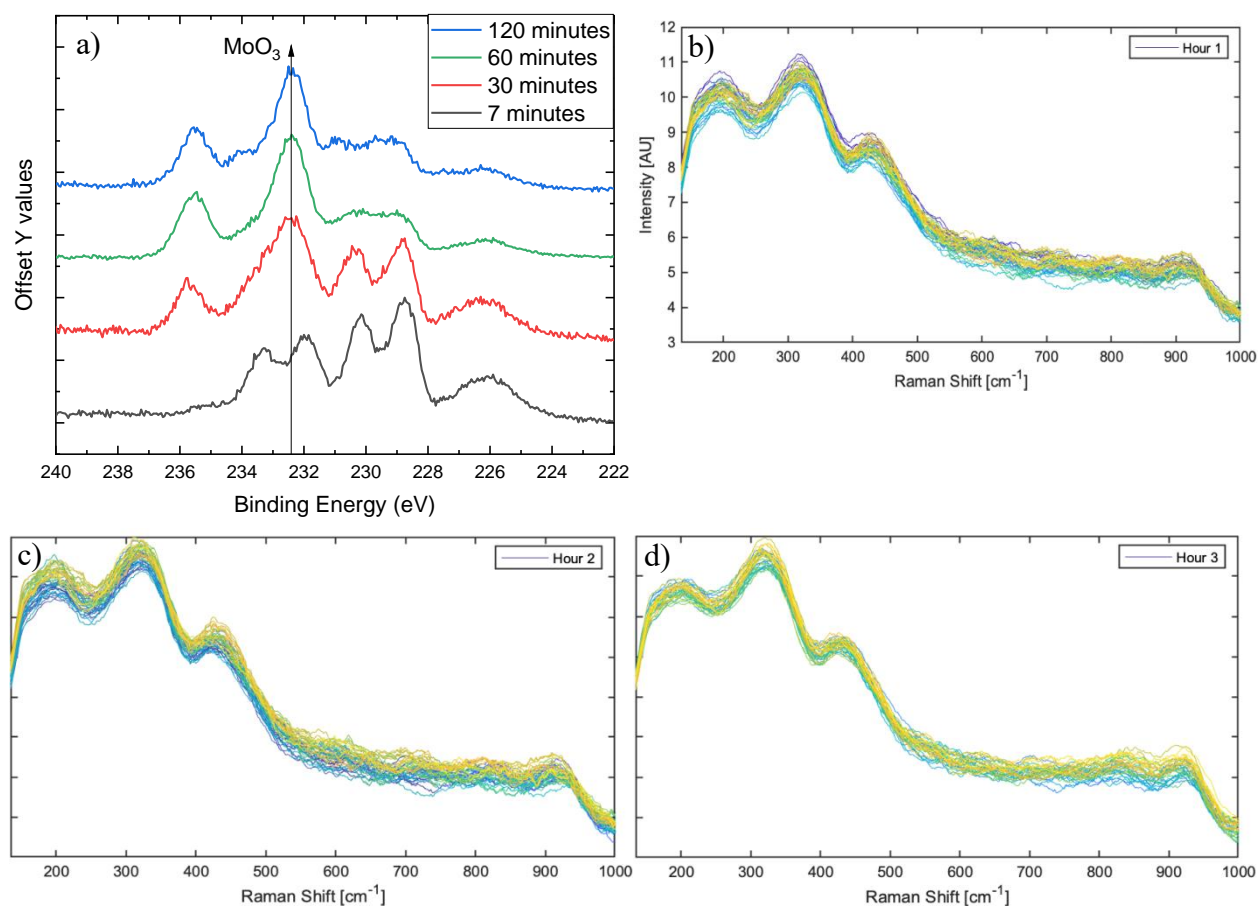


Figure 4.1.5 a) XPS spectrum of the Mo 3d core level as a function of time in atmosphere; b-d) Raman spectrum as a function of time in atmosphere where each line represents a 3-minute window and the blue lines being earlier times and yellow representing later times.

took another 4 hours' worth of scans; however, no significant differences were detected. As such, As Deposited samples will be analyzed immediately after synthesis to limit the oxidation of the sample as much as possible.

4.1.2.3 Removal of Oxygen

To effectively remove oxygen, we hypothesized that a low temperature anneal in an inert environment could successfully remove the oxygen without crystallizing the material. Our first approach was to use DSC to determine the crystallization temperature, as seen in Figure 4.1.6. This was carried out in collaboration with Mackenzie Ridley in Professor Opila's group. The crystallization event begins around 400°C with the crystallization peak occurring at 421°C. The crystallization is not reversible, with the peak on cooling being attributed to the furnace quickly changing heating directions. Upon running a second time (i.e. after crystallization had occurred), no peak was observed, further confirming the peak at 421°C is attributable to the crystallization of MoS_xO_y . There was negligible mass change detected with the TGA, although any change in the film's mass is likely below the detection limit of the instrument.

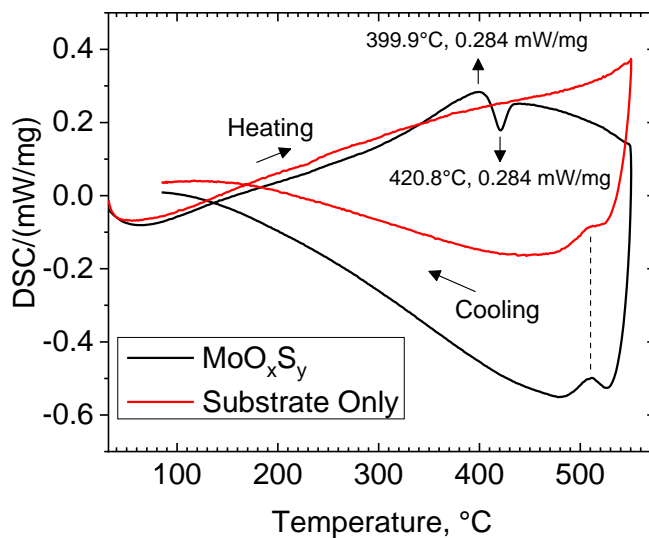


Figure 4.1.6: DSC of $\text{-MoS}_x\text{O}_y$ catalyst heated at a rate of 10°C/min

However, when annealed in a tube furnace at temperatures slightly below the crystallization temperature, such as at 350°C, we do observe crystallization events below this crystallization temperature of 421°C. This can be demonstrated in the Raman spectra in Figure 4.1.7a, the low temperature regime as when the temperature is below 275°C, the polymeric structure of the As Deposited sample is retained. However, at 275°C, we begin to see the presence of the MoS₂ crystalline phase, as represented by the sharp peaks at ~382 cm⁻¹ and ~407 cm⁻¹.

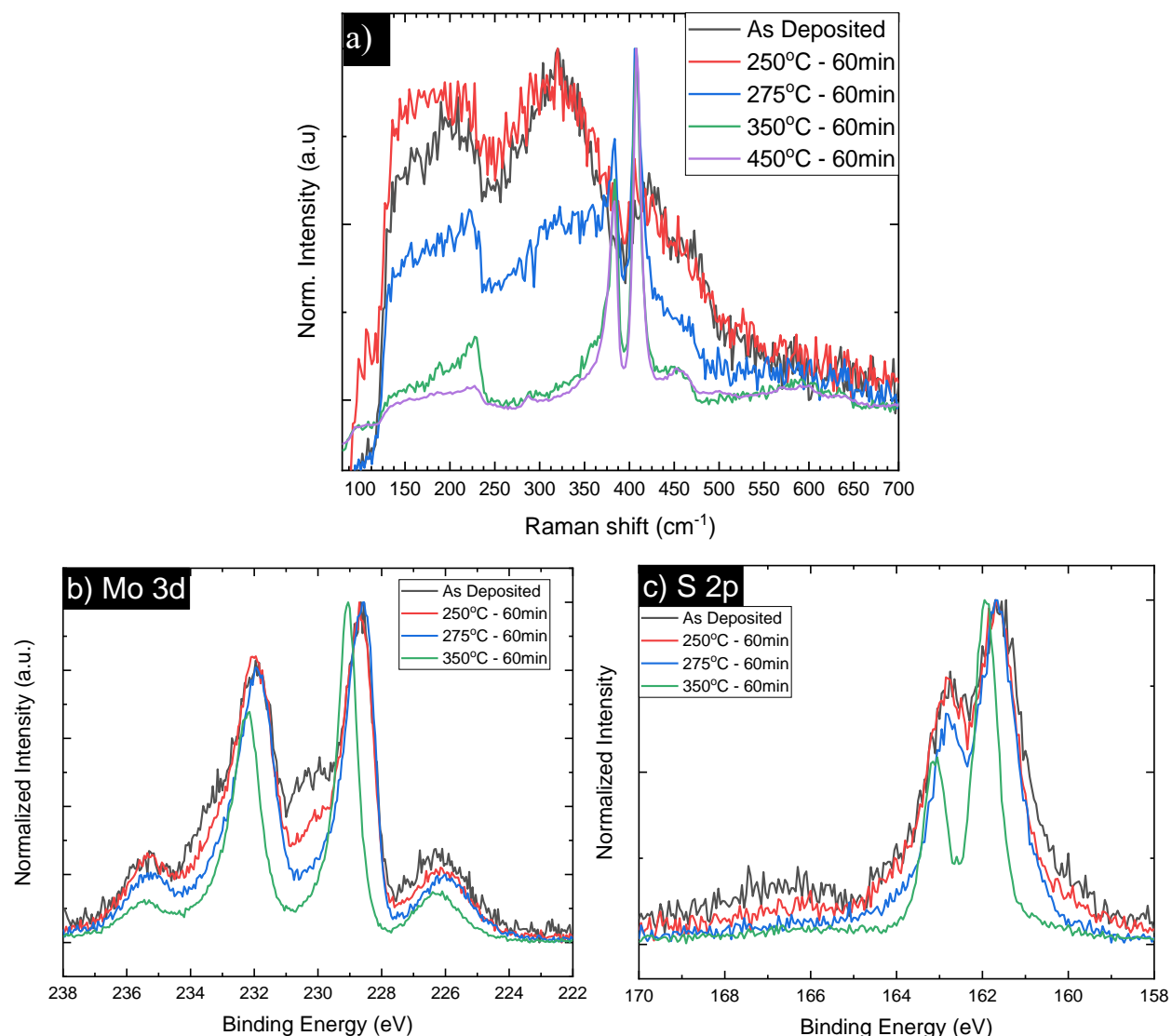


Figure 4.1.7: a) Raman spectra showing various MoS_xO_y catalysts as a function of annealing temperature, b) Mo 3d as a function of annealing temperature and c) S 2p as a function of annealing temperature.

Above this temperature, the crystalline phase of MoS₂ dominates the spectra. This is also exhibited in the in-vacuo annealing where there is a significant difference between the samples that retain an amorphous like structure and the 350°C sample which underwent crystallization, as seen in Figure 4.1.7. This indicates to use that the DSC data is not completely representative of our material, as crystallization is found below the temperature predicted by DSC.¹⁸⁴ Therefore, this is likely also a kinetically sluggish process and that the DSC ramp rate and lack of holding at any temperature led to an overestimate in the crystallization temperature. Therefore, to remain below the crystallization temperature, all subsequent anneals in this chapter will be done at 250°C for 60 minutes and will be characterized immediately following processing.

4.1.3 Results of As Deposited, Oxidized, Inert Anneal, and Sulfur Anneals

4.1.3.1 Structural Properties

To test the impact that oxygen incorporation has on the chemistry, structure, and catalytic efficacy of MoS_xO_y, a sample set of As Deposited, Air Exposed, Inert Anneal, and a Sulfur Anneal were examined. The As Deposited samples were all tested immediately following deposition to limit any potential oxidation. The Air Exposed samples were exposed to atmosphere for several days. The Inert Anneal and Sulfur anneal were accomplished by annealing in a nitrogen purged tube furnace at 250°C for one hour with a ramp rate of 7.5°C/min. The elemental sulfur was placed upstream so that the sublimation temperature (~120°C at 1 atm) was reached at the final hold temperature. All materials were tested immediately following any processing to limit oxidation.

Figure 4.1.8 shows the resonance Raman spectrum of the various MoS_xO_y catalysts that were deposited at $-1.5 V_{\text{MSE}}$. The $\alpha\text{-MoS}_x\text{O}_y$ material exhibits nearly identical Raman features to that of isolated $(\text{NH}_4)_2[\text{Mo}_3\text{S}_{13}]$ clusters.^{11,185} The molybdenum sulfide bonds of $\nu(\text{Mo-S})$ were found at $283\text{-}385\text{ cm}^{-1}$ and the $\nu(\text{Mo-S}_{\text{apical}})$ vibrations were observed in the $450\text{-}475\text{ cm}^{-1}$ region, while the $\nu(\text{Mo-S-Mo})$ vibrations were observed around 425 cm^{-1} . Additionally, the bands of $\nu(\text{Mo=O})$ and $\nu(\text{Mo(=O)}_2)$ vibrations (with $A_g\text{-}\delta(\text{O}_2\text{MoO}_2)_n$ and $A_g\text{-}\delta(\text{OMoO}_2)_n$ being specific vibrations of the system) were observed between $180\text{ cm}^{-1}\text{-}215\text{ cm}^{-1}$, 560 cm^{-1} in the range of $800\text{-}960\text{ cm}^{-1}$.¹⁸⁶ The freshly deposited film does not show strong $\nu(\text{S-S})_{\text{terminal}}$ or $\nu(\text{S-S})_{\text{bridging}}$ Raman peaks at 520 cm^{-1} or 550 cm^{-1} , respectively.^{42-45,187-189} This missing feature has been ascribed to unsaturated S^{2-} species as revealed by XPS and will be expanded upon in later chapters where we can see the variation in these vibration modes as a function of sulfur precursor.⁴⁴ As the samples remained below the crystallization temperature, there is no presence of the sharp E_{2g}^1 and A_{1g} that are indicative of the crystalline phases that are present when crystallized. This is also evident in the XRD where a crystallized sample exhibits strong diffraction of the MoS_2 (002) plane whereas the samples annealed at 250°C only exhibit a very slight bump, likely indicative of short range

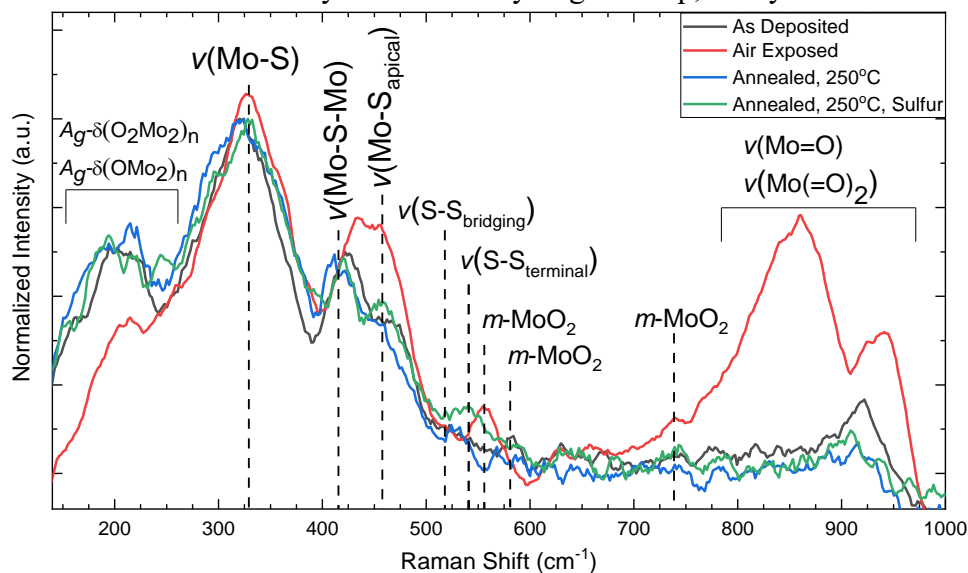


Figure 4.1.8: Resonance Raman spectra of MoS_xO_y catalysts

ordering as can be seen in Figure 4.1.9.^{190,191} The air exposed samples show a strong increase in the features associated with Mo=O vibrations.^{11,186} Both of the annealed samples are very similar to the As Deposited sample, however there are some small differences. The sulfur anneal sample exhibits a slightly enhanced (Mo-S_{apical}) vibration mode around 450 cm⁻¹, demonstrating an increase in apical sulfur ligands.

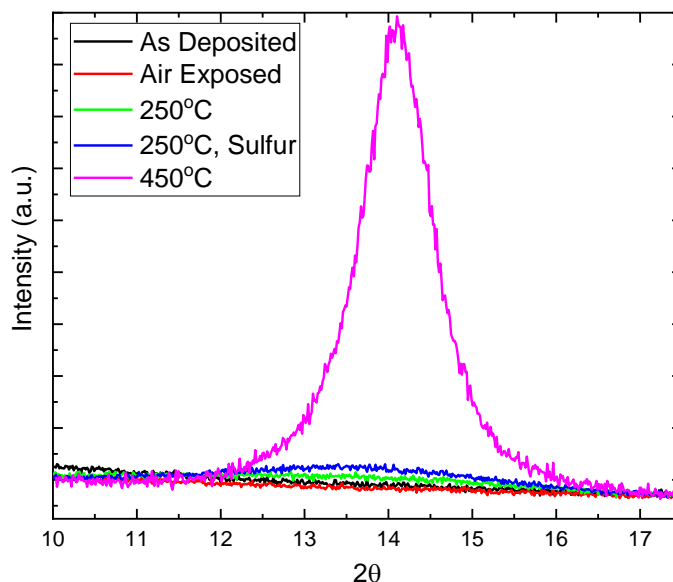


Figure 4.1.9: XRD of the MoS_xO_y catalysts

4.1.3.2 Chemical Properties

XPS was utilized to investigate the chemistry of the Mo and S species of the various MoS_xO_y catalysts and can be seen in Figure 4.1.10 - Figure 4.1.12. All spectra were deconvoluted with Voight functions. The Mo 3d spectra can be deconvoluted into four distinct doublets (3d_{5/2} and 3d_{3/2}) of Mo⁶⁺, Mo⁵⁺, Mo*, and Mo⁴⁺, with the singlets of the various overlapping S 2s states that occur within the same energy range (fitting parameters obtained from S 2p spectra). As the oxidation number of the Mo increases, the respective doublets are found at higher binding energies and agree with previous literature.^{10,42,192-194} Mo⁴⁺ is attributed to the MoS_x center where Mo is only bonded to S. Mo⁵⁺ is attributed to Mo center of MoS_xO_y and Mo⁶⁺ is attributed to the Mo

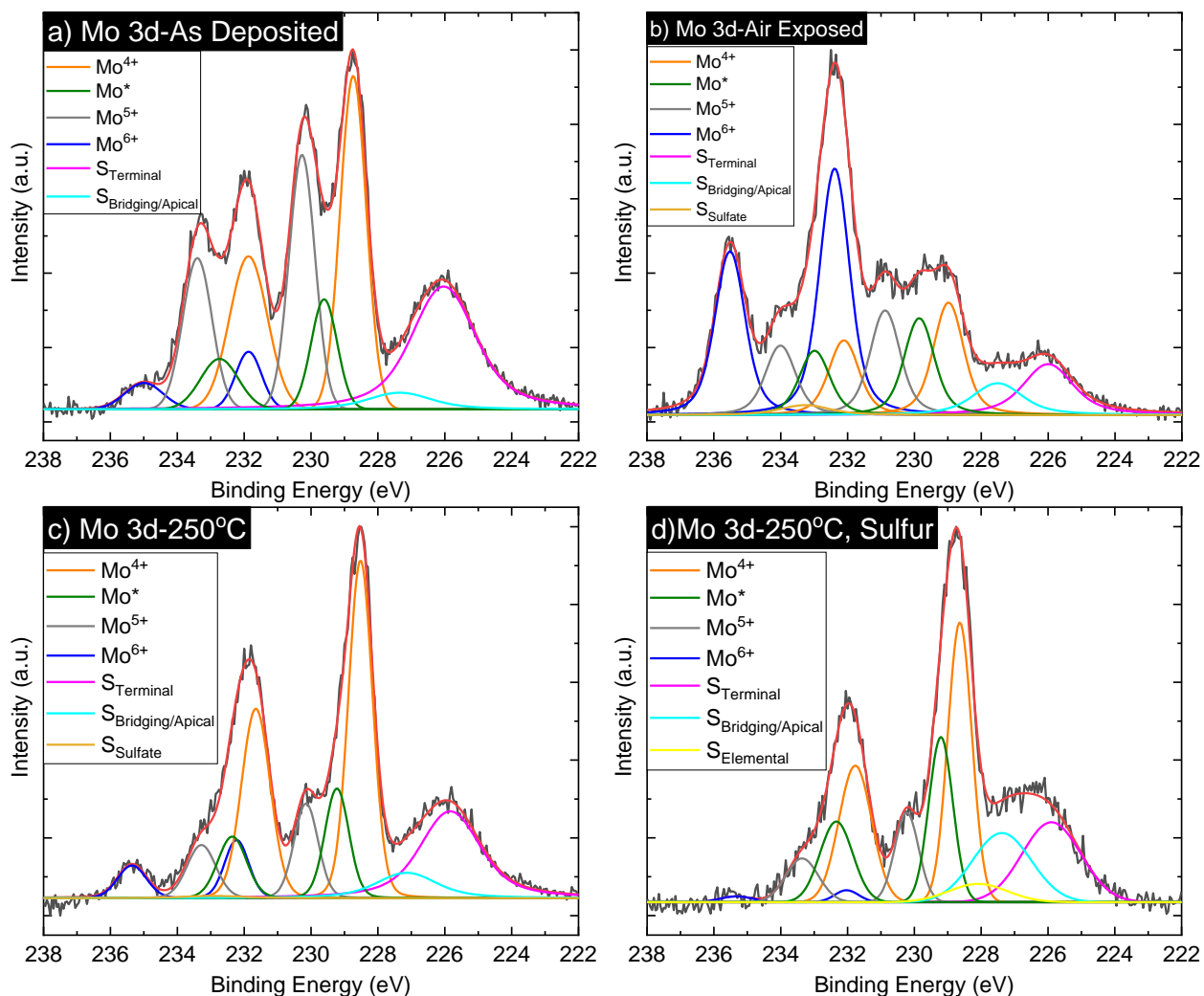


Figure 4.1.10: XPS of Mo 3d core electrons of the (a) As Deposited, (b) Air Exposed, (c) Inert Anneal, and (d) Sulfur Annealed MoS_xO_y catalysts

center of MoO₃. To date, there has been no report on the intermediate state, Mo^{*}, between the Mo⁴⁺ and Mo⁵⁺ states. This particular state is clearly evident in Figure 4.1.10b, even upon visual inspection of the raw data. We propose that this peak is either associated with the incomplete oxidation of the sulfur ligand or is associated with MoO₂. We believe that it is more likely that this intermediate state is when oxygen has only replaced one of the sulfur ligands and not both, resulting in a single oxygen bond, rather than a double bond, to Mo. This is further supported by the UV-Vis spectra in Figure 4.1.3 in which species with only one oxygen ligand are present. However, we do want to point out that trace amounts of monoclinic MoO₂ were detected in the

Raman spectra. However, as the Raman m-MoO₂ features are small, or non-existent in some samples, it is possible they are not related to this feature. While both explanations could explain the Mo* chemical species, the constant presence of the Mo* feature in XPS and lack of m-MoO₂ in every Raman spectrum, along with the UV-Vis spectra, leads credence to the partial oxidation of MoS_xO_y.

As seen in Figure 4.1.10, the main differences in the chemical state of the catalysts are the oxidation state of molybdenum. In the As Deposited sample, the primary molybdenum species present are the Mo⁴⁺ and Mo⁵⁺ states with minimal Mo⁶⁺ as shown in Figure 4.1.10a. It is important to note that the Mo⁵⁺ state is a minor component, or not observed, in electrodeposited MoS_x films when synthesized via (NH₄)₂MoS₄. We attribute this large presence of the Mo⁵⁺ to the dual precursor synthesis approach, as demonstrated via the UV-Vis of the electrolyte and as will be discussed later. However, when exposed to ambient conditions over two days as shown in Figure 4.1.10b, the primary species is now the Mo⁶⁺ state, indicating that the insulating MoO₃ is present, impeding electron transport.⁴¹ When a freshly deposited sample is annealed under an inert environment, the primary species that are present are the tetravalent state of Mo⁴⁺ with minimal Mo*, Mo⁵⁺, and Mo⁶⁺. The freshly deposited sample annealed under a sulfur flux demonstrates similar composition as the sample annealed under an inert environment; however, this has a slightly stronger Mo* peak. Additionally, there are significant changes from the S 2s features which will be explained further by analyzing the S 2p peak.

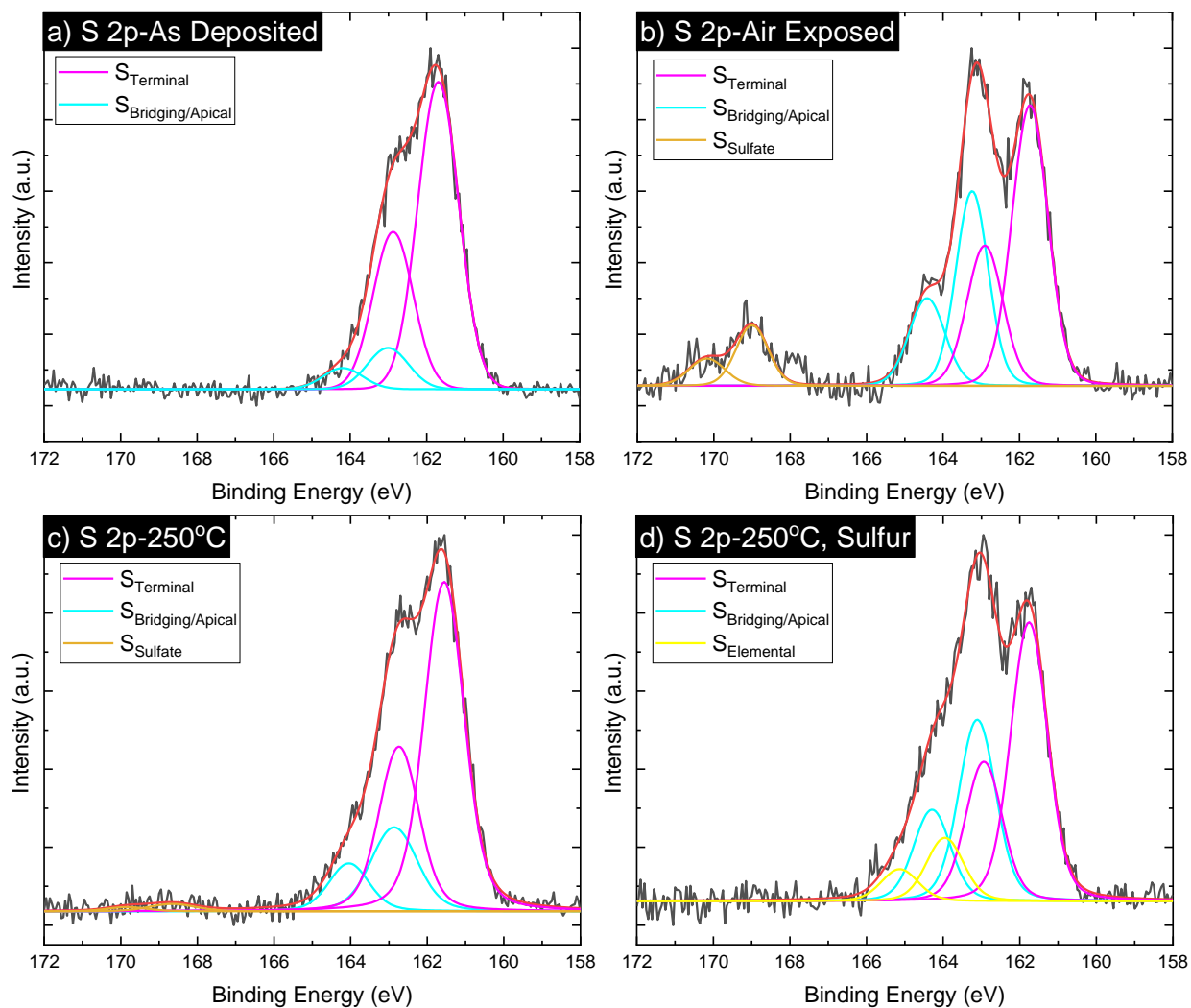


Figure 4.1.11: XPS of S 2p core electrons of the (a) As Deposited, (b) Air Exposed, (c) Inert Anneal, and (d) Sulfur Annealed MoO_xS_y catalysts

The deconvoluted S 2p spectra consists of four main features of increasing binding energy: (i) terminal S_2^{2-} ligands, (ii) bridging S_2^{2-} and apical S^{2-} ligands, (iii) elemental sulfur, and (iv) sulfates. The As Deposited sample is comprised primarily of the S_2^{2-} terminal ligands while after exposure to atmosphere the ratio between the terminal and bridging/apical ligands decreases sharply. This agrees with previous literature, suggesting that the terminal sulfurs are preferentially substituted by oxygen over bridging sulfurs due to a lower thermodynamic barrier.^{182,183} The sample annealed under an inert environment maintained relatively similar ratios of terminal to bridging/apical bonds as the freshly deposited sample, while the sample annealed under a sulfur

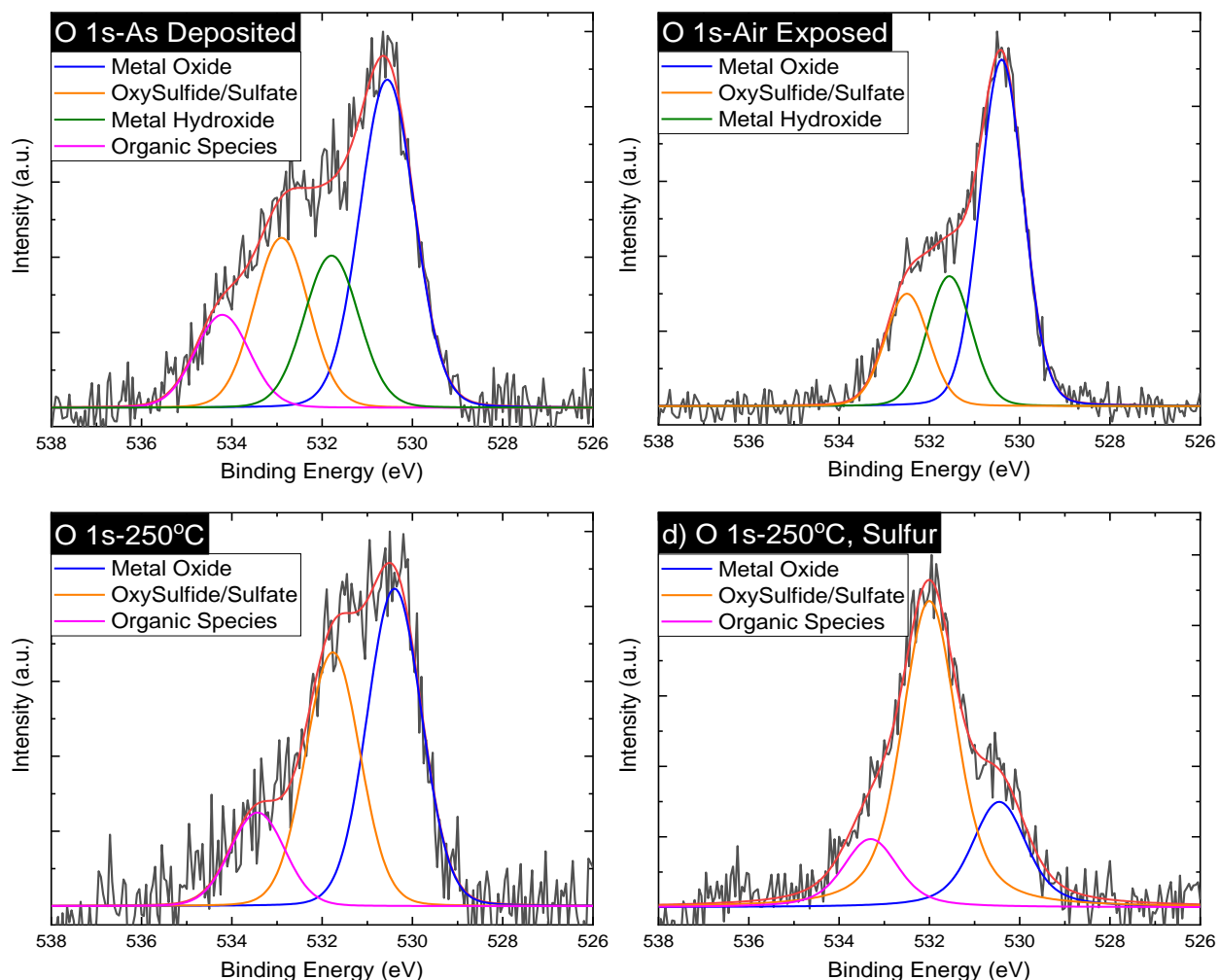


Figure 4.1.12: XPS of O 1s core electrons of the (a) As Deposited, (b) Air Exposed, (c) Inert Anneal, and (d) Sulfur Annealed MoO_xS_y catalysts

flux demonstrated a decreased ratio of terminal to bridging/apical bonds. This increase in bridging/apical bonds is likely primarily apical sulfur ligands since the associated Raman vibration mode for apical bonds increases as well.

The deconvoluted O 1s spectra, found in Figure 4.1.12, consist of a variety of features, such as the primary metal oxide, oxysulfide/sulfate, metal hydroxide, and organic species. The As Deposited sample exhibits all four features, with the metal oxide peak dominating the spectra. Following air exposure, the metal oxide peak increases in intensity which agrees with the increase in the Mo^{6+} feature associated with MoO_3 . Following annealing in the inert environment, the metal

oxide peak decreases in intensity, again consistent with the reduction of the Mo^{5+} species. After the sulfur anneal, the oxysulfate/sulfate peak increases in intensity due to the increase in sulfur concentration.

4.1.3.3 Electrocatalytic Properties

To determine the impact that the structure and chemistry of the catalysts have on the catalytic performance for HER, polarization experiments were performed, and the results are shown in Figure 4.1.13. As can be seen, the freshly deposited sample performed the best by exhibiting the lowest overpotential to reach 10 mA/cm^2 (171 mV). When the As Deposited film is exposed to atmosphere for extended periods of time, the activity of the catalyst decreases, consistent with previous findings.⁹⁰ Additionally, the performance of the annealed samples became worse, with the sample annealed in the presence of sulfur performing worse than the sample annealed in an inert environment. The sample that was annealed at 450°C exhibited the worst

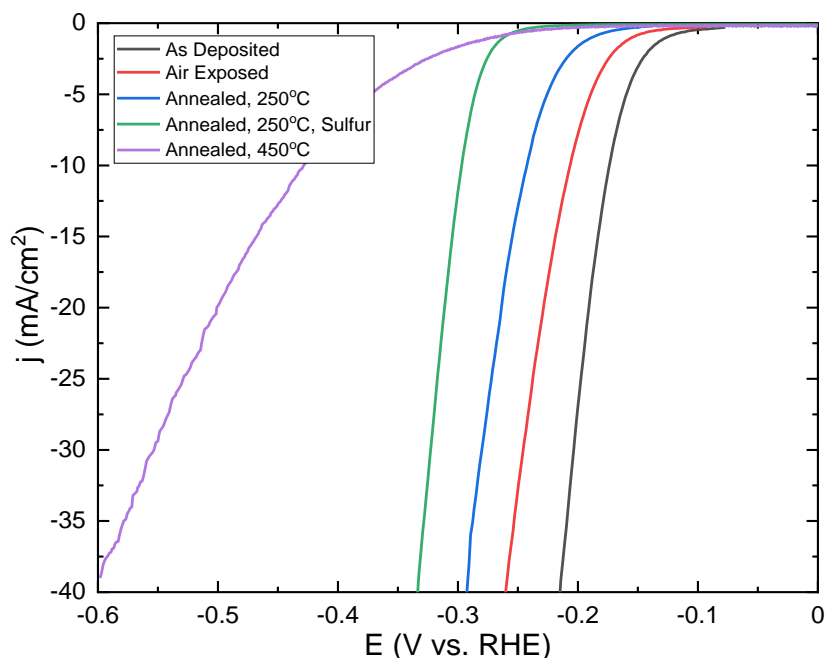


Figure 4.1.13: Polarization curves of MoS_xO_y catalysts

performance due to its crystalline nature as it was annealed above the crystallization temperature as was determined earlier.

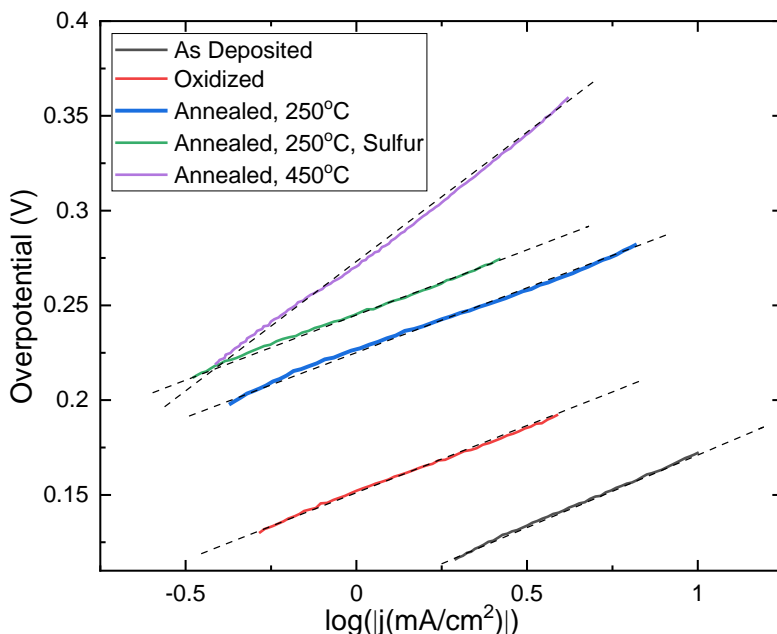


Figure 4.1.14: Tafel plots of the MoS_xO_y catalysts

As a reminder, the Tafel slope (b), i.e. the slope of the linear, low overpotential regime in the Tafel plot shown in Figure 4.1.14, is the overpotential required to increase the current density by one order of magnitude. Therefore, it is advantageous to have a catalyst with a lower Tafel slope for HER applications. The data in Figure 4.1.14 show that there was little difference between the Tafel slopes of the As Deposited sample and oxidized samples, while all annealed samples resulted in slightly lower Tafel slopes. As the Tafel slope is dictated by the reaction mechanism as outlined in the experimental section, we can determine that the Volmer-Heyrovsky is the mechanism for the MoS_xO_y catalysts with the crystallized MoS_2 catalyst following the Volmer-Tafel mechanism. The overpotentials and Tafel slopes are summarized in Table 4.1.1.

Table 4.1.1: Summary of the electrochemical measurements of the MoS_xO_y catalysts

Sample	η_{10} (mV)	b (mV/dec)
As Deposited	173	52
Air Exposed	207	59
Annealed, 250°C	241	59
Annealed, 250°C, Sulfur	297	40
Annealed, 450°C	428	123

The As Deposited sample performed the best out of all tested samples. This can be correlated to the significant presence of Mo⁵⁺. We believe that the presence of the Mo⁵⁺ can be attributed to the two-precursor synthesis route as it is only present in samples prepared this way or purposefully oxidized in literature.^{11,42,195} Therefore, it can be concluded that this is likely the primary reason the Levinas study observed superior performance to the single precursor methods.^{44,90,172} The Mo⁵⁺ state increases the overall conductivity of the sample but can also act as additional active sites for HER and would explain the superior performance of the MoS_xO_y films.^{11,195} However, XPS performed following polarizations shows that the Mo⁵⁺ state decreased in intensity while the Mo* state increased significantly in relative intensity as shown in Figure 4.1.15a. This demonstrates that the extremely high concentration of Mo⁵⁺ found in the samples is not completely stable under HER conditions and that the Mo* state might play a significant role in the HER capabilities of the As Deposited sample. Additionally, as seen in Figure 4.1.15b, the terminal to bridging/apical sulfur ligand ratio increases very slightly. This instability over time is further demonstrated by conducting a 1000 cycle cyclic voltammetry where performance begins to suffer after roughly 20 scans (Figure 4.1.15c). It has been debated in literature of the origin of

the catalytic centers. The first to report on this was Tran et al. in which they proposed the elimination of terminal sulfur ligands during HER to be the catalytic centers. However, Ting et al. later showed with in-operando Raman that the temporary breaking of bridging bonds during HER serves as the main catalytic center. Our work here supports Ting et al. as when we completely removed the bridging bonds, the HER performance suffered.^{11,172} The oxidized sample demonstrated poorer performance with respect to the freshly deposited film, as was expected based on Levinas et. al. observations of decreased performance the longer the sample is exposed to the environment.⁹⁰ We attribute this decrease in performance to the oxidation of the MoS_xO_y catalyst to

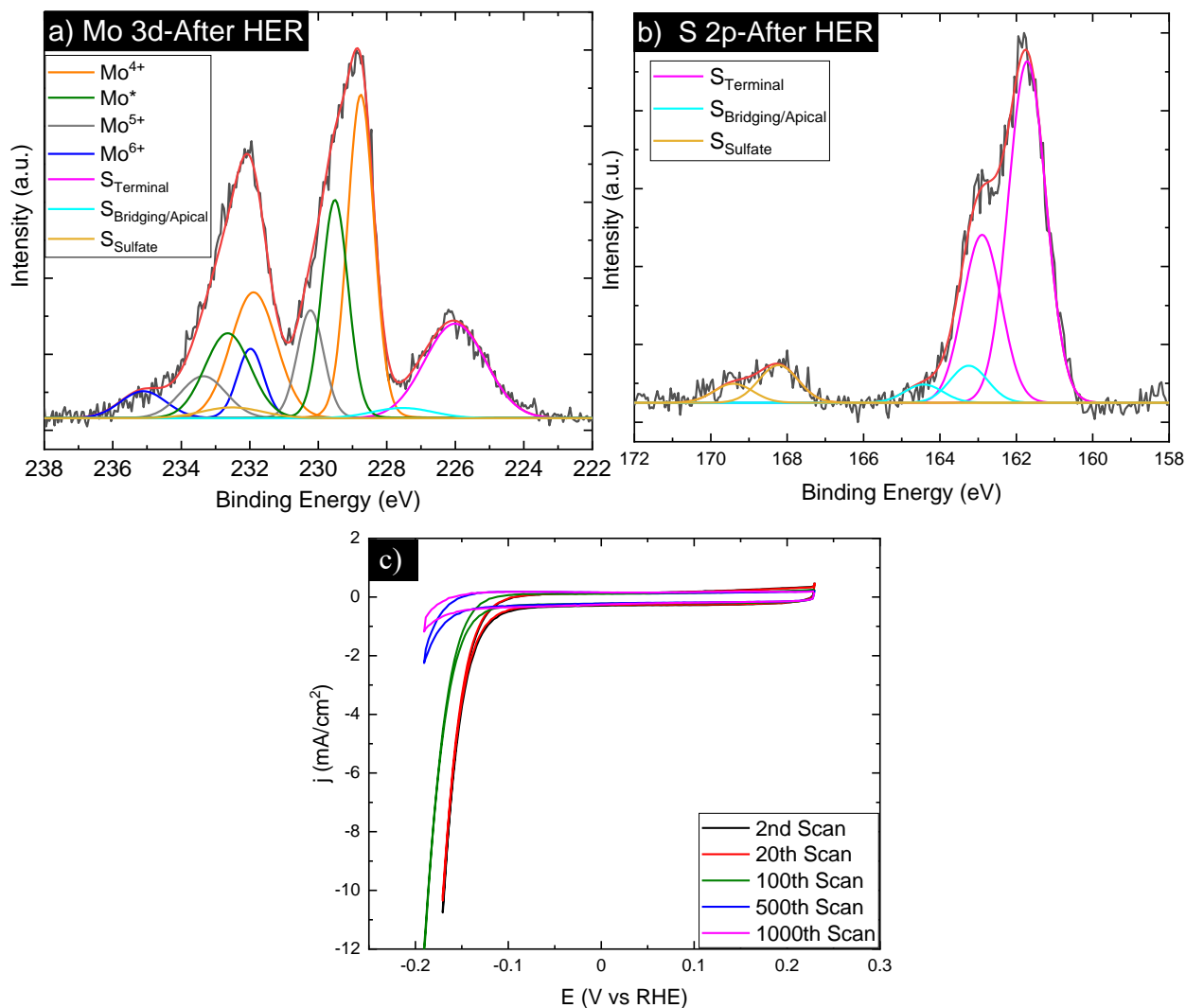


Figure 4.1.15: XPS Spectra of a) Mo 3d after polarizations, b) S 2p after polarizations, and c) polarization curves as a function of scans

a more MoO_3 like material, which can be seen in Figure 4.1.10b. The intensity of the Mo^{6+} oxidation state drastically increases with the insulating state of MoO_3 leading to overall worse performance due to reduced electron transfer kinetics. This is supported by the increase in ratio of bridging to terminal sulfur bonds seen in Figure 4.1.11 as oxygen will preferentially substitute the terminal sulfur bonds.

The annealed samples showed worse performance compared to the As Deposited sample, even without the presence of the insulating Mo^{6+} state. The sample annealed in the inert environment retained a similar ratio of bridging to terminal sulfur bonds as the freshly deposited sample. However, the inert anneal removed the oxygen dopants associated to the Mo^{5+} as can be seen in Figure 4.1.10c. This result emphasizes the importance of oxygen dopants and the Mo^{5+} oxidation state to the overall HER performance. The sample annealed within the sulfur environment exhibited the worst performance of all polymeric catalysts. This again has been attributed to the loss of incorporated oxygen associated with the Mo^{5+} oxidation state. Additionally, the ratio of bridging/apical to terminal bonds increased substantially. We attribute this observation to the increase of apical bonds instead of bridging bonds as there is an increase in apical sulfur

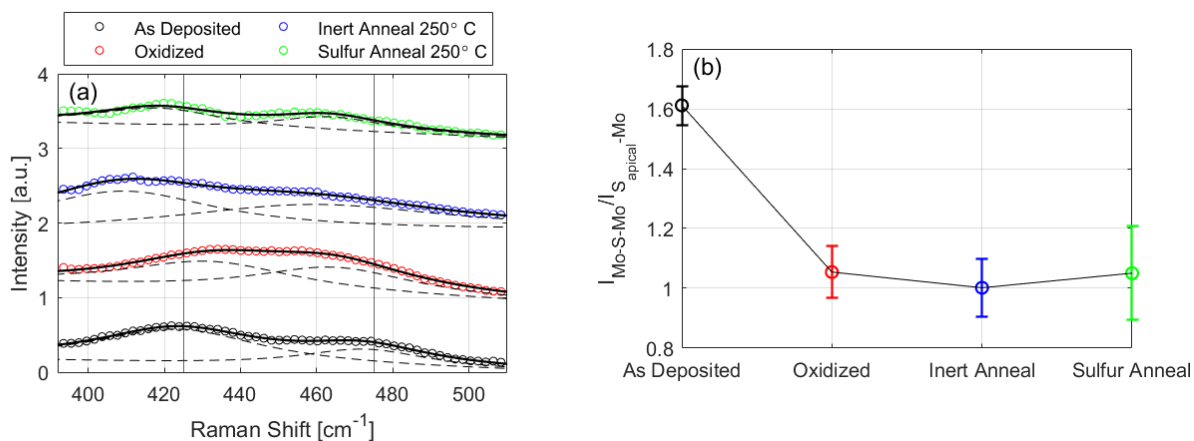


Figure 4.1.16: a) Fits of Raman spectra in the region between 390 and 510 cm^{-1} , representing the $\nu(\text{Mo-S-Mo})$ and $\nu(\text{Mo-S}_{\text{apical}})$ respectively, b) The integrated intensity ratio of $\nu(\text{Mo-S-Mo})$ and $\nu(\text{Mo-S}_{\text{apical}})$ fitted lineshapes

ligands within the Raman spectra. Additionally, it has been reported via quantum chemical simulations that apical bonds are quite inert while bridging bonds are catalytically active.¹⁷² Those results agree with the findings here in which the increase of apical bonds corresponded to the worse performance of the sulfur annealed film. Figure 4.1.16 shows the amount of apical sulfur ligands, determined by the integrated Raman peak intensity of the $\nu(\text{S}_{\text{apical}}\text{-Mo})$ vibration relative to the $\nu(\text{Mo-S-Mo})$ vibration. The largest ratio (i.e. smallest amount of apical sulfur bonds) is observed for the best performing sample, the As Deposited sample. This ratio and η_{10} decrease for the other samples. These results further demonstrate that an increase in apical bonds hinders catalytic performance.

Overall, it was shown that the As Deposited sample exhibited superior performance due to the presence of the Mo^{5+} oxidation state associated with incorporated oxygen, even though the Mo^{5+} concentration decreases after polarizations. When left in ambient conditions, the intensity of the insulating Mo^{6+} oxidation increased, leading to decreased performance. The annealing in an inert environment highlighted the importance of the Mo^{5+} oxidation state and that when removed the HER performance suffers. When annealed in a sulfur environment, not only was the Mo^{5+} oxidation state removed, but the concentration of apical sulfur ligands increased substantially, leading to even further reduced HER performance.

4.1.4 Conclusions

This study has established the importance of the Mo^{5+} oxidation state arising from oxygen dopants for the HER electrocatalytic performance of MoS_xO_y . When oxygen dopants are removed through annealing, the HER performance of the catalyst is drastically reduced due to the removal of Mo^{5+} . Additionally, this study supports the hypothesis that oxidation via atmospheric exposure worsens catalytic performance due to the presence of Mo^{6+} , in line with Levinas et. al.

observations. The difference in performance difference between the inert and sulfur anneals demonstrated the importance of the terminal and bridging sulfur bonds to the catalytic performance of the MoS_xO_y catalyst and the reduced performance of apical sulfur bonds, confirming quantum chemical simulations.¹⁷² Finally, this work revealed the presence of a new Mo chemical state within a MoS_xO_y catalyst, Mo^* , which is potentially critical for the catalytic activity of these films. While the focus of this work was not in determining the origin of this feature, this could lead to future investigations of this chemical state.

4.2 Selenium Incorporation into MoS_x via Electrodeposition to form a Ternary Se-MoS_x Alloy for HER

4.2.1 Background and Motivation

MoS_{2x}Se_{2(1-x)} has recently been discussed as a potential candidate for the use as a catalytically active material for HER.^{196–198} This is partly due to several experimental studies that demonstrated the increased catalytic performance of MoS_{2x}Se_{2(1-x)} alloys, where it was shown that the HER performance of crystalline MoS_{2x}Se_{2(1-x)} was significantly superior to those of 2H-MoS₂, or of MoSe₂.¹⁹⁷ Indeed, the addition of a different chalcogen atoms produced new active sites in the basal plane of MoS₂ via defect generation.¹⁹⁶ Additionally, DFT studies have examined the electronic structure and hydrogen adsorption energy for MoS_{2x}Se_{2(1-x)} and determined that the band gap for the alloyed material was lower than that of the semiconducting 2H-MoS₂ and 2H-MoSe₂ by reducing the conduction band minimum (CBM).^{197,198} This feature reveals a two-fold in improving the electrocatalysis of the alloy. First, the lowered bandgap boosts the HER performance by increasing the conductivity of the material.¹⁹⁸ Second, it has been reported that facilitation of hydrogen adsorption on transition metal dichalcogenides is strongly dependent to the conduction band minimum, rather than the traditional d-band center.^{199,200} Overall, these improvements to the alloy over the binary constituents lead to significantly more thermoneutral values for the sulfur and selenium sites.¹⁹⁷ This work aims to apply these results of increased HER performance conducted within the crystalline system to that of the polymeric MoS_x system.

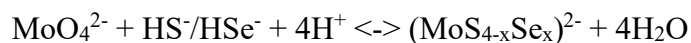
Overall, the MoS_x system has shown greater catalytic activity over the traditional MoS₂ based systems, due to the absence of discrete basal plane, and differing structural arrangement that increased the overall catalytic site density alongside with adequate electronic conductivity from short-range atomic arrangements, that allow for use in electrochemical processes.^{11,42–46} This effort aims to translate the results within the crystalline system to the polymeric system as several of the

active sites in the a-MoS_x have similar motifs and bonding environments as those found in MoS₂. Furthermore, no work has been performed on the synthesis of Se incorporated MoS_x as the literature has focused on crystalline systems. **This effort will be using a single-electrolyte electrodeposition synthesis technique in order to provide a scalable, low-cost material.** This work will demonstrate the influence of the electrolyte conditions on the films physical, chemical, electronic, and catalytic properties as a function of selenium content through a comprehensive study via Raman spectroscopy, X-ray photoelectron spectroscopy (XPS), UV-Vis spectroscopy, and electrochemical methods. **Together, these results highlight selenium’s role in the Se-MoS_x system in promoting the catalytic efficacy of these catalysts.**

4.2.2 Synthesis Methods

4.2.2.1 Electrolyte Preparation of Se-MoS_x

The synthesis of Se-MoS_x catalysts were prepared similarly to those in Chapter 4.1 with a chemical bath containing Mo⁶⁺ and S²⁻, with the addition of Se²⁻. The electrolyte was prepared from sodium molybdate dihydrate (Na₂MoO₄ · 2H₂O), sodium sulfide hydrate (Na₂S · H₂O), and selenium dioxide (SeO₂). SeO₂ was chosen for its abundance and solubility within water and sulfur rich electrolytes. We hypothesize the sulfidation/selenization of molybdate ions to the chalcogen-based ions follow a four-step reaction described by the equation:



The pH of the electrolyte was acidified from its initial pH of roughly 13 down to a pH of 8. This was done to help facilitate the formation of the final reactants over the intermediates. A notable difference from Chapter 4.1 is the order that the reactants were added. Notably, the Na₂MoO₄ and Na₂S were added prior to any titration whereas the SeO₂ was added to the electrolyte only after the pH had reached ~9. This was done as it was observed that SSe₂ precipitates would

preferentially form at higher pHs when SeO₂ was added before titration. To circumvent this, the SeO₂ was added later in titration. The following table shows the various electrolyte compositions that were tested.

Table 4.2.1: Overview of the investigated electrolyte compositions

Electrolyte Composition (mM) 50 mM Na₂MoO₄	50mM Na ₂ S	200mM Na ₂ S	400mM Na ₂ S
0mM SeO ₂	✓	✓	✓
5mM SeO ₂	✓	✓	✓
15mM SeO ₂	✓	✓	✓
25mM SeO ₂	✓	✓	✓
50mM SeO ₂	✓	✓	✓
100mM SeO ₂	✓	✓	✓

The overall synthesis of HS⁻ and HSe⁻ and the heat map of the (MoSe⁴⁻) ion can be seen in the Pourbaix diagrams in Figure 4.2.1. Using these diagrams, the thermodynamics of the synthesis conditions can be investigated. Like the reaction in Chapter 4.1, the electrolyte is clear prior to titration. Upon adding small amounts of SeO₂, there is no immediate difference. However, at high concentrations of SeO₂, the precipitation of SSe₂ is unavoidable as the increased Se concentration eventually overwhelms the buffer.

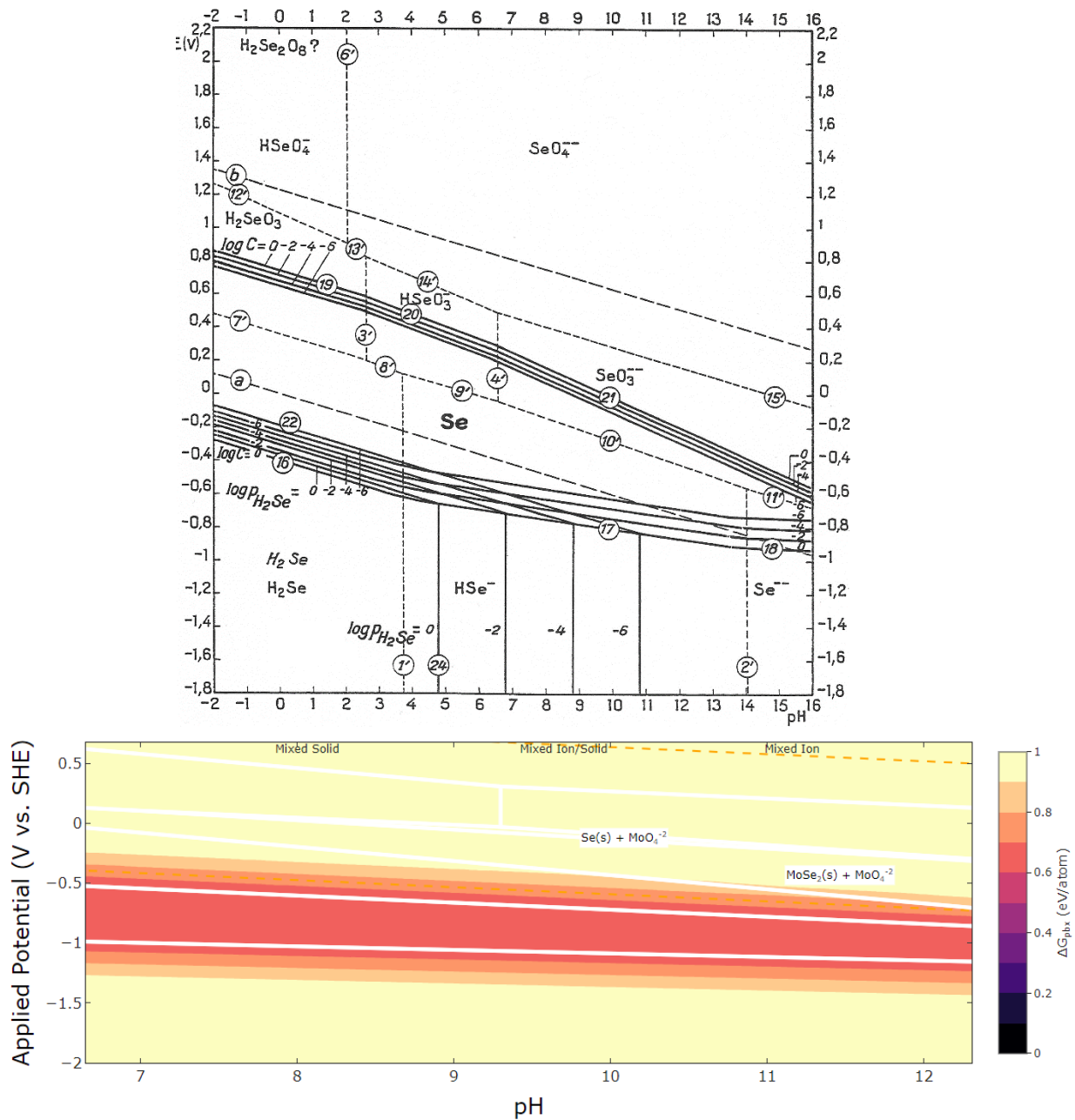


Figure 4.2.1: a) Pourbaix diagram for Selenium-water¹⁷⁴ and b) heatmap of $(MoSe_4)^{2-}$ ions on a calculated Pourbaix diagram from The Materials Project¹⁷⁴⁻¹⁷⁸

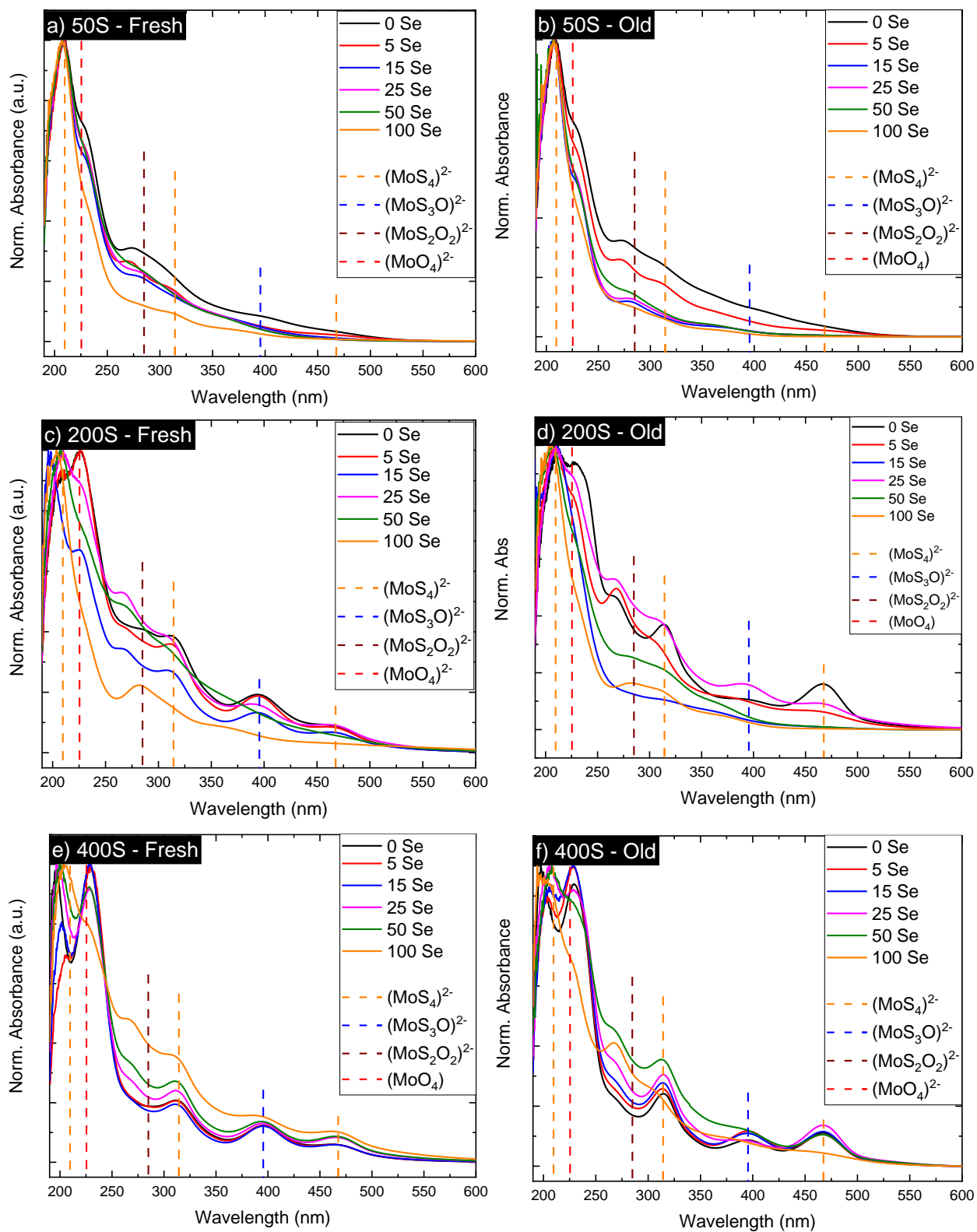


Figure 4.2.2: UV-Vis spectra of Se-MoS_x electrolytes: a) sample set with 50 mM Na₂S immediately after synthesis, b) sample set with 50 mM Na₂S after two days, c) sample set with 200 mM Na₂S immediately after synthesis, d) sample set with 200 mM Na₂S after two days, e) sample set with 400 mM Na₂S immediately after synthesis, f) sample set with 400 mM Na₂S after two days

To investigate the electrolyte prior to electrodeposition, UV-Vis spectroscopy was carried out immediately following synthesis as well as after two days as can be seen in Figure 4.2.2. Similar to the UV-Vis found in Chapter 4.1, The peak at 225 nm is attributed to the $(\text{MoO}_4)^{2-}$ anion and matches literature well.¹⁷⁹ The peaks measure at 463 nm, 312 nm, and 207 nm have been attributed to the $(\text{MoS}_4)^{2-}$ ion, the peak at 395 nm to the $(\text{MoS}_3\text{O})^{2-}$, and the peak at 287 nm to the $(\text{MoS}_2\text{O}_2)^{2-}$, matching well with literature.¹⁷⁹⁻¹⁸¹ However, note that for all oxysulfide absorption peaks, there is a significant overlap between some and/or all the various chemical states. As such, the peaks have been labelled with the primary absorption species, but it is difficult to say if only one species is present at a time. Regarding any $(\text{MoSe}_4)^{2-}$ species, there is sparse literature to compare to, with the most recent reports being from 1975 out of West Germany (and in German).^{179,201-203} The spectra of $(\text{MoSe}_4)^{2-}$ has two primary peaks at 550 nm and at 358 nm and are not readily apparent in the spectra. There is no literature for UV-Vis of oxyselenides, but their color has been described in literature as being orange while pure $(\text{MoSe}_4)^{2-}$ is described as red-violet. Additionally, one would expect a blue shift towards lower wavelengths as Se is added. As can be seen in Figure 4.2.2, there is little evidence of $(\text{MoSe}_4)^{2-}$ in the UV-Vis spectra. This refutes the hypothesis that the reaction will spontaneously occur as it did for $(\text{MoS}_4)^{2-}$, however, this isn't completely surprising. Considering the Pourbaix diagrams in Figure 4.2.1b, the $(\text{MoSe}_4)^{2-}$ anion does not form until lower potentials, $\sim -0.5 \text{ V}_{\text{SHE}}$. The open circuit potential of the electrolyte is $\sim -0.21 \text{ V}_{\text{SHE}}$, plenty in the range for $(\text{MoS}_4)^{2-}$ to form but not complete $(\text{MoSe}_4)^{2-}$ anions. However, the electrolyte still looks visually different depending on the concentration of added Se as shown in Figure 4.2.3a. To rule out any influence from the Se precursor, SeO_2 , UV-Vis spectra was collected which can be seen in Figure 4.2.3b. As can be seen, there is some overlap at short wavelengths, but no overlap between the peaks that are indicative of the other species present.

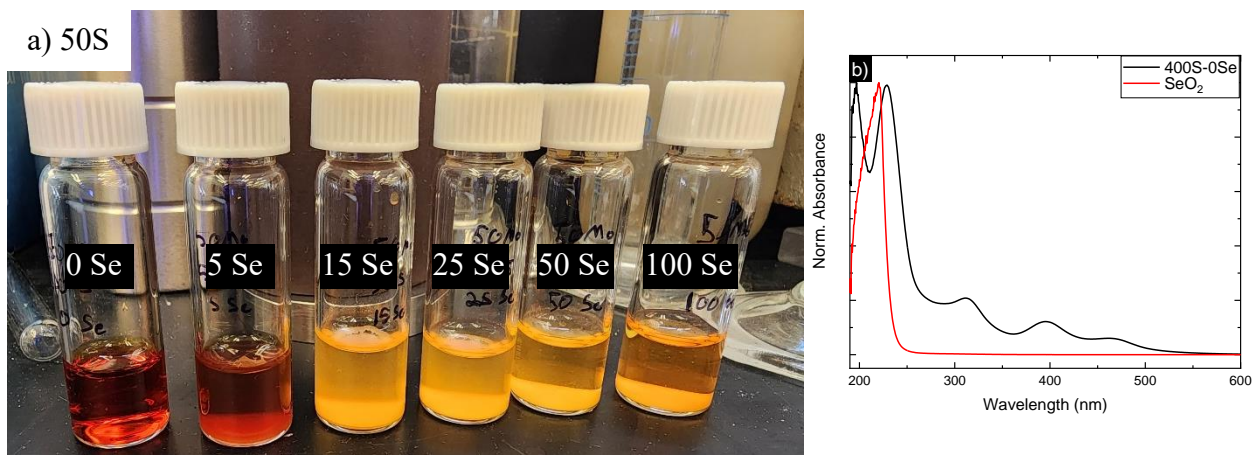


Figure 4.2.3: a) Sample electrolytes taken from various Se concentrations of the 50S sample set. 50S was chosen as it is the most visual apparent due to the lower concentration of sulfur, but the trend is the same across all samples. b) UV-Vis comparing the 400S – 0Se sample to the selenium precursor, SeO₂

4.2.2.2 Electrodeposition of Se-MoS_x

The films were electrodeposited on (0001)-textured polycrystalline ruthenium (80 nm) sputtered onto a Si (100) wafer or an indium tin oxide (ITO) coated polyethylene terephthalate (PET) substrate. The films were deposited under potentiostatic conditions at -1.55 V vs Hg/Hg₂SO₄ for 300 seconds on Ru and 10 seconds on ITO/PET unless noted otherwise. The samples deposited on Ru were used in XPS, Raman, and electrochemical measurements while the samples deposited on ITO/PET were used for UV-Vis measurements.

4.2.3 Results of Se-MoS_x

4.2.3.1 Chemical Properties of Se-MoS_x

XPS was conducted on every sample to analyze the chemical states of Mo, S, and Se species. A representative spectrum can be seen in Figure 4.2.4 with the rest of the deconvoluted data shown in Figure 4.2.5, Figure 4.2.6, and Figure 4.2.7. The XPS of the Mo 3d spectra were deconvoluted into binding energies of four doublets (3d_{5/2} and 3d_{3/2}) of Mo⁴⁺, Mo⁵⁺, Mo*, and Mo⁴⁺ with singlets of the various S 2s states and Se 3s as shown in Figure 4.2.4.

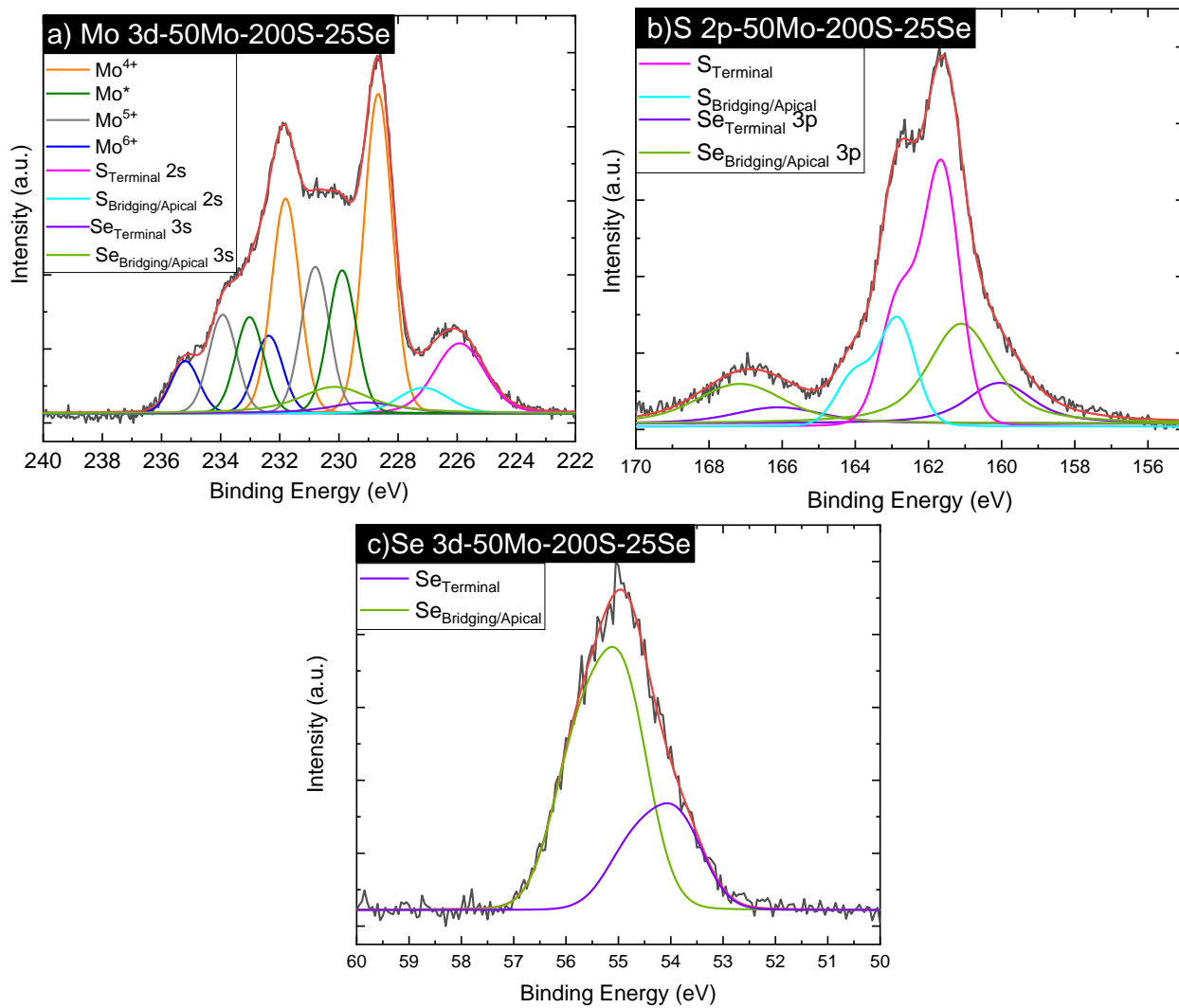


Figure 4.2.4: XPS of (a) the Mo 3d spectra, (b) the S 2p spectra, and (c) the Se 3d spectra of a representative sample

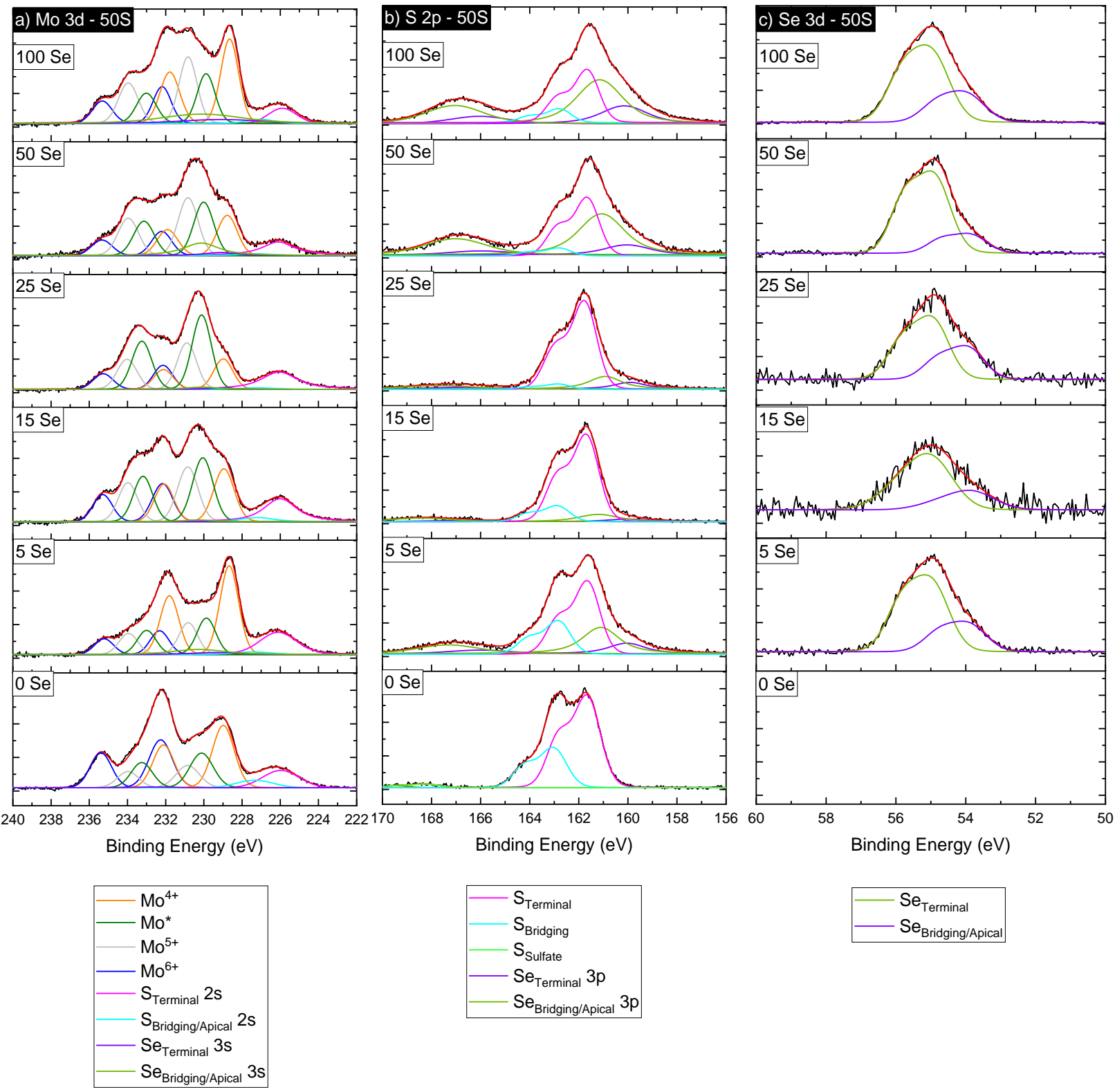


Figure 4.2.5: XPS of all samples within the 50S sample set, with a) Mo3d, b) S 2p, and c) Se 3d

As the oxidation number of Mo increases, the binding energies at which the respective doublets are found agree with previous literature.^{10,42,50,192–194} Mo⁴⁺ is attributed to the chalcogen saturated Mo center within the polymeric chain of MoS_x(Se_y), Mo⁵⁺ has been attributed to oxidation of the molybdenum-sulfide bonds, primarily terminal bonds as found in prior literature where Mo* has been attributed to an intermediate state of incomplete oxidation between Mo⁴⁺ and Mo⁵⁺.⁵⁰ Mo⁶⁺ has been attributed to the Mo center of MoO₃. The Mo 3d peaks were deconvoluted with a binding energy difference of 3.13 eV between the 3d_{5/2} and 3d_{3/2} and with a fixed intensity ratio of 3:2. The sulfur 2s is also present within the Mo 3d spectra and is fit using parameters from the S 2p spectra. The deconvolution of the S 2p spectra consists of three primary features: (i) terminal S₂²⁻ ligands (ii) bridging S₂²⁻ and apical S²⁻ ligands, and (iii) the overlapping Se 3p spectra as can be seen in Figure 1b. The sulfur spectrum was deconvoluted with two doublets, with the constraints of an energy difference of 1.18 eV between the 2p_{3/2} and 2p_{1/2} and with an intensity ratio of 2:1. The overlapping Se 3p spectra was fitted using fitting parameters obtained from electrodeposited Se and the peak position and intensity of the Se 3p was referenced against the primary peak of Se 3d. The Se 3d spectra was fitted with two doublets that represent the Se²⁻ and Se₂²⁻ ligand.^{204–207} The Se spectra was deconvoluted with two doublets, with the constraints of an energy difference of 0.86 eV and an intensity ration of 0.735 between the 3d_{3/2} and the 3d_{5/2}. The S 2p and Se 3d spectra are represented here as two summed together doublets for ease of visualization.

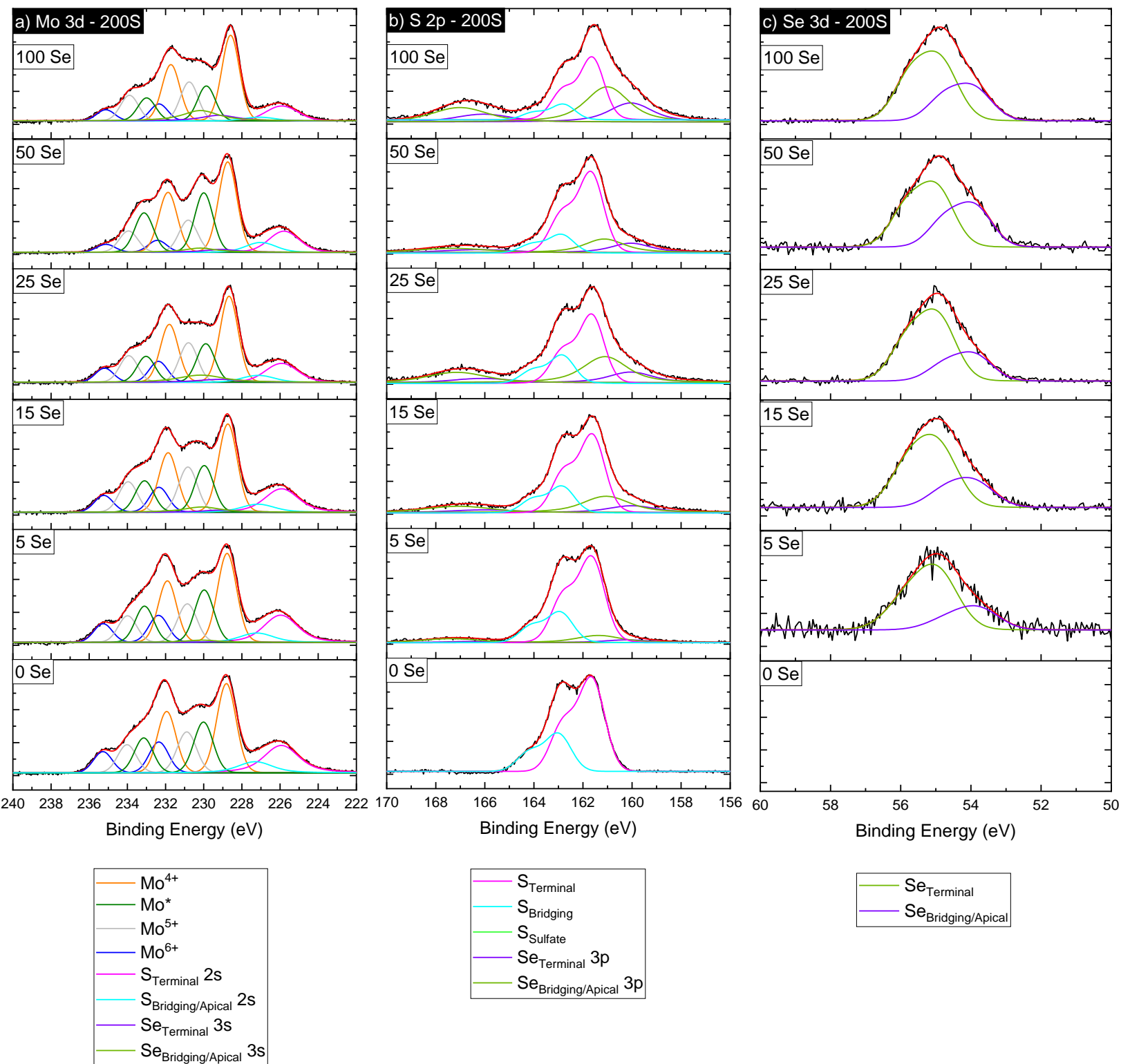


Figure 4.2.6: XPS of all samples within the 200S sample set, with a) Mo3d, b) S 2p, and c) Se 3d

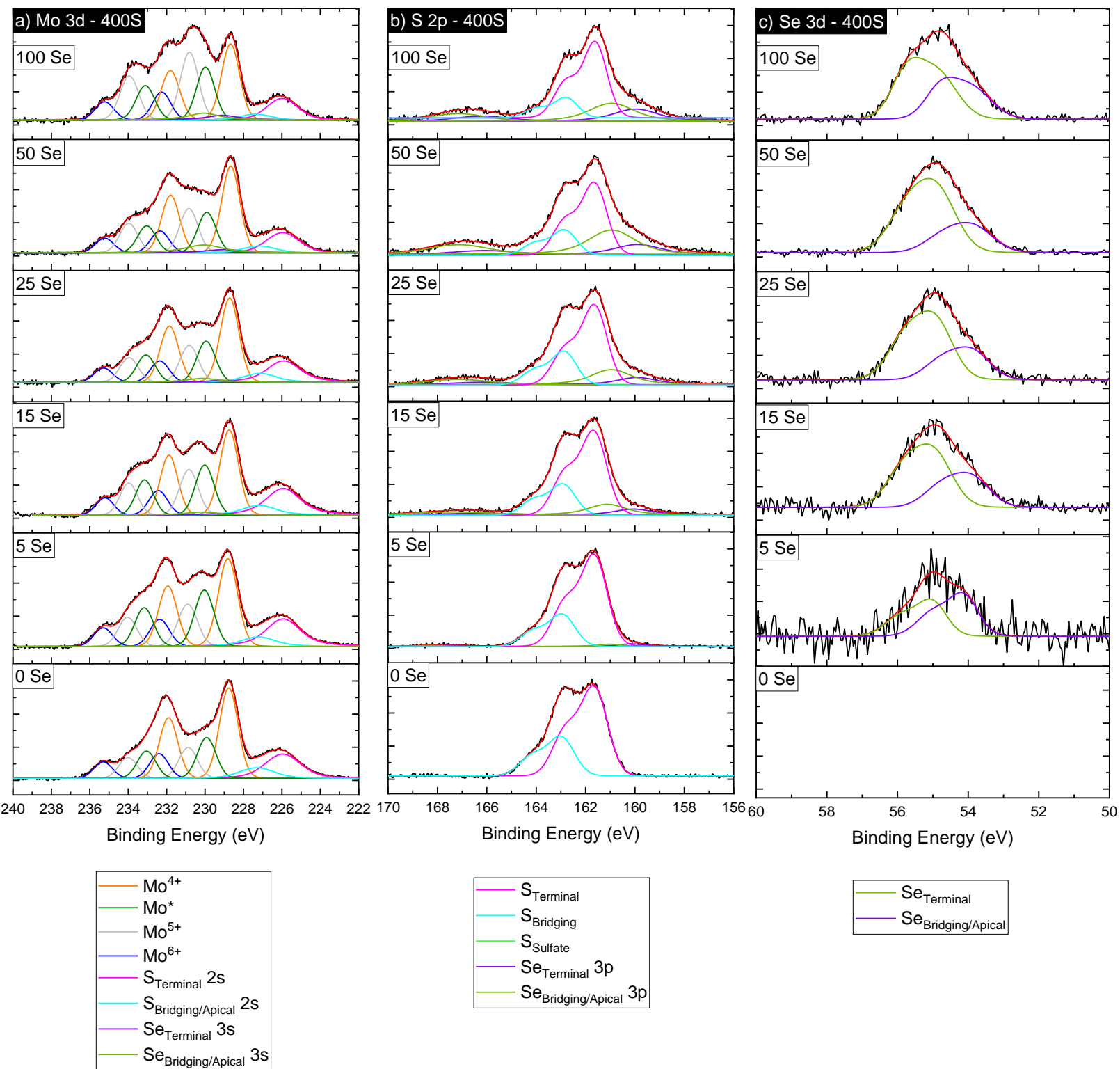


Figure 4.2.7: XPS of all samples within the 200S sample set, with a) Mo3d, b) S 2p, and c) Se 3d

Using the XPS spectra the overall ratio of Se to S in the film can be obtained for the various samples, as can be seen in Figure 2. These reported values are the total value of molybdenum bonded selenium and sulfur bonds. The addition of more selenium precursors in the electrolyte generally lead to an increase in incorporated selenium found within the film. However, at a given selenium concentration, a colloidal suspension of SeS_2 formed and can be seen in Figure 4.2.8b and c. While matching spectra has been found, the literature does not specify which vibration

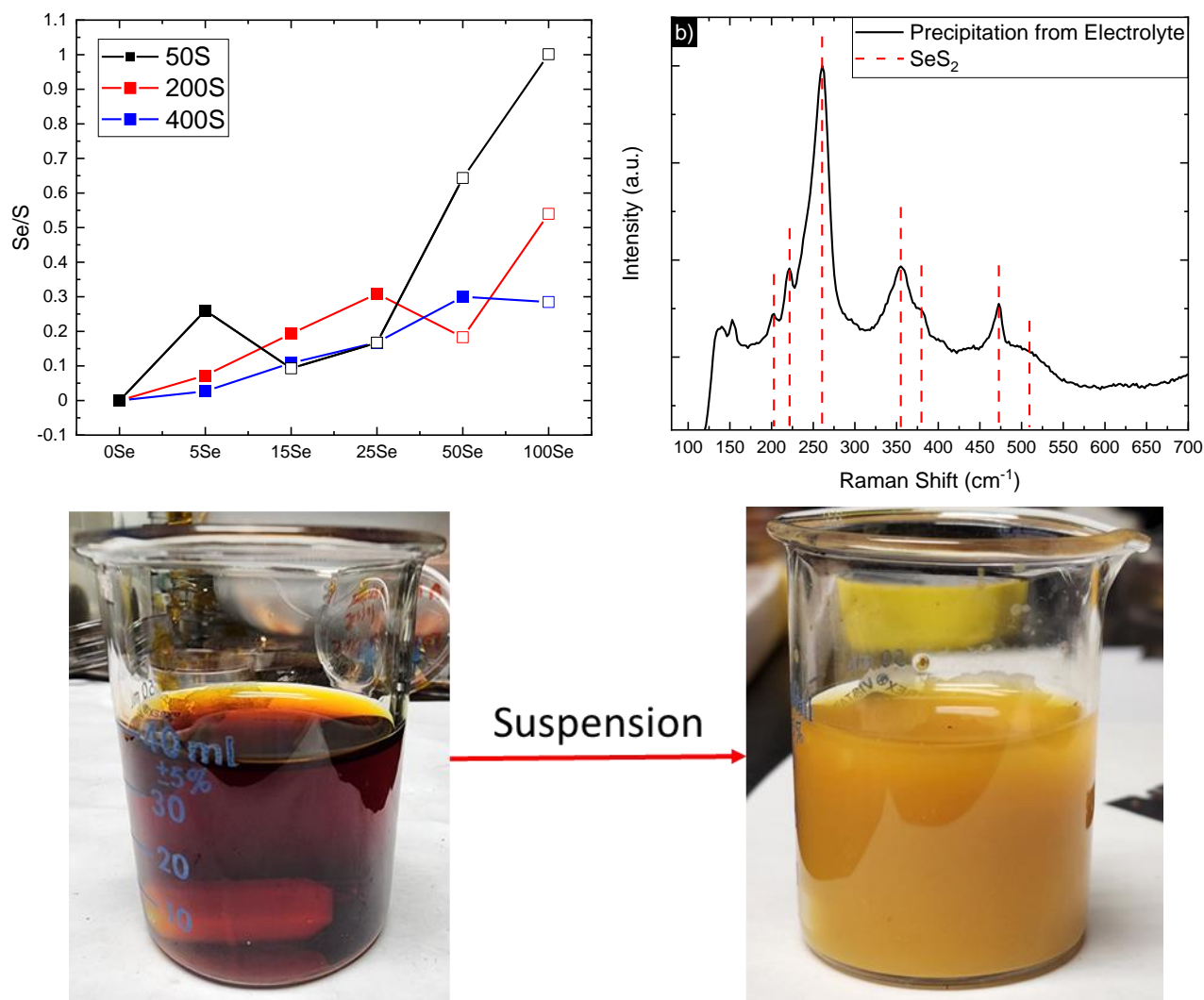


Figure 4.2.8: a) Se/S ratio obtained via XPS for the various films as a function of sulfur precursor concentration and as a function of selenium precursor concentration. The open boxes represent samples where the electrolyte had formed a suspension. b) Raman spectra of the filtered and rinsed precipitate. c) The formation of the suspension upon adding excess SeO_2

modes each peak represents, but the data here matches literature well.^{208,209} The increased presence of sulfur precursor delays this formation due to NaOH forming a basic buffer and preventing the precipitation of SeS_2 which is caused in the presence of a weak acid.²¹⁰ This formation of a suspension lead to a decrease in selenium found within the film as excess selenium is removed from the active electrolyte and therefore it likely does not participate in the deposition reaction.

To confirm that alloying occurred within the Se-MoS_x film, the binding energy of the chalcogen bonded Mo^{4+} was plotted as a function of Se/S as seen in Figure 4.2.9a. It is expected that Mo^{4+} shifts towards a lower binding energy as the selenium concentration increases due to the less electronegative selenium atoms.^{211,212} This further suggests that the electronic structure is being modified by varying the Se/S ratio, something that will be explored later. Additionally, it can be seen in Figure 4.2.9b that the Se is preferentially filling the apical/bridging bond-moiety, consistent with the reduction in those vibration modes found in the Raman spectra.

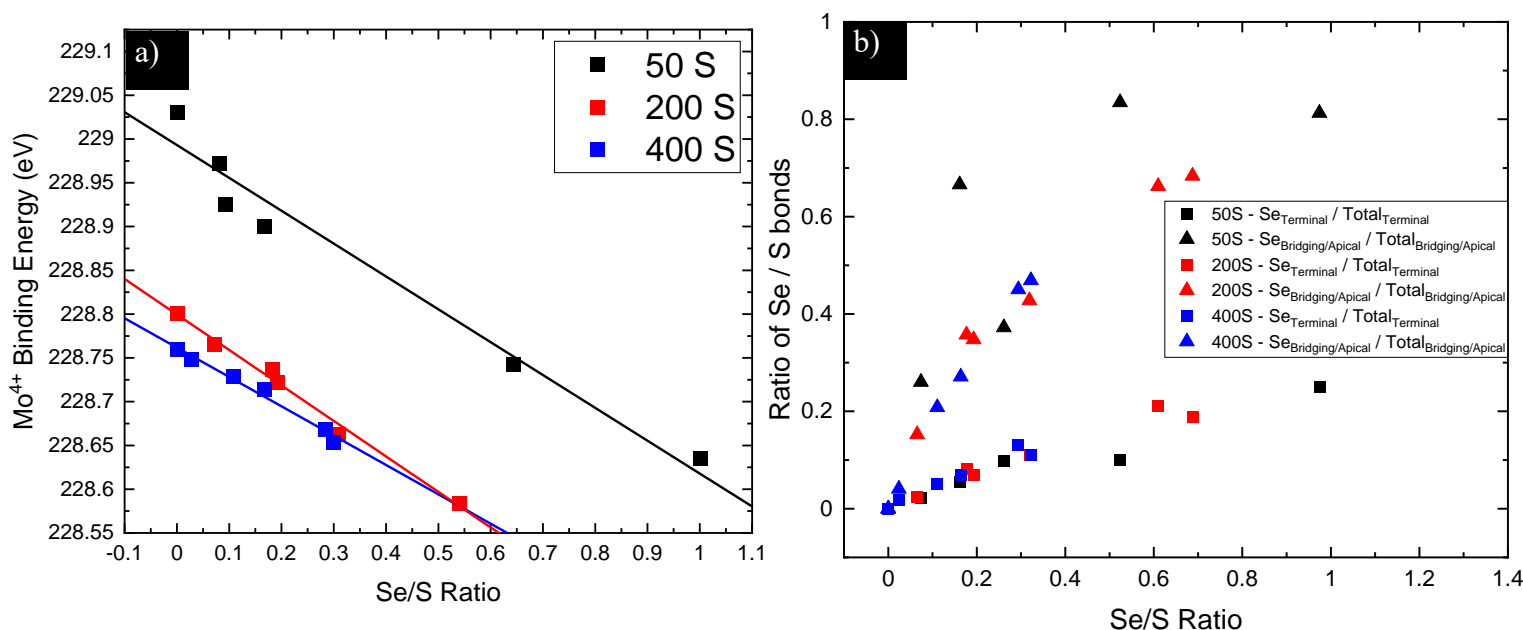


Figure 4.2.9: a) Binding energy of Mo^{4+} as a function of Se/S ratio and b) Ratio of Se/S bonds as a function of Se/S. The triangles represent the ratio of $\text{Se}_{\text{Bridging/Apical}} / \text{Total}_{\text{Bridging/Apical}}$ whereas the boxes represent the ratio of $\text{Se}_{\text{Terminal}} / \text{Total}_{\text{Terminal}}$. The different colors represent the different sample sets.

4.2.3.2 Structural Properties of Se-MoS_x

Raman spectroscopy was used to investigate the structure of the various Se-MoS_x electrocatalysts and can be seen in Figure 4.2.10. The Raman signatures of the Se-MoS_x material shows very similar Raman signatures to those reported for [Mo₃S₁₃](NH₄)₂ clusters.^{11,185} The molybdenum sulfide $\nu(\text{Mo-S})$ were found at 283-385 cm⁻¹ and the $\nu(\text{Mo-S}_{\text{apical}})$ vibrations were observed in the 450-475 cm⁻¹ region where the $\nu(\text{Mo-S-Mo})$ vibrations were observed around 425 cm⁻¹. The $\nu(\text{S-S})_{\text{terminal}}$ and $\nu(\text{S-S})_{\text{bridging}}$ were observed around 520 cm⁻¹ and 550 cm⁻¹, respectively. Additionally, there is a peak around 195 cm⁻¹ that has been recorded but not identified in previous literature. Further compounding is the lack of reports that include wavenumbers down in this range.^{11,44,213} The peak at 255 cm⁻¹ could either be attributed to amorphous selenium or to a $\nu(\text{Mo-Se})$ bond. Both may contribute to the presence of this peak, but as amorphous selenium was not observed in any of the XPS data (the 3d_{5/2} would lie around 55.5 eV), it is unlikely. However, it has been reported that amorphous selenium build-up is caused by the irradiation of the laser on the sample²¹⁴. To determine any impact this has on the resulting spectra, we see the peak slightly evolving over time, suggesting the accumulation of amorphous selenium as seen in Figure 4.2.10e. This phenomenon was observed within the amorphous MoSe_x system.²⁰⁷

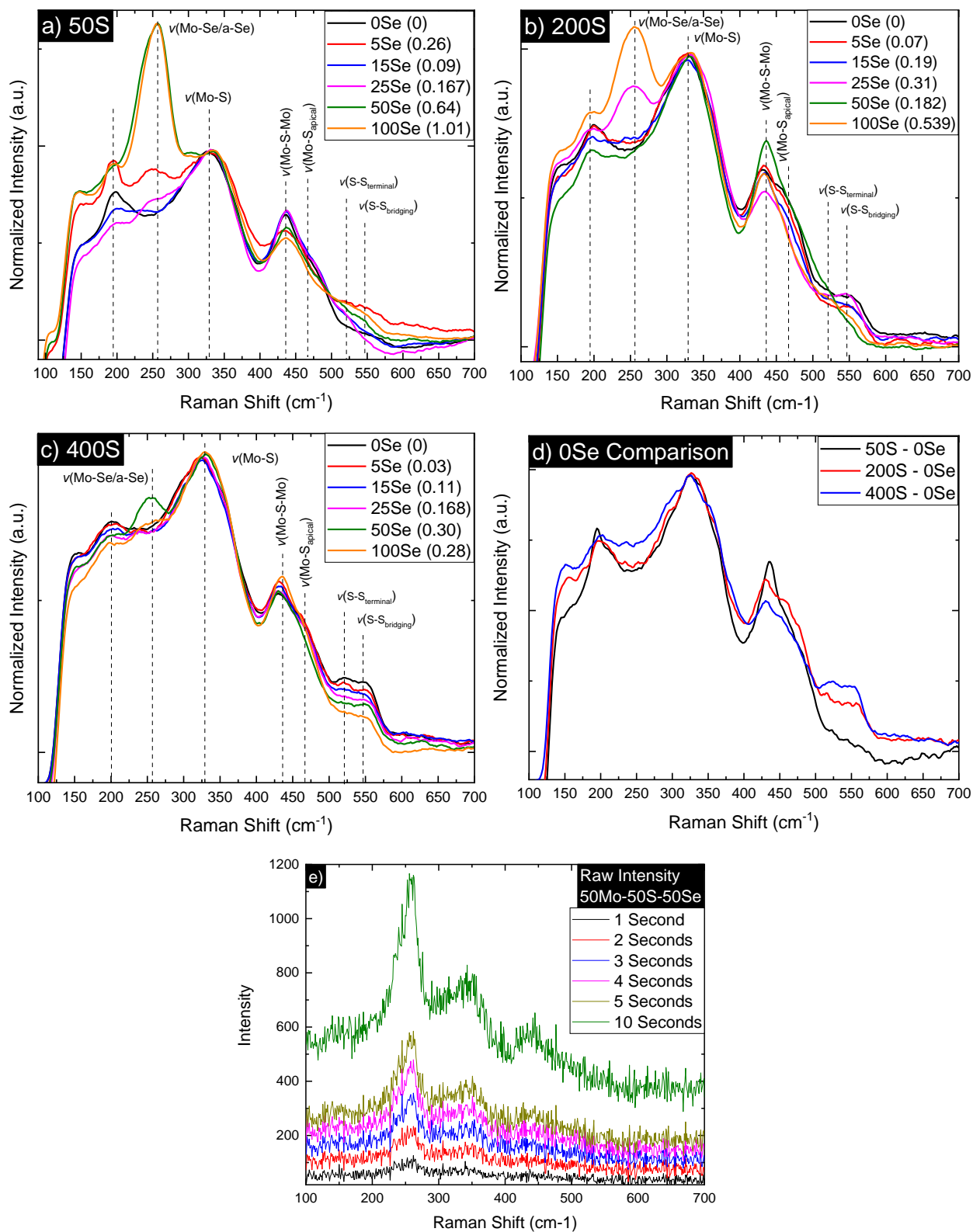


Figure 4.2.10: Raman of the various Se-MoS_x electrocatalysts as a function of the Se precursor (the Se/S ratio is given in parenthesis) with a) 50S, b) 200S, and c) 400S sample sets. d) is a comparison between the various films prior to any addition of SeO₂ and f) is a time series of the 50Mo-50S-50Se sample where the scans were summed for the given amount of time to demonstrate any changes as a function of laser irradiation

Other changes that are found are within the (Mo-S-Mo), (S-S_{terminal}), and (S-S_{bridging}) bonds. When comparing these bonds between the different samples sets, it is clear that the starting, non-selenium incorporated samples, are distinctly different from each other, and therefore each sample set has a distinctly different structure and can be seen in Figure 4.2.10d. Notably, the 50S sample has the highest concentration of (Mo-S-Mo) modes relative to (Mo-S) and it decreases in intensity as the sulfur concentration increases. The (S-S_{terminal}) and (S-S_{bridging}) vibration modes are the lowest for the 50S sample and increase in intensity as the sulfur concentration increases to 200 S and 400 S. This agrees with the XPS data from the 50 S in Figure 4.2.5 as there is significantly less Mo⁴⁺ than in the other samples. This can be tied back to the initial electrolyte in Figure 4.2.2 as the initial 400S electrolyte has stronger absorbance peaks for the (MoS₄)²⁻ anion compared to 50S. This demonstrates that the low sulfur samples have unsaturated bonds, something that has been reported in literature.^{44,215} Within the 50 S sample set, there are subtle changes within the (Mo-S-Mo) and (Mo-S_{apical}) vibration modes. The main changes can be seen in the (S-S_{terminal}) and (S-S_{bridging}) vibration modes where the intensity and broadening generally increases with increased selenium content. The main spectral changes within the 200S sample set are a suppression of the (S-S_{terminal}) and (S-S_{bridging}) bonds. A similar trend is found within the 400S sample set. Within literature, electrodeposited MoSe_x does not exhibit vibration modes at these wavenumbers, potentially explaining the reduction in these bonds. The correlation between incorporated Se, these bonds, and the catalytic properties will be explored later.

4.2.3.3 Electronic Properties of Se-MoS_x

To investigate possible changes in electronic structure, UV-Vis spectroscopy was conducted and can be seen in Figure 4.2.11. There is a primary absorption peak between 360 nm and 385 nm, and a secondary peak from the ITO,²¹⁶ is located around 320 nm. Additionally, interference patterns between the electrodeposited films and the ITO substrate can be seen within the low absorption regions. The primary absorption peak has been reported in literature previously and has been attributed to the direct transition from the deep valence band of S 2p to the conduction band of Mo 3d.²¹⁷⁻²¹⁹ As the sulfur concentration increases, the primary absorption peak shifts towards higher wavelength, suggesting that the increased saturation of sulfur bonds found within the Raman spectrum leads to this shift. A similar shift has been reported in literature where the undercoordinated molecule is shifted to the left with respect to a fully saturated molecule.¹⁸⁰ Performing a Tauc analysis, as shown in Figure 4.2.11b,d,f, the optical direct band gap transition can be calculated. These calculations are plotted as a function of incorporated Se as shown below and are what is expected for a-MoS_x based materials in Figure 4.2.12.²¹⁷ What is seen is a slight decrease in the direct band gap value for the low Se/S ratios, in which the band gap quickly rises after a certain point. This trend, along with the lack of a large overall change, was expected based on previous literature and density of states calculations.²²⁰⁻²²²

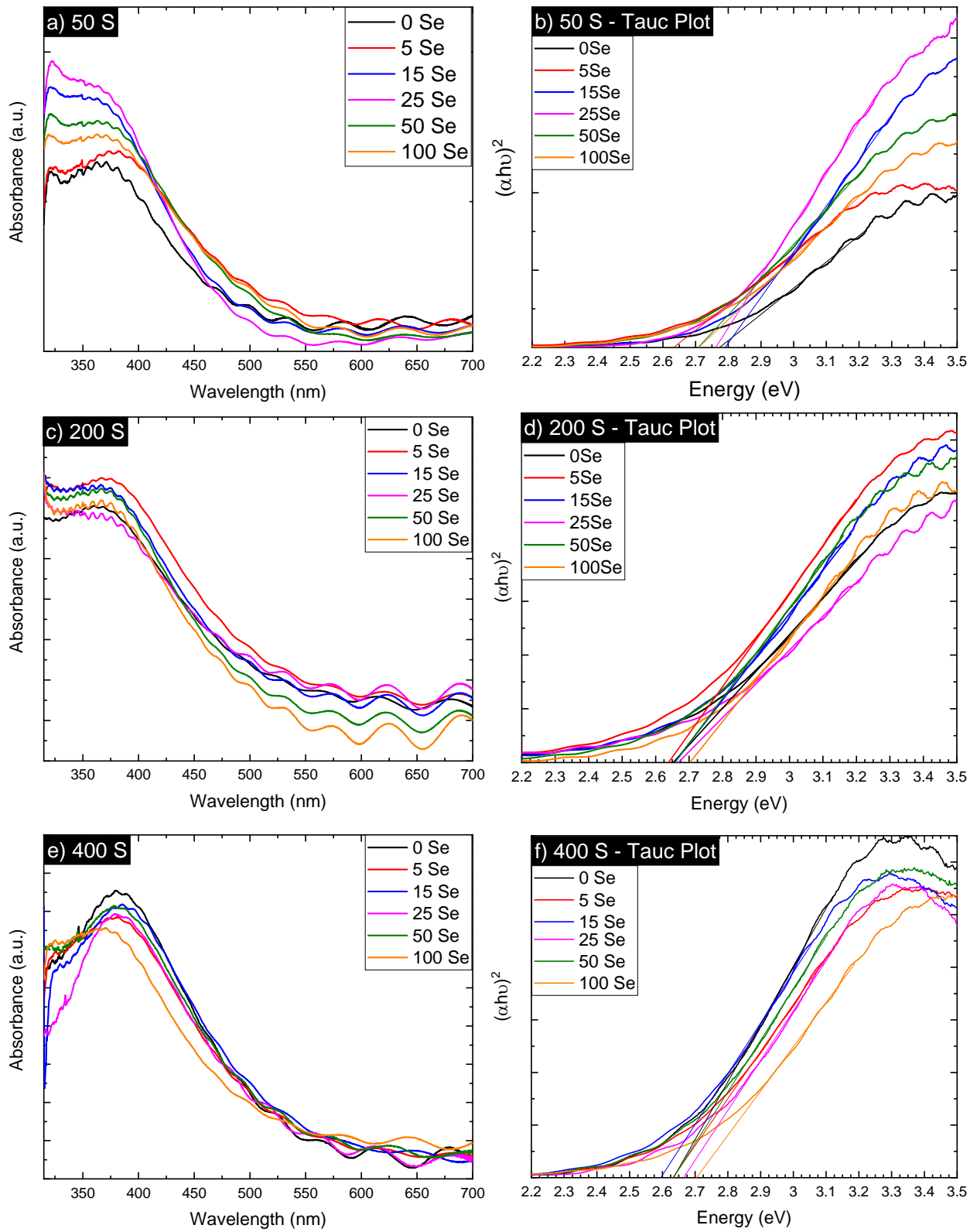


Figure 4.2.11: UV-Vis spectrum for the various sample sets, with a) 50 S, c) 200 S, and e) 400 S with the corresponding Tauc plots to the right, with b) 50S, d) 200S, and c) 400S

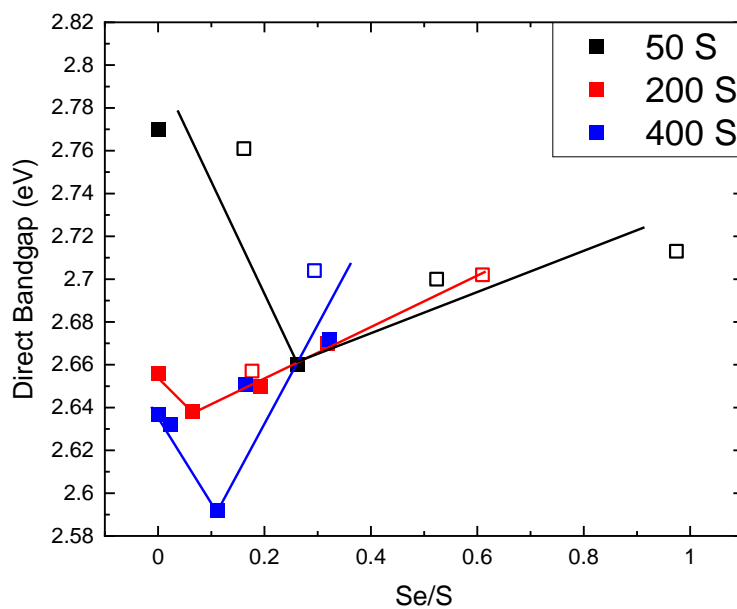


Figure 4.2.12: Graphical representation of the direct bandgap calculated via Tauc plots as a function of Se/S in the film, note: open boxes demonstrate when a suspension was present; the lines are not calculated linear relationships, only a means to help guide the reader's eye

4.2.3.4 Electrocatalytic Properties of Se-MoS_x

To examine the impact that the selenium incorporation into MoS_x has on the catalytic performance for HER, polarization experiments were conducted and are shown in Figure 4.2.13. To compare the various catalysts, the overpotential required to reach 10 mA/cm² (η_{10}) and the Tafel slope are recorded and can be seen in Table 4.2.2. As can be seen, the sample that exhibited the lowest overpotential was the 400 S – 15 Se sample at only 153 mV to reach 10 mA/cm², which is competitive with the best a-MoS_x style materials, many of which require a 3D support to reach this activity. Additionally, the sample is quite stable as shown in Figure 4.2.13e, improving over the standard catalyst from Chapter 4.1. The overpotentials as well as the associated Tafel slopes are summarized in Table 4.2.2. Regarding the Tafel slope, there are two possible combinations for the overall mechanism, the Volmer-Tafel and the Volmer-Heyrovsky. If the adsorption of the hydrogen

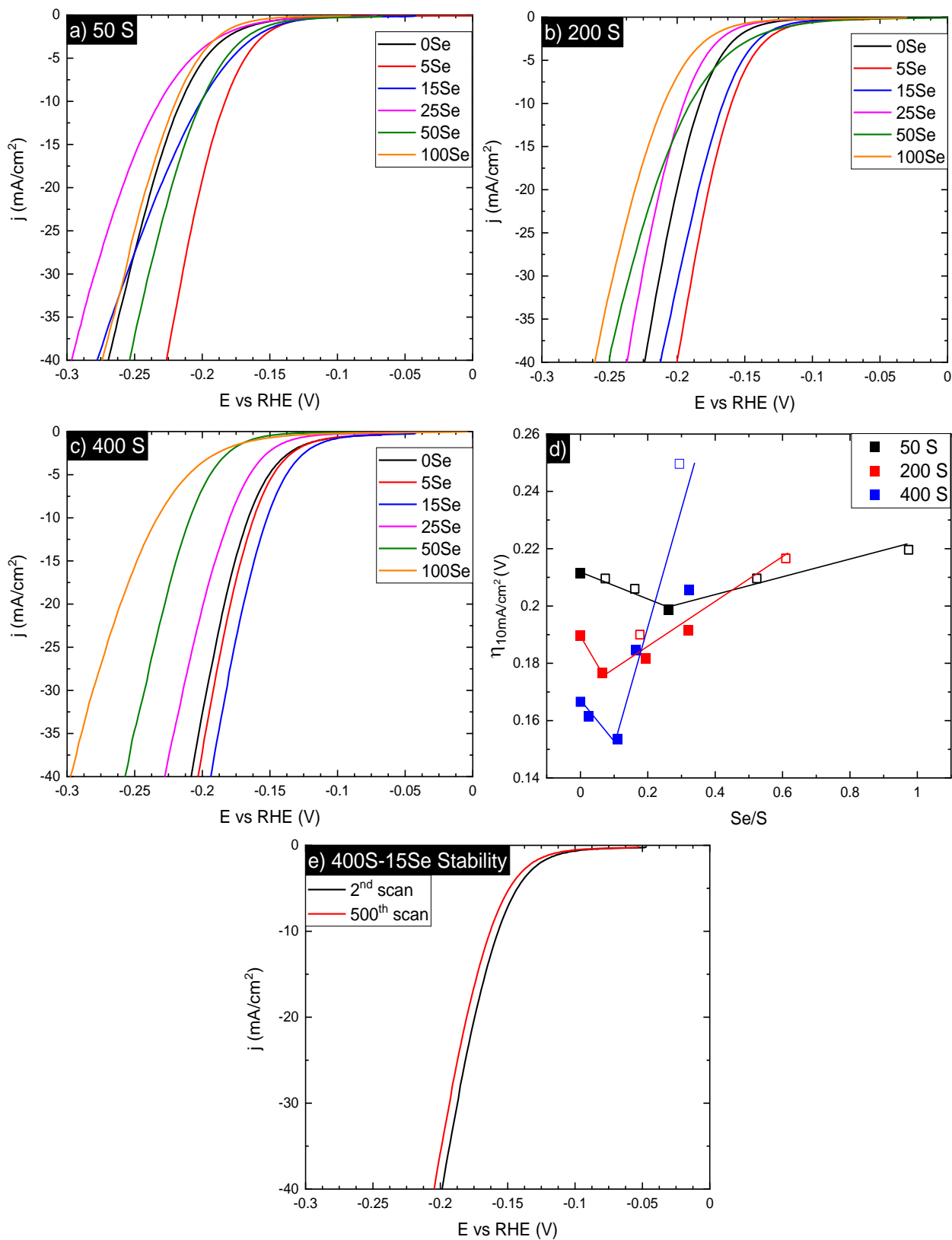


Figure 4.2.13: Polarization curves for the various samples sets, with a) 50 S, b) 200 S, and c) 400 S. In d) the overpotential is plotted as a function of Se/S ratio. The lines are there to guide the reader and are not linearly fit lines. e) stability of the best performing catalyst, 400S-15Se

was the limiting step, a Tafel slope of 120 mV/dec would be anticipated. If the Tafel or Heyrovsky mechanisms are the limiting step, a Tafel slope of 30 or 40 mV/dec are expected, respectively. As such, the majority of the samples follow the Volmer-Heyrovsky mechanism, consistent with previous reports of a-MoS_x-based materials. Of note, when the precipitation reaction occurs in 50 S – 15 Se, 200 S – 50 Se, and 400 S – 100 Se, the Tafel slope increases significantly. The catalytic properties of the Se-MoS_x initially increase with increasing concentrations of Se, however, decrease significantly once higher concentrations of Se are incorporated as seen in Figure 4.2.13d.

Table 4.2.2: Overpotentials and Tafel slopes of the catalysts

η₁₀ (mV) Tafel slope (mV/dec)	50mM Na ₂ S	200mM Na ₂ S	400mM Na ₂ S
0mM SeO ₂	212 mV 56 mV/dec	190 mV 43 mV/dec	166 mV 51 mV/dec
5mM SeO ₂	198 mV 43 mV/dec	177 mV 45 mV/dec	162 mV 47 mV/dec
15mM SeO ₂	209 mV 71 mV/dec	182 mV 43 mV/dec	153 mV 46 mV/dec
25mM SeO ₂	206 mV 68 mV/dec	192 mV 44 mV/dec	185 mV 44 mV/dec
50mM SeO ₂	210 mV 52 mV/dec	190 mV 73 mV/dec	206 mV 42 mV/dec
100mM SeO ₂	220 mV 47 mV/dec	217 mV 52 mV/dec	250 mV 72 mV/dec

When comparing the initial catalytic properties of the samples prior to introducing selenium, 50 S had the poorest activity with 400 S having the greatest. This is likely due to the increased saturation of the (S-S_{bridging}) and (S-S_{terminal}) bonds found in the high S samples. It has been reported in literature that these bonds, and especially (S-S_{bridging}), are the main sites for HER catalytic activity and therefore the more saturated those bonds are, the higher the catalytic activity.²²³ This lack of sulfur bonding can be seen in both the XPS and Raman, where in XPS there is subdued Mo⁴⁺ and in the Raman spectra there is a lack of (S-S_{bridging}) and (S-S_{terminal}) modes. At high Se/S concentrations, the (S-S_{bridging}) and (S-S_{terminal}) have been significantly replaced by selenium, leading to worse catalytic performance. This is expected as electrodeposited a-MoSe_x has worse catalytic performance than similarly synthesized a-MoS_x so as it becomes more MoSe_x like, performance is expected to suffer.²⁰⁷ Additionally, as the (S-S_{bridging}) are the most catalytically active, the preferential replacement of the bridging modes decreases the catalytic efficacy of those samples.

However, this does not completely explain the increase in performance for those alloys at low Se/S ratios. It is known that by lowering the band gap, the catalytic activity should increase as conductivity is critical in electro-catalysis.¹⁹⁸ To examine this, the η_{10} has been plotted against the direct optical bandgap as seen in Figure 4.2.14a. It demonstrates that the 200 S and 400 S have a relationship between the overpotential required and direct optical bandgap. This is expected as the lowered bandgap would increase the conductivity of the sample, allowing for increased electron transfer. However, the 50 S sample set does not seem to be significantly impacted by the changing band gap. We hypothesize that this occurs because of the lack of saturation in the bonding environment, overriding any positive benefit towards increasing the catalytic activity that decreasing the bandgap would yield. This highlights that the catalytic sites need to be sufficiently

saturated before small changes in the bandgap will demonstrate any significant improvement to the catalytic efficacy of the catalyst.

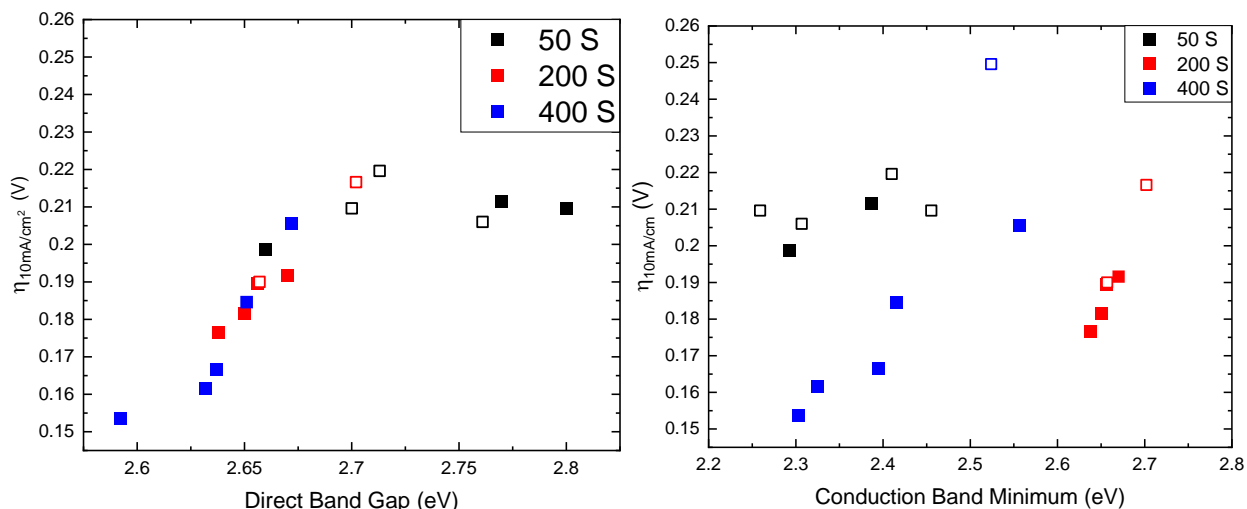


Figure 4.2.14: a) The overpotential of the various catalysts as a function of their direct optical bandgap and b) the overpotential as a function of the conduction band minimum obtained via XPS and the Tauc analysis

It has been reported that within transition metal dichalcogenides the reduction of the conduction band minimum (CBM) is attributed to the increased HER catalytic activity due to the increase of overlapping states with the states of adsorbed hydrogen. To examine this, the η_{10} has been plotted against the conduction band minimum that was calculated from the valence band maximum obtained via XPS, seen in Figure 4.2.15, and the optical bandgap from the Tauc analysis. It should be noted that this technique of calculating the VBM from XPS data is somewhat subjective of where the linear line is drawn and its relationship with the Urbach tail, although it is a widely used and accepted technique. A similar trend from the direct bandgap figure holds, where the reduction of the CBM impacts the catalytic activity of the 200 S and 400 S samples, however it does not seem to significantly alter the 50 S sample set. This further demonstrates that the catalytic efficiency can't solely be increased by reducing the bandgap or CBM, but that there must be sufficient catalytic sites to take advantage of the synergistic impact.

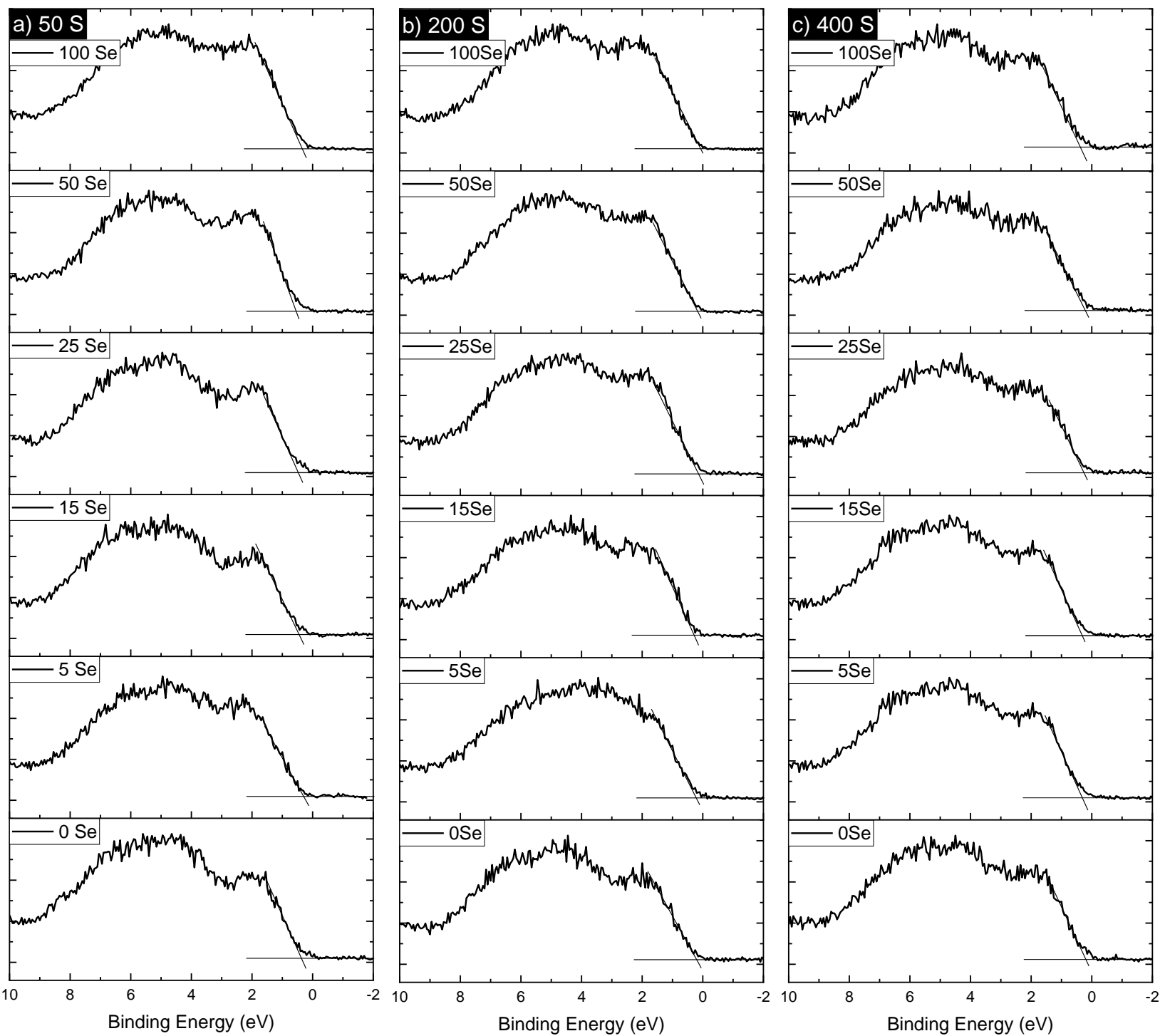


Figure 4.2.15: XPS of the Valence Band for the sample sets of a) 50S, b) 200S, and c) 400S

4.2.4 Conclusions

In summary, we have synthesized a series of Se-MoS_x films across a variety of selenium and sulfur precursor concentrations utilizing a potentiostatic electrodeposition technique. Our results demonstrate that we are able to control the chemical composition, structure, electronic properties, and catalytic efficacy of the resulting film by tailoring our starting electrolyte composition. This study has demonstrated that the saturation of the (S-S_{bridging}) and (S-S_{terminal}) bonds are critical to the HER catalytic properties and that by substituting them with low amounts of Se, the catalytic properties can be enhanced. However, when in high concentration, the films catalytic properties suffer. Additionally, this study investigated the impact of Se incorporation has on the bandgap and CBM of the resulting films and ties it to catalytic properties, supporting prior research that the films with the smallest bandgap and lowest CBM exhibited the greatest catalytic performance if the active sites are present. Overall, a highly active catalyst that only requires an overpotential of 153 mV with a low Tafel slope of 46 mV/dec was developed that takes advantage of synergistic properties of alloying a-MoS_x with Se.

4.3 Te Incorporation into MoS_x via Electrodeposition to Form a Two Phase MoTe_x/MoS_x Matrix

4.3.1 Background and Motivation

There is currently significantly less work on tellurium based MoS₂ alloys for HER, with the first and only paper published in 2021.²²⁴ Similar to MoS_{2x}Se_{2(1-x)} alloys, it was found that the MoS_{2x}Te_{2(1-x)} alloys exhibited greater catalytic performance over the constituents of MoS₂ and MoTe₂ and can compete with 10% by weight Pt loaded on a graphite substrate.²²⁴ These experimental results were then corroborated with DFT to gain further insight into the mechanistic behaviors that promoted the catalytic performance of the MoS_{2x}Te_{2(1-x)} alloys.²²⁴

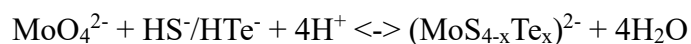
As mentioned earlier in Chapter 4.2, the addition of a different chalcogen atom has been shown to produce catalytically active sites due to defect generation in addition to shortening the electron transfer pathways. Furthermore, the DFT studies have examined the electronic structure and hydrogen adsorption energy for the MoS_{2x}Te_{2(1-x)} material and found that the Mo edge, previously relatively inert, exhibits the most thermoneutral value of only -0.052 eV and is therefore the most optimal active site for HER. Other sites that exhibited close to zero $\Delta G_{0,ads}^H$ were the exposed Mo corner and the sulfur bridge site between a Mo corner and Mo edge atom. Additionally, it has been shown that the electron effective mass (m_e^*) is significantly lower and the carrier mobility (μ) of the alloyed material is significantly higher than that of the binary compounds.²²⁵ Similar to Chapter 4.2, we aimed to apply these investigations to the as of yet unstudied MoS_xTe_y. However, we found that MoTe_y formed within a MoS_x matrix, and those results will be the focus of the following discussion.

4.3.2 Synthesis Methods

4.3.2.1 Electrolyte Preparation

The synthesis of Te-MoS_x catalysts were prepared similarly to those in Chapter 4.2 with a chemical bath containing Mo⁶⁺ and S²⁻, with the addition of Te²⁻. The electrolyte was prepared from

sodium molybdate dihydrate ($\text{Na}_2\text{MoO}_4 \cdot 2\text{H}_2\text{O}$), sodium sulfide hydrate ($\text{Na}_2\text{S} \cdot \text{H}_2\text{O}$), and tellurium dioxide (TeO_2), given its low cost, availability, and safety. However, as TeO_2 has negligible solubility in water, special attention has to be given to properly add it to the electrolyte. Namely, TeO_2 is soluble in the presence of alkali metal hydroxides, such as NaOH , which is formed when both the Na_2S and Na_2MoO_4 dissociate.²²⁶ As such, TeO_2 can be dissolved with this recipe, whereas it would be difficult, if not impossible, to add it to the traditional $(\text{MoS}_4)^{2-}$ containing precursor, $(\text{NH}_4)_2\text{MoS}_4$, without further modification. Similarly, to Chapter 4.1 and 4.2, we hypothesize that the sulfurization/tellurization of the molybdate ions to the chalcogen-based ions follow a four-step reaction described by the equation:



The following table shows the various compositions that were tested:

Table 4.3.1 Electrolyte Compositions to be Studied

Electrolyte Composition (mM)	50mM Na_2S	200mM Na_2S	400mM Na_2S
50 mM Na_2MoO_4			
0mM TeO_2	✓	✓	✓
5mM TeO_2	✓	✓	✓
15mM TeO_2	✓	✓	✓
25mM TeO_2	✓	✓	✓
50mM TeO_2	✓	✓	✓
100mM TeO_2	✓	✓	✓

The overall synthesis of HTe^- can be seen in the Pourbaix diagram in Figure 4.3.1. Like the reaction from Chapter 4.1, the electrolyte is clear prior to titration. There was no discernible difference with the addition of TeO_2 once enough NaOH has been produced via dissociation of the other precursors. If TeO_2 was added too soon or prior to titration, the entire electrolyte formed precipitates and crashed out of solution, leaving an electrolyte that was not able to undergo any further reactions.

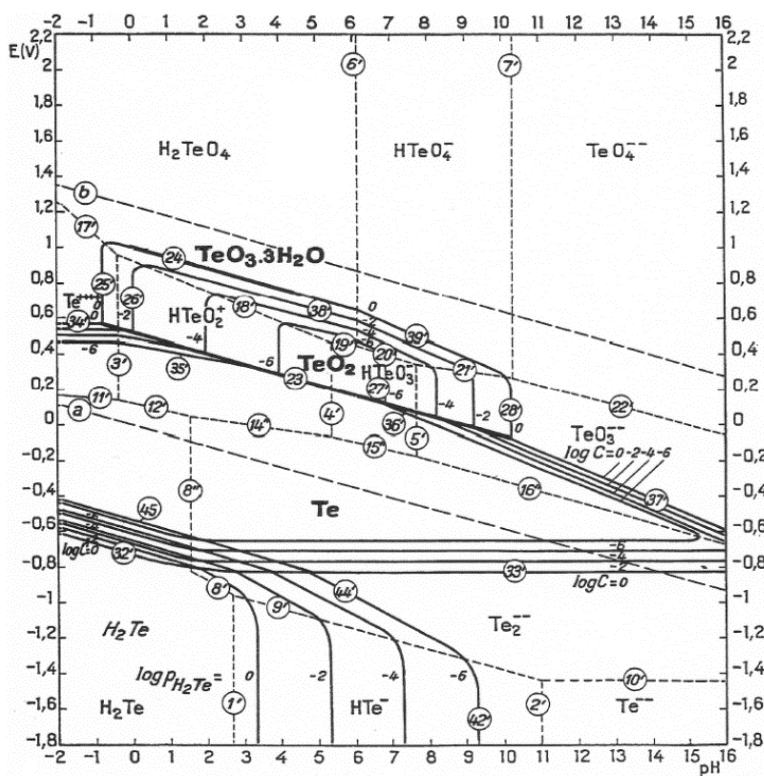


Figure 4.3.1: Pourbaix diagram for Tellurium-water¹⁷⁴

To investigate the electrolyte prior to electrodeposition, UV-Vis spectroscopy was carried out immediately following synthesis, as can be seen in Figure 4.3.2. The peak at 225 nm is attributed to the $(\text{MoO}_4)^{2-}$ anion and matches literature well.¹⁷⁹ The peaks measure at 463 nm, 312 nm, and 207 nm have been attributed to the $(\text{MoS}_4)^{2-}$ ion, the peak at 395 nm to the $(\text{MoS}_3\text{O})^{2-}$, and the peak at 287 nm to the $(\text{MoS}_2\text{O}_2)^{2-}$, matching well with literature.¹⁷⁹⁻¹⁸¹ However, note that for all oxysulfide absorption peaks, there is a significant overlap between some and/or all the

various chemical states. As such, the peaks have been labelled with the primary absorption species, but it is difficult to say if only one species is present at a time. Regarding the peak at 262 nm, while no direct reference is made to it within literature, a small hump is noticed at 262 nm in Diemann et. al's paper on $(\text{MoS}_4)^{2-}$ ions, suggesting that it likely is related to the $(\text{MoS}_4)^{2-}$ ion.¹⁸¹ No study of the $(\text{MoTe}_4)^{2-}$ ion has been conducted, however given the negligible differences in the UV-Vis spectra, we conclude that the fully tellurium saturated bonds are not present. However, the electrolyte is visually different, suggesting that some modification to the electrolyte did occur.

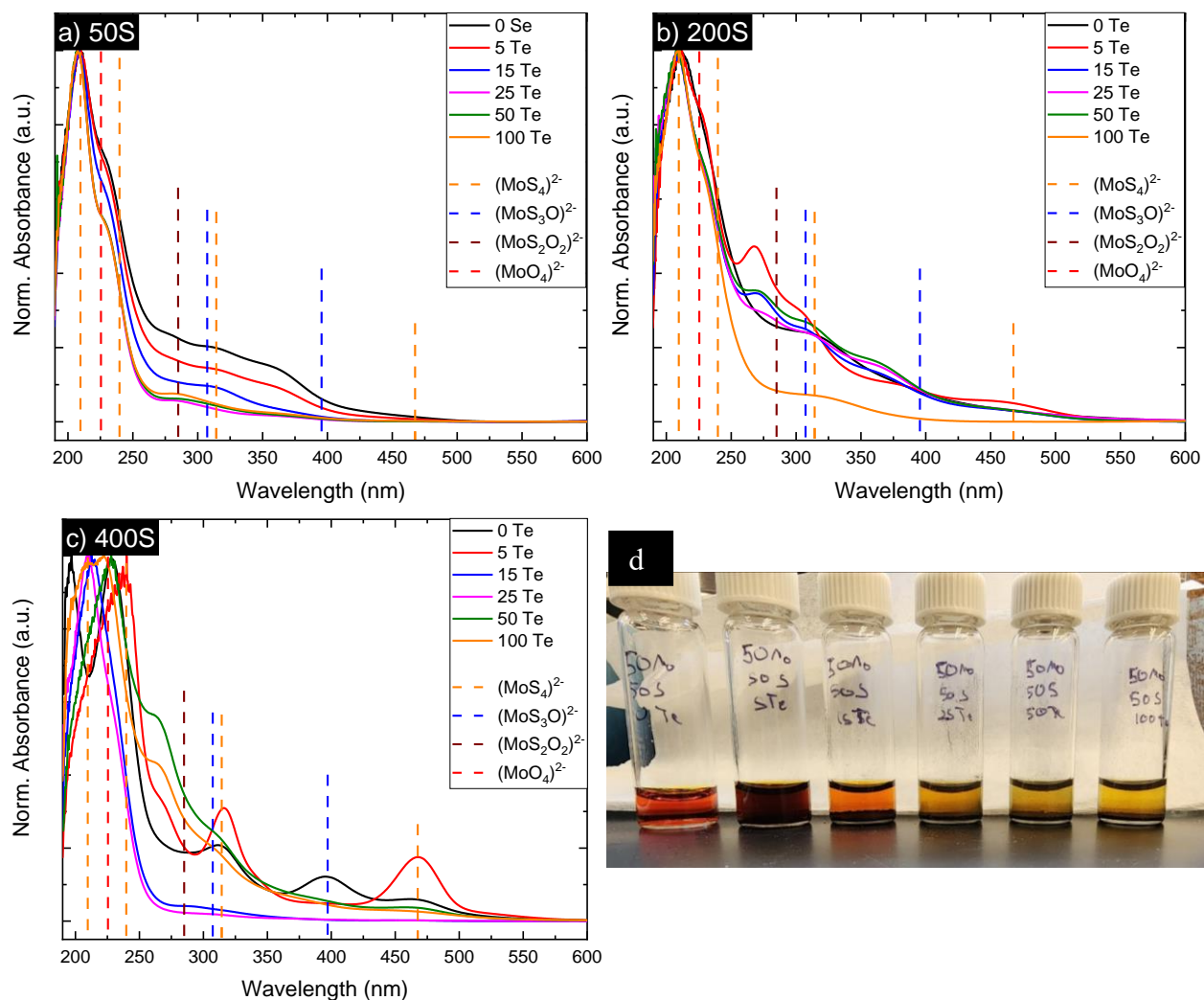


Figure 4.3.2: UV-Vis spectra of Te-MoS_x electrolyte: a) sample set with 50 mM Na₂S immediately after synthesis, b) sample set with 200 mM Na₂S immediately after synthesis, c) sample set with 400 mM Na₂S immediately after synthesis, and d) image of electrolytes

4.3.2.2 Electrodeposition of MoTe_y/MoS_x

The films were electrodeposited on (0001)-textured polycrystalline ruthenium (80 nm) sputtered onto a Si (100) wafer. The films were deposited under potentiostatic conditions at -1.7 V vs Hg/Hg₂SO₄ for 300 seconds on Ru unless noted otherwise. Several depositions were attempted at lower potentials to match the Se-MoS_x study, however no film was deposited when a potential less than -1.7 V vs Hg/Hg₂SO₄ was applied. The samples deposited on Ru were used in XPS, Raman, and electrochemical measurements.

4.3.3 Results

4.3.3.1 Chemical Properties

XPS was conducted on every sample to analyze the chemical states of Mo, S, and Te species. A representative spectrum can be seen in Figure 4.3.3 with the rest of the deconvoluted data shown in Figure 4.3.4, Figure 4.3.5, and Figure 4.3.6.

The XPS of the Mo 3d spectra were deconvoluted into binding energies of five doublets (3d_{5/2} and 3d_{3/2}) of Mo⁴⁺ (S or Te bonded), Mo*, Mo⁵⁺, and Mo⁶⁺ with singlets of the various S 2s states. As the oxidation number of Mo increases, the binding energies at which the respective doublets are found agree with previous literature.^{10,42,50,192-194} Mo⁴⁺-S is attributed to the chalcogen saturated Mo center within the polymeric chain of MoS_x, Mo⁵⁺ has been attributed to oxidation of the molybdenum-sulfide bonds, primarily terminal bonds as found in prior literature where Mo* has been attributed to an intermediate state of incomplete oxidation between Mo⁴⁺ and Mo⁵⁺.⁵⁰ Mo⁶⁺ has been attributed to the Mo center of MoO₃. Regarding Mo⁴⁺-Te, an asymmetric component needed to be included to successfully fit the data. If a Voigt function was used in place, the data could not be fit. This matches with the asymmetric feature found in the Te 3d_{5/2} where an asymmetric peak shape needed to be used. The deconvolution of the S 2p spectra consists of two primary features: (i) terminal S₂²⁻ ligands and (ii) bridging S₂²⁻ and apical S²⁻ ligands. The doublets

are summed together for ease of viewing. The Te $3d_{5/2}$ spectra can be fit with a single asymmetric peak, representing the Mo-Te bond, along with symmetric peaks associated with TeO_2 at ~ 575 eV and TeO_3 at ~ 576.2 eV. The asymmetric peak cannot be associated with elemental tellurium as that has a symmetric peak shape as shown in Figure 4.3.3d. Additionally, Raman data that will be shown later supports this finding. Semi-conducting 2H-MoTe₂ also has a symmetric peak shape whereas the semimetal 1T'-MoTe₂ has an asymmetric peak shape.²²⁷

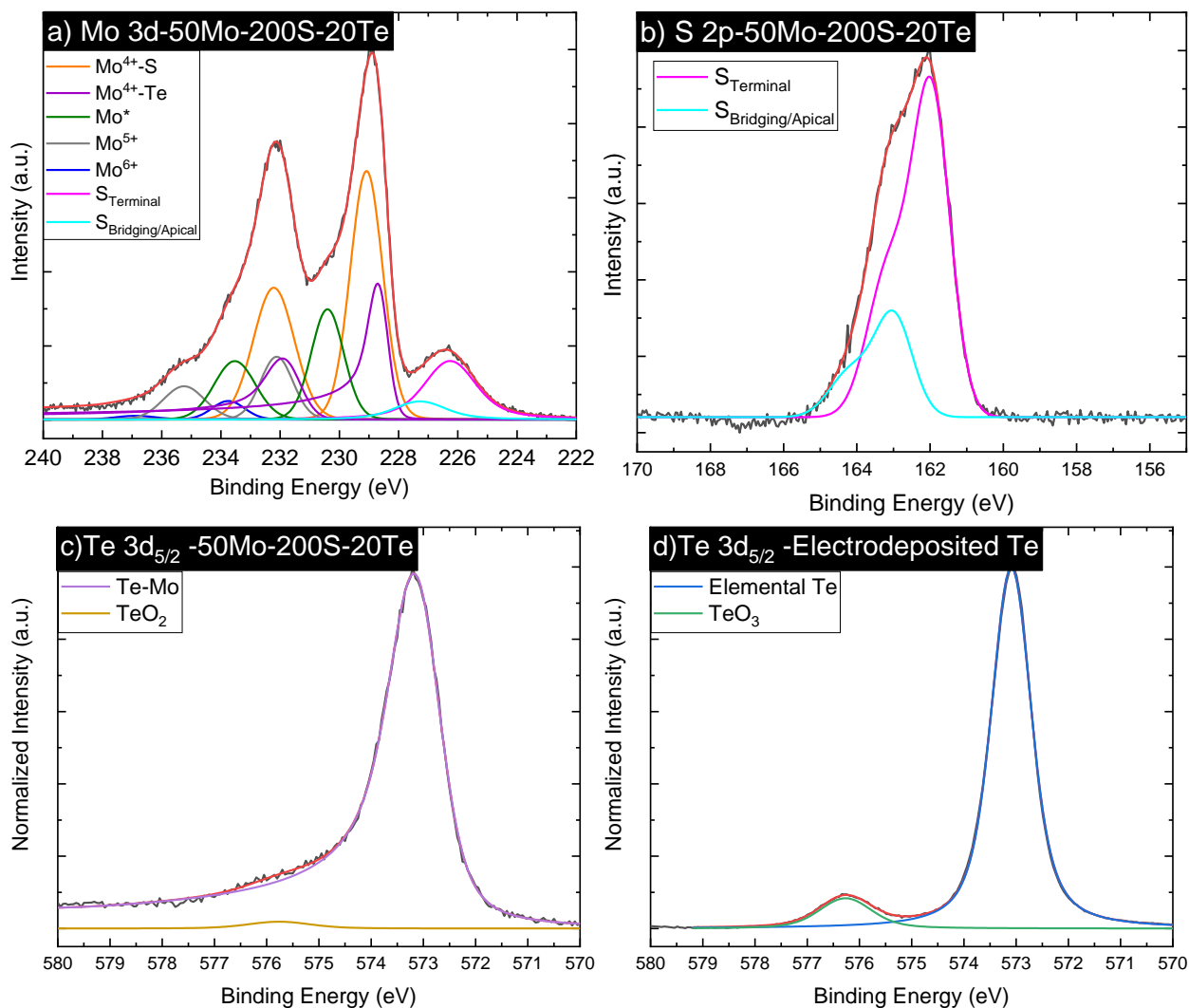


Figure 4.3.3: XPS of (a) the Mo 3d spectra, (b) the S 2p spectra, and (c) the Se 3d spectra of a representative sample that is free from oxide d) is a Te 3d_{5/2} spectra from an electrodeposited elemental Te sample

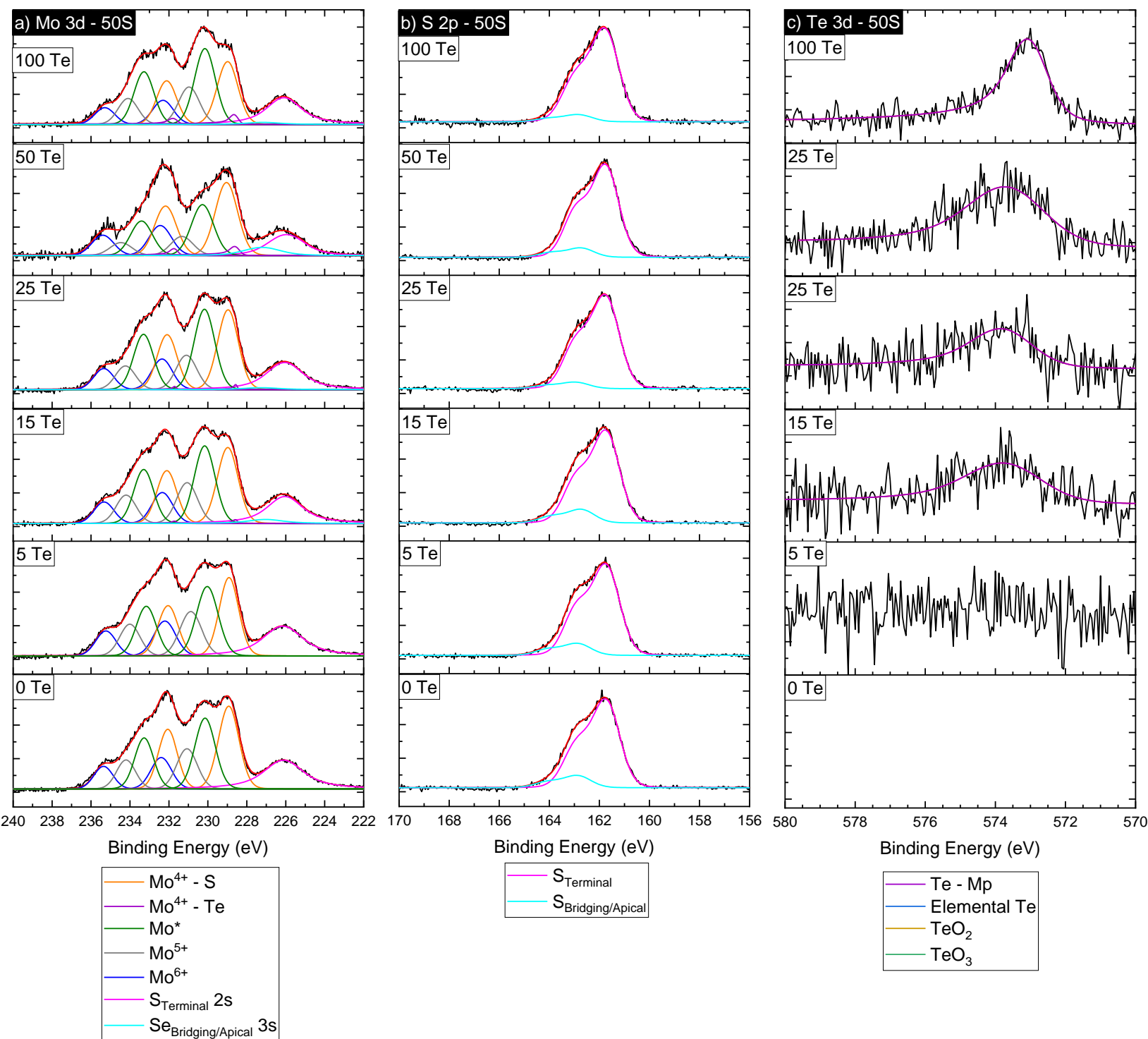


Figure 4.3.4: XPS of all samples within the 50S sample set, with a) Mo3d, b) S 2p, and c) Te 3d

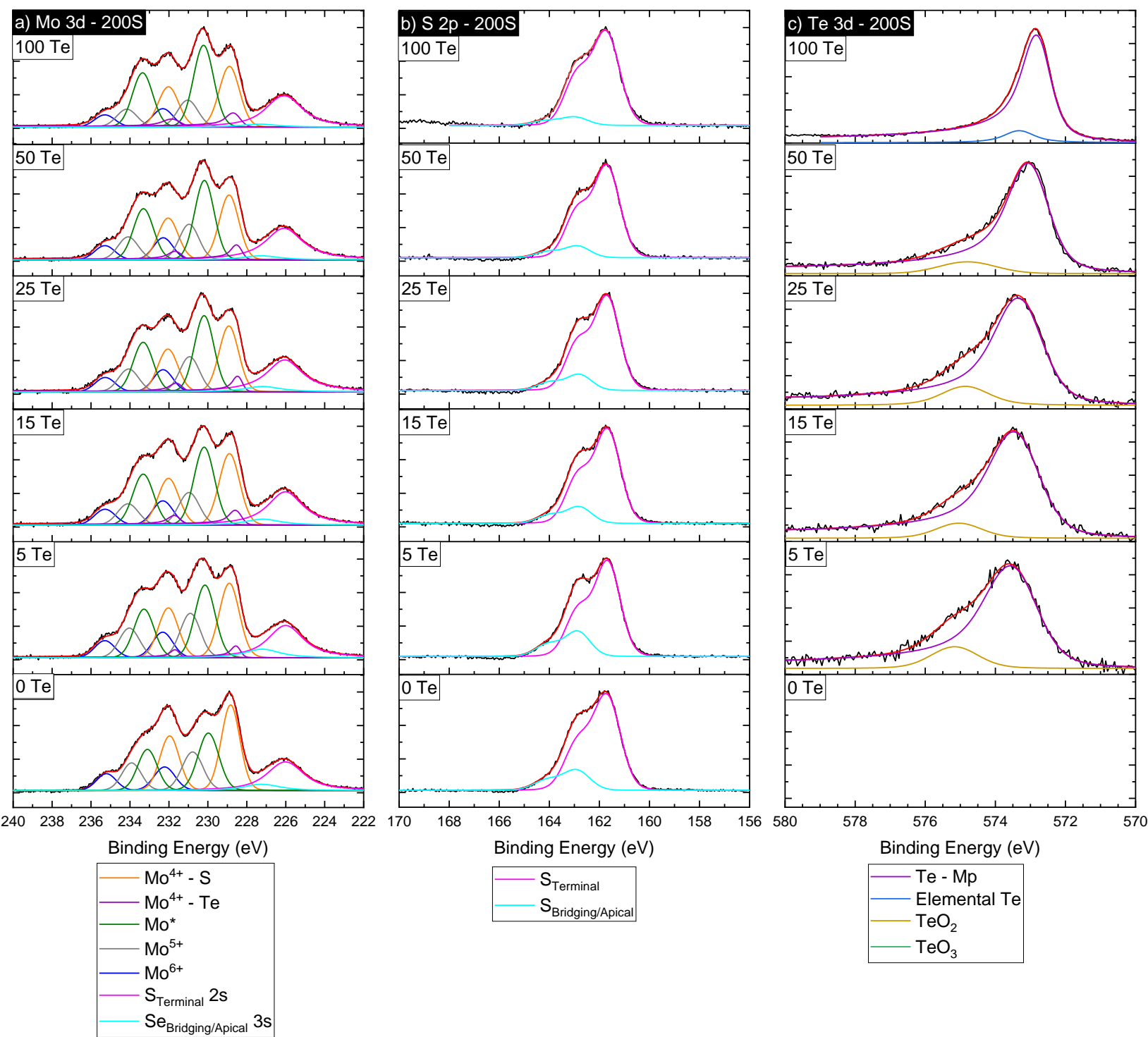


Figure 4.3.5: XPS of all samples within the 200S sample set, with a) Mo3d, b) S 2p, and c) Te 3d

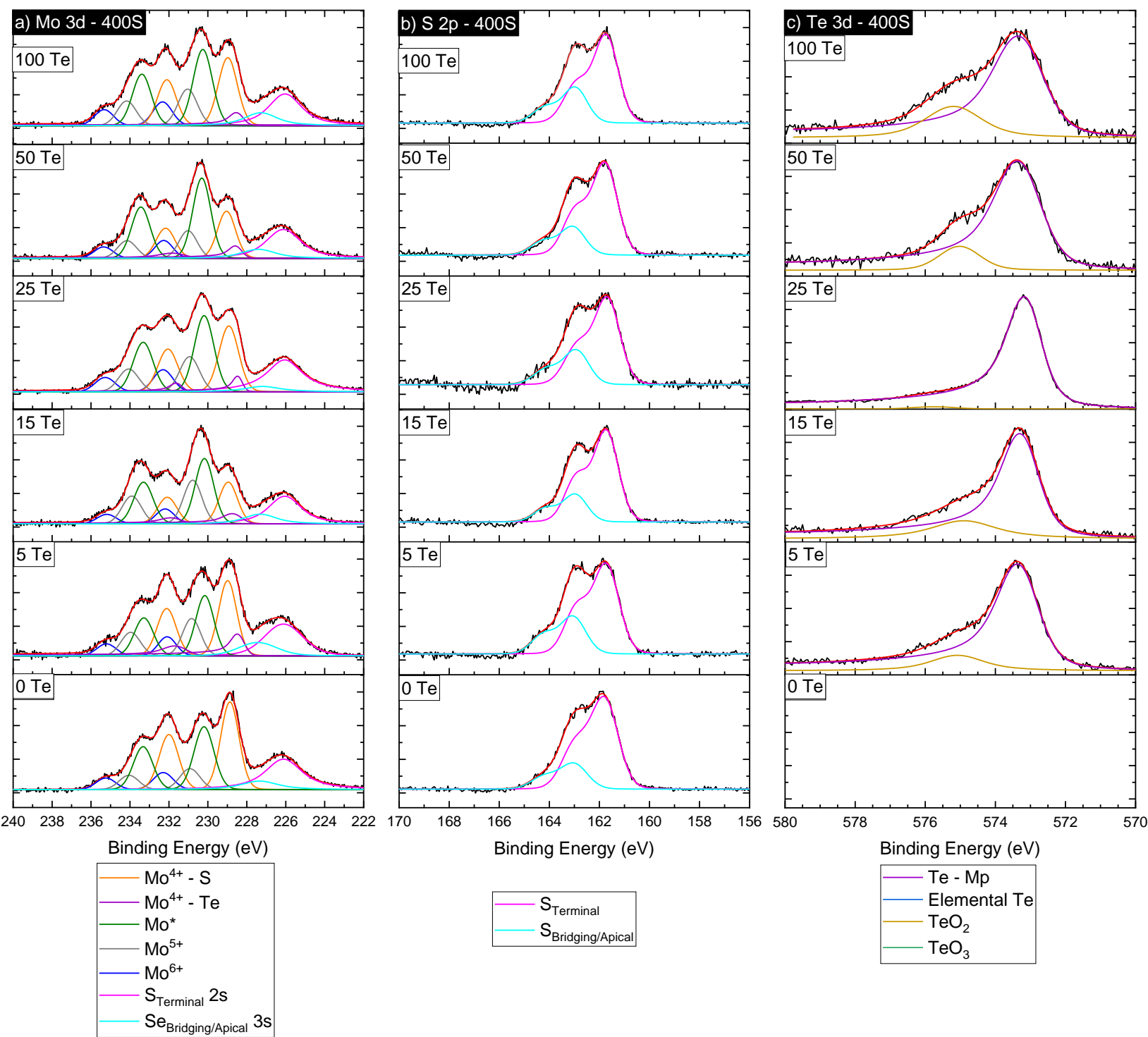


Figure 4.3.6: XPS of all samples within the 50S sample set, with a) Mo3d, b) S 2p, and c) Te 3d

Compared to the Selenium Chapter, Chapter 4.2, there was no XPS evidence that an alloy was formed. This was concluded as there was no Mo^{4+} peak shift towards lower binding energy which would be expected based on the difference in electronegativity between sulfur and tellurium. Additionally, the oxide free film, as shown in Figure 4.3.3b, could not be fit with solely symmetric peak shapes and needed an asymmetric feature to fit the data. Finally, there was no correlation between S_{terminal} or $S_{\text{bridging/apical}}$ concentrations when adding tellurium to the system. Overall, this suggests that a two phase was formed instead of an alloy and will be explored further later on in the chapter.

Using the XPS spectra, the overall ratio of Te to S ratio in the film can be obtained for the various samples and can be seen in Figure 4.3.7. These reported values are for only the sulfur or tellurium that are bonded to Mo and do not include any oxides. It can be seen that for the higher sulfur concentrations the addition of even a small amount of tellurium had an initial drastic change in tellurium concentration in the film. This is the opposite of what was shown in the selenium chapter where the low sulfur electrolyte was more sensitive to the addition of selenium. It should

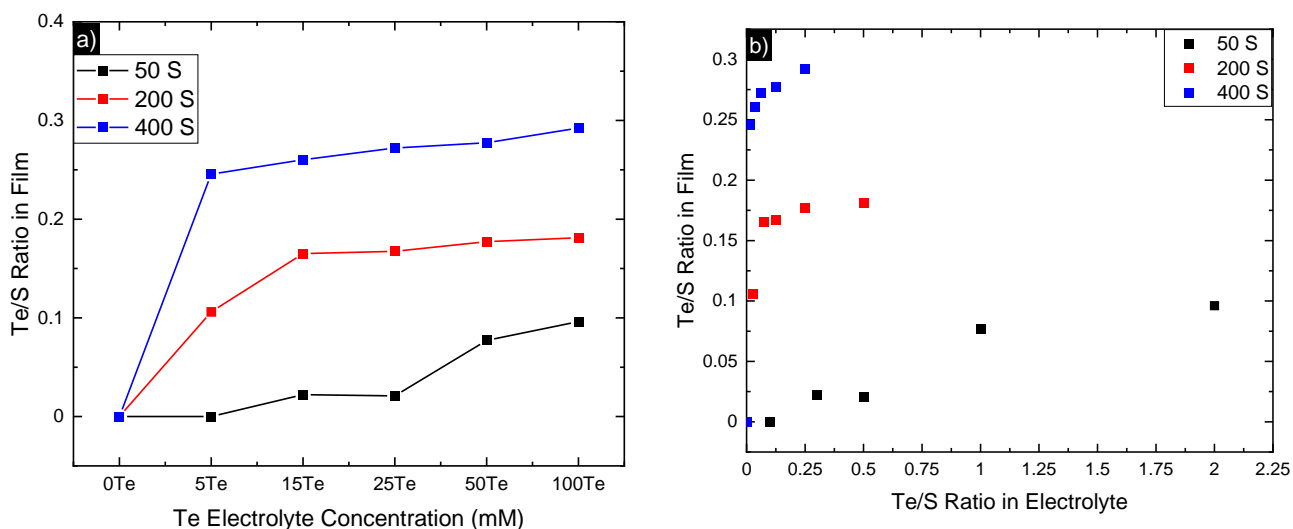


Figure 4.3.7: a) Te/S Ratio obtained via XPS for the various films as a function of tellurium precursor concentration and b) Te/S Ratio obtained via XPS for the various films as a function of Te/S in the electrolyte.

be noted that precipitation occurred after the electrolyte sat for some time, as shown in Figure 4.3.2d, and has a similar composition to that of the films, albeit with increased oxide present, according to XPS. This precipitation likely initiated during TeO_2 addition and could explain the plateau of tellurium incorporation in the film, although it was not nearly as apparent as the colloidal suspension from the Se chapter.

4.3.3.2 Structural Properties

Raman spectroscopy was used to investigate the structure of the various $\text{MoS}_x/\text{MoTe}_y$ electrocatalysts and can be seen in Figure 4.3.8. The Raman signatures of the base MoS_x material shows very similar Raman signatures to those reported for $[\text{Mo}_3\text{S}_{13}](\text{NH}_4)_2$ clusters.^{11,185} The molybdenum sulfide $\nu(\text{Mo-S})$ were found at 283-385 cm^{-1} and the $\nu(\text{Mo-S}_{\text{apical}})$ vibrations were observed in the 450-475 cm^{-1} region where the $\nu(\text{Mo-S-Mo})$ vibrations were observed around 425 cm^{-1} . The $\nu(\text{S-S})_{\text{terminal}}$ and $\nu(\text{S-S})_{\text{bridging}}$ were observed around 520 cm^{-1} and 550 cm^{-1} , respectively. Additionally, there is a peak around 195 cm^{-1} that has been recorded but not identified in previous

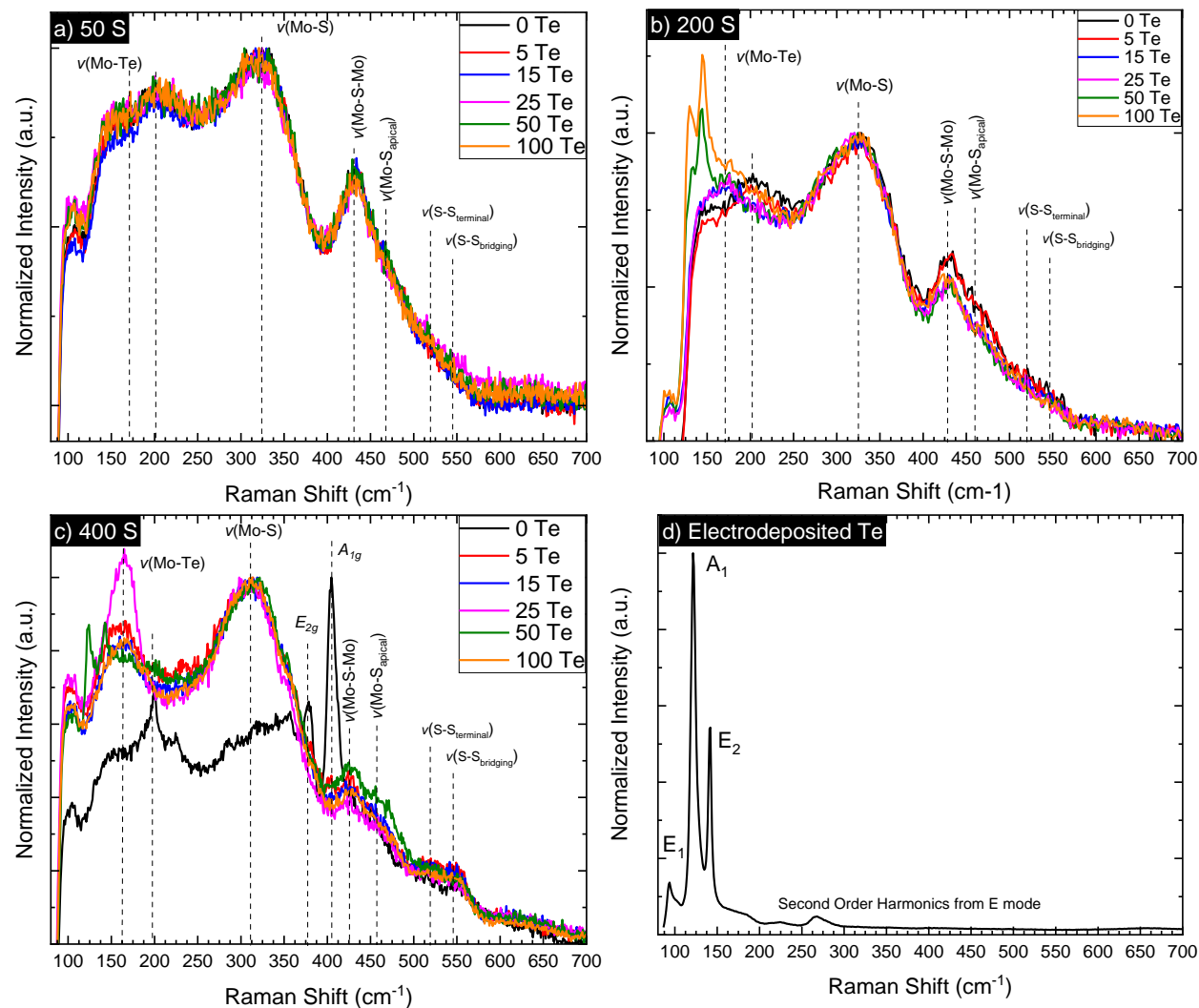


Figure 4.3.8: Raman of the various $\text{MoS}_x/\text{MoTe}_y$ electrocatalysts as a function of the Te precursor with a) 50S, b) 200S, and c) 400S sample sets. d) is a Raman spectra of electrodeposited Te

literature. This is more evident in the semi-crystallized sample of 400S-0Te but does not correlate to any peak found in crystalline MoS₂. Further compounding is the lack of reports that include wavenumbers down in this range. We are attributing the peak at 164 cm⁻¹ to a Mo-Te bond as it increases when the tellurium concentration in the film increases and matches the A_g peak found in MoTe₂ well.²²⁸ Also, this peak does not correlate to elemental, crystalline tellurium which is shown in Figure 4.3.8d. Some elemental Te is present in the Raman scans of high tellurium samples but does not dominate the spectra. We can likely rule out any possibility of amorphous tellurium as the crystallization temperature is reported to be around -10°C.²²⁹ Additionally, these samples were then annealed at 250°C for one hour and no crystalline elemental tellurium was noted, as seen in Figure 4.3.9.

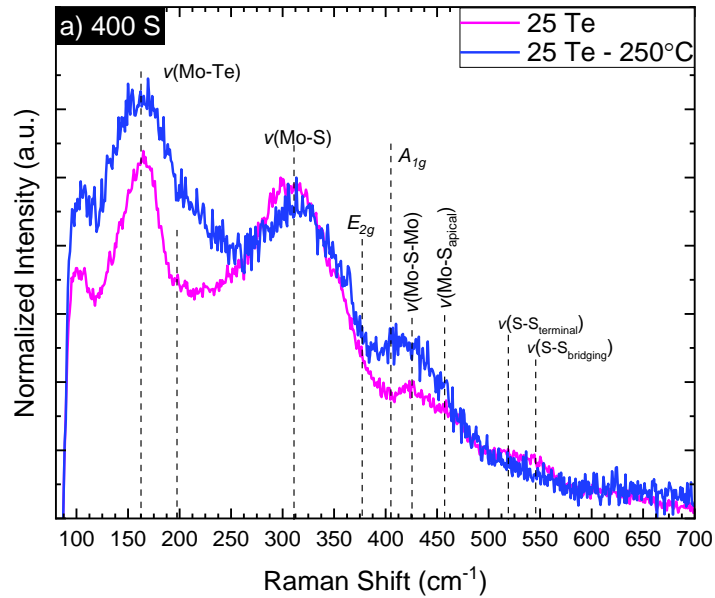


Figure 4.3.9: Raman spectra comparing samples before and after a low temperature, below MoS₂ crystallization, temperature.

While there weren't many changes within the Raman spectra, there were several things of note. In the 400S – 0Te sample, the Raman spectra indicated that the sample was partially crystalline, with the presence of both amorphous features as well as the A_{1g} and E_{2g} peak that is

associated with crystalline MoS₂. This is likely due to the higher potential that this film was deposited at, along with the higher saturation of sulfur ligands, causing crystallization. Overall, the Raman spectra associated with MoS_x did not change to any significant degree regardless of the Te concentration, unlike those samples with Se incorporated. This further supports that alloying was not successful and instead two separate phases were formed.

4.3.3.2 Electrocatalytic Properties

To examine the impact that the tellurium has on the catalytic performance for HER, polarization experiments were conducted and are shown in Figure 4.3.10. To compare the various catalysts, the overpotential to reach 10 mA/cm² (η_{10}) and the Tafel slope are recorded in Table 4.3.2. As can be seen across all sample sets, the addition of Te decreased the catalytic performance of the films and the film that had the best performance 400S – 0Te, had no Te added. This demonstrates that the MoS_x/MoTe_y film has degraded performance compared to only a MoS_x film regardless of the electrolyte or film composition. It is interesting to note that the base MoS_x samples deposited at -1.7 V_{MSE} performed considerably better than samples deposited at -1.55 V_{MSE} from Chapter 4.2. For example, the 200S MoS_x samples, deposited at -1.7 V_{MSE}, required only 152 mV to reach 10 mA/cm² whereas the 200S MoS_x sample, deposited at -1.55 V_{MSE}, required 190 mV to reach 10 mA/cm². Overall, this reduction in performance with the addition of MoTe_y can be explained by the simple fact that MoTe_y is less catalytically active, just as both 2H-MoTe₂ and 1T'-MoTe₂ are less catalytically active than 2H-MoS₂ and 1T-MoS₂.

Regarding the Tafel slope, there are two possible combinations for the overall mechanism, the Volmer-Tafel and the Volmer-Heyrovsky. If the adsorption of the hydrogen was the limiting step, a Tafel slope of 120 mV/dec would be anticipated. If the Tafel or Heyrovsky mechanisms are the limiting step, a Tafel slope of 30 or 40 mV/dec are expected, respectively. As such, the

majority of the samples follow the Volmer-Heyrovsky mechanism, consistent with previous reports of a-MoS_x-based materials. Elemental Te has a reported Tafel slope of ~120 mV/dec.²³⁰

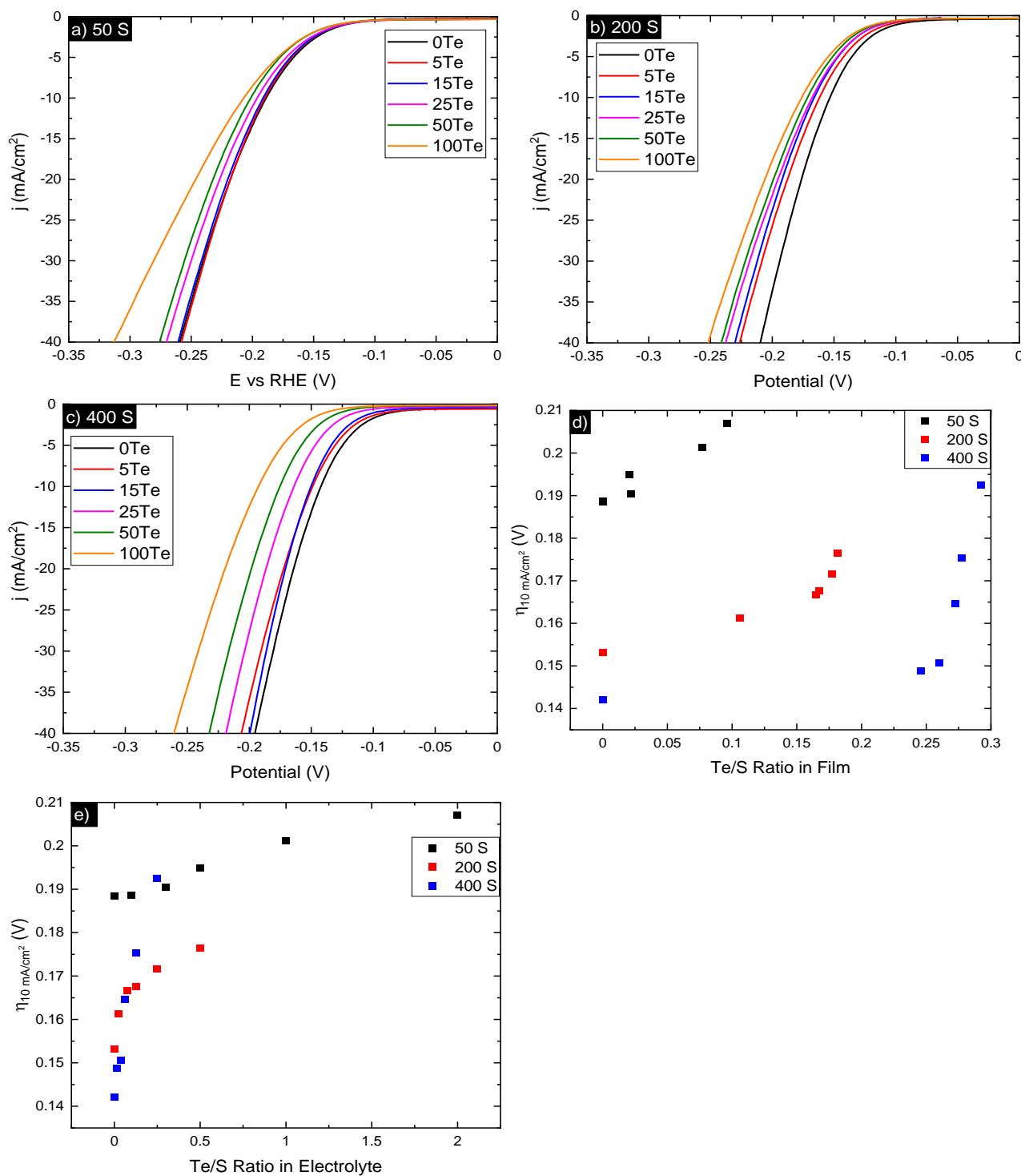


Figure 4.3.10: Polarization curves for the various samples sets, with a) 50 S, b) 200 S, and c) 400 S. In d) and e) the overpotential is plotted as a function of Te/S ratio in the Film and in the electrolyte, respectively.

Table 4.3.2 Electrochemical properties of the MoS_x/MoTe_y films

η₁₀ (mV) Tafel slope (mV/dec)	50mM Na ₂ S	200mM Na ₂ S	400mM Na ₂ S
0mM TeO ₂	189 mV 60 mV/dec	152 mV 56 mV/dec	142 mV 57 mV/dec
5mM TeO ₂	188 mV 58 mV/dec	161 mV 56 mV/dec	148 mV 55 mV/dec
15mM TeO ₂	190 mV 60 mV/dec	166 mV 52 mV/dec	150 mV 50 mV/dec
25mM TeO ₂	195 mV 61 mV/dec	167 mV 52 mV/dec	164 mV 49 mV/dec
50mM TeO ₂	201 mV 66 mV/dec	171 mV 54 mV/dec	175 mV 46 mV/dec
100mM TeO ₂	207 mV 67 mV/dec	177 mV 55 mV/dec	193 mV 49 mV/dec

The following section will be exploring potential reasons for the decrease in performance when MoTe_y is added to the system as well as why MoTe_y formed in the first place as opposed to an alloy like originally hypothesized.

To begin, there has been no study of amorphous MoTe_y and so there is no literature to compare directly against. As such, literature referencing the crystalline systems will be used to speculate the reason behind the formation of MoTe_y. One of the important parameters that can dictate the feasibility of the alloy in the mixing energy. In Figure 4.3.11a, the mixing enthalpy of MoS_{2(1-x)}Se_{2x} can be seen as calculated via DFT²³¹. This alloy is known to be miscible which was confirmed in Hemmat et. al's paper.²³¹⁻²³³ In Figure 4.3.11b, the free energy of mixing as well as the equilibrium phase diagram for MoS_{2(1-x)}Te_{2x} is shown as calculated via first principles.²³⁴ The phase diagrams shows a single stable region and a single unstable region with two metastable regions connected at the critical point, also known as the miscibility temperature. This phase diagram predicts that we would expect to be able to successfully alloy and has been proven experimentally.^{224,225,228} However, there are competing claims, as shown in Figure 4.3.11c, where

the mixing energies of both $\text{MoS}_{2(1-x)}\text{Se}_{2x}$ and $\text{MoS}_{2(1-x)}\text{Te}_{2x}$ are positive with $\text{MoS}_{2(1-x)}\text{Te}_{2x}$ having much greater energy.²³⁵ The authors noted that this large difference is likely due to the bond length ordering being that of $\text{Mo-Te} > \text{Mo-Se} > \text{Mo-S}$ and that the strain induced by the varying bonds increase the energy of mixing, necessitating that alloying takes place at a higher temperature. As such, depending on the basis for the computations, various authors achieved differing results for the crystalline system.

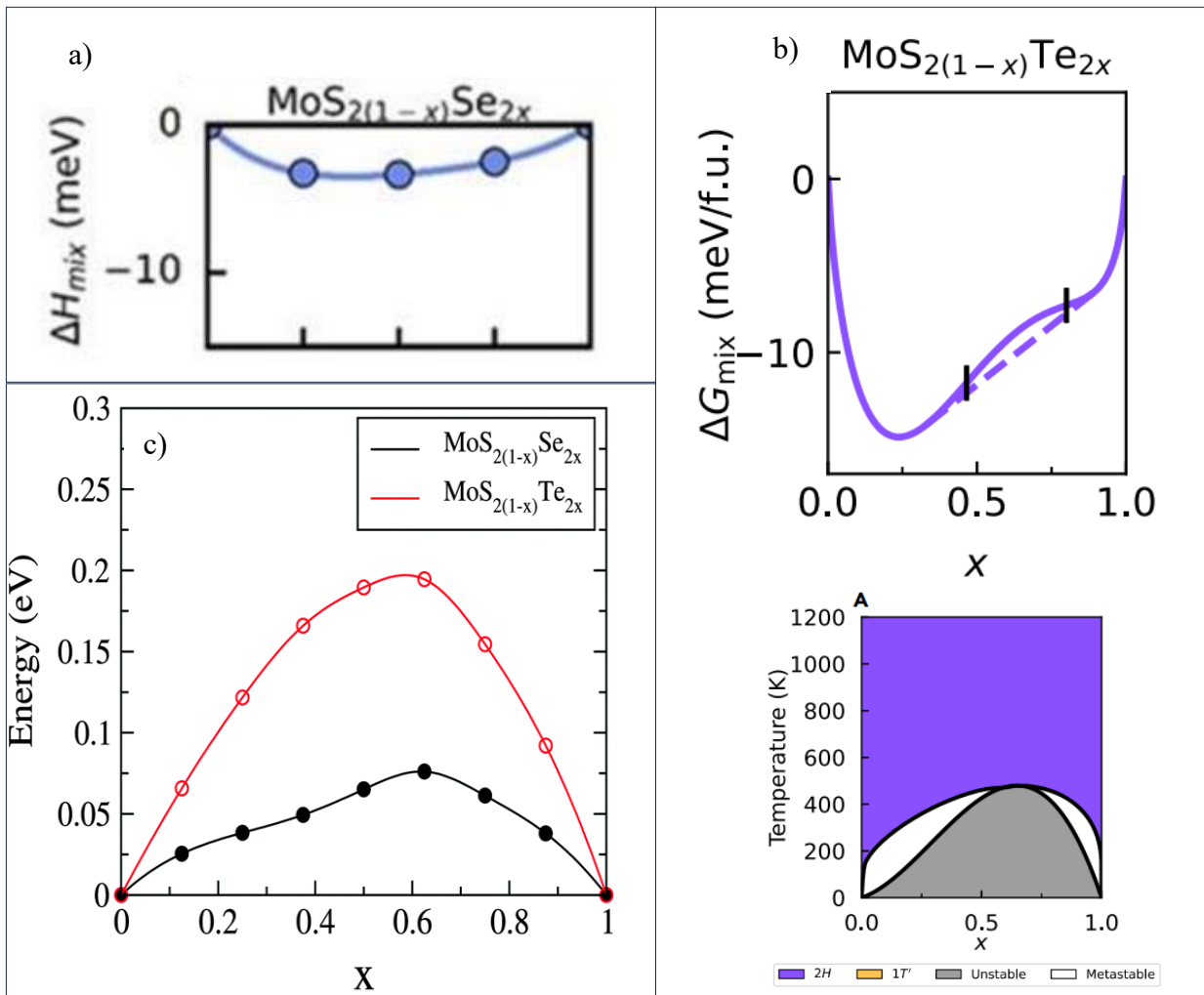
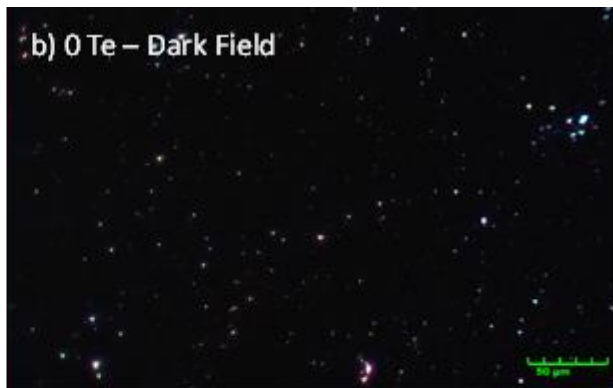
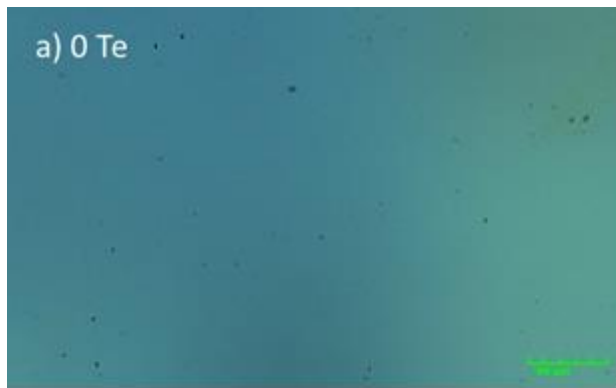


Figure 4.3.11: a) Mixing enthalpies of $\text{MoS}_{2(1-x)}\text{Se}_{2x}$ as a function of the relative concentration of the chalcogen²³¹, b) free energy of $\text{MoS}_{2(1-x)}\text{Te}_{2x}$ as a function of the relative concentration of the chalcogen and the equilibrium phase diagram, and c) Mixing energy of $\text{MoS}_{2(1-x)}\text{Se}_{2x}$ and $\text{MoS}_{2(1-x)}\text{Te}_{2x}$ vs the relative concentration of chalcogen atoms, x .



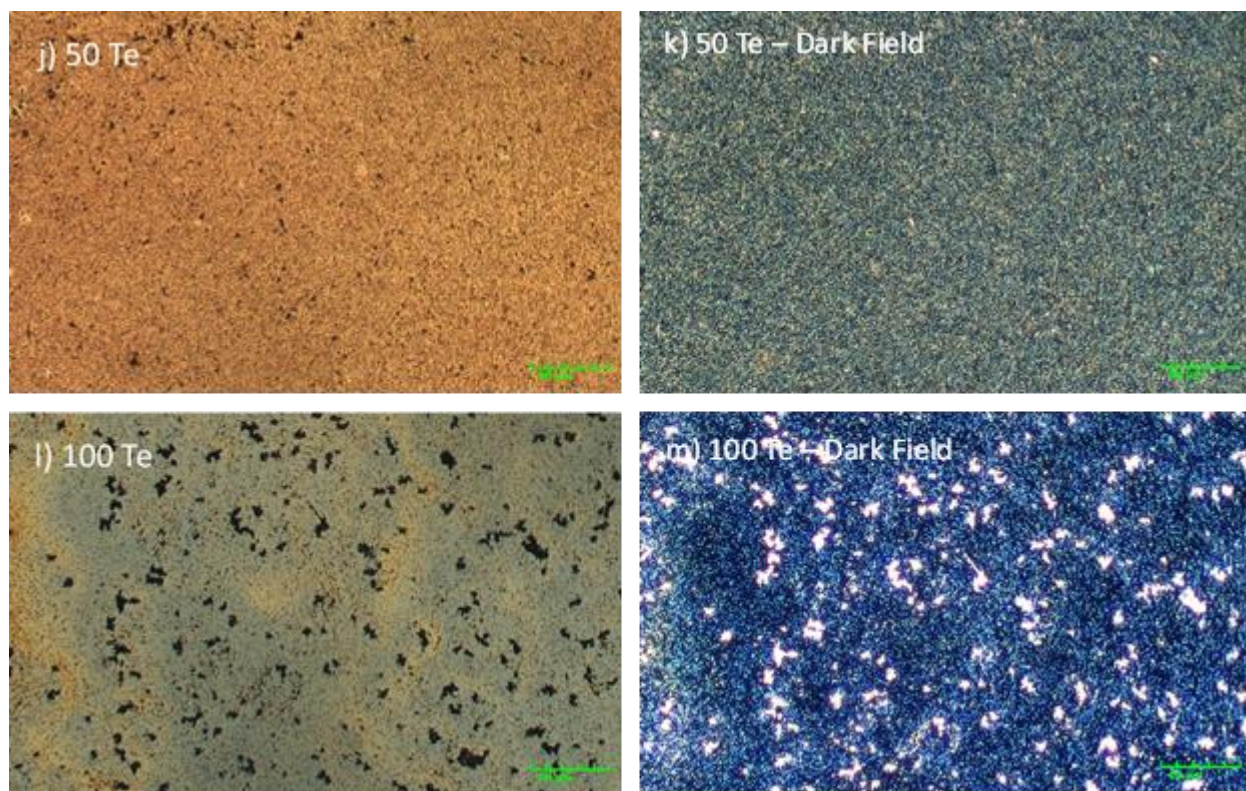


Figure 4.3.12: Optical Micrographs of the 400 S sample set as a function of Te. The left hand side images are shown in bright field mode where the images on the right hand side are shown in dark field mode

Additionally, there has been a recent study on the electrodeposition of MoTe_2 .²³⁶ While I disagree with a portion of their results, namely that they were unable to form MoTe_2 . This is based on the questionable interpretation of their XPS data, however, they did include an interesting EQCM study and speculated on the electrodeposition mechanism of MoTe_2 and indicated that there was a Te stripping effect to HTe^- prior to MoTe_2 deposition (again, speculative given their XPS results). If this is the case, this could potentially explain how MoS_x and MoTe_y were deposited seemingly independent of each other.

To further examine the film, confirm phase separation and help explain the loss in catalytic performance, SEM and optical microscopy were conducted on the samples from the 400S sample set. In Figure 4.3.12, the bright field and dark field images are shown. The sample with no tellurium

starts off very smooth and with very few visual defects. When just 5 mM of Te is added to the electrolyte, a drastic change in the film morphology occurs, with the 5 mM sample exhibiting rod-like structures. Moving up to through the rest of the samples, texturing increases until what looks like significant pitting occurs at 100 Te. This is identified by the dark field imaging, where light that is being scattered is collected by the microscope. So not only is the film's composition and structure changing, but the overall morphology is changing as well. Typically, an increase in texturing/increase in surface area would lead to an increase in catalytic activity due to the increase in total active sites. However, even with the increase in surface area of the 100 Te sample, the performance is markedly worse than the 0 Te sample.

SEM micrographs in backscattered mode is shown in Figure 4.3.13. Similar to the optical micrographs, the 0 Te sample is extremely smooth with virtually zero features (took significant time just to find something to focus on). When Te is added, the film exhibits a variety of features and is no longer smooth in nature. The 5 Te sample seen in Figure 4.3.13b has a scale-like appearance where the following samples again look textured in nature. These images were taken with the backscattered detector where the contrast mode is z-contrast, where the brighter parts of the image have a higher atomic number. As such, the bright spots found in the micrographs are likely the MoTe_y phase among the MoS_x phase. EDS was conducted to confirm this; however the interaction volume of the x-rays is significantly larger than the electrodeposited film as the Ru substrate could be seen, along with Si base substrate. As such, all the elements showed up mostly uniformly, with only slight differences in the bright spots, as shown in Figure 4.3.13g. This helps confirm that two separate phases and not an alloy were electrodeposited, confirming the XPS and Raman investigation.

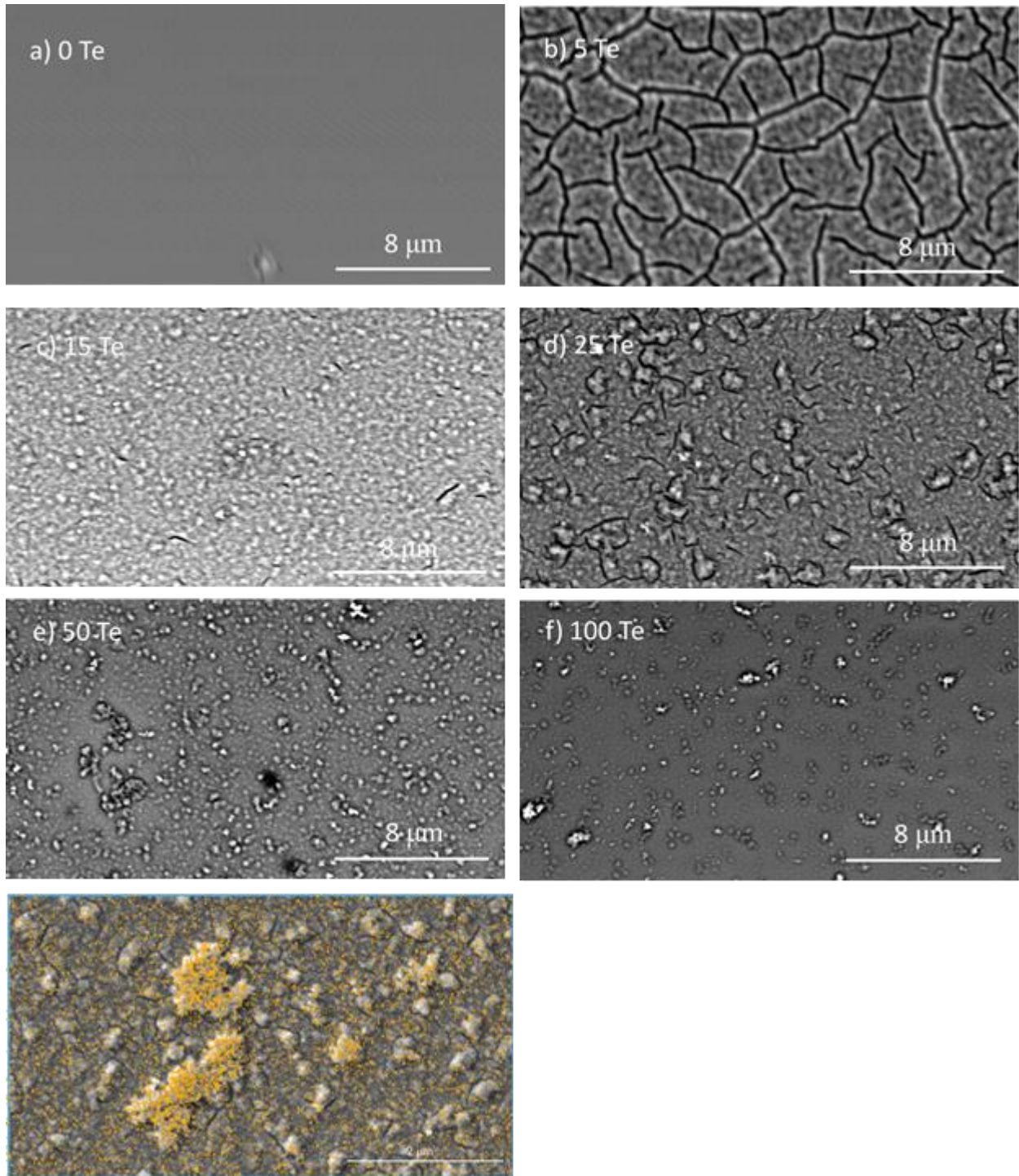


Figure 4.3.13: a-f) SEM BSD micrographs of the various films within the 400 S sample set and g) EDS of 50 Te where the orange color corresponds to Te

4.3.4 Conclusions

In summary, we have synthesized a series of $\text{MoS}_x/\text{MoTe}_y$ films across a variety of tellurium and sulfur precursor concentrations utilizing a potentiostatic electrodeposition technique. Characterization demonstrated that we were unsuccessful in synthesizing an amorphous tellurium incorporated MoS_x alloy, however a two-phase film was demonstrated, with the first report of amorphous MoTe_y . We were able to control the chemical composition, structure, and catalytic efficacy of the resulting film by tailoring the starting composition via electrolyte control. This study demonstrated that the inclusion of MoTe_y in the MoS_x matrix resulted in worse HER catalytic performance than just MoS_x across all compositions tested. However, it was noted that the increased potential that was used for this study did decrease the overpotential required across the board, improving the performance of the MoS_x samples. Overall, while this study was not able to increase the HER catalytic activity of MoS_x by alloying it with Te, a first of its kind study developed the synthesis of amorphous MoTe_y that was deposited in a matrix of MoS_x .

5.0 Future Works

5.1 Designing an Amorphous MoO₃/Se-MoS_x Catalyst for OER

5.1.1 Background and Motivation

As noted earlier, all sites on MoS₂ are catalytically inactive for OER.²³⁷ However, there has been some work that have shown promising results in heterostructure based materials that form a type II heterostructure, yielding more thermoneutral values and enabling resonant electron transfer.²³⁸ As a common strategy for increasing OER activity is to raise the level of the valence band maximum (VBM), a system that

achieves this will be investigated. As such, we are interested in the hybridization of MoS_x, and later Se-MoS_x, with MoO₃.

Within the crystalline system, it has been shown that MoS₂/MoO₃ heterostructures perform significantly better than either constituent for OER for a few reasons.²³⁹

Firstly, the CBM is successfully decreased because of the high-lying Se 4p-derived states that facilitate the adsorption of oxygen intermediates. Additionally, there is a decreased bandgap with an increased valence band minimum (VBM) because of

the Mo 4d – O 2p states.²³⁹ These results can be seen in Figure 5.1.1b and were experimentally validated via X-ray

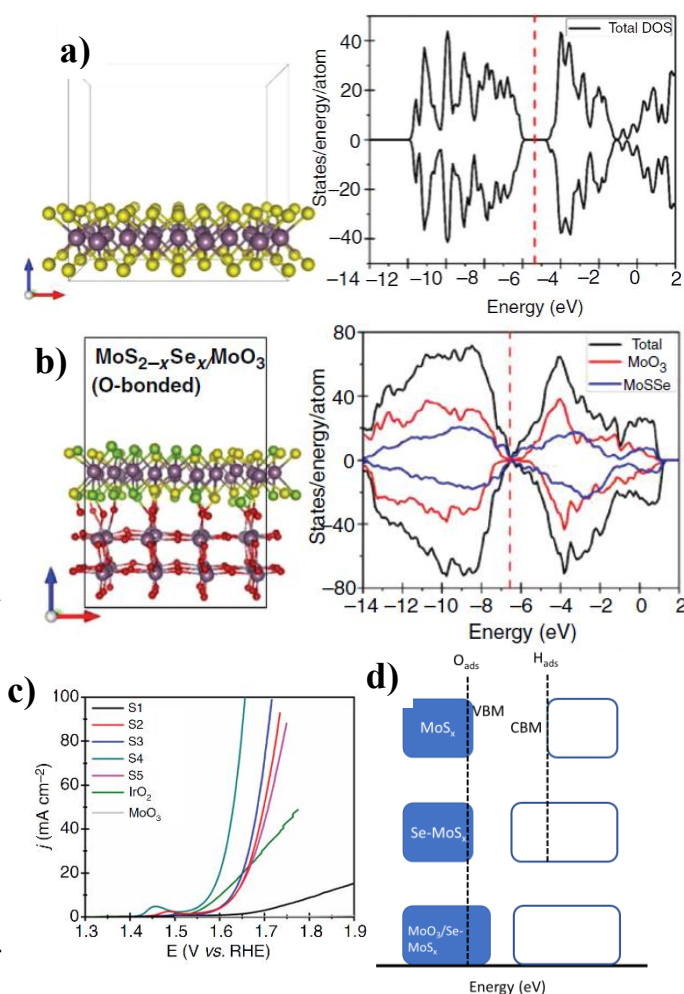


Figure 5.1.1: Supercell geometry and the corresponding DOS and PDOS for a) MoS₂ and b) MoS_{2-x}Se_x/MoO₃, c) polarization curves for crystalline MoS_{2-x}S_x/MoO₃, and d) modification of CBM and VBM via MoO₃/Se-MoS_x

absorption near edge spectroscopy (XANES). These electronic properties yielded significant improvements in the OER capabilities over both MoS₂ and MoO₃ as well as the canonical OER catalyst IrO₂ which can be seen as samples S2-S5 in Figure 5.1.1c. Other results have demonstrated that MoS₂ can facilitate OER more effectively through the oxidation of the sulfur edges which naturally occurs within oxidative conditions.²⁴⁰ However, these results are for only the crystalline system and the following proposed work aims to expand them to the amorphous system.

5.1.2 Research Methodology

To accomplish this, this would expand upon both the oxygen and selenium incorporation into MoS_x by using electrodeposition and post treatment to modify the catalyst. This would control the oxygen and selenium content in order to determine the effect each has on the OER activity. To control the oxygen content, several post-deposition techniques would be used immediately following deposition. The as deposited sample will act as a baseline. In order to decrease the oxygen content, we would employ a low temperature anneal (as to remain amorphous) to remove oxygen, as demonstrated in our previous study, Chapter 4.1.⁵⁰ We would control the amount of removed oxygen by

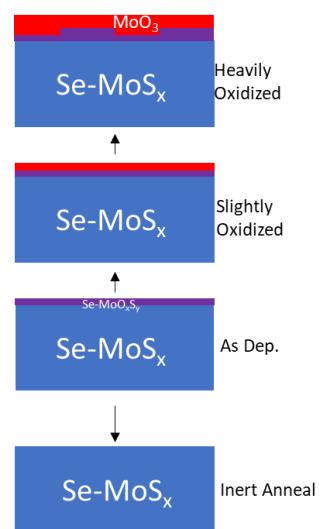


Figure 5.1.2: Simplified schematic of MoO₃/Se-MoS_x Heterostructure

changing the annealing time. To increase the oxygen content, one can simply leave the sample exposed to atmosphere and after roughly 30 minutes the surface is significantly oxidized (as determined via XPS) and after roughly 2.5 hours the entire sample reaches saturation of oxide (as determined by Raman). However, to better control the oxidation process to increase repeatability, reduce variation, and be able to push past that oxygen saturation limit, this work would use a UV-Ozone treatment as it is a well-established method for oxidizing TMDCs.^{241,242} By applying varying times of UV-Ozone treatment, we could systematically study the impact that the MoO₃

content has on the OER activity of MoO₃/Se-MoS_x. This can be seen in Figure 5.1.1 where it can heavily oxidize the sample via UV-Ozone as well as precisely control the oxide thickness, represented by slightly oxidized. The oxysulfide present is due to the rapid oxidation of the very top surface of the material, resulting in the presence of MoO₃ but also that of substitutional oxygen, essentially acting as an interlayer. The amount of Se present in the films can be controlled by applying what knowledge from the Se-MoS_x chapter, Chapter 4.2, to this study. The concentration of both Se and oxygen and their impact on OER activity would be characterized via the techniques outlined in the Experimental Chapter. In summary, this will identify the optimal material for OER as well as elucidating any underlying mechanisms by modifying the oxide and selenium content.

5.1.3 Preliminary Data

We have demonstrated the viability of using UV-Ozone to modulate the thickness of the MoO₃ layer. This was demonstrated by exposing the As-Deposited samples to UV-Ozone immediately after synthesis for 30 seconds and 120 seconds. They were then immediately transferred to the XPS where Angle Resolved XPS (ARXPS) was conducted. As shown in Figure 5.1.3, there is a significant difference in the Mo⁶⁺ feature which is assigned to MoO₃. This is qualitatively shown by the arrow which points to an isolated Mo⁶⁺ peak (the Mo 3d_{3/2}). When the sample is oriented at 35°, the most surface sensitive of the data collected, there is a significant difference when comparing the 30 second UV-Ozone treatment to the 120 second treatment. This demonstrates the viability of utilizing UV-Ozone to control the thickness and amount of the MoO₃ overlayer.

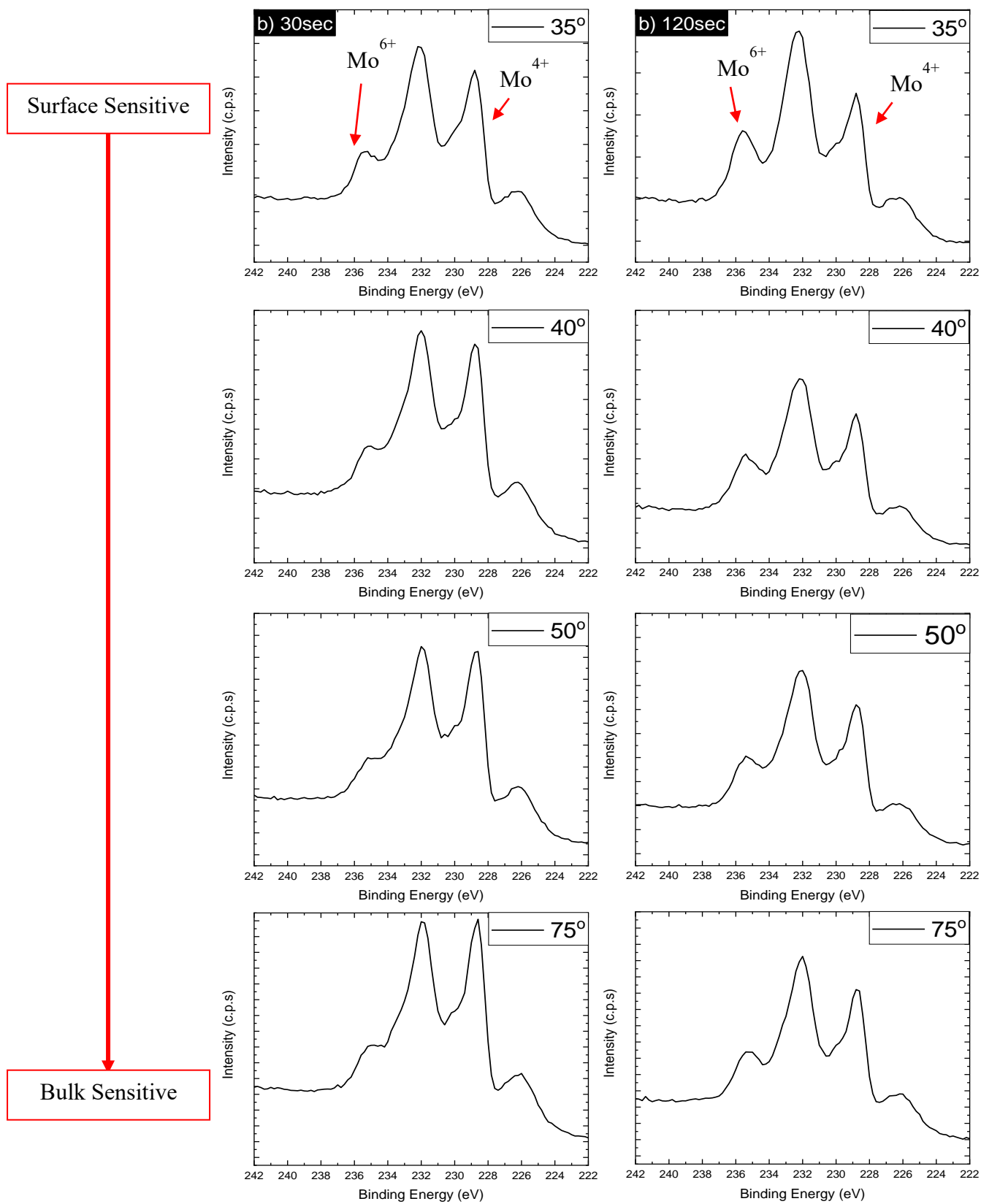


Figure 5.1.3 XPS spectra at varying angles for UV-Ozoned samples for a)30 secs and b)120 sec

5.1.4 Summary

Overall, this section of the future work aims to take advantage of the change in electronic structure caused by the heterostructure formed between MoO_3 and Se-MoS_x . This heterostructure combination brings up the VBM which facilitates the adsorption and reaction of oxygen intermediates, the traditional rate-limiting step of OER. To synthesize the $\text{MoO}_3/\text{Se-MoS}_x$, electrodeposition will be used, followed by either inert annealing to remove oxygen or UV-Ozone to increase the oxygen content. Preliminary work has demonstrated the selective removal of oxygen while maintaining the same structure, shown in Chapter 4.1, and that the oxide overlayer can be controlled and added upon via UV-Ozone treatments. Overall, this future work proposes $\text{MoO}_3/\text{Se-MoS}_x$ heterostructures with varying amounts of selenium and oxygen content in order to determine their respective impacts on the OER catalytic properties of $\text{MoO}_3/\text{Se-MoS}_x$.

5.2 Growth of $\text{MoS}_{2x}\text{Se}_{2(1-x)}$

5.2.1 Background and Motivation

This future work would build off the electrodeposition of the amorphous Se-MoS_x that was demonstrated in this work by crystallizing the material into $\text{MoS}_{2x}\text{Se}_{2(1-x)}$. $\text{MoS}_{2x}\text{Se}_{2(1-x)}$ would allow for the mixing of properties of MoS_2 and MoSe_2 with a tunable band gap by alloy composition. Alloying semiconductors with different bandgaps has been widely used in the bandgap engineering of bulk semiconductors for some time. For nanoelectronics and nanophotonics, it is very important to obtain semiconductors with continuously tuned bandgaps.²⁴³⁻²⁴⁵

$\text{MoS}_{2x}\text{Se}_{2(1-x)}$ has been successfully synthesized previously, however many of the techniques require either suitable, crystallographic substrates, high temperatures, toxic gasses like H_2Se and H_2S , and limited deposition areas.^{246,247} Additionally, many of these synthesized materials form in nanoflakes that do not provide uniform coverage. However, with

electrodeposition, one could achieve very similar results of successfully alloying $\text{Mo}_{2x}\text{Se}_{2(1-x)}$ using the same electrodeposition technique as described in Chapter 4.2 which is followed by a low temperature anneal of $\sim 350^\circ\text{C}$ (significantly lower than the 820°C that was used in CVD studies). This would allow for a much wider substrate choice without the need for transferring of the $\text{MoS}_{2x}\text{Se}_{2(1-x)}$ with the only requirements now being that the substrate must be non-insulative and it must be able to be annealed at 350°C . This allows a much broader range of substrates, even flexible polymers, to enable flexible electronics. Additionally, electrodeposition provide a nice, uniform deposition surface, even at low deposition times.⁵¹

5.2.2 Research Methodologies

As mentioned above, this would use the same electrolyte conditions as described in Chapter 4.2. However, to allow for more compatibility for structures as well as aiding in the shrinking of devices, extremely short electrodeposition times (~ 0.5 -5 seconds) would be used. This would allow for nanometer thick films that then would be annealed to crystallize to form $\text{MoS}_{2x}\text{Se}_{2(1-x)}$. Additionally, electrodeposition enables large areas to be uniformly covered, or if desired, be selectively patterned and only depositing where it is desired. With this, device structures could be built using electrodeposition.^{248,249} Through this, a variety of structures could be built on most substrates of choice to enable the device of choosing.

5.2.3 Preliminary Data

I deposited films that were similar in composition to those found in Chapter 4.2, with a base of 200 mM Na_2S and 50 mM Na_2MoO_4 . The SeO_2 concentration was varied, with concentrations of 0 mM, 15 mM, 100 mM, and 200 mM, to determine the impact of the various Se concentrations. Raman spectra of $\text{MoS}_{2x}\text{Se}_{2(1-x)}$ are shown in Figure 5.2.1, with Figure 5.2.1a being from literature and Figure 5.2.1b being from this preliminary work. As can be seen, they match quite well. It is important to note that in both figures there is the broadening of MoS_2 features

while Se increases, indicating that an alloy was formed and not just two separate phases. Further compositions and electrolyte chemistries would need exploring to fully understand and control this process. Additional work has been done on electrodeposited MoS_2 with XRR and depth calculations with XPS to demonstrate that nanometer thick films could successfully be deposited, but to what extent this could be controlled and while visually and theoretically it is uniform, a more detailed study would be required.

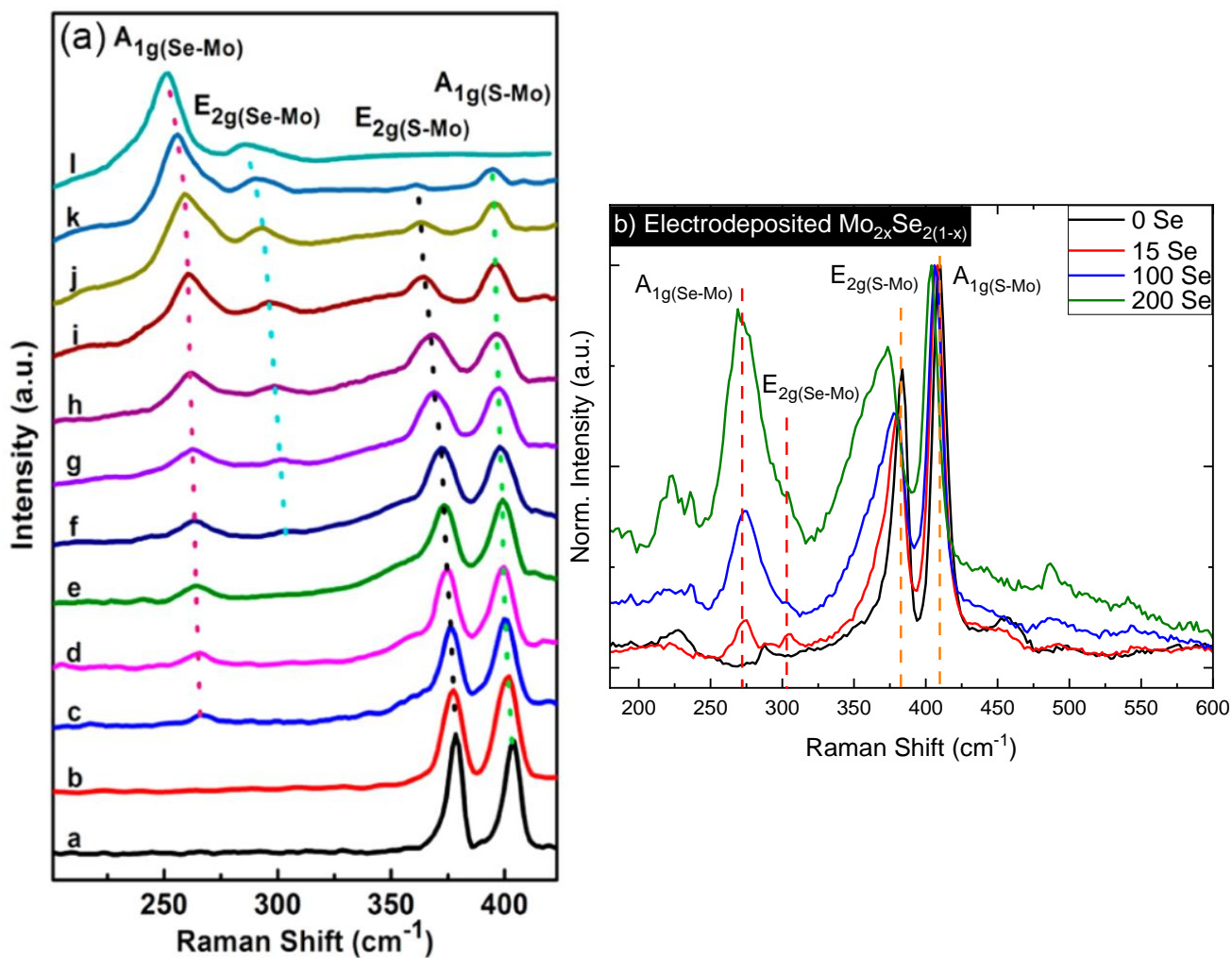


Figure 5.2.1: Raman spectra of $\text{MoS}_{2x}\text{Se}_{2(1-x)}$ synthesized via a) Chemical Vapor Deposition where the bottom spectra is pure MoS_2 and the top spectra is pure MoSe_2 ²⁴⁷ and b) electrodeposition and annealing (this preliminary work)

5.2.4 Summary

In summary, electrodeposition followed by a low-temperature anneal would be used to synthesize $\text{MoS}_{2x}\text{Se}_{2(1-x)}$. This would enable $\text{MoS}_{2x}\text{Se}_{2(1-x)}$ to be more readily integrated with a large variety of substrates by reducing the requirements drastically. By achieving this, many applications that require the ability to tune electronic structure by alloying could be enabled, including devices such as flexible electronics. By coupling this with photoresist patterning, complex designs could be achieved in a rapid, scalable fashion.

6.0 Thesis Conclusions

This thesis reports on the use of hydrothermal, electrodeposition, and post-growth treatments to synthesize a variety of crystalline MoS₂-based heterostructure and amorphous MoS_x-based alloys and two-phase matrixes. All but one material group was found to increase the electrocatalytic activity towards HER over the base material, and even the *unsuccessful* attempt yielded a material that has not been synthesized previously.

Chapter 3.1 presented ZnO-MoS₂ and ZnO-Zn-/MoS₂ nanowire heterostructures synthesized via hydrothermal methods for the ZnO nanowire growth, electrodeposition for the MoS_x coating, and annealing to crystallize the material. What was elucidated was the various type-I and type-II heterojunctions, along with the increase in surface area, provided an increase in catalytic activity over the base materials. Both the ZnO-MoS₂ and ZnO-ZnS-MoS₂ saw a marked improvement in acidic conditions, with the ZnO-ZnS-MoS₂ heterostructure also providing an improvement in alkaline conditions. Additionally, the 1T-MoS₂ phase was also noted in the ZnO-MoS₂ heterojunction. Overall, the synthesized nanowire heterostructures were found to be highly performing and gives insight into how the changing band alignment and morphology can play a significant role in increasing the catalytic performance towards HER.

Chapter 3.2 presented the results of the electrodeposition and annealing to form catalytically active, crystalline CoS_x/MoS₂ structures. The catalysts were extremely active in acidic conditions and even more so within alkaline conditions. The synergistic properties between Co and Mo sulfides, attributed strongly to their active linking disulfides, facilitated the adsorption and desorption of hydrogen along the interfaces of the electrode/electrolyte and nano-interfaces between the c-CoS_x and MoS₂. We noted some unusual morphologies that formed that have not

been reported in the system before and could have contributed to the increase in catalytic activity. This work has been reported in the Journal of The Electrochemical Society (10.1149/1945-7111/acc9e0)

Chapter 4.1 laid the foundation for the work done on amorphous MoS_x . It was among the first work that I undertook as a graduate student and gaining an understanding of the system was pivotal through the rest of the Section 4 chapters. Overall, this study established the importance of the detrimental state of Mo^{6+} , an insulative oxide, and the importance of Mo^{5+} , a chemical state from oxygen dopants, towards the HER catalytic activity of this material. This study also highlighted the catalytic differences between bridging and terminal sulfur bonds and contributed to an ongoing discussion within the literature regarding these features. Lastly, this work noted an unreported chemical state of Mo^* , one that we attributed to partially oxidized sulfur ligands, that seemed to be loosely correlated with the electrocatalytic activity of the material. This work was published in ACS Applied Energy Materials (<https://doi.org/10.1021/acsaem.1c02234>)

Chapter 4.2 built upon the work in Chapter 4.1 by adding selenium to the electrolyte in order to form an amorphous molybdenum sulfoselenide alloy. We investigated this by using a matrix of selenium and sulfur concentrations in order to determine the optimal sulfur to selenium electrolyte ratio for the film's performance. Our results demonstrated that we could control the films composition, structure, electronic properties, and catalytic properties by simply tuning the electrolyte. By substituting some of the sulfur bridging and terminal ligands with selenium, we demonstrated an increase in catalytic efficacy. We also tied this chemistry to other properties, such as the conduction band minimum, and related that back to the catalytic performance of the films, with several compositions exhibiting greater catalytic properties than the non-selenium alloyed material.

Chapter 4.3 attempted to yield similar results as Chapter 4.2 but with tellurium instead of selenium. However, instead of forming a uniform alloy as in Chapter 4.2, a two-phase matrix of MoS_x and MoTe_y was formed. This was the first report of amorphous- MoTe_y in literature. However, the presence of the MoTe_y phase decreased the catalytic performance across the board, regardless of the preparation. Additionally, this study noted that the increased potential required for deposition yielded a better starting MoS_x material than previously studied, which goes against conventional wisdom of lower potential generally being better for the electrodeposition of films. Overall, this study wasn't able to increase the catalytic performance of MoS_x by alloying it with Te, but it did provide a first of its kind synthesis of the amorphous MoTe_y phase.

7.0 Appendix

7.1 Attempt at Synthesizing Free-standing MoS₂ nanowires

In attempts to form free-standing MoS₂ nanowires, a chemical etch was used to attack the underlying ZnO scaffold. This was attempted via the use of HCl, an acid that ZnO dissolves readily in given its amphoteric nature. We attempted a couple of different concentrations for varying time and the resulting morphology can be seen in Figure 7.1.1. As can be seen in Figure 7.1.1, the nanowire morphology was maintained. However, upon further Raman and Energy Dispersive Spectroscopy (EDS), we found there was still some presence of Zn species. However, due to the penetration depth of both EDS and the 3D nature's impact on Raman, it is difficult to ascertain which part of the sample that the signal is coming from. One possible theory is that the Zn species signal is coming from the base of the nanowire as well as any that is left-over from coating the carbon paper strands during the first process.

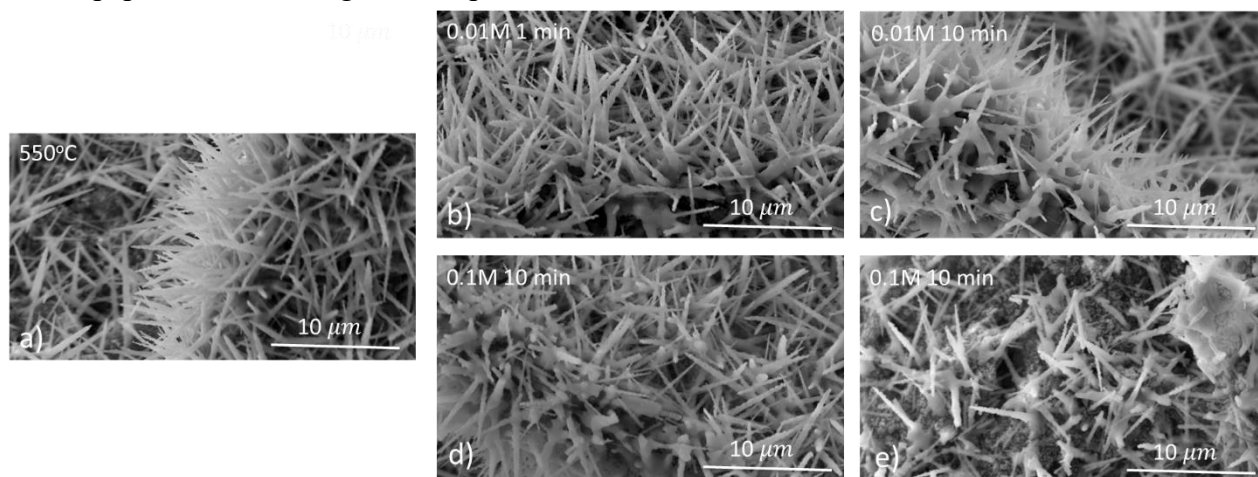


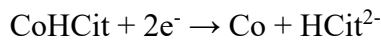
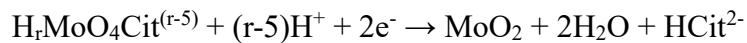
Figure 7.1.1: SEM images of a) un-etched NWs, b) 0.01 M for 1 minute, c) 0.01 M for 10 minutes, d) 0.1 M for 1 minute, and e) 0.1 M for 10 minutes

We also conducted electrochemical experiments to provide motivation for continuing this approach with the possibility of having several nanowires investigated with transmission electron microscopy, but with worse performance and lack of concrete evidence that this method would

yield freestanding MoS₂ nanowires, there was not suitable motivation for these additional investigations.

7.2 Attempt at Synthesizing c/CoS_x/MoS₂ via sulfurization of metal Electrodeposition

To prepare the electrolyte, a mixture of Cobalt Sulfate (CoSO₄), Trisodium Citrate (Na₃C₆H₅O₇), Potassium Pyrophosphate (K₄P₂O₇), Sodium Sulfate (Na₂SO₄), and Sodium Molybdate (Na₂MoO₄) was used. The pH was adjusted to 4 by adding H₂SO₄. This recipe was based on Zhou, Krohn, Podlaha, and namely Kublanovsky's respective works on the electrodeposition of Cobalt-Molybdenum alloys.^{144,250–252} The main role of Na₂SO₄ is to act as a source of dissolved ions to increase the conductivity of the electrolyte.²⁵³ Potassium Pyrophosphate was included to form the soluble complex Co₉(P₂O₇)₅²⁻ and to prevent the formation of insoluble complexes. There have also been some indication that molybdenum may also form a complex with the pyrophosphate.²⁵⁰ This complex also helps lower the redox potential, aiding in the deposition of the metals. To further aid the deposition and suppress cracking associated with pyrophosphate baths, a citrate was used and follows the following reactions



where Co aided in the induced co-deposition of Mo via²⁵⁴



The investigated electrolyte baths are as follows:

Table 7.2.1: Component concentration (M) in electrolytes for metallic electrodeposition of Co-Mo alloys

Sample ID	CoS ₄	Na ₂ MoO ₄	Na ₃ Cit	K ₄ P ₂ O ₇	Na ₂ SO ₄
A	0.1	0	0.2	0.2	0.5
B	0.1	0.005	0.2	0.2	0.5
C	0.1	0.010	0.2	0.2	0.5
D	0.1	0.020	0.2	0.2	0.5
E	0.1	0.100	0.2	0.2	0.5

Similar to that of previous chapters, a sulfurization step was performed by annealing samples in the presence of sulphur. Following sulfurization, the samples were tested for their efficacy towards HER. As shown in Figure 7.2.1, none of the catalysts showed activity towards HER, indicated by the low current density, even at high overpotentials. An interesting note is that the performance deteriorated when more Mo was added to the electrolyte bath. This is likely due to a decrease in efficiency of the plating process.²⁵⁰

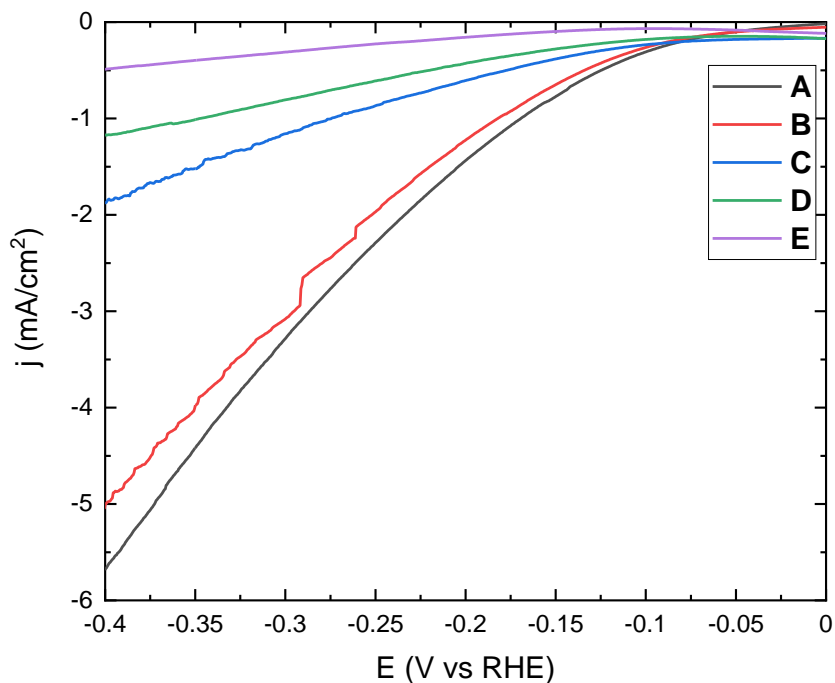


Figure 7.2.1: Polarizations of the various catalysts following sulfurization in 0.5M H₂SO₄

Raman spectroscopy was used to investigate the structure of the formed films. As seen in Figure 7.2.2, no metal sulfides were formed throughout the process. This is likely the case as elemental metals are much more difficult to sulfurize and oxides are traditionally used.¹⁴¹ This process demonstrates the importance of careful consideration of the electrodeposited material, namely the use of oxides, in order to form TMDCs via sulfurization.

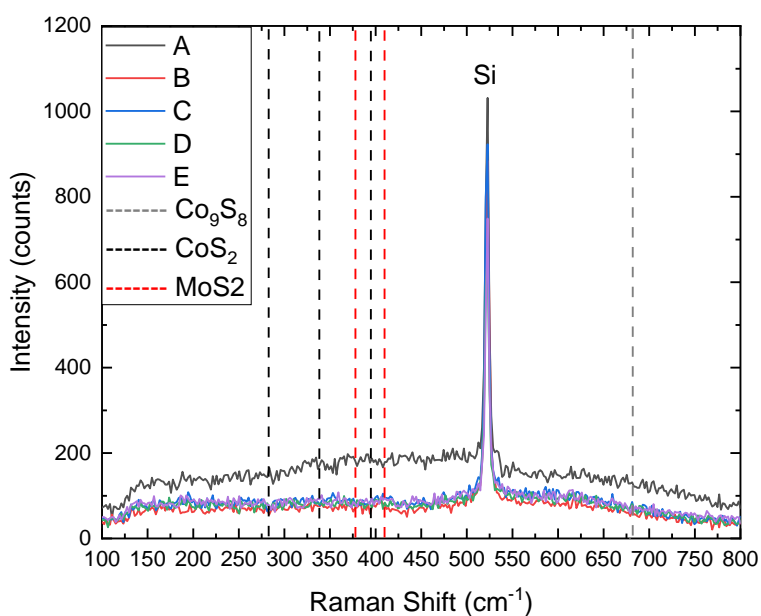


Figure 7.2.2: Raman spectroscopy of the various catalysts following sulfurization.

7.3 Raman Analysis of Amorphous MoS_x

The primary way to probe the structure of these polymeric a-MoS_x is the use of Raman spectroscopy. To facilitate discussion later in the thesis, a preview tying the vibration modes found in Raman to the structure above follows. Figure 7.3.1a is the spectra of a slightly oxidized MoS_x sample that was made in our lab and Figure 7.3.1b is a cluster of (Mo₃S₁₃)²⁻ from literature.¹¹ The main features are

- i) molybdenum sulfide bonds of $\nu(\text{Mo-S})$ were found at 283-385 cm⁻¹
- ii) $\nu(\text{Mo-S-Mo})$ vibrations were observed around 425 cm⁻¹
- iii) $\nu(\text{Mo-S}_{\text{apical}})$ vibrations were observed in the 450-475 cm⁻¹ region,
- iv) $\nu(\text{S-S})_{\text{terminal}}$ vibrations were observed around 520 cm⁻¹
- v) $\nu(\text{S-S})_{\text{bridging}}$ vibrations were observed around 550 cm⁻¹
- vi) molybdenum oxide features were observed between 180 – 215 cm⁻¹ and 800 – 1000 cm⁻¹

As can be seen, the primary characteristics between the synthesized film and (Mo₃S₁₃)²⁻ cluster are very similar, albeit with a few key differences. In the Raman spectra from the cluster, discrete signals for $\nu(\text{Mo-S})$ are reported, however since we electrodeposited our film at a working potential similar to the black line in Figure 7.3.1b, it matches well. The other notable difference is that in our samples the $\nu(\text{Mo-S-Mo})$ are observed, whilst they are absent in the as-prepared (Mo₃S₁₃)²⁻ cluster. This is because the $\nu(\text{Mo-S-Mo})$ is attributed to the shared disulfide between clusters, and only appears in the polymeric chains, as can be seen in Figure 7.3.1c.¹¹

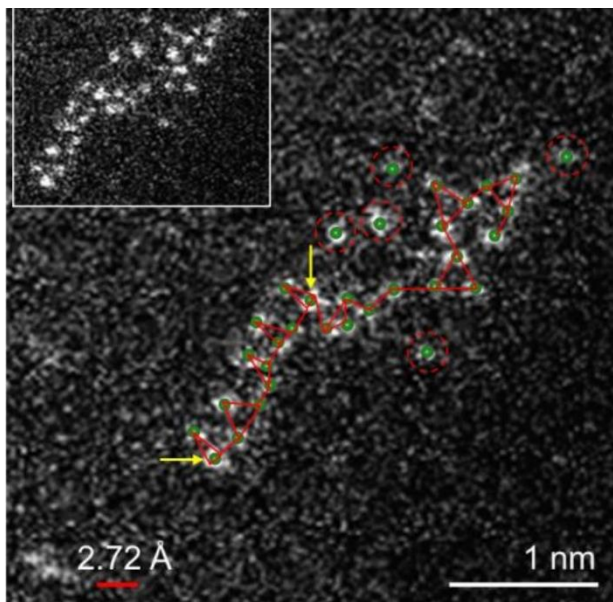
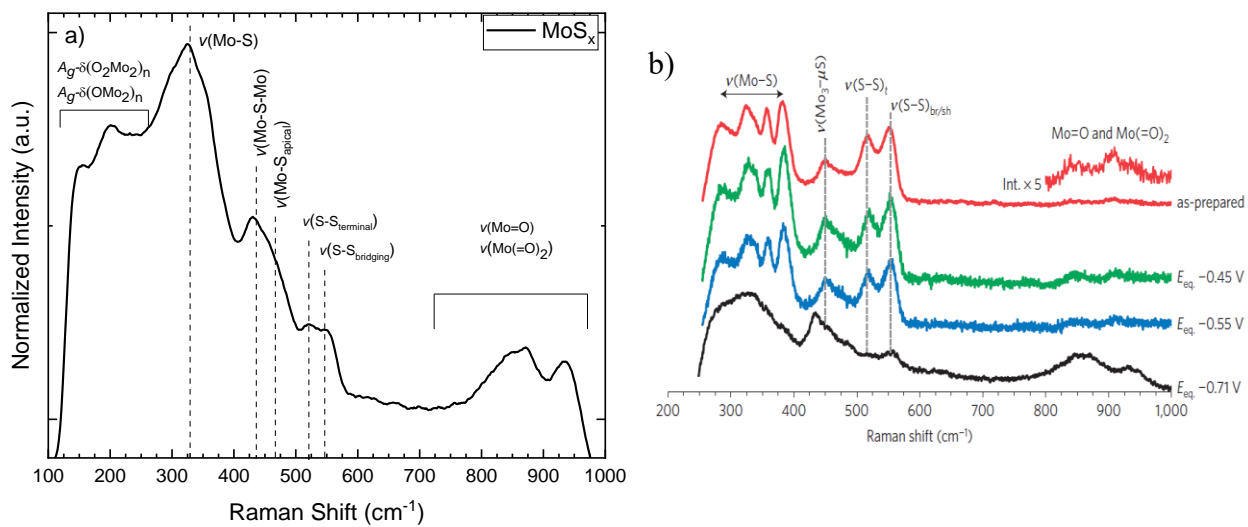


Figure 7.3.1: Raman spectra of a) MoS_x synthesized film and b) (Mo₃S₁₃)²⁻ clusters¹¹ and c) HAADF-STEM images of (Mo₃S₁₃)²⁻ clusters and a-MoS_x chains

8.0 References

1. Bauen, A. Future energy sources and systems-Acting on climate change and energy security. *J. Power Sources* (2006) doi:10.1016/j.jpowsour.2006.03.034.
2. Luo, X., Wang, J., Dooner, M. & Clarke, J. Overview of current development in electrical energy storage technologies and the application potential in power system operation. *Appl. Energy* (2015) doi:10.1016/j.apenergy.2014.09.081.
3. Schlapbach, L. & Züttel, A. Hydrogen-storage materials for mobile applications. *Nature* (2001) doi:10.1038/35104634.
4. Ritchie, H. & Roser, M. Emissions by sector. <https://ourworldindata.org/emissions-by-sector>.
5. Zou, X. & Zhang, Y. Noble metal-free hydrogen evolution catalysts for water splitting. *Chem. Soc. Rev.* (2015) doi:10.1039/c4cs00448e.
6. Sapountzi, F. M., Gracia, J. M., Weststrate, C. J. (Kee, J., Fredriksson, H. O. A. & Niemantsverdriet, J. W. (Hans. Electrocatalysts for the generation of hydrogen, oxygen and synthesis gas. *Progress in Energy and Combustion Science* (2017) doi:10.1016/j.pecs.2016.09.001.
7. Lang, Y., Arnepalli, R. R. & Tiwari, A. A review on hydrogen production: Methods, materials and nanotechnology. in *Journal of Nanoscience and Nanotechnology* (2011). doi:10.1166/jnn.2011.4157.
8. Levin, D. B., Pitt, L. & Love, M. Biohydrogen production: Prospects and limitations to practical application. *Int. J. Hydrogen Energy* (2004) doi:10.1016/S0360-3199(03)00094-6.
9. Wang, F. *et al.* Recent advances in transition-metal dichalcogenide based nanomaterials for water splitting. *Nanoscale* (2015) doi:10.1039/c5nr06718a.
10. Morales-Guio, C. G. & Hu, X. Amorphous molybdenum sulfides as hydrogen evolution catalysts. *Acc. Chem. Res.* (2014) doi:10.1021/ar5002022.
11. Tran, P. D. *et al.* Coordination polymer structure and revisited hydrogen evolution catalytic mechanism for amorphous molybdenum sulfide. *Nat. Mater.* **15**, 640–646 (2016).
12. Shi, Y. & Zhang, B. Recent advances in transition metal phosphide nanomaterials: Synthesis and applications in hydrogen evolution reaction. *Chemical Society Reviews* (2016) doi:10.1039/c5cs00434a.
13. Chen, W. F., Muckerman, J. T. & Fujita, E. Recent developments in transition metal carbides and nitrides as hydrogen evolution electrocatalysts. *Chem. Commun.* (2013) doi:10.1039/c3cc44076a.
14. Wei, Y. *et al.* Controllable synthesis of P-doped MoS₂ nanopetals decorated N-doped hollow carbon spheres towards enhanced hydrogen evolution. *Electrochim. Acta* (2019) doi:10.1016/j.electacta.2018.12.019.

15. Li, G. *et al.* All the Catalytic Active Sites of MoS₂ for Hydrogen Evolution. *J. Am. Chem. Soc.* (2016) doi:10.1021/jacs.6b05940.
16. Ambrosi, A. & Pumera, M. Templated Electrochemical Fabrication of Hollow Molybdenum Sulfide Microstructures and Nanostructures with Catalytic Properties for Hydrogen Production. *ACS Catal.* **6**, 3985–3993 (2016).
17. Murugesan, S. *et al.* Room temperature electrodeposition of molybdenum sulfide for catalytic and photoluminescence applications. *ACS Nano* **7**, 8199–8205 (2013).
18. Gao, M. R., Chan, M. K. Y. & Sun, Y. Edge-terminated molybdenum disulfide with a 9.4-Å interlayer spacing for electrochemical hydrogen production. *Nat. Commun.* **6**, (2015).
19. Jin, Q. *et al.* H₂-Directing Strategy on In Situ Synthesis of Co-MoS₂ with Highly Expanded Interlayer for Elegant HER Activity and its Mechanism. *Adv. Energy Mater.* **10**, 1–12 (2020).
20. Jaramillo, T. F. *et al.* Identification of active edge sites for electrochemical H₂ evolution from MoS₂ nanocatalysts. *Science (80-.)*. **317**, 100–102 (2007).
21. Wan, Y. *et al.* Engineering active edge sites of fractal-shaped single-layer MoS₂ catalysts for high-efficiency hydrogen evolution. *Nano Energy* (2018) doi:10.1016/j.nanoen.2018.02.027.
22. Chen, Z. *et al.* Core-shell MoO₃-MoS₂ nanowires for hydrogen evolution: A functional design for electrocatalytic materials. *Nano Lett.* (2011) doi:10.1021/nl2020476.
23. Bonde, J., Moses, P. G., Jaramillo, T. F., Nørskov, J. K. & Chorkendorff, I. Hydrogen evolution on nano-particulate transition metal sulfides. *Faraday Discuss.* (2008) doi:10.1039/b803857k.
24. Tokash, J. C. & Logan, B. E. Electrochemical evaluation of molybdenum disulfide as a catalyst for hydrogen evolution in microbial electrolysis cells. *Int. J. Hydrogen Energy* (2011) doi:10.1016/j.ijhydene.2011.05.080.
25. Wang, T. *et al.* Enhanced electrocatalytic activity for hydrogen evolution reaction from self-assembled monodispersed molybdenum sulfide nanoparticles on an Au electrode. *Energy Environ. Sci.* (2013) doi:10.1039/c2ee23513g.
26. Li, Y. *et al.* MoS₂ nanoparticles grown on graphene: An advanced catalyst for the hydrogen evolution reaction. *J. Am. Chem. Soc.* **133**, 7296–7299 (2011).
27. Liao, L. *et al.* MoS₂ formed on mesoporous graphene as a highly active catalyst for hydrogen evolution. *Adv. Funct. Mater.* (2013) doi:10.1002/adfm.201300318.
28. Lin, T. W., Liu, C. J. & Lin, J. Y. Facile synthesis of MoS₃/carbon nanotube nanocomposite with high catalytic activity toward hydrogen evolution reaction. *Appl. Catal. B Environ.* (2013) doi:10.1016/j.apcatb.2013.01.004.
29. Kong, D. *et al.* Synthesis of MoS₂ and MoSe₂ films with vertically aligned layers. *Nano Lett.* (2013) doi:10.1021/nl400258t.
30. Wang, P., Wan, L., Lin, Y. & Wang, B. MoS₂ supported CoS₂ on carbon cloth as a high-

- performance electrode for hydrogen evolution reaction. *Int. J. Hydrogen Energy* **44**, 16566–16574 (2019).
31. Bose, R. *et al.* Co-catalytic Effects of CoS₂ on the Activity of the MoS₂ Catalyst for Electrochemical Hydrogen Evolution. *Langmuir* **33**, 5628–5635 (2017).
 32. Sun, X. *et al.* Interface Engineering in Two-Dimensional Heterostructures: Towards an Advanced Catalyst for Ullmann Couplings. *Angew. Chemie - Int. Ed.* (2016) doi:10.1002/anie.201508571.
 33. Li, J. *et al.* In situ phase transition induced TM-MoC/Mo₂C (TM= Fe, Co, Ni, and Cu) heterostructure catalysts for efficient hydrogen evolution. *J. Mater. Chem. A* (2022) doi:10.1039/d2ta00727d.
 34. Jiang, J., Wang, X., Liang, X., Zhang, J. & Ai, L. Superwetting molybdenum-based sulfide/phosphide heterostructures for efficient water electrolysis and solar thermoelectricity self-powered hydrogen production. *Appl. Surf. Sci.* (2023) doi:10.1016/j.apsusc.2023.157482.
 35. Zhang, C. *et al.* High-throughput production of cheap mineral-based two-dimensional electrocatalysts for high-current-density hydrogen evolution. *Nat. Commun.* (2020) doi:10.1038/s41467-020-17121-8.
 36. Luo, Q. *et al.* Synergistic effects of 1T MoS₂ and interface engineering on hollow NiCoP nanorods for enhanced hydrogen evolution activity. *J. Mater. Sci. Technol.* (2023) doi:10.1016/j.jmst.2022.10.044.
 37. Zhang, B. *et al.* Interface engineering: The Ni(OH)₂/MoS₂ heterostructure for highly efficient alkaline hydrogen evolution. *Nano Energy* (2017) doi:10.1016/j.nanoen.2017.05.011.
 38. Hu, J. *et al.* Nanohybridization of MoS₂ with Layered Double Hydroxides Efficiently Synergizes the Hydrogen Evolution in Alkaline Media. *Joule* (2017) doi:10.1016/j.joule.2017.07.011.
 39. Kim, M. *et al.* Covalent 0D–2D Heterostructuring of Co₉S₈–MoS₂ for Enhanced Hydrogen Evolution in All pH Electrolytes. *Adv. Funct. Mater.* (2020) doi:10.1002/adfm.202002536.
 40. Yu, S. H. *et al.* Engineering Sulfide-Phosphide Based Double Catalysts on 3D Nickel Phosphides Framework for Electrolytic Hydrogen Evolution: Activating Short-range Crystalline MoS₂ with Ni₅P₄-Ni₂P Template. *J. Electrochem. Soc.* (2020) doi:10.1149/1945-7111/ab6a85.
 41. Zhang, C., Jiang, L., Zhang, Y., Hu, J. & Leung, M. K. H. Janus effect of O₂ plasma modification on the electrocatalytic hydrogen evolution reaction of MoS₂. *J. Catal.* (2018) doi:10.1016/j.jcat.2018.03.018.
 42. Shin, S. *et al.* Effect of oxygen incorporation in amorphous molybdenum sulfide on electrochemical hydrogen evolution. *Appl. Surf. Sci.* **487**, 981–989 (2019).
 43. Benck, J. D., Chen, Z., Kuritzky, L. Y., Forman, A. J. & Jaramillo, T. F. Amorphous

- molybdenum sulfide catalysts for electrochemical hydrogen production: Insights into the origin of their catalytic activity. *ACS Catal.* **2**, 1916–1923 (2012).
44. Deng, Y. *et al.* Operando Raman Spectroscopy of Amorphous Molybdenum Sulfide (MoS_x) during the Electrochemical Hydrogen Evolution Reaction: Identification of Sulfur Atoms as Catalytically Active Sites for H⁺ Reduction. *ACS Catal.* **6**, 7790–7798 (2016).
 45. Weber, T., Muijsers, J. C. & Niemantsverdriet, J. W. Structure of amorphous MoS₃. *J. Phys. Chem.* (1995) doi:10.1021/j100022a037.
 46. Hibble, S. J., Rice, D. A., Pickup, D. M. & Beer, M. P. Mo K-Edge EXAFS and S K-Edge Absorption Studies of the Amorphous Molybdenum Sulfides MoS_{4.7}, MoS₃, and MoS₃·nH₂O (n ~ 2). *Inorg. Chem.* (1995) doi:10.1021/ic00125a006.
 47. Merki, D., Vrubel, H., Rovelli, L., Fierro, S. & Hu, X. Fe, Co, and Ni ions promote the catalytic activity of amorphous molybdenum sulfide films for hydrogen evolution. *Chem. Sci.* **3**, 2515–2525 (2012).
 48. Vrubel, H., Moehl, T., Grätzel, M. & Hu, X. Revealing and accelerating slow electron transport in amorphous molybdenum sulphide particles for hydrogen evolution reaction. *Chem. Commun.* (2013) doi:10.1039/c3cc45416a.
 49. Redman, D. W., Rose, M. J. & Stevenson, K. J. Electrodeposition of Amorphous Molybdenum Chalcogenides from Ionic Liquids and Their Activity for the Hydrogen Evolution Reaction. *Langmuir* **33**, 9354–9360 (2017).
 50. Kendall, L. *et al.* Influence of Oxygen Dopants on the HER Catalytic Activity of Electrodeposited MoO_xS_y Electrocatalysts. *ACS Appl. Energy Mater.* **4**, 13676–13683 (2021).
 51. Gamburg, Y. & Zangari, G. *Theory and Practice of Metal Electrodeposition*. (Springer US, 2011).
 52. A. Brenner: Electrodeposition of Alloys. Principle and Practice. Academic Press, New York and London 1963. Band I: General Survey, Principles, and Alloys of Copper and of Silver. 714 S. mit 212 Bildern und 45 Tab. DIN A5. Preis: \$ 24.-. *Berichte der Bunsengesellschaft für Phys. Chemie* (1964) doi:10.1002/bbpc.19640680319.
 53. Keyser, P. T. The purpose of the Parthian Galvanic cells: a first-century A.D. electric battery used for analgesia. *J. Near East. Stud.* (1993) doi:10.1086/373610.
 54. Soonmin, H., Vanalakar, S. A., Galal, A. & Singh, V. N. A review of nanostructured thin films for gas sensing and corrosion protection. *Mediterr. J. Chem.* (2018) doi:10.13171/MJC7618111916HS.
 55. Prokkola, H., Nurmesniemi, E. T. & Lassi, U. Removal of metals by sulphide precipitation using Na₂S and HS⁻-solution. *ChemEngineering* (2020) doi:10.3390/chemengineering4030051.
 56. Vickerman, J. C. & Gilmore, I. S. *Surface Analysis - The Principal Techniques: Second Edition*. *Surface Analysis - The Principal Techniques: Second Edition* (2009). doi:10.1002/9780470721582.

57. Kamarulzaman, N., Kasim, M. F. & Chayed, N. F. Elucidation of the highest valence band and lowest conduction band shifts using XPS for ZnO and Zn_{0.99}Cu_{0.01}O band gap changes. *Results Phys.* (2016) doi:10.1016/j.rinp.2016.04.001.
58. Jablonski, A. & Powell, C. J. The electron attenuation length revisited. *Surf. Sci. Rep.* (2002) doi:10.1016/s0167-5729(02)00031-6.
59. Powell, C. J. & Jablonski, A. The NIST Electron Effective-Attenuation-Length Database. *J. Surf. Anal.* (2002) doi:10.1384/jsa.9.322.
60. Powell, C. J. Practical guide for inelastic mean free paths, effective attenuation lengths, mean escape depths, and information depths in x-ray photoelectron spectroscopy. *J. Vac. Sci. Technol. A* (2020) doi:10.1116/1.5141079.
61. Moulder, J. F., Stickle, W. F., Sobol, P. E. & Bomben, K. D. *Handbook of X-ray photoelectron spectroscopy: a reference book of standard spectra for identification and interpretation of XPS data. Surface and Interface Analysis* (1992).
62. B, J. Symmetry and spectroscopy; an introduction to vibrational and electronic spectroscopy. *J. Mol. Struct.* (1980) doi:10.1016/0022-2860(80)85247-1.
63. Agilent. The Basics of UV-Vis Spectrophotometry. *The basics of UV-Vis Spectrophotometry* 36 (2021).
64. Kubelka, P.; Munk, F. A Contribution to the Optics of Pigments. *Z. Technol. Phys.* (1931).
65. Kiessig, H. Untersuchungen zur Totalreflexion von Röntgenstrahlen. *Ann. Phys.* (1931) doi:10.1002/andp.19314020607.
66. Morales-Guio, C. G., Stern, L. A. & Hu, X. Nanostructured hydrotreating catalysts for electrochemical hydrogen evolution. *Chemical Society Reviews* (2014) doi:10.1039/c3cs60468c.
67. Wang, L., Tian, G., Chen, Y., Xiao, Y. & Fu, H. In situ formation of a ZnO/ZnSe nanonail array as a photoelectrode for enhanced photoelectrochemical water oxidation performance. *Nanoscale* (2016) doi:10.1039/c6nr01969b.
68. Cho, S. *et al.* Solution-based fabrication of ZnO/ZnSe heterostructure nanowire arrays for solar energy conversion. *J. Mater. Chem.* (2011) doi:10.1039/c1jm14014k.
69. Xu, H. *et al.* ZnSe/CdS/CdSe triple-sensitized ZnO nanowire arrays for multi-bandgap photoelectrochemical hydrogen generation. *RSC Adv.* (2014) doi:10.1039/c4ra08335k.
70. Ouyang, W. X., Yu, Y. X. & Zhang, W. De. High and stable photoelectrochemical activity of ZnO/ZnSe/CdSe/Cu_xS core-shell nanowire arrays: Nanoporous surface with Cu_xS as a hole mediator. *Phys. Chem. Chem. Phys.* (2015) doi:10.1039/c5cp01421b.
71. Chen, Y., Wang, L., Wang, W. & Cao, M. Enhanced photoelectrochemical properties of ZnO/ZnSe/CdSe/Cu_{2-x}Se core-shell nanowire arrays fabricated by ion-replacement method. *Appl. Catal. B Environ.* (2017) doi:10.1016/j.apcatb.2017.02.049.
72. Fu, Y. *et al.* Synthesis of ternary ZnO/ZnS/MoS₂ piezoelectric nanoarrays for enhanced photocatalytic performance by conversion of dual heterojunctions. *Appl. Surf. Sci.* (2021)

- doi:10.1016/j.apsusc.2021.149695.
73. Osterloh, F. E. Inorganic nanostructures for photoelectrochemical and photocatalytic water splitting. *Chem. Soc. Rev.* (2013) doi:10.1039/c2cs35266d.
 74. Kumar, S. *et al.* Defect-Rich MoS₂ Ultrathin Nanosheets-Coated Nitrogen-Doped ZnO Nanorod Heterostructures: An Insight into in-Situ-Generated ZnS for Enhanced Photocatalytic Hydrogen Evolution. *ACS Appl. Energy Mater.* (2019) doi:10.1021/acsaem.9b00790.
 75. Wang, S., Tian, H., Ren, C., Yu, J. & Sun, M. Electronic and optical properties of heterostructures based on transition metal dichalcogenides and graphene-like zinc oxide. *Sci. Rep.* (2018) doi:10.1038/s41598-018-30614-3.
 76. Esposito, V. & Castelli, I. E. Metastability at Defective Metal Oxide Interfaces and Nanoconfined Structures. *Advanced Materials Interfaces* (2020) doi:10.1002/admi.201902090.
 77. Li, H. *et al.* MoS₂ nanosheet/ZnO nanowire hybrid nanostructures for photoelectrochemical water splitting. *J. Am. Ceram. Soc.* (2018) doi:10.1111/jace.15540.
 78. Nguyen, T. D., Man, M. T., Nguyen, M. H., Seo, D. B. & Kim, E. T. Effect of few-layer MoS₂ flakes deposited ZnO/FTO nanorods on photoelectrochemical characteristic. *Mater. Res. Express* (2019) doi:10.1088/2053-1591/ab208a.
 79. Trung, T. N., Seo, D. B., Quang, N. D., Kim, D. & Kim, E. T. Enhanced photoelectrochemical activity in the heterostructure of vertically aligned few-layer MoS₂ flakes on ZnO. *Electrochim. Acta* (2018) doi:10.1016/j.electacta.2017.11.089.
 80. Ye, J., Liu, J. & An, Y. Electric field and strain effects on the electronic and optical properties of g-C₃N₄/WSe₂ van der Waals heterostructure. *Appl. Surf. Sci.* (2020) doi:10.1016/j.apsusc.2019.144262.
 81. Su, J. *et al.* Unusual properties and potential applications of strain BN-MS₂ (M = Mo, W) heterostructures. *Sci. Rep.* (2019) doi:10.1038/s41598-019-39970-0.
 82. Bolar, S., Shit, S., Murmu, N. C., Samanta, P. & Kuila, T. Activation Strategy of MoS₂ as HER Electrocatalyst through Doping-Induced Lattice Strain, Band Gap Engineering, and Active Crystal Plane Design. *ACS Appl. Mater. Interfaces* (2021) doi:10.1021/acsaami.0c20500.
 83. Arotiba, O. A., Orimolade, B. O. & Koiki, B. A. Visible light-driven photoelectrocatalytic semiconductor heterojunction anodes for water treatment applications. *Current Opinion in Electrochemistry* (2020) doi:10.1016/j.coelec.2020.03.018.
 84. Fareza, A. R., Nugroho, F. A. A. & Fauzia, V. One-Step Coating of a ZnS Nanoparticle/MoS₂ Nanosheet Composite on Supported ZnO Nanorods as Anodes for Photoelectrochemical Water Splitting. *ACS Appl. Nano Mater.* (2022) doi:10.1021/acsanm.2c01434.
 85. Kumar, S. *et al.* Efficient Electron Transfer across a ZnO–MoS₂–Reduced Graphene Oxide Heterojunction for Enhanced Sunlight-Driven Photocatalytic Hydrogen Evolution.

- ChemSusChem* (2017) doi:10.1002/cssc.201701024.
86. Flores, E. M. *et al.* Optical and structural investigation of ZnO@ZnS core-shell nanostructures. *Mater. Chem. Phys.* (2016) doi:10.1016/j.matchemphys.2016.02.022.
 87. Wu, H. *et al.* Fabrication of ZnO@MoS₂ nanocomposite heterojunction arrays and their photoelectric properties. *Micromachines* (2020) doi:10.3390/mi11020189.
 88. Lee, G. C. *et al.* Induction of a piezo-potential improves photocatalytic hydrogen production over ZnO/ZnS/MoS₂ Heterostructures. *Nano Energy* (2022) doi:10.1016/j.nanoen.2021.106867.
 89. Wang, J., Zhong, H. X., Wang, Z. L., Meng, F. L. & Zhang, X. B. Integrated Three-Dimensional Carbon Paper/Carbon Tubes/Cobalt-Sulfide Sheets as an Efficient Electrode for Overall Water Splitting. *ACS Nano* **10**, 2342–2348 (2016).
 90. Levinas, R., Tsyntaru, N. & Cesiulis, H. Insights into electrodeposition and catalytic activity of MoS₂ for hydrogen evolution reaction electrocatalysis. *Electrochim. Acta* **317**, 427–436 (2019).
 91. Sun, P., Zhang, W., Hu, X., Yuan, L. & Huang, Y. Synthesis of hierarchical MoS₂ and its electrochemical performance as an anode material for lithium-ion batteries. *J. Mater. Chem. A* **2**, 3498–3504 (2014).
 92. Zhou, J., Fang, G., Pan, A. & Liang, S. Oxygen-Incorporated MoS₂ Nanosheets with Expanded Interlayers for Hydrogen Evolution Reaction and Pseudocapacitor Applications. *ACS Appl. Mater. Interfaces* (2016) doi:10.1021/acsami.6b11811.
 93. Guo, J., Li, F., Sun, Y., Zhang, X. & Tang, L. Oxygen-incorporated MoS₂ ultrathin nanosheets grown on graphene for efficient electrochemical hydrogen evolution. *J. Power Sources* (2015) doi:10.1016/j.jpowsour.2015.05.034.
 94. Mamaghani, K. R. & Parvin, N. Preparation and properties of bulk ZnO/MoS₂ nanocomposite by cold sintering process with three-component solvent. *J. Mater. Sci.* (2023) doi:10.1007/s10853-023-08787-8.
 95. Khan, S. A., Khan, T., Zulfiqar & Khan, M. Enhanced photoluminescence performance of MoS₂ nanostructures after amalgamation with ZnO NPs. *Optik (Stuttg)*. (2020) doi:10.1016/j.ijleo.2020.165201.
 96. Liang, L. & Meunier, V. First-principles Raman spectra of MoS₂, WS₂ and their heterostructures. *Nanoscale* **6**, 5394–5401 (2014).
 97. Guo, Y. *et al.* Discovering the forbidden Raman modes at the edges of layered materials. *Sci. Adv.* (2018) doi:10.1126/sciadv.aau6252.
 98. Attanayake, N. H. *et al.* Effect of Intercalated Metals on the Electrocatalytic Activity of 1T-MoS₂ for the Hydrogen Evolution Reaction. *ACS Energy Lett.* (2018) doi:10.1021/acsenerylett.7b00865.
 99. Heising, J. & Kanatzidis, M. G. Exfoliated and restacked MoS₂ and WS₂: Ionic or neutral species? Encapsulation and ordering of hard electropositive cations. *J. Am. Chem. Soc.*

- (1999) doi:10.1021/ja991644d.
100. Er, E. *et al.* High-Yield Preparation of Exfoliated 1T-MoS₂ with SERS Activity. *Chem. Mater.* (2019) doi:10.1021/acs.chemmater.9b01698.
 101. Pak, S. *et al.* Strain-Mediated Interlayer Coupling Effects on the Excitonic Behaviors in an Epitaxially Grown MoS₂/WS₂ van der Waals Heterobilayer. *Nano Lett.* (2017) doi:10.1021/acs.nanolett.7b02513.
 102. Lee, J. U. *et al.* Strain-shear coupling in bilayer MoS. *Nat. Commun.* (2017) doi:10.1038/s41467-017-01487-3.
 103. Zhang, L. *et al.* 2D atomic crystal molecular superlattices by soft plasma intercalation. *Nat. Commun.* (2020) doi:10.1038/s41467-020-19766-x.
 104. Zhao, J. *et al.* Intercalation oxidation: A strategy for MoS₂ modification to enable photodegradation of pollutants. *Appl. Surf. Sci.* (2023) doi:10.1016/j.apsusc.2023.157316.
 105. Brown, N. M. D., Cui, N. & McKinley, A. An XPS study of the surface modification of natural MoS₂ following treatment in an RF-oxygen plasma. *Appl. Surf. Sci.* (1998) doi:10.1016/S0169-4332(98)00252-9.
 106. Xiong, X. *et al.* Oxygen Incorporated MoS₂ for Rectification-Mediated Resistive Switching and Artificial Neural Network. *Adv. Funct. Mater.* (2023) doi:10.1002/adfm.202213348.
 107. Liu, A., Zhao, L., Zhang, J., Lin, L. & Wu, H. Solvent-Assisted Oxygen Incorporation of Vertically Aligned MoS₂ Ultrathin Nanosheets Decorated on Reduced Graphene Oxide for Improved Electrocatalytic Hydrogen Evolution. *ACS Appl. Mater. Interfaces* (2016) doi:10.1021/acsami.6b06031.
 108. Kraut, E. A., Grant, R. W., Waldrop, J. R. & Kowalczyk, S. P. Precise determination of the valence-band edge in X-Ray photoemission spectra: Application to measurement of semiconductor interface potentials. *Phys. Rev. Lett.* (1980) doi:10.1103/PhysRevLett.44.1620.
 109. Wang, W. *et al.* Investigation of the band alignment at MoS₂/PtSe₂ heterojunctions. *Appl. Phys. Lett.* (2019) doi:10.1063/1.5097248.
 110. Yu, Y. *et al.* Layer-dependent electrocatalysis of MoS₂ for hydrogen evolution. *Nano Lett.* (2014) doi:10.1021/nl403620g.
 111. Mugheri, A. Q., Otho, A. A. & Mugheri, A. A. Hierarchical fibrous bimetallic electrocatalyst based on ZnO-MoS₂ composite nanostructures as high performance for hydrogen evolution reaction. *J. Electroanal. Chem.* (2021) doi:10.1016/j.jelechem.2021.115061.
 112. Sun, H. *et al.* Synthesis and hydrogen evolution reaction of nanosized Ag - ZnO coated MoS₂. *Ceram. Int.* (2021) doi:10.1016/j.ceramint.2021.01.268.
 113. Thomas, S. A., Roy, N., Sharaf Saeed, W., Sreedhar, A. & Cherusseri, J. Hydrothermally synthesized MoS₂/ZnS heterostructure with efficient catalytic performance for hydrogen

- evolution. *Int. J. Hydrogen Energy* (2023) doi:10.1016/j.ijhydene.2023.06.302.
114. Rasool, F. *et al.* Interfacial engineering of ZnS–ZnO decorated MoS₂ supported on 2D Ti₃C₂T_x MXene sheets for enhanced hydrogen evolution reaction. *Int. J. Hydrogen Energy* **59**, 63–73 (2024).
 115. Gnanasekar, P., Ranjith, K. S., Manivel, P., Han, Y. K. & Kulandaivel, J. Hierarchical NbS₂/MoS₂-Carbon Nanofiber Electrode for Highly Efficient and Stable Hydrogen Evolution Reaction at All Ranges of pH. *ACS Appl. Energy Mater.* (2020) doi:10.1021/acsaem.0c00856.
 116. Wu, W. *et al.* Activation of MoS₂ Basal Planes for Hydrogen Evolution by Zinc. *Angew. Chemie - Int. Ed.* **58**, 2029–2033 (2019).
 117. Xiong, L. *et al.* Zns@Mos₂ Core/Shell Heterojunctions as Efficient Electrocatalysts for Hydrogen Evolution Reaction. *SSRN Electron. J.* (2022) doi:10.2139/ssrn.4102991.
 118. Trasatti, S. & Petrii, O. A. Real surface area measurements in electrochemistry. *Journal of Electroanalytical Chemistry* (1992) doi:10.1016/0022-0728(92)80162-W.
 119. Connor, P., Schuch, J., Kaiser, B. & Jaegermann, W. The Determination of Electrochemical Active Surface Area and Specific Capacity Revisited for the System MnO_x as an Oxygen Evolution Catalyst. *Zeitschrift fur Phys. Chemie* (2020) doi:10.1515/zpch-2019-1514.
 120. Morales, D. M. & Risch, M. Seven steps to reliable cyclic voltammetry measurements for the determination of double layer capacitance. *JPhys Energy* (2021) doi:10.1088/2515-7655/abee33.
 121. Cruz-Manzo, S. & Greenwood, P. Electrochemical impedance spectroscopy in PEM fuel cells. in *Electrochemical Phenomena in the Cathode Impedance Spectrum of PEM Fuel Cells* (2022). doi:10.1016/b978-0-323-90607-4.00004-5.
 122. Bard, A. J. & Faulkner, L. R. *Electrochemical Methods: Fundamentals and Applications, 2nd Edition. Electrochemical Methods - Fundamentals and Applications* (2001).
 123. Huang, S. *et al.* N-, O-, and S-Tridoped Carbon-Encapsulated Co₉S₈ Nanomaterials: Efficient Bifunctional Electrocatalysts for Overall Water Splitting. *Adv. Funct. Mater.* **27**, 1–10 (2017).
 124. Guan, C. *et al.* Metal-organic framework derived hollow CoS₂ nanotube arrays: An efficient bifunctional electrocatalyst for overall water splitting. *Nanoscale Horizons* **2**, 342–348 (2017).
 125. Souleyman, R., Wang, Z., Qiao, C., Naveed, M. & Cao, C. Microwave-assisted synthesis of graphene-like cobalt sulfide freestanding sheets as an efficient bifunctional electrocatalyst for overall water splitting. *J. Mater. Chem. A* **6**, 7592–7607 (2018).
 126. Ma, X. *et al.* Phase and composition controlled synthesis of cobalt sulfide hollow nanospheres for electrocatalytic water splitting. *Nanoscale* **10**, 4816–4824 (2018).
 127. Wang, J. *et al.* Synthesis and characterization of nanosize cobalt sulfide for rechargeable

- lithium batteries. *J. Power Sources* (2006) doi:10.1016/j.jpowsour.2006.04.092.
128. Choi, S. H., Boo, S. J., Lee, J. H. & Kang, Y. C. Electrochemical properties of tungsten sulfide-carbon composite microspheres prepared by spray pyrolysis. *Sci. Rep.* (2014) doi:10.1038/srep05755.
 129. Zhang, J., Yu, L. & Lou, X. W. D. Embedding CoS₂ nanoparticles in N-doped carbon nanotube hollow frameworks for enhanced lithium storage properties. *Nano Res.* (2017) doi:10.1007/s12274-016-1394-1.
 130. Zhou, X. *et al.* Symmetrical synergy of hybrid Co₉S₈-MoS_x electrocatalysts for hydrogen evolution reaction. *Nano Energy* (2017) doi:10.1016/j.nanoen.2017.01.011.
 131. Yan, K. L. *et al.* Organic-inorganic hybrids-directed ternary NiFeMoS anemone-like nanorods with scaly surface supported on nickel foam for efficient overall water splitting. *Chem. Eng. J.* (2018) doi:10.1016/j.cej.2017.10.074.
 132. Yang, W. & Chen, S. Recent progress in electrode fabrication for electrocatalytic hydrogen evolution reaction: A mini review. *Chemical Engineering Journal* (2020) doi:10.1016/j.cej.2020.124726.
 133. Chanda, D., Hnát, J., Paidar, M., Schauer, J. & Bouzek, K. Synthesis and characterization of NiFe₂O₄ electrocatalyst for the hydrogen evolution reaction in alkaline water electrolysis using different polymer binders. *J. Power Sources* (2015) doi:10.1016/j.jpowsour.2015.03.067.
 134. Xiang, Z. C., Zhang, Z., Xu, X. J., Zhang, Q. & Yuan, C. MoS₂ nanosheets array on carbon cloth as a 3D electrode for highly efficient electrochemical hydrogen evolution. *Carbon N. Y.* (2016) doi:10.1016/j.carbon.2015.10.071.
 135. Zhang, N. *et al.* Growth Control of MoS₂ Nanosheets on Carbon Cloth for Maximum Active Edges Exposed: An Excellent Hydrogen Evolution 3D Cathode. *ACS Appl. Mater. Interfaces* **7**, 12193–12202 (2015).
 136. Yan, Y. *et al.* Vertically oriented MoS₂ and WS₂ nanosheets directly grown on carbon cloth as efficient and stable 3-dimensional hydrogen-evolving cathodes. *J. Mater. Chem. A* **3**, 131–135 (2015).
 137. Nikam, R. D. *et al.* Three-Dimensional Heterostructures of MoS₂ Nanosheets on Conducting MoO₂ as an Efficient Electrocatalyst to Enhance Hydrogen Evolution Reaction. *ACS Appl. Mater. Interfaces* **7**, 23328–23335 (2015).
 138. Liu, B. *et al.* In Situ Electrodeposition of Cobalt Sulfide Nanosheet Arrays on Carbon Cloth as a Highly Efficient Bifunctional Electrocatalyst for Oxygen Evolution and Reduction Reactions. *ACS Appl. Mater. Interfaces* (2018) doi:10.1021/acsami.8b10645.
 139. Lide, D. R. Handbook of Chemistry and Physics 101st Edition. *CRC Handbook of Chemistry and Physics* (2019).
 140. Chapter 6 Reduction of Oxides. in (1989). doi:10.1016/s0167-2991(08)60929-5.
 141. Pondick, J. V., Woods, J. M., Xing, J., Zhou, Y. & Cha, J. J. Stepwise Sulfurization from

- MoO₃ to MoS₂ via Chemical Vapor Deposition. *ACS Appl. Nano Mater.* (2018) doi:10.1021/acsanm.8b01266.
142. Geller, S. Refinement of the crystal structure of Co₉S₈. *Acta Crystallogr.* **15**, 1195–1198 (1962).
 143. Nowack, E., Schwarzenbach, D. & Hahn, T. Charge densities in CoS₂ and NiS₂ (pyrite structure). *Acta Crystallogr. Sect. B* **47**, 650–659 (1991).
 144. Podlaha, E. J. & Landolt, D. Induced Codeposition: III. Molybdenum Alloys with Nickel, Cobalt, and Iron. *J. Electrochem. Soc.* **144**, 1672–1680 (1997).
 145. Lyapin, S. G. *et al.* Raman studies of nearly half-metallic ferromagnetic CoS₂. *J. Phys. Condens. Matter* **26**, 1–6 (2014).
 146. Wang, H. *et al.* Graphene/Co₉S₈ nanocomposite paper as a binder-free and free-standing anode for lithium-ion batteries. *J. Mater. Chem. A* **3**, 23677–23683 (2015).
 147. Dai, X. *et al.* Co-Doped MoS₂ Nanosheets with the Dominant CoMoS Phase Coated on Carbon as an Excellent Electrocatalyst for Hydrogen Evolution. *ACS Appl. Mater. Interfaces* **7**, 27242–27253 (2015).
 148. Asadi, M. *et al.* Cathode Based on Molybdenum Disulfide Nanoflakes for Lithium-Oxygen Batteries. *ACS Nano* **10**, 2167–2175 (2016).
 149. Yan, Y. *et al.* Facile synthesis of low crystalline MoS₂ nanosheet-coated CNTs for enhanced hydrogen evolution reaction. *Nanoscale* (2013) doi:10.1039/c3nr02994h.
 150. Shit, S. *et al.* Hierarchical Cobalt Sulfide/Molybdenum Sulfide Heterostructure as Bifunctional Electrocatalyst towards Overall Water Splitting. *ChemElectroChem* **6**, 430–438 (2019).
 151. Chebrolu, V. T., Balakrishnan, B., Selvaraj, A. R. & Kim, H. J. A core-shell structure of cobalt sulfide//G-ink towards high energy density in asymmetric hybrid supercapacitors. *Sustain. Energy Fuels* (2020) doi:10.1039/d0se00189a.
 152. Chen, H. *et al.* Assembling Hollow Cobalt Sulfide Nanocages Array on Graphene-like Manganese Dioxide Nanosheets for Superior Electrochemical Capacitors. *ACS Appl. Mater. Interfaces* (2017) doi:10.1021/acsami.7b12069.
 153. Mahmood, N. *et al.* Electrocatalysts for Hydrogen Evolution in Alkaline Electrolytes: Mechanisms, Challenges, and Prospective Solutions. *Adv. Sci.* **5**, (2018).
 154. Zhu, H. *et al.* When Cubic Cobalt Sulfide Meets Layered Molybdenum Disulfide: A Core-Shell System Toward Synergetic Electrocatalytic Water Splitting. *Adv. Mater.* **27**, 4752–4759 (2015).
 155. Gong, L. *et al.* Carbon-coated Co-Mo-P nanosheets supported on carbon cloth as efficient electrocatalyst for Hydrogen Evolution Reaction. *Int. J. Hydrogen Energy* (2020) doi:10.1016/j.ijhydene.2019.10.248.
 156. Zhang, N. *et al.* Controlled electrodeposition of CoMoS_x on carbon cloth: A 3D cathode for highly-efficient electrocatalytic hydrogen evolution. *Int. J. Hydrogen Energy* **41**,

- 3811–3819 (2016).
157. Feng, L. L. *et al.* Metallic Co₉S₈ nanosheets grown on carbon cloth as efficient binder-free electrocatalysts for the hydrogen evolution reaction in neutral media. *J. Mater. Chem. A* **4**, 6860–6867 (2016).
 158. Sun, Y. *et al.* Electrodeposited cobalt-sulfide catalyst for electrochemical and photoelectrochemical hydrogen generation from water. *J. Am. Chem. Soc.* (2013) doi:10.1021/ja4094764.
 159. Xiao, P. *et al.* Molybdenum phosphide as an efficient electrocatalyst for the hydrogen evolution reaction. *Energy Environ. Sci.* (2014) doi:10.1039/c4ee00957f.
 160. Wu, H. Bin, Xia, B. Y., Yu, L., Yu, X. Y. & Lou, X. W. Porous molybdenum carbide nano-octahedrons synthesized via confined carburization in metal-organic frameworks for efficient hydrogen production. *Nat. Commun.* (2015) doi:10.1038/ncomms7512.
 161. Tian, J., Liu, Q., Asiri, A. M. & Sun, X. Self-supported nanoporous cobalt phosphide nanowire arrays: An efficient 3D hydrogen-evolving cathode over the wide range of pH 0–14. *J. Am. Chem. Soc.* (2014) doi:10.1021/ja503372r.
 162. Zheng, G., Peng, Z., Jia, D., Al-Enizi, A. M. & Elzatahry, A. A. From water oxidation to reduction: Homologous Ni-Co based nanowires as complementary water splitting electrocatalysts. *Adv. Energy Mater.* (2015) doi:10.1002/aenm.201402031.
 163. Zhu, M. *et al.* Hydrophilic cobalt sulfide nanosheets as a bifunctional catalyst for oxygen and hydrogen evolution in electrolysis of alkaline aqueous solution. *J. Colloid Interface Sci.* (2018) doi:10.1016/j.jcis.2017.09.076.
 164. Lin, H. *et al.* Hierarchical CoS/MoS₂ and Co₃S₄/MoS₂/Ni₂P nanotubes for efficient electrocatalytic hydrogen evolution in alkaline media. *J. Mater. Chem. A* (2017) doi:10.1039/c7ta08760h.
 165. Ma, X. *et al.* Phase and composition controlled synthesis of cobalt sulfide hollow nanospheres for electrocatalytic water splitting. *Nanoscale* **10**, 4816–4824 (2018).
 166. Li, Y., Hasin, P. & Wu, Y. Ni₃Co₃-XO₄ nanowire arrays for electrocatalytic oxygen evolution. *Adv. Mater.* (2010) doi:10.1002/adma.200903896.
 167. Xiao, Y. *et al.* Three-dimensional cross-linked Co-MoS₂ catalyst on carbon cloth for efficient hydrogen evolution reaction. *Dalt. Trans.* (2022) doi:10.1039/d1dt03411a.
 168. Liu, X. *et al.* The synergistic effect of light irradiation and interface engineering of the Co(OH)₂/MoS₂ heterostructure to realize the efficient alkaline hydrogen evolution reaction. *Electrochim. Acta* (2019) doi:10.1016/j.electacta.2019.01.014.
 169. Lukowski, M. A. *et al.* Enhanced hydrogen evolution catalysis from chemically exfoliated metallic MoS₂ nanosheets. *J. Am. Chem. Soc.* **135**, 10274–10277 (2013).
 170. Senthil, R. A. *et al.* A facile one-pot synthesis of microspherical-shaped CoS₂/CNT composite as Pt-free electrocatalyst for efficient hydrogen evolution reaction. *Int. J. Hydrogen Energy* **44**, 16537–16547 (2019).

171. Kornienko, N. *et al.* Operando Spectroscopic Analysis of an Amorphous Cobalt Sulfide Hydrogen Evolution Electrocatalyst. *J. Am. Chem. Soc.* **137**, 7448–7455 (2015).
172. Ting, L. R. L. *et al.* Catalytic Activities of Sulfur Atoms in Amorphous Molybdenum Sulfide for the Electrochemical Hydrogen Evolution Reaction. *ACS Catal.* **6**, 861–867 (2016).
173. MUELLER, A., DIEMANN, E., JOSTES, R. & BOEGGE, H. ChemInform Abstract: TRANSITION METAL THIO ANIONS: PROPERTIES AND SIGNIFICANCE FOR COMPLEX CHEMISTRY AND BIOINORGANIC CHEMISTRY. *Chem. Informationsd.* (1982) doi:10.1002/chin.198209360.
174. Bouroushian, M. Electrochemistry of the Chalcogens. 57–75 (2010) doi:10.1007/978-3-642-03967-6_2.
175. Patel, A. M., Nørskov, J. K., Persson, K. A. & Montoya, J. H. Efficient Pourbaix diagrams of many-element compounds. *Phys. Chem. Chem. Phys.* (2019) doi:10.1039/c9cp04799a.
176. Singh, A. K. *et al.* Electrochemical Stability of Metastable Materials. *Chem. Mater.* (2017) doi:10.1021/acs.chemmater.7b03980.
177. Persson, K. A., Waldwick, B., Lazic, P. & Ceder, G. Prediction of solid-aqueous equilibria: Scheme to combine first-principles calculations of solids with experimental aqueous states. *Phys. Rev. B - Condens. Matter Mater. Phys.* (2012) doi:10.1103/PhysRevB.85.235438.
178. Jain, A. *et al.* Commentary: The materials project: A materials genome approach to accelerating materials innovation. *APL Materials* (2013) doi:10.1063/1.4812323.
179. Muller, A. & Diemann, E. Higher Energy Bands in the Electronic Absorbtion Spectra of CrO4²⁻, RuO4, OsO4, WS4²⁻, MoS4²⁻, WSe4²⁻, and MoSe4²⁻. *Chem. Phys. Lett.* 1–6 (1971).
180. McDonald, J. W., Friesen, G. D., Rosenhein, L. D. & Newton, W. E. Syntheses and characterization of ammonium and tetraalkylammonium thiomolybdates and thiotungstates. *Inorganica Chim. Acta* (1983) doi:10.1016/S0020-1693(00)81720-X.
181. Neste, V. Übergangsmetallchalkogenverbindungen : Photometrische Bestimmung von Molybd in mit Hilfe des MoS²-Ions. 116–118 (1971).
182. Martincová, J., Otyepka, M. & Lazar, P. Is Single Layer MoS₂ Stable in the Air? *Chem. - A Eur. J.* **23**, 13233–13239 (2017).
183. Gao, J. *et al.* Aging of Transition Metal Dichalcogenide Monolayers. *ACS Nano* (2016) doi:10.1021/acsnano.5b07677.
184. Wagner, M. Thermal Analysis in Practice. in *Thermal Analysis in Practice* (2017). doi:10.3139/9781569906446.fm.
185. Kibsgaard, J., Jaramillo, T. F. & Besenbacher, F. Building an appropriate active-site motif into a hydrogen-evolution catalyst with thiomolybdate [Mo₃S₁₃]²⁻ clusters. *Nat. Chem.* **6**, 248–253 (2014).

186. Camacho-López, M. A. *et al.* Micro-Raman study of the m-MoO₂ to α -MoO₃ transformation induced by cw-laser irradiation. *Opt. Mater. (Amst)*. (2011) doi:10.1016/j.optmat.2010.10.028.
187. Chang, C. H. & Chan, S. S. Infrared and Raman studies of amorphous MoS₃ and poorly crystalline MoS₂. *J. Catal.* (1981) doi:10.1016/0021-9517(81)90085-3.
188. Müller, A., Wittneben, V., Krickemeyer, E., Bögge, H. & Lemke, M. Studies on the triangular cluster [Mo₃S₁₃]²⁻: Electronic structure (X α calculations, XPS), crystal structure of (Ph₄As)₂[Mo₃S₁₃]. 2CH₃CN and a refinement of the crystal structure of (NH₄)₂[Mo₃s₁₃]·H₂O. *ZAAC - J. Inorg. Gen. Chem.* (1991) doi:10.1002/zaac.19916050121.
189. Fedin, V. P., Kolesov, B. A., Mironov, Y. V. & Fedorov, V. Y. Synthesis and vibrational (IR and Raman) spectroscopic study of triangular thio-complexes [Mo₃S₁₃]²⁻ containing ⁹²Mo, ¹⁰⁰Mo and ³⁴S isotopes. *Polyhedron* (1989) doi:10.1016/S0277-5387(89)80005-1.
190. Shyam, B. *et al.* Measurement and Modeling of Short and Medium Range Order in Amorphous Ta₂O₅ Thin Films. *Sci. Rep.* **6**, 1–7 (2016).
191. Ronge, E. *et al.* Structure of Nanocrystalline, Partially Disordered MoS₂+ δ Derived from HRTEM—An Abundant Material for Efficient HER Catalysis.
192. Bélanger, D., Laperrière, G., Girard, F., Guay, D. & Tourillon, G. Physicochemical Characteristics of Electrochemically Deposited Molybdenum Sulfide and Polypyrrole-Tetrathiomolybdate/Molybdenum Trisulfide Composite Electrodes. *Chem. Mater.* (1993) doi:10.1021/cm00030a024.
193. Vrabel, H. & Hu, X. Growth and activation of an amorphous molybdenum sulfide hydrogen evolving catalyst. *ACS Catal.* **3**, 2002–2011 (2013).
194. Stevens, G. C. & Edmonds, T. Electron spectroscopy for chemical analysis spectra of molybdenum sulfides. *J. Catal.* (1975) doi:10.1016/0021-9517(75)90190-6.
195. Schmidt, E., Sourisseau, C., Meunier, G. & Levasseur, A. Amorphous molybdenum oxysulfide thin films and their physical characterization. *Thin Solid Films* (1995) doi:10.1016/0040-6090(94)06463-6.
196. Ren, X. *et al.* A Se-doped MoS₂ nanosheet for improved hydrogen evolution reaction. *Chem. Commun.* **51**, 15997–16000 (2015).
197. Wang, R. *et al.* Beyond 1T-phase? Synergistic Electronic Structure and Defects Engineering in 2H-MoS₂xSe₂(1-x) Nanosheets for Enhanced Hydrogen Evolution Reaction and Sodium Storage. *ChemCatChem* **11**, 3200–3211 (2019).
198. Mann, J. *et al.* 2-Dimensional transition metal dichalcogenides with tunable direct band gaps: MoS₂(1-x)Se₂x monolayers. *Adv. Mater.* **26**, 1399–1404 (2014).
199. Andrews, J. L. *et al.* Hole Extraction by Design in Photocatalytic Architectures Interfacing CdSe Quantum Dots with Topochemically Stabilized Tin Vanadium Oxide. *J. Am. Chem. Soc.* (2018) doi:10.1021/jacs.8b09924.

200. Liu, Y. *et al.* Self-optimizing, highly surface-active layered metal dichalcogenide catalysts for hydrogen evolution. *Nat. Energy* **2**, 1–7 (2017).
201. Se, M. O. & So, M. O. S. Schwingungsspektren und Kraftkonstanten von MoS ~ Se ~ - und WSSe ~ ~ -. (1976).
202. Diemann, E. & Müller, A. Thio and seleno compounds of the transition metals with the do configuration. *Coord. Chem. Rev.* **10**, 79–122 (1973).
203. Wo, M. Schmmzen. **1075**, (1972).
204. Krbal, M. *et al.* 2D MoSe₂ Structures Prepared by Atomic Layer Deposition. *Physica Status Solidi - Rapid Research Letters* (2018) doi:10.1002/pssr.201800023.
205. Roy, A. *et al.* Structural and Electrical Properties of MoTe₂ and MoSe₂ Grown by Molecular Beam Epitaxy. *ACS Appl. Mater. Interfaces* (2016) doi:10.1021/acsami.6b00961.
206. Nguyen, Q. T. *et al.* Novel Amorphous Molybdenum Selenide as an Efficient Catalyst for Hydrogen Evolution Reaction. *ACS Appl. Mater. Interfaces* **10**, 8659–8665 (2018).
207. Redman, D. W., Rose, M. J. & Stevenson, K. J. Electrodeposition of Amorphous Molybdenum Chalcogenides from Ionic Liquids and Their Activity for the Hydrogen Evolution Reaction. *Langmuir* **33**, 9354–9360 (2017).
208. Li, Z., Zhang, J., Lu, Y. & Lou, X. W. A pyrolyzed polyacrylonitrile/selenium disulfide composite cathode with remarkable lithium and sodium storage performances. *Sci. Adv.* (2018) doi:10.1126/sciadv.aat1687.
209. Hu, J., Ren, Y. & Zhang, L. Dual-confined SeS₂ cathode based on polyaniline-assisted double-layered micro/mesoporous carbon spheres for advanced Li–SeS₂ battery. *J. Power Sources* (2020) doi:10.1016/j.jpowsour.2020.227955.
210. Geoffroy, N. & Demopoulos, G. P. The elimination of selenium(IV) from aqueous solution by precipitation with sodium sulfide. *J. Hazard. Mater.* (2011) doi:10.1016/j.jhazmat.2010.09.009.
211. Xiang, B., Huang, J., Yang, L. & Fu, Q. (Invited) Band Gap Tunable Monolayer WSe₂(1-x)S_{2x} Synthesis, Characterization and Device Applications. *ECS Meet. Abstr.* (2015) doi:10.1149/ma2015-02/31/1144.
212. Gong, Q. *et al.* Ultrathin MoS₂(1-x)Se_{2x} Alloy Nanoflakes for Electrocatalytic Hydrogen Evolution Reaction. *ACS Catal.* **5**, 2213–2219 (2015).
213. Xi, F. *et al.* Structural Transformation Identification of Sputtered Amorphous MoS_x as an Efficient Hydrogen-Evolving Catalyst during Electrochemical Activation. *ACS Catal.* (2019) doi:10.1021/acscatal.8b04884.
214. Lioi, D. B., Gosztola, D. J., Wiederrecht, G. P. & Karapetrov, G. Photon-induced selenium migration in TiSe₂. *Appl. Phys. Lett.* (2017) doi:10.1063/1.4976745.
215. Kendall, L. *et al.* Influence of Oxygen Dopants on the HER Catalytic Activity of Electrodeposited MoO_xS_y Electrocatalysts. *ACS Appl. Energy Mater.* (2021)

doi:10.1021/acsaem.1c02234.

216. Thirumoorthi, M. & Thomas Joseph Prakash, J. Structure, optical and electrical properties of indium tin oxide ultra thin films prepared by jet nebulizer spray pyrolysis technique. *J. Asian Ceram. Soc.* (2016) doi:10.1016/j.jascer.2016.01.001.
217. Liu, Z. *et al.* Amorphous MoS_x-Coated TiO₂ Nanotube Arrays for Enhanced Electrocatalytic Hydrogen Evolution Reaction. *J. Phys. Chem. C* **122**, 12589–12597 (2018).
218. Ambrosi, A., Sofer, Z. & Pumera, M. 2H → 1T phase transition and hydrogen evolution activity of MoS₂, MoSe₂, WS₂ and WSe₂ strongly depends on the MX₂ composition. *Chem. Commun.* (2015) doi:10.1039/c5cc00803d.
219. Gopalakrishnan, D., Damien, D. & Shaijumon, M. M. MoS₂ quantum dot-interspersed exfoliated MoS₂ nanosheets. *ACS Nano* (2014) doi:10.1021/nn501479e.
220. Lin, Y. R. *et al.* Band Edge Tailoring in Few-Layer Two-Dimensional Molybdenum Sulfide/Selenide Alloys. *J. Phys. Chem. C* **124**, 22893–22902 (2020).
221. Mosconi, D. *et al.* One-pot synthesis of MoS₂(1-x)Se_{2x} on N-doped reduced graphene oxide: tailoring chemical and structural properties for photoenhanced hydrogen evolution reaction. *Nanoscale Adv.* **2**, 4830–4840 (2020).
222. Feng, Q. *et al.* Growth of large-area 2D MoS₂(1-x)Se_{2x} semiconductor alloys. *Adv. Mater.* **26**, 2648–2653 (2014).
223. Ting, L. R. L. *et al.* Catalytic Activities of Sulfur Atoms in Amorphous Molybdenum Sulfide for the Electrochemical Hydrogen Evolution Reaction. *ACS Catal.* (2016) doi:10.1021/acscatal.5b02369.
224. Sarwar, S. *et al.* Enhancement of hydrogen evolution reaction activity using metal-rich molybdenum sulfotelluride with graphene support: A combined experimental and computational study. *Nano Energy* **90**, 106599 (2021).
225. Ding, Z., Yang, S. W., Wu, G. & Yang, X. Geometry and Greatly Enhanced Thermoelectric Performance of Monolayer MXY Transition-Metal Dichalcogenide: MoSTe as an Example. *Phys. Status Solidi - Rapid Res. Lett.* **15**, 1–9 (2021).
226. Coleman, D. Concise encyclopedia of chemistry Edited by H.-D. Jakubke and H. Jeschkeit, Walter de Gruyter & Co., Berlin, 1994 (1201 pages), DM 128.00, US\$ 69.95, ISBN 3-11-011451-8. *TrAC Trends Anal. Chem.* (1995) doi:10.1016/0165-9936(95)90004-7.
227. Shallenberger, J. R., Katz, R. & Mao, Z. 1T'-MoTe₂ and 2H-MoTe₂ by XPS. *Surf. Sci. Spectra* **28**, 024001 (2021).
228. Hussain, S. *et al.* Enhanced electrocatalytic properties in MoS₂/MoTe₂ hybrid heterostructures for dye-sensitized solar cells. *Appl. Surf. Sci.* **504**, 144401 (2020).
229. Zhao, C. *et al.* Tellurium Single-Crystal Arrays by Low-Temperature Evaporation and Crystallization. *Adv. Mater.* **33**, 1–9 (2021).

230. Walter, C. *et al.* Elemental chalcogens acting as metal-free electrocatalysts for effective alkaline and acidic hydrogen evolution reaction. *Catal. Today* (2023) doi:10.1016/j.cattod.2022.09.023.
231. Hemmat, Z. *et al.* Quasi-Binary Transition Metal Dichalcogenide Alloys: Thermodynamic Stability Prediction, Scalable Synthesis, and Application. *Adv. Mater.* (2020) doi:10.1002/adma.201907041.
232. Mirabelli, G. *et al.* Air sensitivity of MoS₂, MoSe₂, MoTe₂, HfS₂, and HfSe₂. *J. Appl. Phys.* (2016) doi:10.1063/1.4963290.
233. Feng, Q. *et al.* Growth of MoS₂(1-x)Se₂x (x = 0.41-1.00) Monolayer Alloys with Controlled Morphology by Physical Vapor Deposition. *ACS Nano* **9**, 7450–7455 (2015).
234. Cavin, J. & Mishra, R. Equilibrium phase diagrams of isostructural and heterostructural two-dimensional alloys from first principles. *iScience* (2022) doi:10.1016/j.isci.2022.104161.
235. Rajbanshi, B., Sarkar, S. & Sarkar, P. The electronic and optical properties of MoS₂(1-x)Se₂x and MoS₂(1-x)Te₂x monolayers. *Phys. Chem. Chem. Phys.* (2015) doi:10.1039/c5cp04653j.
236. Myung, N. *et al.* Electrosynthesis of MoTe₂ Thin Films: A Combined Voltammetry-Electrochemical Quartz Crystal Microgravimetry Study of Mechanistic Aspects. *J. Electrochem. Soc.* **167**, 116510 (2020).
237. German, E. & Gebauer, R. Why are MoS₂ monolayers not a good catalyst for the oxygen evolution reaction? *Appl. Surf. Sci.* **528**, 146591 (2020).
238. Cheng, K. *et al.* Carrier Dynamics and Transfer across the CdS/MoS₂ Interface upon Optical Excitation. *J. Phys. Chem. Lett.* (2020) doi:10.1021/acs.jpcclett.0c01188.
239. Parija, A. *et al.* Electronic structure modulation of MoS₂ by substitutional Se incorporation and interfacial MoO₃ hybridization: Implications of Fermi engineering for electrocatalytic hydrogen evolution and oxygen evolution. *Chem. Phys. Rev.* **2**, 011401 (2021).
240. Karmodak, N. & Andreussi, O. Oxygen Evolution on MoS₂ Edges: Activation through Surface Oxidation. *J. Phys. Chem. C* **125**, 10397–10405 (2021).
241. Freedy, K. M. *et al.* MoS₂ cleaning by acetone and UV-ozone: Geological and synthetic material. *Appl. Surf. Sci.* **478**, 183–188 (2019).
242. Hoffman, A. N. *et al.* Tuning the electrical properties of WSe₂ via O₂ plasma oxidation: Towards lateral homojunctions. *2D Mater.* (2019) doi:10.1088/2053-1583/ab2fa7.
243. Tang, P. *et al.* Rapid Wafer-Scale Growth of MoS₂(1-x)Se₂x Alloy Monolayers with Tunable Compositions and Optical Properties for High-Performance Photodetectors. *ACS Appl. Nano Mater.* (2021) doi:10.1021/acsnano.1c03137.
244. Sun, Y. *et al.* Hybrid System Combining Two-Dimensional Materials and Ferroelectrics and Its Application in Photodetection. *ACS Nano* (2021) doi:10.1021/acsnano.1c01735.

245. Wu, L. *et al.* Observation of Strong Valley Magnetic Response in Monolayer Transition Metal Dichalcogenide Alloys of Mo_{0.5}W_{0.5}Se₂ and Mo_{0.5}W_{0.5}Se₂/WS₂ Heterostructures. *ACS Nano* (2021) doi:10.1021/acsnano.0c10478.
246. Li, H. *et al.* Growth of alloy MoS₂xSe₂(1-x) nanosheets with fully tunable chemical compositions and optical properties. *J. Am. Chem. Soc.* (2014) doi:10.1021/ja500069b.
247. Luan, X., Zhu, K., Zhang, X. & Yang, P. MoS₂-₂ xSe₂ xNanosheets Grown on Hollow Carbon Spheres for Enhanced Electrochemical Activity. *Langmuir* (2021) doi:10.1021/acs.langmuir.1c01122.
248. Romankiw, L. T. Electroforming of Electronic Devices. *Plat. Surf. Finish.* (1997).
249. Dharmadasa, I. M. & Echendu, O. K. Electrodeposition of Electronic Materials for Applications in Macroelectronic- and Nanotechnology-Based Devices. in *Encyclopedia of Applied Electrochemistry* (2014). doi:10.1007/978-1-4419-6996-5_37.
250. Krohn, A. & Brown, T. M. Electrodeposition of Cobalt-Molybdenum Alloys. *J. Electrochem. Soc.* (1961) doi:10.1149/1.2428011.
251. Zhou, Q., Ge, H., Wei, G. & Wu, Q. Influence of bath composition on the electrodeposition of cobalt-molybdenum amorphous alloy thin films. *J. Univ. Sci. Technol. Beijing Miner. Metall. Mater. (Eng Ed)* (2008) doi:10.1016/S1005-8850(08)60114-0.
252. Kublanovsky, V. S. & Yapontseva, Y. S. Electrocatalytic Properties of Co-Mo Alloys Electrodeposited from a Citrate-Pyrophosphate Electrolyte. *Electrocatalysis* (2014) doi:10.1007/s12678-014-0197-y.
253. Pavlov, D. Secondary Batteries - Lead- Acid Systems | Electrolyte. in *Encyclopedia of Electrochemical Power Sources* (2009). doi:10.1016/B978-044452745-5.00133-7.
254. Gómez, E., Pellicer, E. & Vallés, E. Electrodeposited cobalt-molybdenum magnetic materials. *J. Electroanal. Chem.* (2001) doi:10.1016/S0022-0728(01)00682-9.